2004

Experimental Studies on Nucleation, Nanoparticle's Formation and Polymerization from the Vapor Phase

Victor Maher Abdelsayed
Virginia Commonwealth University

EXPERIMENTAL STUDIES ON NUCLEATION, NANOPARTICLE'S FORMATION AND POLYMERIZATION FROM THE VAPOR PHASE

A Dissertation submitted in partial fulfillment of the requirements for the degree of doctor of philosophy at Virginia Commonwealth University.

by

VICTOR MAHER ABDELSAYED
Bachelor of Science, Ain Shams University, Cairo, Egypt, 1996

Director: M. SAMY EL-SHALL
PROFESSOR, DEPARTMENT OF CHEMISTRY

Virginia Commonwealth University
Richmond, Virginia
December, 2004

Acknowledgement

This work is dedicated to my parents. To my father, who devoted all his life in raising, encouraging, and supporting me. To my wife and daughter. To my brothers.

I would like to acknowledge my advisor Dr. M. Samy El-Shall for his endless support, advice, and patience throughout the course of this research.

I would like also to thank the Department of Chemistry at Virginia Commonwealth University for the financial support via Teaching Assistantship. I would like to thank Dr Mark Rusyniak for his help in teaching me the nucleation experiments, Dr Takafumi Seto for his help with the DMA work and Dr James Howe for his help in the TEM microscopy. Finally, thanks to my colleges in the lab. Dr Hatem Mahmoud, Dr. Edreese Alsharaeh, Dr Yehia Ibrahim, Ridha Mabrouki, Khaled Saoud.

Table of Contents

List of Tables

List of Figures

Abstract

EXPERIMENTAL STUDIES ON NUCLEATION, NANOPARTICLE'S FORMATION AND POLYMERIZATION FROM THE VAPOR PHASE.

By Victor Maher Abdelsayed

A dissertation submitted in partial fulfillment of the requirements for the degree of Doctor of Philosophy at Virginia Commonwealth University.

Virginia Commonwealth University, 2004

Major Director: M. Samy El-Shall
Professor, Department of Chemistry

This research is divided into three major parts. In part I, the critical supersaturations required for the homogeneous nucleation of 2,2,2-trifluorothanol (TFE) vapor have been measured over a temperature range (266-296 K) using an upward thermal diffusion cloud chamber (DCC). The measured supersaturations are in agreement with the predictions of both the classical and the scaled theory of nucleation. Moreover, the condensation of supersaturated TFE vapor on laser-vaporized magnesium nanoparticles has been studied under different experimental conditions, such as the supersaturation, the pressure and the electric field. In part II, the laser vaporization

controlled condensation (LVCC) technique was used to prepare Au-Ag alloy nanoparticles in the vapor phase using designed targets of compressed Au and Ag micron-sized powder mixtures of selected composition. The results showed that the optical properties of these nanoparticles could be tuned depending on the alloy composition and the laser wavelength. Different intermetallic nanoparticles (FeAl and NiAl) from the vapor phase has also been prepared, using the same approach.

In this work, the fraction of the charged particles generated during the laser vaporization process was used to prepare a new class of nanoparticle assemblies in the LVCC chamber under the influence of an electric field. The results showed that the electric field required to induce the formation of these nanoassemblies is material and field dependent. By coupling the LVCC chamber with the differential mobility analyzer, size-selected nanoparticles have been prepared in the vapor phase. The prepared nanoparticles were characterized by different techniques such as scanning electron microscopy (SEM), X-ray diffraction (XRD), transmission electron microscopy (TEM) and UV-visible spectroscopy.

In part III, new methods were developed to prepare nanoparticle-polymer composites from the vapor phase. In the first method, the LVCC method was used to prepare a carbonaceous cross-linked resin, with different nanoparticles (Ni, Pt and FeAl) embedded inside. In the second method, free radical-thermally initiated polymerization was used to polymerize a monomer vapor of styrene on the surfaces of activated Ni nanoparticles.

Chapter 1 Introduction

Nucleation is an important phenomenon that has many practical applications in science and technology. It plays a crucial role in atmospheric as well as in material sciences.[1,2] Nucleation is a first order phase transition process that can take place in vapor, liquid or solid phase. Generally, the nucleation process can be divided into two main types. The simplest and most studied is homogeneous nucleation, in which spontaneous decay of a supersaturated vapor occurs by thermal fluctuations through the formation of nuclei or embryonic droplets in the liquid phase.[1,2] In the homogeneous nucleation, the nuclei consist of the same molecules as in the condensing vapor. In other words, homogeneous nucleation takes place in the absence of any foreign particles, surfaces, or ions. The other type of nucleation is the heterogeneous process that occurs on pre-existing surfaces, foreign particles, or ions. The homogeneous nucleation process from vapor to liquid phase has been extensively studied, both experimentally and theoretically[3,4], for different compounds. This is, in part, because measuring techniques and theoretical models have been developed rapidly over the past decade.

The most popular nucleation theory, the so-called "classical nucleation theory (CNT)", was developed by Becker and Doring in 1936.[1,2] This theory is based on the capillarity approximation, and treats the condensation nucleus as a small fragment of bulk

liquid with the same macroscopic properties as the bulk such as surface tension and density.

The concepts of the classical nucleation theory are important, in understanding the subsequent discussion of the synthesis of nanomaterials. In order to study these factors that control the nucleation process from supersaturated vapors, homogeneous nucleation of fluoroalcohols was studied.

There is an increasing interest in fluoroalcohols not only because of their important uses in biological systems,[5,6] but also because they have been recently used as vapor surfactants.[7] Fluoroalcohols at low concentrations in the vapor phase exhibited surfactant properties by reducing the surface tension of organic and inorganic liquids.[7] Based on these results, trifluoroethanol was used as a nucleating agent in supersaturated vapors of aliphatic alcohols and water, simply by reducing the surface free energy of the nucleation barrier that depends on the cube of the surface tension, and hence increasing their nucleation rates.[8] Therefore, it is of interest to study its vapor-liquid transition.

In this dissertation, the main focus is on the study of the nucleation process from supersaturated vapors that are generated from liquids as well as from metals. Unlike the simple homogeneous transition from vapor to liquid phase, the nucleation of supersaturated metallic vapors has a more complicated pattern that probably involves more than one nucleation mechanism.

Nanomaterials have drawn special attention over the past decade, in part due to their unique properties which are usually very different from bulk properties.[9,10] For example, nanoparticles usually exhibit unique mechanical, electronic, optical and

magnetic properties that have inspired several applications in catalysis, nanodevices and sensors.[9,10] Many of these unique properties are dependent on the size and shape of the nanoparticles.[9,10]

The interest in nanoparticles has stimulated many improvements in the preparation methods involved in the chemical and the physical techniques used. Recently, a novel technique used to synthesize nanoparticles of controlled size and composition, was reported.[11-13] This technique (LVCC) uses laser vaporization of bulk materials, under controlled condensation conditions, to prepare a wide variety of metallic and semiconductor nanoparticles.[11-13] Because of the many advantages over the chemical methods, the LVCC method was used in this dissertation to investigate metallic alloying from the vapor phase and the preparation of size-selected metal nanoparticles.

Shown in Figure 1 are the different research areas that were explored in this study. There are two main topics; a) homogeneous nucleation from supersaturated vapor to liquid phase and b) nanoparticle formation from the vapor phase using the laser vaporization technique. The commonality of these two projects was also explored. The condensation of supersaturated vapor, under well-defined nucleation conditions, on neutral and charged nanoparticles generated from laser vaporization of a metallic target was studied.

The assembly of nanoparticles, under the influence of an electric field offers many opportunities for the fabrication of microwires,[14] nanostructured films,[15] ordered arrays,[16] and dendritic structures.[17] These assemblies are usually established by the means of electrophoretic,[15,16] dielectrophoretic,[14,17] and electrochemical[18,19] forces that act on the

particles. The capability of the LVCC method has also been enhanced by taking advantage of the fact that laser vaporization produces a significant fraction of charged nanoparticles (by ions or free electrons). Typically, a 10 ns laser pulse with power density of (10^6-10^7 W/cm^2) produces about 10^{14} atoms and 10^6 ions from any metal or solid target.[11] In this dissertation, the effect of an electric field on charged nanoparticles, generated by the laser vaporization in an inert gas (He) and in supersaturated vapor of fluoroalcohols was investigated. Additionally, the electric field was used to sort charged nanoparticles according to their sizes. The Differential Mobility Analyzer (DMA)[20] was used to prepare monodispersed nanoparticles and to measure the size distribution under given nucleation conditions during the LVCC process. Figure 2 shows a schematic with the different aspects and uses of the electric field effects on charged nanoparticles prepared in the vapor phase by laser vaporization.

A new method was developed to prepare nanoparticle-polymer composites from the vapor phase. Free-radical thermally initiated polymerization was used to polymerize a monomer vapor on the surfaces of activated nanoparticles. The polymer component in the nanocomposite was characterized by FT-IR and ^{1}H-NMR spectroscopy. The nanoparticles dispersity in the polymer matrix and their crystalline nature were analyzed under the scanning transmission electron microscope (STEM) and XRD.

The chapters covered in this dissertation are as follows: Chapter Two begins with a review of the classical nucleation theory followed by the experimental measurements of the homogeneous nucleation rate of 2,2,2-trifluoroethanol. Chapter Three, the synthesis and characterization of intermetallic alloys nanoparticles, prepared from the vapor phase

are presented alond with the investigation of the effect of an electric field on the assemblies and growth of nanoparticles from the vapor phase. In Chapter Four, the condensation of the supersaturated vapor on neutral and charged nanoparticles was explored. Finally, in Chapter Five, new methods for incorporation of nanoparticles in polymers were investigated.

In general, the overall work presented in this dissertation illustrates the importance of nucleation studies in understanding the mechanisms of nanoparticle's formation from the vapor phase and the role of ion-induced nucleation in the growth mechanism and the morphology of the resulting nanoparticles. Future studies could specifically deal with using the concept of surface enrichment to control the surface properties of nanoparticles prepared from the vapor phase. Other possibilities include the application of ion-induced nucleation to produce metallic filaments and fibers embedded within polymer films generated by gas phase polymerization.

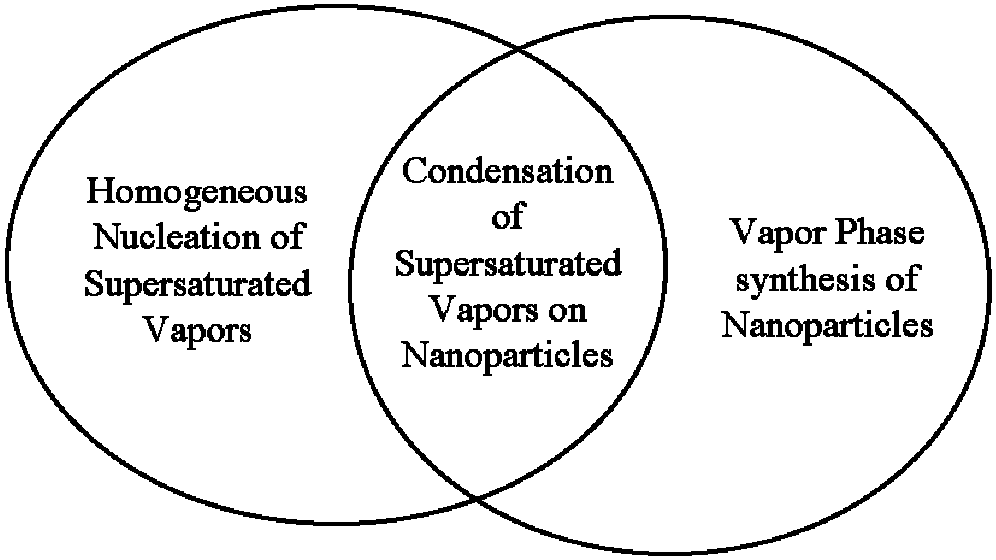

Figure 1. A sketch shows areas of study explored in this dissertation.

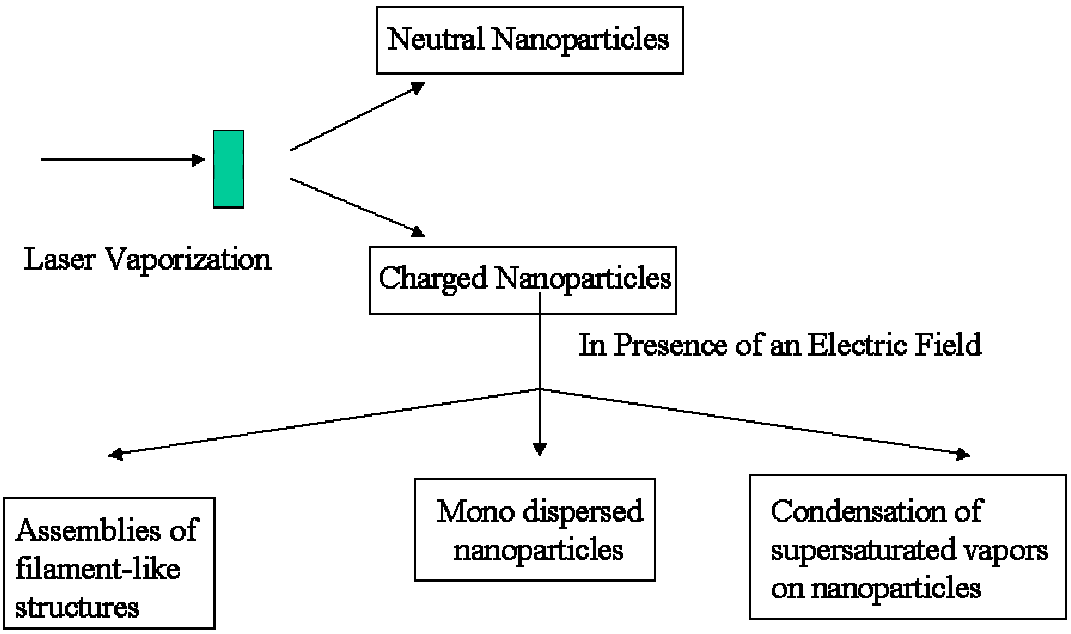

Figure 2. A schematic shows different aspects and uses of the electric field effect on charged nanoparticles prepared in the vapor phase by laser vaporization.

Chapter 2 Homogeneous Nucleation of Single Component

2-1 Introduction

Nucleation is an important phenomenon in science and technology. It plays a crucial role in aerosol and cloud formation, in materials science,[1,2,21] as well as in production and purification of chemicals and pharmaceuticals.[22] The study of homogeneous nucleation processes of supersaturated vapors to liquids has become of interest. This interest has stimulated many experimental and theoretical developments over the last decade.[3,4] To extend the current level of understanding of homogeneous nucleation, different models have been developed to gain a better understanding of the experimental results.[23-25]

The approach taken in this study was to measure the critical supersaturations of 2,2,2-trifluoroethanol (TFE), and then to compare the experimental results obtained with the theoretical predictions of different models. Critical supersaturation (S_{cr}) is defined as the ratio of actual partial pressure of the vapor to the equilibrium vapor pressure of the bulk liquid that is required for the onset of nucleation at a rate of 1-3 drop/cm^3/s. The onset of nucleation of many substances is well predicted by the classical theory, however, the agreement between the predictions by classical nucleation theory (CNT) and experimental data is not comparable for all substances.[26-28] For substances such as highly polar liquids, deviation from the theory is very significant.[28] The deviation from the CNT

predictions led many scientists to develop new theories and proposals for the nucleation mechanism. Among these theories are the scaled models that provide useful ways to correlate the experimental data of a series of different materials with their molecular properties. Two scaling models were used in this study; the corresponding states approach, which was developed by McGraw to predict the nucleation properties of different substances under constant reduced nucleation barrier height,[25] and the scaled model, which was developed by Hale to predict the critical supersaturation and nucleation rates.[23,24]

TFE is a fluoroalcohol widely used in biomedical applications, especially in determining protein folding and denaturation mechanisms where it is known to stabilize the α-helical structure in proteins.[5,6] Recent studies have suggested that TFE, at low concentrations in the vapor phase, exhibits surfactant properties by essentially reducing the surface tension of organic and inorganic liquids.[7] More recently, El-Shall and coworkers used TFE as a nucleating agent in supersaturated vapors of different alcohols.[8] They have reported that the addition of TFE traces to supersaturated vapor of ethanol leads to a significant enhancement in the ethanol nucleation rate by about four orders of magnitude. They explained this effect by the surface enrichment phenomenon where the surface composition of the nucleating cluster becomes enriched with the low surface tension component (TFE). As a result, the surface tension of the nucleating cluster would decrease, and hence the nucleation barrier would significantly decrease, leading to a high rate of nucleation.[8] In spite of its important applications, either when it is in the liquid or

the vapor phase, the homogeneous nucleation of TFE, to the best of our knowledge, has never been studied before.

The research presented in this chapter involves the study of the homogeneous nucleation of TFE using the diffusion cloud chamber. Specifically, the measurments of the critical supersaturations will be presented and compared with three different models. These models are the classical nucleation theory, the corresponding state model, and the scaling model.

2-2 Classical Nucleation Theory

The history of the nucleation theory goes back to J. Willard Gibbs (1876-1878) who developed the thermodynamic theory of curved surfaces. In 1926, Volmer and Weber argued that the nucleation rate was proportional to an exponential term that included the energy barrier for nucleation. However, they did not determine the pre-exponential factor. In 1927, Farkas started to develop a kinetic approach to vapor-liquid phase transition. The work by Becker-Doring (1935), Zeldovich (1943) and Frenkel (1946) developed the so-called "classical nucleation theory (CNT)". The CNT theory adopted two major approximations. First, it was assumed that the macroscopic thermodynamic properties of bulk substance are equal to the microscopic properties of a cluster for the same substance. For example, the surface tension of a bulk, planer liquid was assumed to be the same as the surface tension of a small spherical cluster (i.e. $n \approx 100$) in a supersaturated vapor. The latter assumption has caused a great deal of controversy. Secondly, a steady state distribution of clusters was assumed.

When a liquid is heated under well-defined temperature and pressure, its vapor pressure (P) can exceed its equilibrium vapor pressure (P_e). In this case, the vapor is known to be "supersaturated". Thermodynamically, this vapor is in a metastable state and can be easily condensed back to liquid through homogeneous nucleation. In homogeneous nucleation, supersaturated vapor, which is composed of a broad cluster-size distribution, starts to nucleate once a cluster reachs a critical size. The Gibbs free energy change during the nucleation process is defined as:

$$G = U - TS + PV \qquad \text{Eq. 2-1}$$

A very small change in Gibbs free energy is given by:

$$dG = dU - TdS - SdT + PdV + VdP \qquad \text{Eq. 2-2}$$

The change in the internal energy (U) is given by:

$$dU = TdS - PdV + \mu_i dN_i \qquad \text{Eq. 2-3}$$

From the above equations (2-2 and 2-3), the change in Gibbs free energy is given by:

$$dG = VdP - SdT + \mu_i dN_i \qquad \text{Eq. 2-4}$$

At constant T and P, the metastable vapor starts to condense and a new energy term must be considered. This term, the surface free energy term, will account for the formation of a new interface between the newly formed cluster (droplet) and the supersaturated vapor. If we consider a system that contains (N_V) molecules at a constant temperature (T) and a constant pressure (P), then the free energy of formation of a nucleus of surface area (A), containing (n) molecules, can be obtained by integrating over the cluster area as well as the number of molecules in the system, which is given by:

$$\int dG = \int_{A}^{} \sigma dA + \int_{}^{n} \mu_l dn + \int_{N_V}^{N_V - n} \mu_V dN_V \qquad \text{Eq. 2-5}$$

The above equation (2-5) can be written as two terms:

$$\Delta G = (\mu_l - \mu_V)n + \sigma A \qquad \text{Eq. 2-6}$$

The first term (left) is due to the bulk contribution and is given by the change in the chemical potential per molecule between the liquid and the supersaturated vapor multiplied by number of molecules in the cluster (n). This term is a negative term since the chemical potential of the liquid is always less than that of the supersaturated vapor

phase due to stability of the liquid over the supersaturated vapor. The second term is a negative term due to the surface contribution. This term accounts for the energy required to create a new interface between the formed cluster and the supersaturated vapor. It is given by the surface free energy per molecule (σ) multiplied by the surface area of the cluster (A). The bulk contribution (free energy ΔG_{Bulk} term) at constant T can also be written as:

$$\Delta G_{Bulk} = \int_{P}^{Pe} V dP = nkT \int_{P}^{Pe} \frac{1}{P} dP = -nKT \ln S \qquad \text{Eq. 2-7}$$

where, S is the supersaturation ratio of the vapor, given as $S = \frac{P}{P_e}$.

The change in free energy becomes:

$$\Delta G = -nkT \ln S + \sigma A \qquad \text{Eq. 2-8}$$

If we assume spherical nuclei, we can write the free energy of formation of this nucleus as a function of its radius (r):

$$\Delta G(r) = -(\frac{4}{3}\pi r^3)(\frac{\rho}{M})RT \ln S + 4\pi r^2 \sigma \qquad \text{Eq. 2-9}$$

where, ρ is the bulk density, σ is the surface energy per molecule for the bulk material, and M is the molecular weight. By using the relationship between the number of molecules per cluster (n) and the radius of cluster (r), which is given by:

$$\frac{4}{3}\pi r^3 = \frac{nM}{\rho N_A} \qquad \text{Eq. 2-10}$$

The free energy can be also written as a function of the number of molecules per nucleus (n) as:

$$\Delta G(n) = -nkT\ln S + 4\pi\sigma(\frac{3V}{4\pi})^{2/3} n^{2/3} \qquad \text{Eq. 2-11}$$

It is clear from the previous equations that for small cluster radii the surface energy term will dominate the free energy of formation, but for large clusters the bulk energy term will be dominant. By plotting the free energy of formation as a function of the number of molecules in a cluster (n) at a constant T and P, the free energy would increase until it reaches a maximum value, corresponding to the critical cluster size (nucleus n^*), it then decreases rapidly. The critical size can be determined by equating the first derivative of (ΔG) with respect to n to zero,(i.e: $(\frac{d\Delta G}{dn})_{n=n^*} = 0$), then solving for (n).

$$n^* = \frac{(\frac{8}{3}\pi\sigma)^3 (\frac{3V}{4\pi})^2}{(kT\ln S)^3} \qquad \text{Eq. 2-12}$$

Based on the above equation, the critical number of molecules (n^*) required to start the condensation process (followed by a cluster growth to a macro-size droplet) depends on the vapor supersaturation and the temperature. The more supersaturated the vapor is, the smaller the size of the nucleus required to start the nucleation, and the lower the energy barrier needed, according to the theory. The critical cluster size (n^*) depends on the surface tension of the liquid under investigation in a directly proportional way. The free energy barrier required to start the homogeneous nucleation process can be determined by plugging in (n^*) into (Eq. 1-12), as:

$$\Delta G^* = \frac{16\pi\sigma^3 V^2}{3(kT\ln S)^2} \qquad \text{Eq. 2-13}$$

In a supersaturated vapor, as mentioned before, there is a broad distribution of clusters of different sizes. Among these clusters are (n^*) sized clusters with the highest energy of formation (ΔG^*). The formation of an (n^*) sized cluster in a supersaturated vapor is a prerequisite for the onset of a first order phase transition. Actually, none of the sub critical nuclei (with $n < n^*$) can grow spontaneously due to the fact that this growth is accompanied by an increase in the free energy of formation (ΔG), while for the supercritical nuclei (with $n > n^*$), the clusters can grow spontaneously due to the fact that this growth is accompanied by a decrease in the free energy of formation (ΔG). In conclusion, the driving force for the occurrence of the first order phase transition of a supersaturated vapor is the ability to overcome the energy barrier between a metastable and a truly stable state, by thermal fluctuation. Once that happens, a phase transition takes place. Thermal fluctuation is the only process that takes the small cluster (with $n < n^*$) up the hill through evaporation-condensation processes. By assuming a steady state condition, the CNT prediction for the rate of homogeneous nucleation J is given by:

$$J = K\,exp\left(-\Delta G^*/kT\right) \qquad \text{Eq. 2-14}$$

Where (k) is the Boltzmann constant, (T) is the temperature, and (ΔG^*) is the Gibbs free energy of nucleus formation. The pre-exponential factor K is calculated from:

$$K = \left(2\sigma M/\pi N_A\right)^{1/2}\left(P/kT\right)^2/\rho \qquad \text{Eq. 2-15}$$

Where (ρ) is the liquid density, (N_A)is Avogadro's number, (σ) is the flat surface tension of the liquid, (M) is the molecular weight, and (P) is the pressure of the vapor. By setting $J = 1$

and using the literature values of the equilibrium vapor pressure, the liquid density, and the surface tension, the critical supersaturation can be predicted.

2-3. Experimental

The critical supersaturation of TFE was measured using the upward thermal diffusion cloud chamber (DCC). A detailed description of this chamber is in the literature.[29-31] Only a brief description is given here; the chamber consisted of two aluminum circular plates separated by a glass ring. Circulating fluids (methanol and silicon oil) were used to control the temperatures of the top and bottom plates such that the top plate was maintained at a lower temperature compared to the bottom plate. The bottom plate was covered by a very shallow pool, about (1-2 mm height), of the TFE liquid (75 ml, Aldrich NMR grade, 99.5+ %). By applying a temperature difference between the top and the bottom plates, vapor started to evaporate from the surface of the pool, diffused upward through a noncondensable gas (Helium), and condensed on the cold top plate to form a thin film of liquid. The condensed liquid returned to the liquid pool by flowing along the chamber walls. The experimental setup sketch is shown in Figure 3.

By knowing the temperature of the liquid pool, the temperature of the top plate, and the total pressure inside the chamber, the partial pressure, temperature, density and supersaturation profiles could be calculated by solving the mass and heat transfer equations inside the chamber.[30] For example, the chamber profiles for supersaturated trifluoroethanol vapor at (T_0 = 305 K, T_1 = 267 K and P_{total} = 700 Torr) are given in Figure 4, where T_o is the temperature of the surface of the liquid pool, T_1 is the temperature of the top plate, and P_t is the total pressure inside the chamber. The

supersaturation reaches a maximum at about 0.7 reduced height (nucleation zone) inside the chamber.

The critical supersaturation was measured by varying the temperature difference between the chamber plates until a nucleation rate (1-2 drops cm^{-3} s^{-1}) was achieved. The onset of nucleation was determined by observing the forward scattering of light from drops falling through a horizontal sheet of He-Ne laser beam positioned near the middle of the chamber. Using a photomultiplier that is connected with discriminating and counting electronics, the number of drops within a well-defined volume was measured. An electric field of 65 V/cm was used between the top and bottom plate to remove any unwanted ions resulting from cosmic rays or natural radioactive sources, so that they would not cause interference during the homogeneous nucleation measurements.

2-4 Results and Discussion

The chamber parameters, namely T_o, the surface temperature of the liquid pool, T_1, the upper plate temperature and P_t, the total pressure required to obtain a nucleation rate of 1-3 drops cm^{-3} s^{-1} were listed for each experiment in Table 1. Two stability criteria, the pressure P_t/P_0 ratio and density ρ_1/ρ_0 ratio for each experiment, are also shown in Table 1 where P_0 is the equilibrium vapor pressure at T_0, and ρ_1 and ρ_0 are the total densities of the vapor-He gas mixture at T_1 and T_0, respectively. The first stability condition of the chamber is satisfied by the relation:[32]

$$P_t / P_0 << \frac{1-(M_w / M_g)}{1-(T_0 / T_1)} \qquad \text{Eq. 2-16}$$

M_w and M_g are the molecular weights of the working fluid (TFE) and carrier gas (He), respectively. At lower pressure ratios (less than 2.5), the supersaturation depends on the amount of the carrier gas used,[32] though at higher-pressure ratios convection in the chamber could take place. In all the experiments reported in Table 1, we do not observe any visual convection in the chamber, and the $(1-M_w/M_g)$ / $(1-T_o/T_1)$ ratio ranges from 147-160. The second stability criterion was the density ratio (ρ_1/ρ_0), which is always less than 0.4 (insuring the absence of any convection inside the chamber).

The thermophysical properties needed to calculate the temperature and partial pressure profiles in the chamber for 2,2,2-trifluoroethanol are given in Table 2. Using the data in Table 1 together with the physical properties in Table 2, the solutions of the heat and mass flux equations[30] yield the dependence of supersaturation on elevation inside the chamber for each experiment.

The critical supersaturations of TFE were measured within the temperature range of 266 K to 296 K. Figure 5 shows the dependence of the critical supersaturation on the temperature for TFE. The predictions of the CNT are also shown in Figure 5 as a solid curve. A good agreement was observed between the experimental results and the theory over the entire temperature range. In spite of its approximate nature, the CNT has predicted the critical supersaturations required for homogeneous nucleation for a large variety of simple substances such as n-alkanes,[30] alcohols,[33] alkyl benzenes[34] and halogenated methane and ethane.[35] However, in some cases, the theory prediction deviates from the experimental results. For example, the theory failed to predict the critical supersaturations for associated,[26,27] highly polar,[28] and hydrogen bonded[36] vapors. The CNT has provided a significant progress in qualitatively understanding the factors that control the formation of a new phase. However, it failed to provide a consistent molecular picture of the nucleation process. For instance, various molecular interactions within the nucleating clusters, such as hydrogen bonding and dipole-dipole, were not included in the CNT formalism.

The corresponding states correlation, derived by McGraw[25], was applied in this study in order to compare the nucleation behavior (critical supersaturations) of TFE with that of simple fluids in a dimensionless form. In this approach, the maximum free energy of nucleation (W*) is expressed as:

$$W^*/kT = 282.3G(T_r)(\log S)^{-2} \qquad \text{Eq. 2-17}$$

and:

$$G(T_r) = \frac{T_r^{-3}(1-T_r)^{11/3}}{[1+0.75(1-T_r)+1.75(1-T_r)^{1/3}]^2} \qquad \text{Eq. 2-18}$$

where T_r, is the reduced temperature (= T/T_c) and T_c is the critical temperature. The barrier height given in Eq. 2-17 is based on Guggenheim's empirical correlations of the surface tension and the number density of heavier rare gases. Therefore, it is a good approximation for the reduced barrier height of simple fluids. McGraw found that for simple fluids, the energy barrier for nucleation rate near unity lies between 50 and 70 kT. Figure 6 shows the experimental critical supersaturation plotted as a function of reduced temperature. The solid and the dashed curves represent the upper and lower boundaries for simple fluids, at 50 and 70 kT, respectively, calculated from Eq. 2-17. It is clear that the TFE nucleation behavior is slightly deviated from that of a simple fluid. This deviation could also be discussed in terms of Pitzer's accentric parameter, ($\omega = -\log P_r(T_r = 0.7) - 1$)[37], which is a measure for the increase in the entropy of vaporization over that for a simple fluid. The value of ω for TFE is 0.6372, while for simple fluids, like Ar, it is almost zero.

One of the limitations of the classical nucleation theory was the availability of the experimental physical constants for the fluid under investigation, such as the vapor pressure and the surface tension in order to calculate the critical supersaturation correctly. Hale[23,24] was able to scale the CNT into a material independent by utilizing the critical point quantities. The scaling law for the critical supersaturation is given by:

$$\ln S_c = 0.53(\Omega[(T_c/T)-1])^{3/2} \qquad \text{Eq. 2-19}$$

Where Ω is the excess surface entropy per molecule in the cluster. The bulk liquid value for Ω is approximated by the Eotvos constant, K_e, which is defined by:

$$kN_A^{2/3}\Omega 1 \approx K_e = (M/\rho)^{2/3}\frac{\sigma}{(T_c - T)} \qquad \text{Eq. 2-20}$$

since $kN_A^{2/3}$ is approximately equal to one. N_A, M, ρ and σ are Avogadro's number, molecular weight, liquid density, and surface tension of the liquid. The excess surface entropy Ω can also be calculated from the temperature dependence of the surface energy according to the following equation:

$$\Omega 2 = -\left(\frac{\partial\sigma}{\partial T}\right)/(kn^{2/3}) \qquad \text{Eq. 2-21}$$

Where *n* is the liquid number density.

The critical supersaturation was calculated using the values of Ω given in Eq. (21 and 22) as a function of temperature to demonstrate the predictive ability of the scaling law. The results are shown in Figure 7 where the solid and the dashed curves represent the critical supersaturation calculated from Eq.2-19 using Ω1 and Ω2, respectively. It is clear from this figure that using Ω1, the calculated supersaturation matched the experimental values. On the other hand, using Ω2 resulted in a large discrepancy between calculated and experimental results. It is also worth mentioning that the agreement between the experimental and calculated critical supersaturation extends throughout the entire temperature range studied. The experimental data were also plotted as $\ln S_c/\Omega^{3/2}$ vs. $[(T_c/T)-1]^{3/2}$ as shown in Figure 8, where the solid line in the graph represents the

prediction of the scaling model. It was clear that Hale's model allowed for as accurate a prediction of the threshold of nucleation of TFE as the CNT did.

Additionally, the measured supersaturation could be used to estimate the critical temperature (T_c) of the TFE by rearranging Eq. 2-19 and replotting the experimental data as $(\ln S_c)^{2/3}$ vs. 1/T. The results are shown in Figure 9, where the solid line represents the linear fit. The estimated T_c can be obtained by dividing the slope over the intercept of the least-square-fit line. The estimated T_c value is 505.26 K, which is about 1% higher than the experimental value (499.29 K).[38]

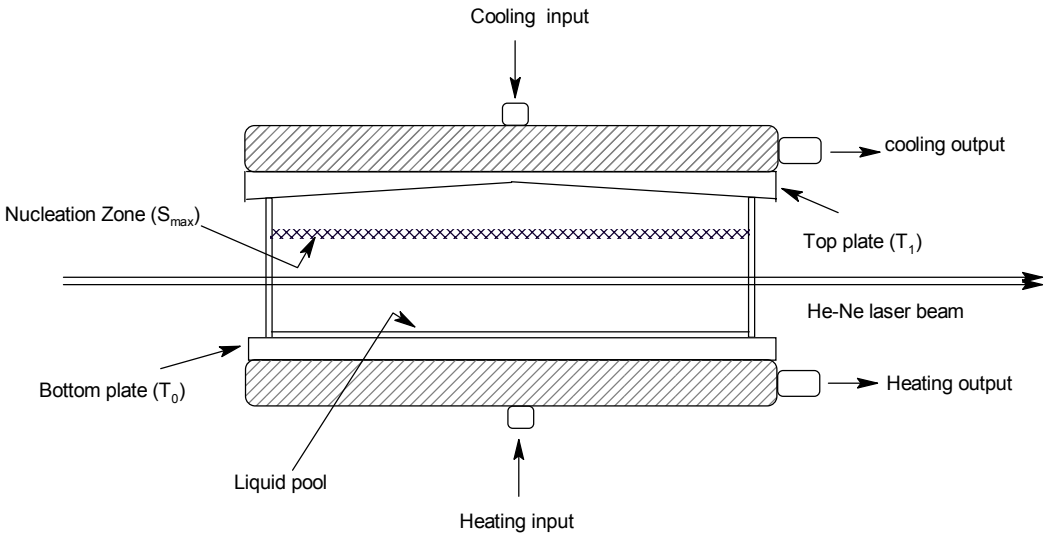

Figure 3. Schematic for the upward diffusion cloud chamber (DCC) used to measure the vapor to liquid nucleation for trifluoroethanol.

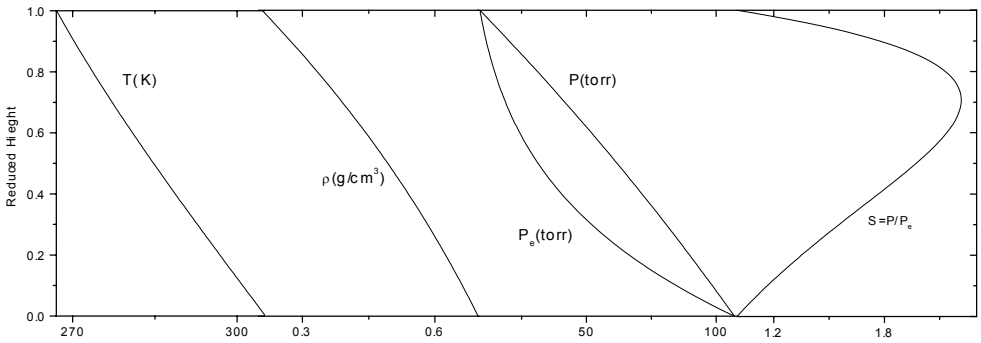

Figure 4. Temperature, total vapor density, equilibrium vapor pressure, partial pressure and supersaturation profiles calculated for the observed nucleation of 1-3 drops cm^{-3} sec^{-1} for trifluoroethanol at T_o=305 K, T_1=267 K and P_t=700 Torr.

Table 1. Measured data for each experiment for 2,2,2-trifluoroethanol. T_0, the temperature of the pool surface in Kelvin; T_1, the temperature of the top plate in Kelvin; P_t, the total pressure in Torr; P_t/P_0, the pressure ratio; and ρ_1/ρ_0 the density ratio. P_0 is the equilibrium vapor pressure of the working fluid at T_0; ρ_1 and ρ_0 are the total density of the vapor-carrier gas mixture at T_1 and T_0, respectively.

Experiment Number	T_o (K)	T_1 (K)	P_t (Torr)	P_t/P_0	ρ_1/ρ_0
1	295.83	254.38	656.6	10.486	0.38527
2	296	254.33	621.1	9.819	0.37005
3	298.45	256.73	655.2	8.965	0.35236
4	300.05	258.38	638.8	7.967	0.32965
5	300.23	258.45	638.9	7.886	0.3275
6	300.37	258.55	675.7	8.273	0.33724
7	300.48	258.83	676.6	8.232	0.33681
8	300.63	258.65	676.8	8.164	0.33438
9	304.23	262.45	657.9	6.477	0.2949
10	304.42	262.52	658.8	6.418	0.2931
11	305.38	263.62	701.4	6.479	0.29646
12	307.98	266.25	676.65	5.425	0.27016
13	308.42	266.65	708.1	5.544	0.27406
14	308.42	266.77	708.4	5.547	0.27461
15	308.65	266.65	681.7	5.272	0.26554
16	309.92	267.95	726.8	5.253	0.26683
17	312.08	269.93	700.4	4.518	0.24704
18	312.97	270.85	708.5	4.364	0.24372
19	314.4	272.37	756.4	4.328	0.24517
20	314.53	272.27	756.1	4.298	0.24337
21	314.58	272.4	756.55	4.29	0.24355
22	316.22	274.23	730.05	3.809	0.23183
23	316.25	274.23	730.2	3.804	0.23157
24	316.85	274.85	737.2	3.726	0.23014
25	316.98	274.57	737.15	3.702	0.22756
26	317.53	275.7	767.8	3.751	0.23288
27	317.62	275.73	768.25	3.736	0.23226
28	319.17	277.02	792.7	3.57	0.22815
29	319.87	278.67	762.7	3.319	0.22622
30	323.9	281.45	835.4	2.993	0.21566
31	325.18	282.55	843.2	2.844	0.21192
32	326.8	284.35	853.8	2.67	0.20997
33	328.45	285.68	884.15	2.563	0.20748

34	328.47	285.7	883.3	2.558	0.20735

Table 2. Thermophysical properties of 2,2,2-trifluoroethanol and helium.

2,2,2-trifluoroethanol

M = 104.04, T_c[a] = 499.29, P_c[a] = 4.8606, T_b[b] =347.04
D_{12}[c] = 0.272702, ΔH_{vap}[d] = 43.97
d[e] = 10^{-3}(2531.269 - 8.5439 T+2.42742 × 10^{-2} T^2 – 2.865 × 10^{-5} T^3)

$$\ln\frac{P_e}{P_c} = \frac{T_c}{T}\sum_{i=1}^{4} a_i\left(1-\frac{T}{T_c}\right)^{\nu_i}$$

where, a1=-8.895557585, a2=2.762807991, a3=-3.310311526, a4=-4.676431484
ν1=1.0, ν2=1.5, ν3=2.0, ν4=3.0 [a]

σ[f] = 21.04673586[(1- T/T_c) / 0.4]$^{0.86253227}$
Cp[g] = 22.571 + 0.31363×T – 2.2228 × 10^{-4} T^2 + 5.7401 × 10^{-8} T^3
η[h] = 1.3086 × 10^{-5} $T^{1.5}$/(T+291.1316)
λ[i] = 2.914138 × 10^{-7} + 1.135173 × 10^{-5} T + 7.9895572.× 10^{-8} T^2 + 3.232073 × 10^{-13} T^3

Helium

M = 4.006
η = 1.455E-5×$T^{1.5}$/(T+74.1)
λ = 7.37697E-5 + 1.139222E-6×T + 6.343536E-10×T^2

Values of M, molecular weight in g/mol; T_c, critical temperature in K; P_c, critical pressure in MPa; T_b, normal boiling point in K; D_{12}, binary diffusion coefficient at 273 K and 101.3 kPa; ΔH_{vap}, the enthalpy of vaporization at the normal boiling point in kJ mol^{-1}; d, the density of the liquid in g/cm^3; P_e, the equilibrium vapor pressure in Pa; σ, the surface tension in dyn/cm; C_p, the isobaric heat capacity of the vapor in J/mol K; η, the viscosity of the vapor in poise; λ, the thermal conductivity of the vapor in J/(m s K). T= temperature in K, t = temperature in °C.

[a]Reference [38]
[b]Reference [39]
[c]Reference [40]
[d]Reference [41]
[e]Reference [42]
[f]Calculated using Riedel correlation method, reference[43]
[g]Reference [44]
[h]Calculated using Reichenberg estimation, reference[43]
[i]Calculated using Roy and Thodus method, reference[43]

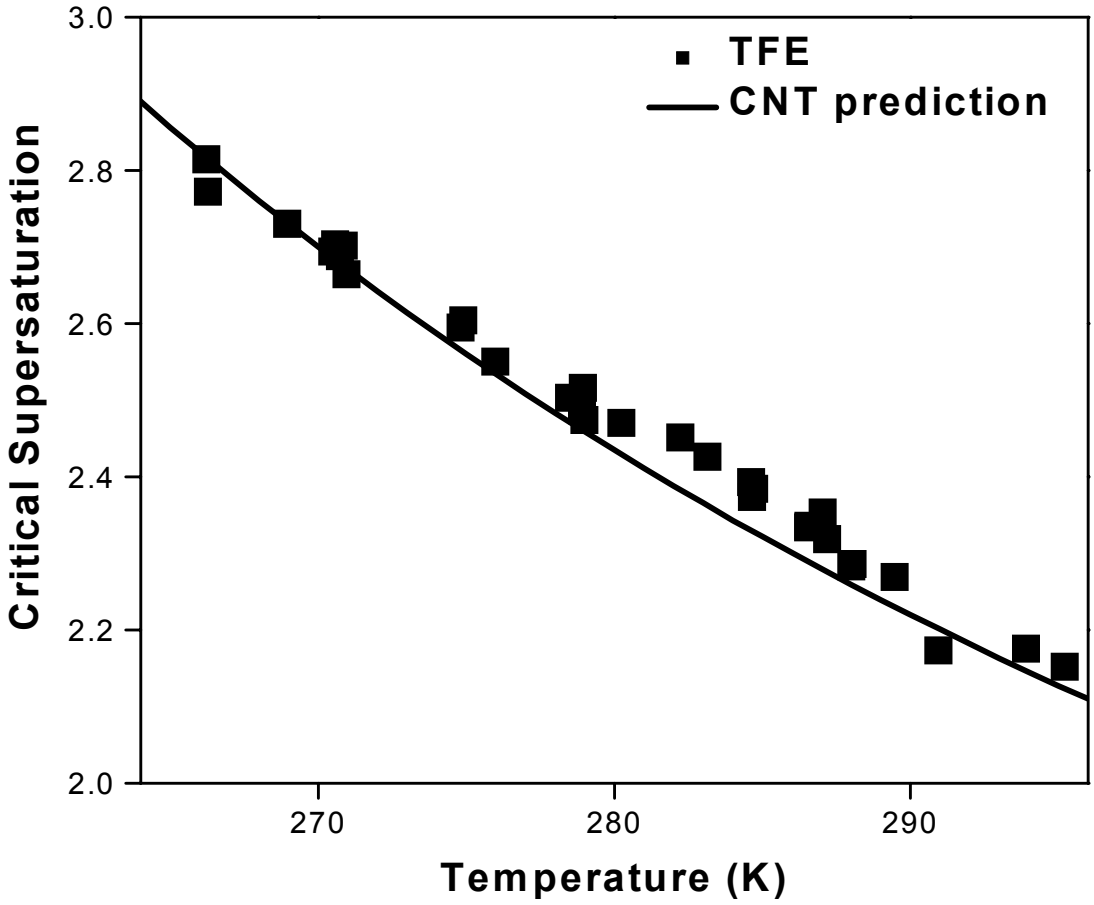

Figure 5. Critical supersaturation vs. temperature for 2,2,2-trifluoroethanol, the solid line represents the classical nucleation theory prediction.

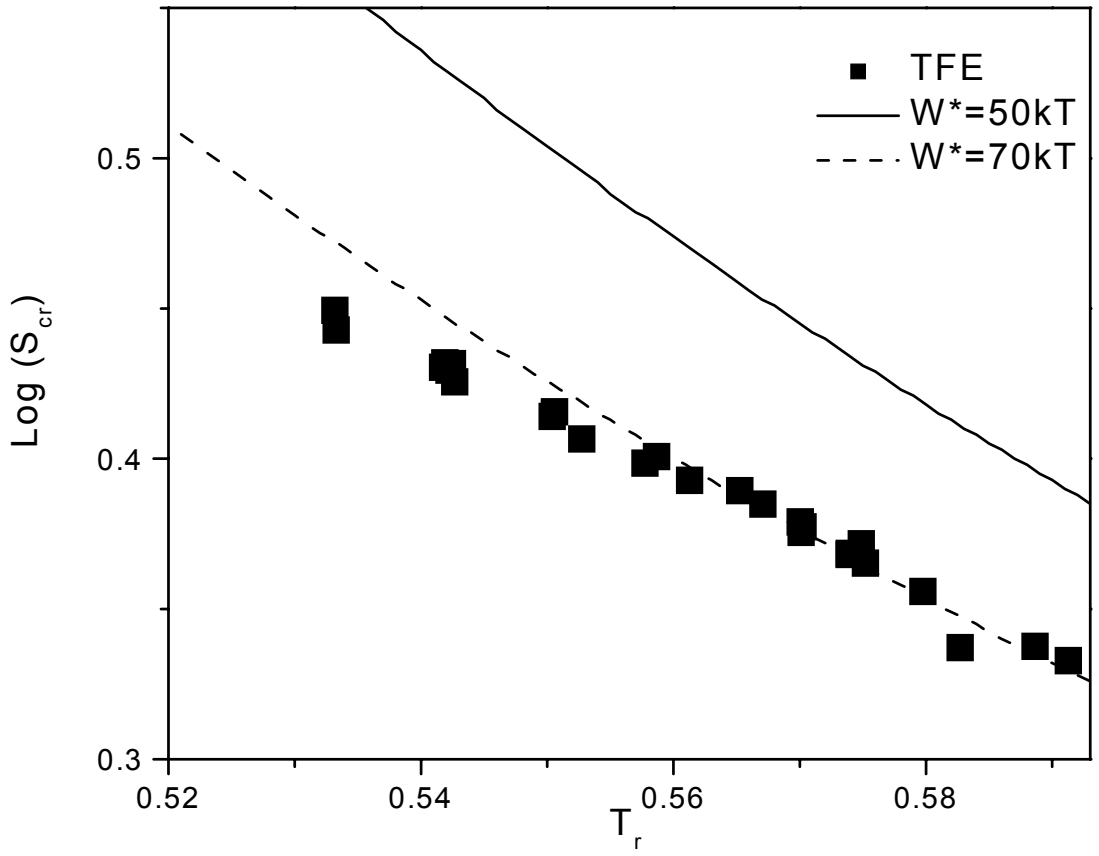

Figure 6. Critical supersaturation vs. reduced temperature for 2,2,2-trifluoroethanol. The upper solid and lower dashed curves are for simple fluids and represent barrier heights of 50 and 70 kT, respectively.

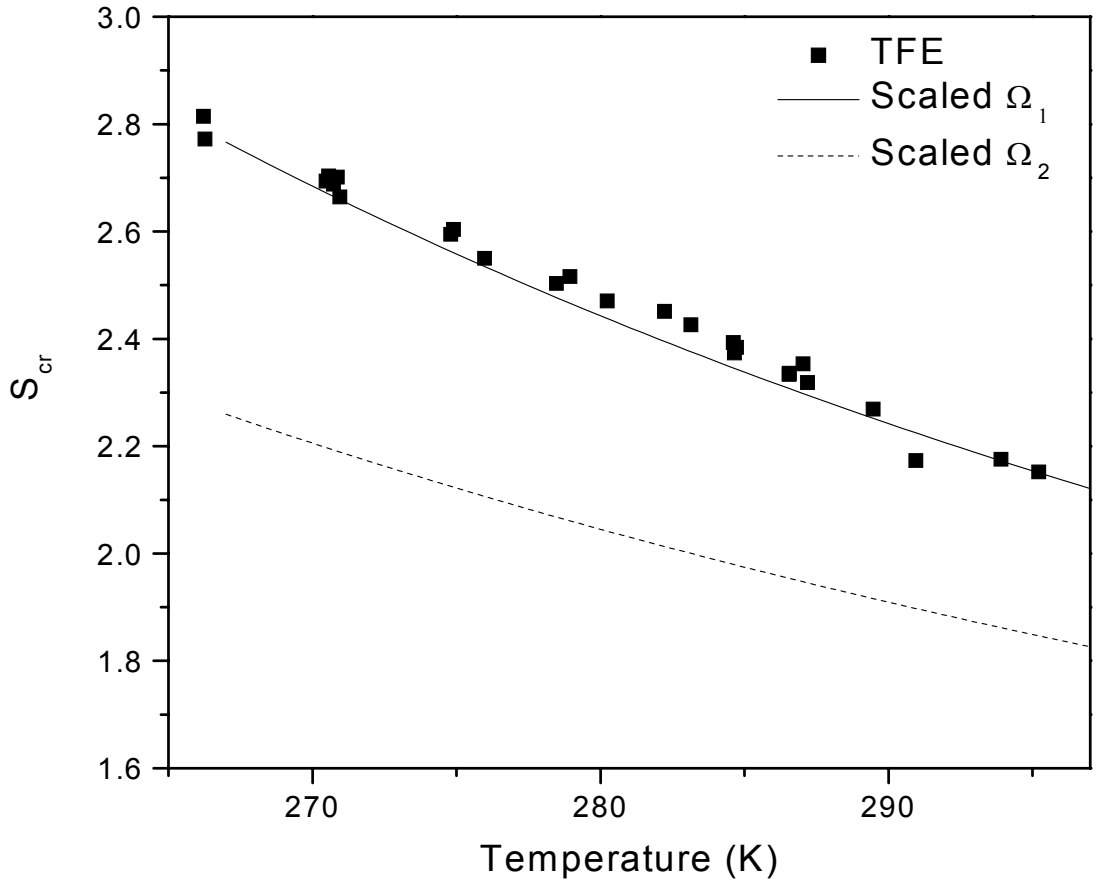

Figure 7. Critical supersaturation vs. temperature for 2,2,2-trifluoroethanol (solid squares). The prediction from the scaling law using Ω1 and Ω2 are presented as solid and dotted curves, respectively.

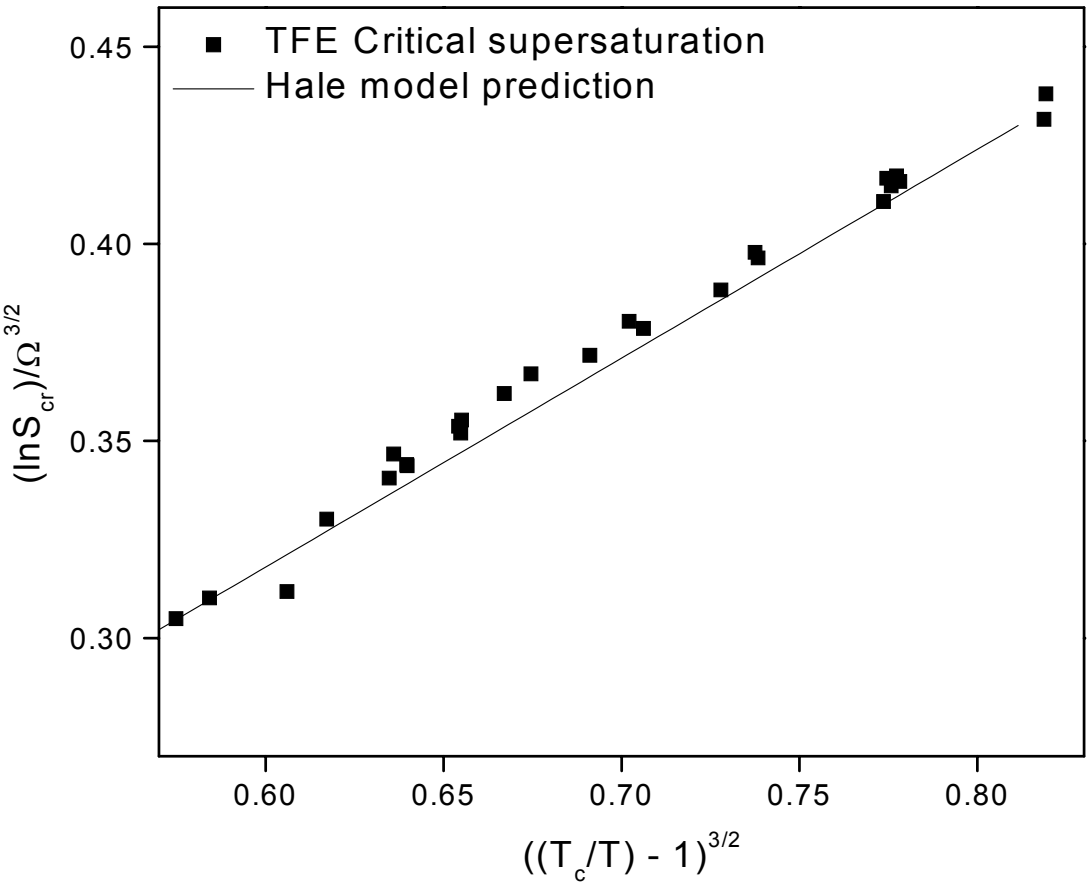

Figure 8. Scaled critical supersaturations of 2,2,2-trifluoroethanol, the solid line represents the prediction from the scaling model.

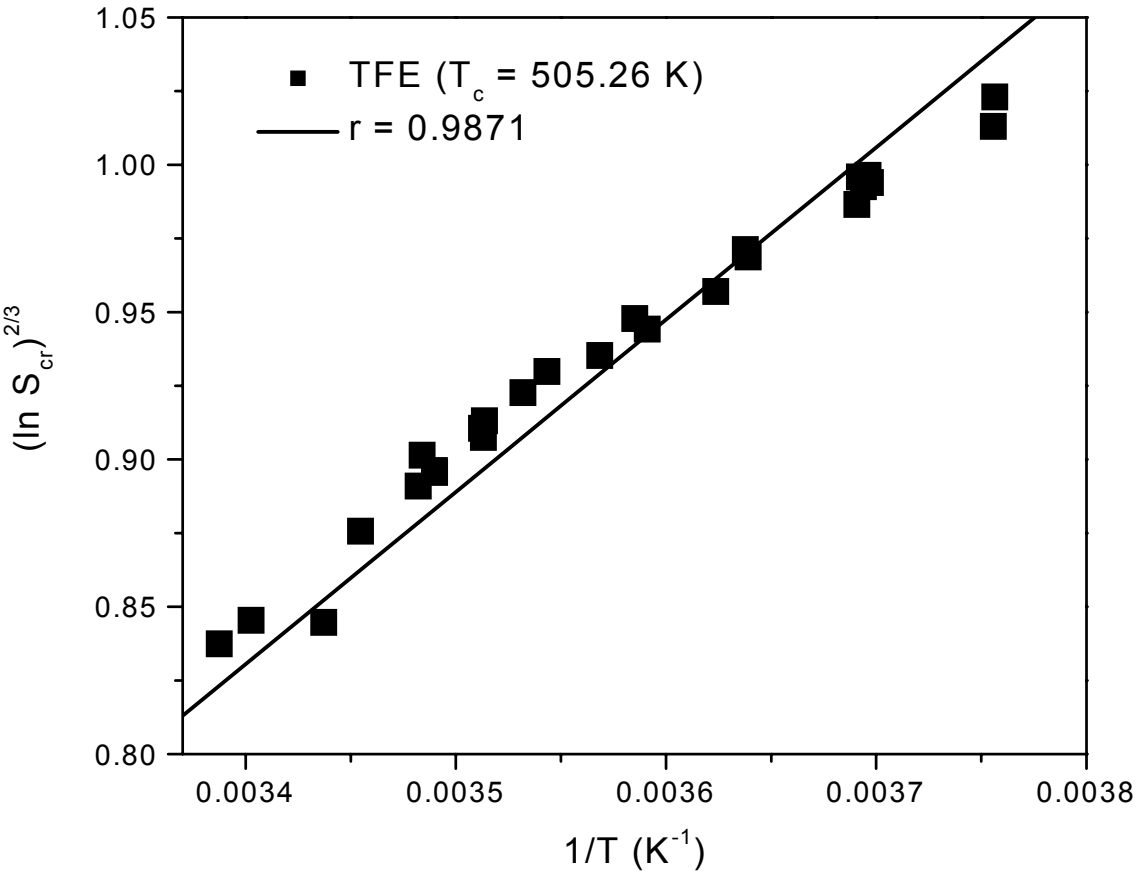

Figure 9. $(\ln S_{cr})^{2/3}$ vs. 1/T for 2,2,2-trifluoroethanol. Least-squares fit is used to determine the estimated value of the critical temperature.

Chapter 3 Nanoparticle Formation from the Vapor Phase

3-1 Outline

This chapter deals with the formation and characterization of several nanoparticle systems. The laser vaporization controlled condensation (LVCC) method was used to prepare size-selected nanoparticles, intermetallic alloy nanoparticles, and nanoassemblies of filaments and tree-like structures.

This chapter is divided into five parts. Described in part I is the experimental method used (LVCC) in the preparation of nanoparticles from the vapor phase. In part II, the preparation and characterization of nickel and iron aluminide intermetallic nanoparticles, prepared by laser vaporization, are presented. The findings indicate that metallic alloying in the vapor phase using the LVCC method is a promising technique to prepare binary alloy systems, and it could be used for multicomponent systems as well. In part III, the preparation and characterization of size-selected nanoparticles from the vapor phase are discribed. In this part the LVCC capabilities have been enhanced, by coupling it to a Differential Mobility Analyzer (DMA). The LVCC chamber was set to operate under a gas flow mode, rather than a static pressure mode, to classify particles according to their electrical mobility. The particle size-distributions were also obtained by coupling the DMA to a Faraday cup electrometer. Discussed in part IV, are the preparation and

characterization of a class of nanoparticle assemblies that were obtained by operating the LVCC chamber under the influence of an electric field. These assemblies were prepared with a potential difference applied between the top and bottom plates (electrodes) of the chamber. Several experiments were carried out to understand this phenomenon. In part V, a unique method to prepare and to study the optical properties of Ag-Au alloy nanoparticles, prepared in the vapor phase, is presented. The interaction between as-prepared Ag-Au nanoparticles and the laser light generated by the fundamental (1064 nm) and the second harmonic (532 nm) wavelengths of a pulsed Nd:YAG laser were also studied. Shown in Figure 10, are the different topics covered in this chapter.

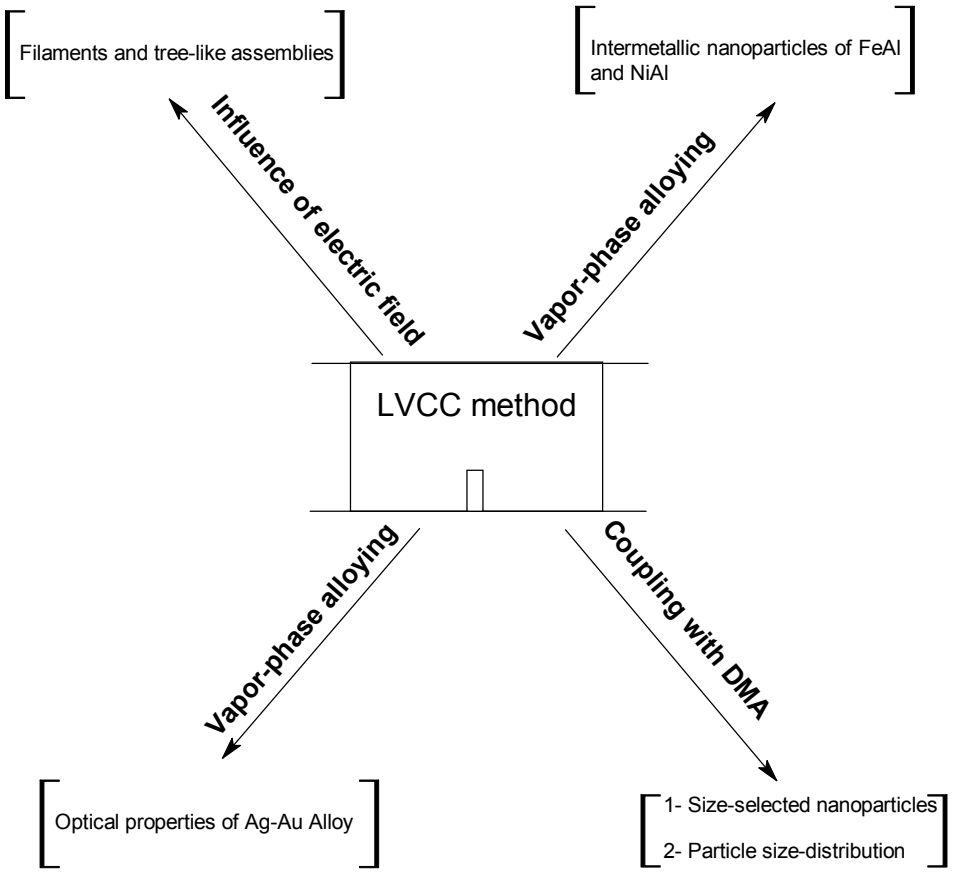

Figure 10. Schematic illustration of the uses of the LVCC method in this chapter.

3-2 Experimental Methods

Laser vaporization controlled condensation technique (LVCC) was used to prepare a wide variety of materials such as metallic,[11] semiconductor,[12,13] and intermetallic[45,46] nanoparticles. This method is based on coupling laser vaporization of metals with controlled condensation from the vapor phase. The experimental setup is shown in Figure 11. This setup consists of a modified upward thermal diffusion cloud chamber (DCC). The detailed description of the chamber can be found elsewhere.[45-47] The chamber consists of two horizontal stainless steel plates separated by a circular quartz ring. A target, which can be made of a pure metal or a mixture of metallic powders, is placed at the center of the bottom plate of the chamber. The target was vaporized by the second harmonic generation of a pulsed nano-second Nd:YAG laser (Quanta-Ray, Spectra-Physics) with 532 nm, 70-250 mJ/pulse (about 10^7-10^9 W/cm^2) and 2-5 ns pulse width, under well-defined condition of pressure and temperature. Immediately after the laser beam hits the target, a shock wave was initiated by the collisions between the gas and the target atoms and a plume is emitted.[48] The evaporated metal atoms collide with the inert gas atoms at the front of the expanding plume. As a result, plume atoms rapidly thermalize in 10-100 microseconds after the laser pulse.[49] The degree of thermalization required for condensation is related to the vapor pressure of the target material and the efficiency of the energy transfer during gas-target atom collision depends on their atomic masses. The cooling plume confined behind the shock wave becomes supersaturated, leading to nanoparticles formation via homogeneous nucleation.

Typically the chamber was filled with a pure carrier gas (He or Ar 99.999 %) or with a gas mixture of inert and reactant gases (O_2 in the case of oxide). The pressure was fixed in all experiments at about 1000 Torr. A temperature gradient (60-70 °C) was applied to the chamber by keeping the top plate at a lower temperature (room temperature) while the bottom plate at a higher temperature (90 °C). The temperature gradient, as well as the high static pressure inside the chamber helped in creating a steady state convection current which carried the generated nanoparticles to the top plate, where particles deposit. The higher the convection rate inside the chamber, the faster the particle can be removed from the nucleating zone (plume generated by the laser) and the smaller the average particle size distribution. After each run the chamber is brought to room temperature before the sample can be collected.

Scanning electron microscopy (SEM), energy dispersive X-ray spectroscopy (EDX) and scanning transmission electron microscopy (STEM) were carried out using a Quantum DS-130S Dual Stage Electron Microscope. A carbon substrate was placed inside the chamber (on the top plate) to observe the as-deposited particles under the SEM. The electron diffraction (ED) and the transmission electron microscope (TEM) images were obtained using a JOEL JEM-FXII TEM operated at 200kV. High- resolution TEM (HRTEM) images were obtained using a JOEL 4000EX operated at 400 kV. Typically, a drop of methanol-dispersed nanoparticles was placed on a carbon-coated copper grid, and left to dry in a desiccator. The crystallinity and the phase measurements of the prepared nanoparticles were analyzed using X-ray powder diffraction (XRD) on an X'Pert Philips Materials Research Diffractometer, with Cu $K_{\alpha 1}$ radiation. The elemental analyses were

done using inductively coupled plasma with an optical emission spectrometer (ICP-OES) by Varian VISTA-MPX instruments. Size-selected particles and equilibrium particle size distribution were prepared and measured by low-pressure differential mobility analyzer (LP-DMA) with a Faraday cup electrometer, coupled with the pulsed laser ablation system. The UV-Vis absorption was done on a Hewlett-Packard HP 8453 diode array spectrometer with a quartz cell of 1 x 1 x 4 cm^3. The laser power was measured using OPHIR optronics LTD., NOVA laser power monitor.

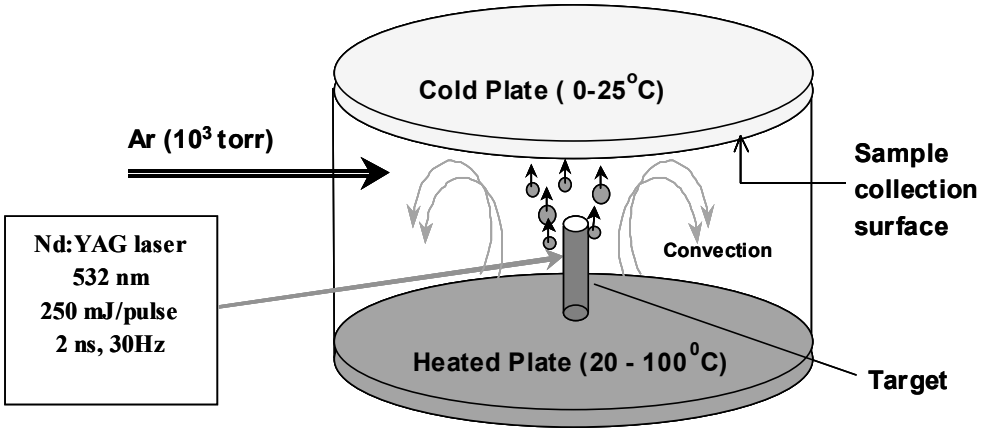

Figure 11. Experimental set-up for the Laser Vaporization Controlled Condensation method (LVCC).

3-3 Transition Metal Aluminides

3-3-1 Introduction

Intermetallic aluminides of nickel and iron alloys have many important applications, especially for high-temperature structural applications due to their high melting points and thermal conductivity. These materials are further characterized by a low density, a high strength to weight ratio, and a corrosion and oxidation resistance especially at high temperatures.[50] However, their poor room-temperature ductility and low high-temperature strength limit their usage.[51] Interestingly, nanoparticles prepared from these materials were proposed to overcome the bulk materials limitations. For example, iron aluminide and nickel aluminide nanoparticles exhibit room-temperature ductility and superplasticity.[52,53] Different techniques were used to prepare nanocrystalline iron and nickel aluminides. El-Shall and coworkers[45,46,54] prepared iron aluminide nanocrystals in the vapor phase from a bulk iron aluminide target using the laser vaporization controlled condensation method (LVCC). He and Ma[55] have used the mechanical alloying technique to prepare Fe_3Al and Ni_3Al nanoparticles that involved high-energy ball milling of a mixture of iron or nickel powder, with aluminum metal powder, with a specific composition. Iron aluminide nanoparticles have also been synthesized by hydrogen plasma-metal reaction[56,57], where an arc-melting technique was used to vaporize Fe-Al ingots in the presence of (50/50 Ar/H_2 by volume) gas mixture. Haber et al.,[58] synthesised nickel aluminide nanoparticles by chemical reduction. Another

method, a self propagating high temperature synthesis (SHS), was reported by Dong et al. to prepare NiAl nanoparticles.[59,60]

3-3-2 Experimental

Aluminum (99.5%) and nickel (99.8%) metal powder (15-44 μm) were purchased from Alfa Aesar. Iron metal powder (99.9+ %) and (< 44 μm) was purchased from Aldrich. In these experiments, a micron-sized powder of aluminum metal was mixed with the nickel or iron metal powder in specific molar ratio using a mortar and a pestle. The mixture was then pressed at 500 MPa, using a hydraulic press, in order to shape it into an ingot (target).

The LVCC method, described in (section 3-2), was used to vaporize the metal ingots. The pressure and the temperature gradients inside the chamber were adjusted to 1000 Torr helium and 60 °C, respectively. The target was placed on the bottom plate of the chamber and vaporized by a second harmonic generation beam (532 nm, 250 mJ/pulse), of a pulsed Nd:YAG laser (Quanta-Ray, Spectra-Physics), operated at 30 Hz and 2 ns pulse width. The laser beam was focused on the target using a lens (focal length 50 cm). The cross-section area of the beam was measured on the target as (0.031 cm^2).

Four different Ni-Al ingots with 75.0, 50.0, 25.0 and 10.0 atomic % Ni were prepared. The elemental analyses for the prepared nanoparticles from the above ingots were determined using the inductive coupled plasma spectroscopy (ICP). For the Fe-Al system, six different nanopowder samples were prepared from the corresponding bulk powder mixtures of (75, 50, 33, 28, 25, and 10 atomic % Fe). Pure Ni, Al and Fe nanoparticles were prepared as well, from bulk metals as reference materials, under the same experimental conditions of temperature gradient, pressure, and laser power in the

LVCC chamber. Shown in Figure 12 is a schematic diagram on how intermetallic nanoparticles were prepared in the vapor phase by the LVCC method.

3-3-3 Results and Discussion

A comparison of the Ni content in the bulk ingot to that in the corresponding nanoparticles prepared is given in Table 3. For the metallic powder-mixtures, containing 75.0, 50.0, 25.0 and 10.0 atomic % Ni, there are 40.84, 31.25, 15.51 and 6.69 atomic % Ni, respectively, in the nanoparticles. It is obvious that the Ni content in the nanoparticles is always less than in the bulk powder mixtures. In fact, the Ni content in Ni-Al nanoparticles is about 45-33 % of those in the bulk metal-powder mixtures. This finding can be explained by considering the evaporation rate of pure Al into vapor, which is higher than pure Ni since Al metal has a higher vapor pressure and a lower enthalpy of vaporization compared to that of Ni metal.[61] Similar results have been reported by Liu and co-workers,[57,62] who studied the preparation of Fe-Al nanoparticles by hydrogen plasma-metal reaction from bulk alloy. They have found that the Al content in the nanoparticles was greater than that in the bulk alloy. They also explained this result in terms of differences in evaporation rate for the pure metals.

Shown in Figure 13 are the SEM images of NiAl intermetallic nanoparticles prepared from a powder mixture with 51.76 atomic % Ni. A typical web-like structure morphology was observed, similar to what has been observed for pure Ni and Fe nanoparticles shown in Figure 14 and Figure 15, respectively. The deposited particles were highly porous with a large surface area based on the SEM micrographs, which could make these particles suitable for catalytic applications. The average pore-size diameter was estimated from SEM to be 0.8 and 3.9 μm for Ni and Fe nanoparticles, respectively.

The x-ray diffraction patterns for nanopowders prepared from pure Ni and Al targets are shown in Figure 16-(b, c). The XRD patterns for Ni and Al nanoparticles have four strong lines assigned to reflections from the 111, 200, 220 and 311 planes at scattering angles of 44.49, 51.81, 76.41 and 92.89, respectively for Ni and 38.47, 44.71, 65.09 and 78.21, respectively for Al. The lattice constant, assuming a cubic unit cell, for Ni and Al nanoparticles were calculated to be 3.5242 and 4.0495, compared to 3.523 and 4.0494 for bulk materials, respectively. The XRD data for nanoparticles sample obtained following ablation of powder Ni-Al mixture with (51.76 atomic % Ni) is shown in Figure 16 a. The XRD pattern does not match any of the XRD peaks of pure Ni or Al nanoparticles. However, it matches the diffraction pattern of bulk $Ni_{0.58}Al_{0.42}$ alloy [68], which means that NiAl intermetallic nanoparticles were formed in the vapor phase using the LVCC method. Based on the XRD diffraction patterns, neither Ni nor Al peaks were present in the spectrum pattern of the prepared intermetallic nanocrystals (NiAl), indicating that the product was not a metallic mixture. The strong diffraction lines at the scattering angles of 31.11, 44.63, 64.97 and 82.27 were assigned to the diffraction from 100, 110, 200 and 211 planes, respectively, of a B2 crystal structure of NiAl. The calculated lattice parameter for NiAl nanoparticles (2.868) is in good agreement with bulk lattice parameter (2.871). Shown in Figure 17 are the XRD patterns of nanoparticle samples prepared from metallic powder mixtures with (75.0, 50.0, 25.0 and 10.0 atomic % Ni) labeled as a, b, c and d, respectively, in the graph. A mixture of Ni and Al nanoparticles, as the major product, were prepared from the vaporization of a powder mixture with (75 atomic % Ni), as identified from the XRD pattern compared to database

patterns of pure Ni and Al metals. When the molar percentage of Ni was decreased to 50 atomic % in the metal ingot, intermetallic alloy nanoparticles (NiAl) of Ni and Al metals were obtained, and the absence of pure Ni and/or Al nanoparticles was evident. The intermetallic alloy nanoparticles were assigned to $Ni_{0.9}Al_{1.1}$ as identified from the XRD spectrum; the diffraction pattern matched ($Ni_{0.9}Al_{1.1}$) bulk alloy. A mixture of pure Al and intermetallic $Ni_{0.9}Al_{1.1}$ nanoparticles was obtained when ingots with 25.0 and 10 atomic % Ni were vaporized in the LVCC chamber. Based on the XRD data, a mixture with more Al nanoparticles were obtained from a sample prepared from 10.0 atomic % Ni target compared to that prepared from a 25.0 atomic % Ni target. It is evident that only one intermetallic phase was obtained, (NiAl) nanoparticles. However, by increasing the molar ratio of Al or Ni content, alloy nanoparticles, in addition to the pure component, (depending on which metal is in excess) were obtained. This result may be due to the greater stability of the NiAl phase compared to other nickel aluminide phases like $NiAl_3$, Ni_2Al_3 and Ni_3Al, where NiAl has the highest heat of formation.[60,63]

Similar results have been obtained for the Fe-Al system. Fe-Al intermetallic nanoparticles were also prepared by the LVCC method using metallic powder mixtures of Fe and Al. Six different nanopowder samples were prepared from bulk powder mixtures with (75, 50, 33, 28, 25 and 10 atomic % Fe). Shown in Figure 18 are the scanning electron microscope images for the as-deposited particles along with the energy dispersive spectra (EDX) for three different nanoparticle compositions prepared from $FeAl_3$, FeAl, and Fe_3Al, respectively. It is clear that the nano-deposited materials are highly porous with a web like structure morphologies and a high surface area, as

observed from the SEM micrographs. The Fe content in the nanopowder samples was determined using two different techniques, the EDX and the ICP, as shown in Table 4. Similar results were obtained using these two techniques, indicating that the Fe/Al ratio is almost homogeneous (constant) throughout the nano sample prepared in the vapor phase. The atomic ratios were determined from the EDX spectra by integrating over the peak area, under the Al Kα and the Fe Kα lines. For example, the metal powder mixture containing 75.0, 50.0, and 25.0 atomic % Fe, have 65.79, 52.03, and 24.62 atomic % Fe, respectively, in the nanoparticles.

The XRD pattern for the nanocrystalline sample prepared from (50:50 atomic %) of Fe and Al metallic powder mixture are shown in Figure 19, along with the diffraction patterns of pure Fe and Al nanoparticles. Neither Fe nor Al diffraction pattern matched the nanopowder sample patterns prepared from the Fe-Al (50:50) powder mixture. By comparing the XRD data to the database, good agreement was found between the XRD patterns of prepared nanopowder and bulk $Fe_{0.5}Al_{0.5}$ intermetallic alloy. The XRD patterns for different nanocrystalline samples prepared from powder mixtures with (75.0, 50.0, 25.0 and 10.0 atomic % Fe) are shown in Figure 20.

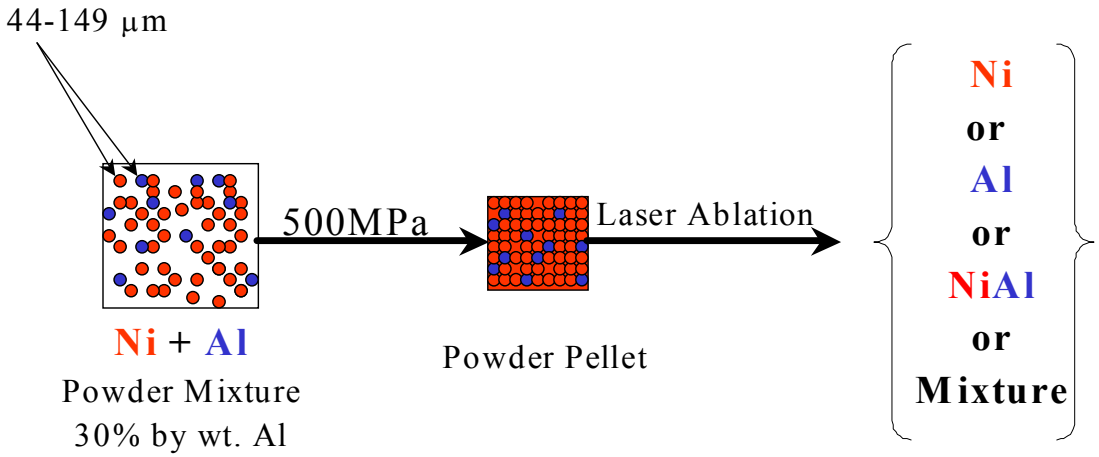

Figure 12. Illustration of the preparation of mixed or alloy nanoparticles by laser vaporization of targets made from micron-sized powders.

Table 3. Atomic percentage of Ni in bulk powder and in nanoparticles using Inductive Coupled Plasma Spectroscopy (ICPS).

Sample	Ni atomic % Bulk.	Ni atomic % nano.
Ni_3Al	75.00	40.84
NiAl	50.00	31.25
$NiAl_3$	25.00	15.51
$NiAl_9$	10.00	6.69

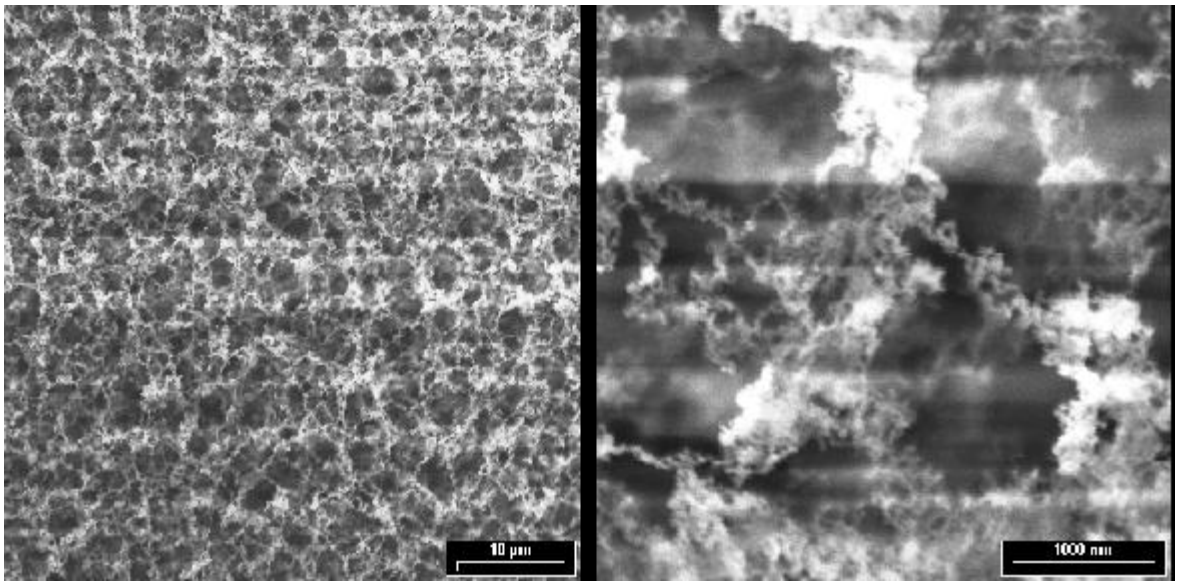

Figure 13. SEM micrographs showing the web like structure for as-deposited nanoparticles prepared from $Ni_{0.52}Al_{0.48}$ powder mixture using the LVCC method under He atmosphere.

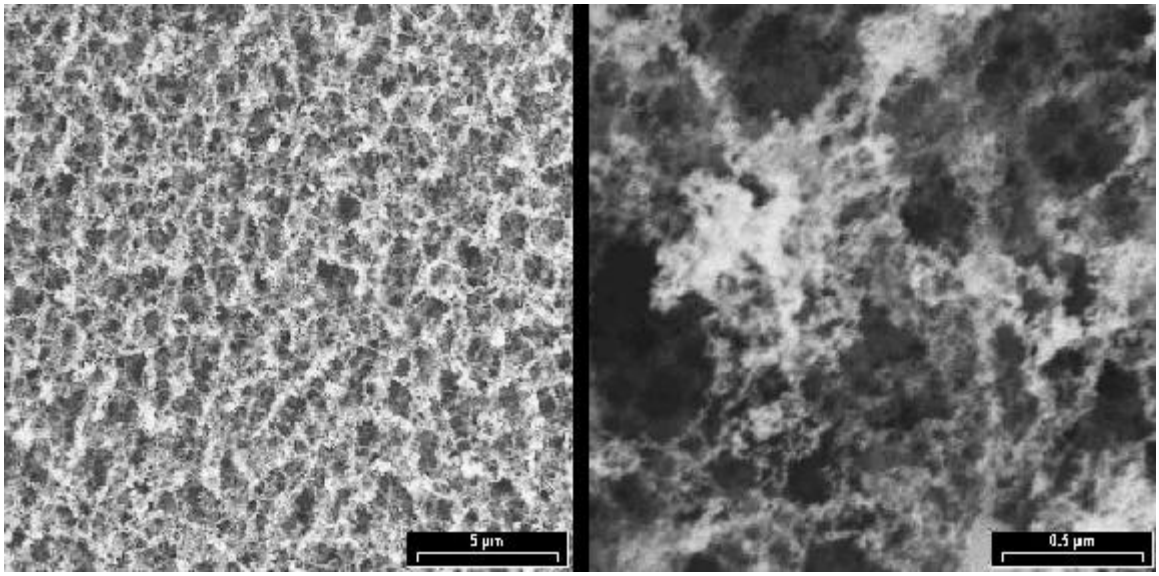

Figure 14. SEM micrographs showing the web like structure for the as-deposited Ni nanoparticles prepared by the LVCC method under He atmosphere.

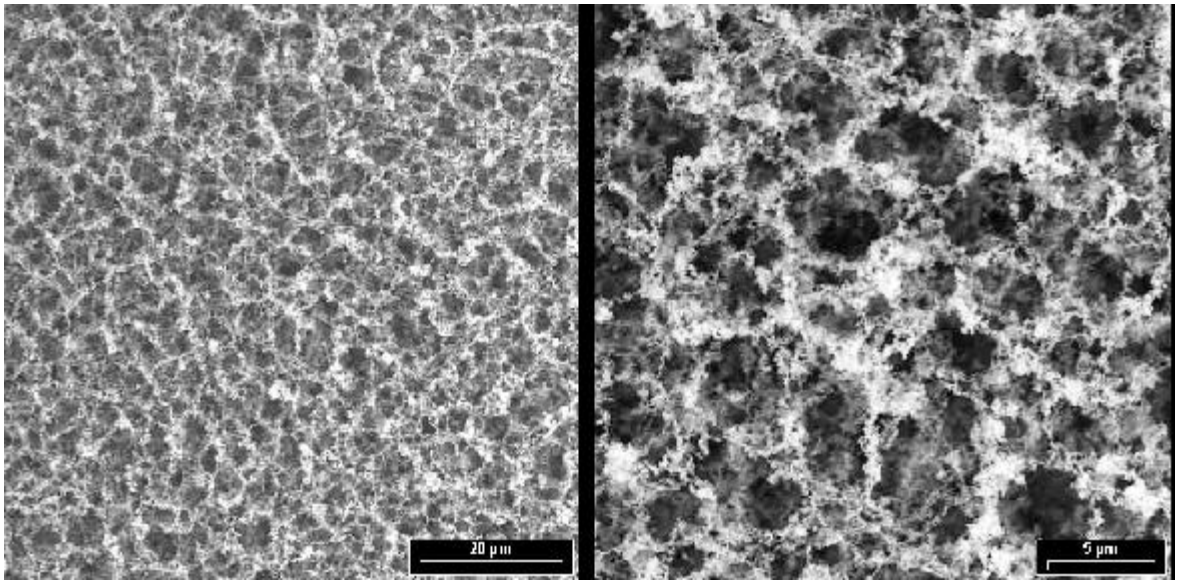

Figure 15. SEM micrographs showing a web-like structure for the as-deposited Fe nanoparticles prepared by the LVCC method under He atmosphere.

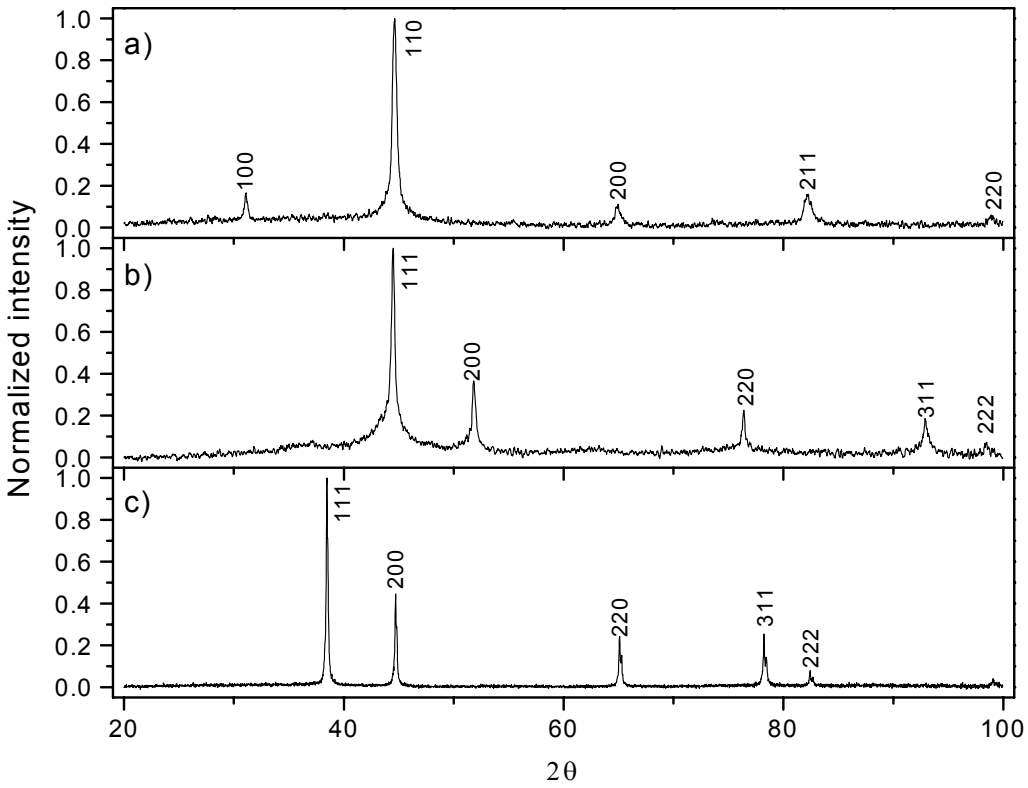

Figure 16. XRD of a) NiAl, b) Ni and c) Al nanoparticles prepared by the LVCC method.

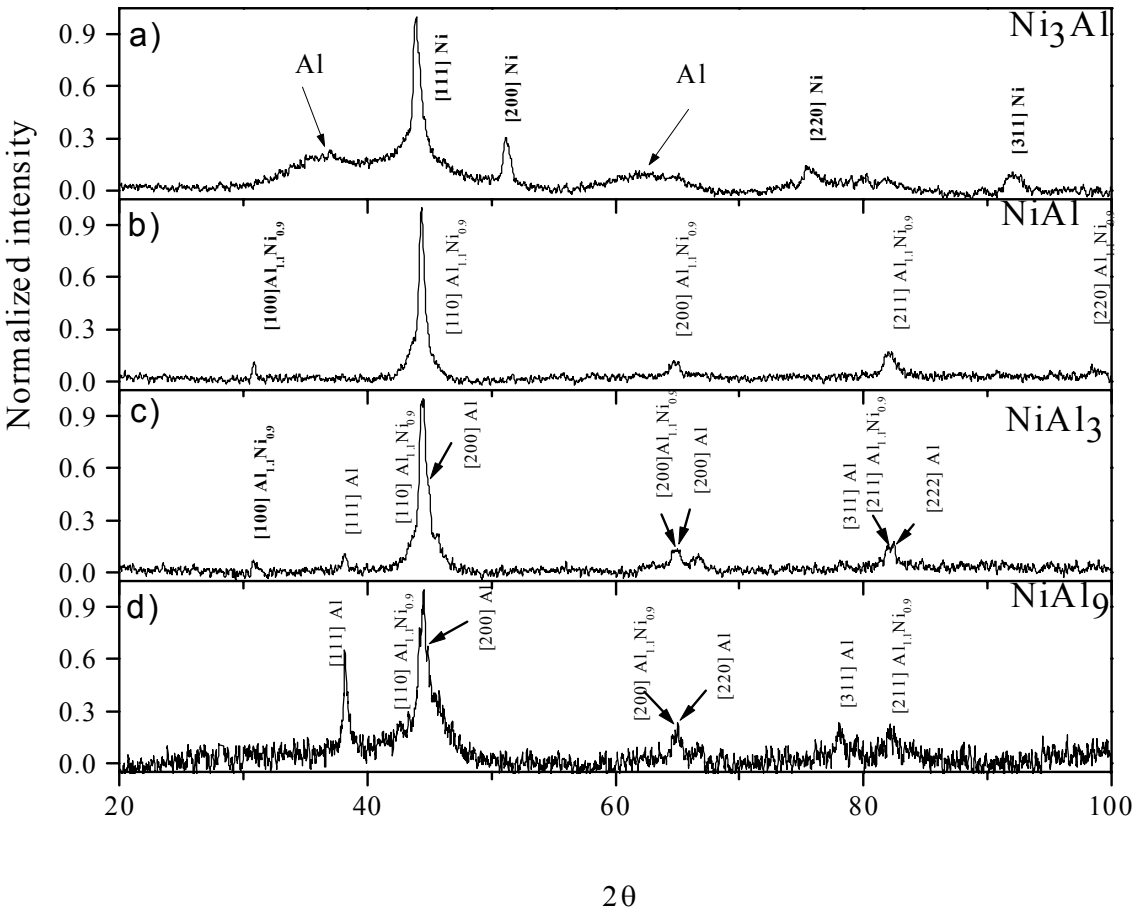

Figure 17. X ray diffraction patterns for Ni-Al nanoparticles prepared from bulk powders with the mixing atomic ratios of 75, 50, 25 and 10 % Ni are in a, b, c, d, e and f, respectively.

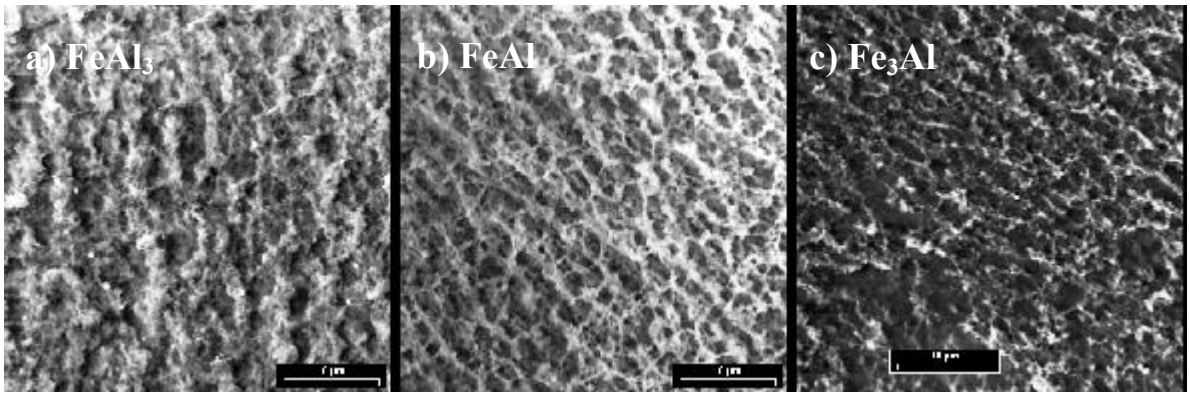

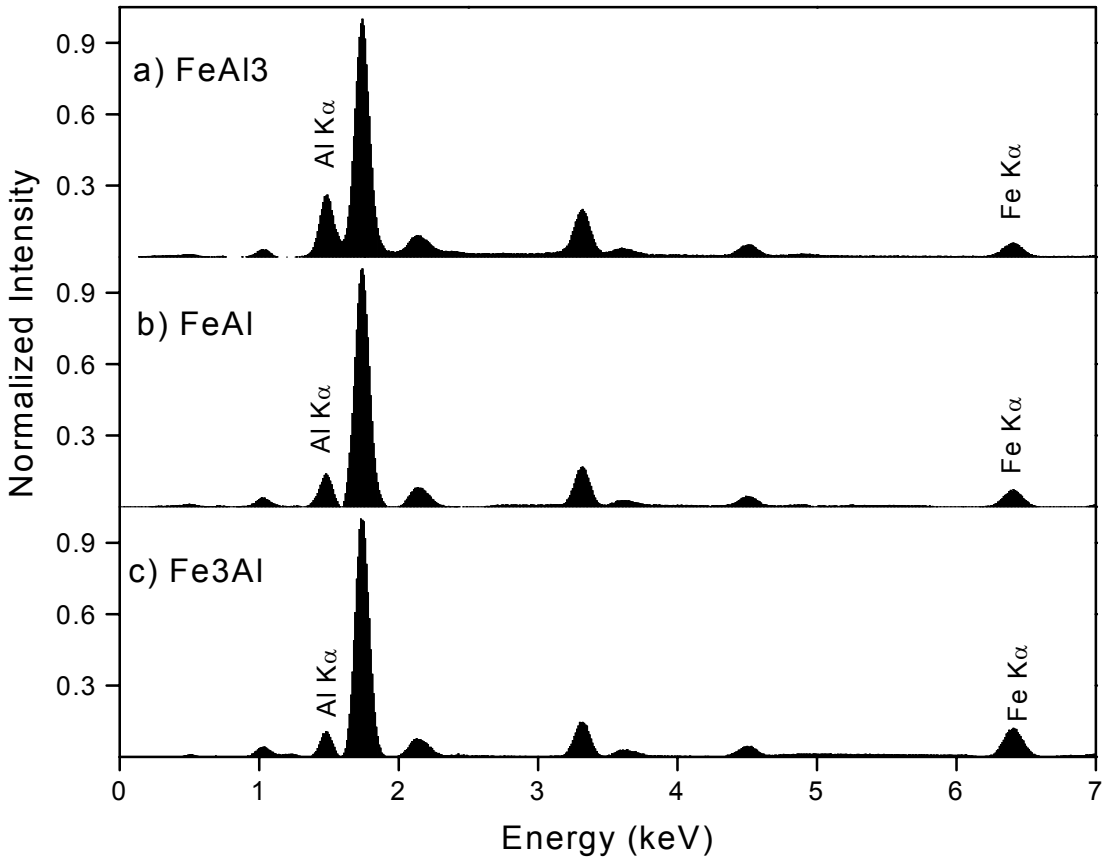

Figure 18. SEM micrographs (10 μm scale bar) and EDX spectra for nanoparticles prepared from a) Fe_3Al, b) FeAl, and c) $FeAl_3$ powder-mixed targets. The scale bar is 10 μm.

Table 4. Atomic percentage of Fe in bulk powders and in nanoparticles using the Inductive Coupled Plasma Spectroscopy (ICPS).

Sample	Fe-Atomic % bulk	Fe-Atomic % nano	
		ICP	EDX
Fe_3Al	75	70	65.79
FeAl	50	54	52.03
$FeAl_3$	25	30	24.62
$FeAl_9$	10	16	--

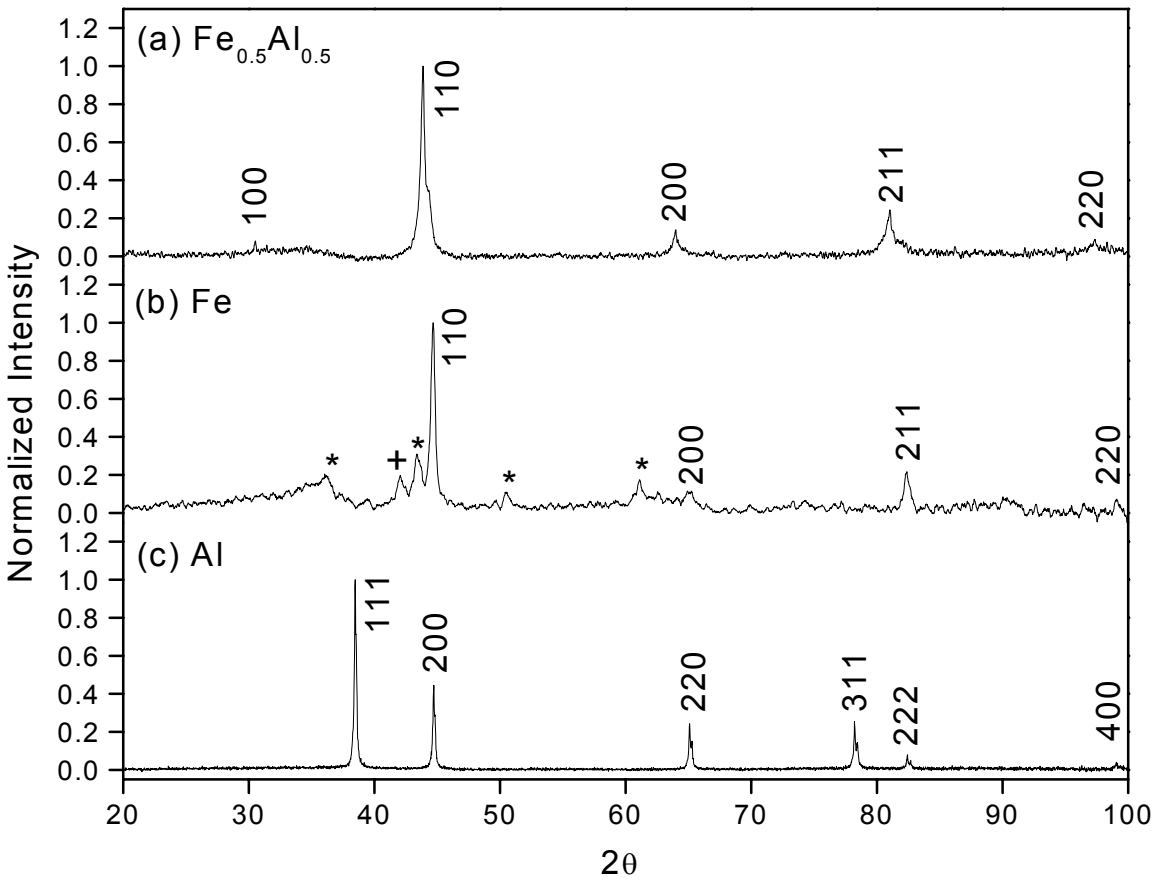

Figure 19. XRD of (a) $Fe_{0.5}Al_{0.5}$, (b) Fe, and (c) Al nanoparticles prepared by the LVCC method.

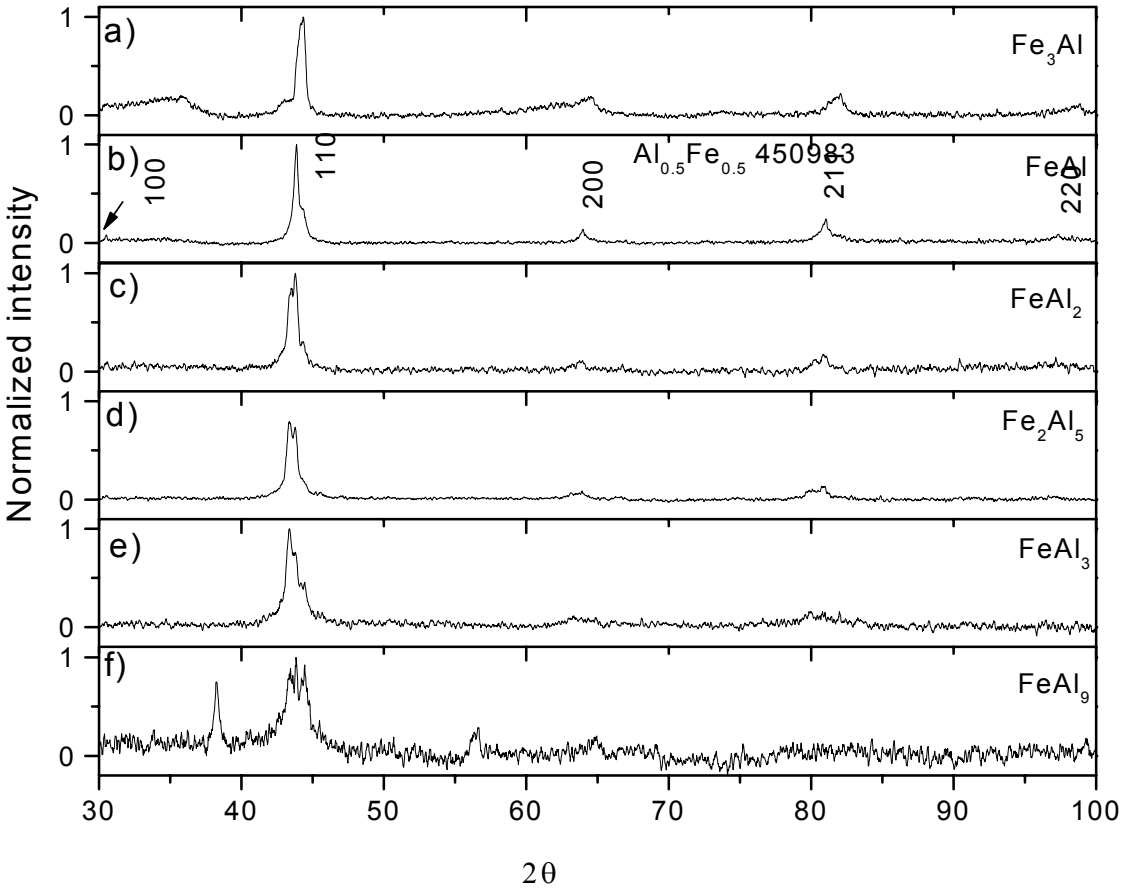

Figure 20. X ray diffraction patterns for Fe-Al nanoparticles prepared from bulk powders with the mixing atomic ratios of 75, 50, 33, 28, 25 and 10 % Fe are in a, b, c, d, e and f, respectively.

3-4 Filaments Formation in Electric Field

3-4-1 Introduction

The assembly of nanoparticles, under the influence of an electric field, offers many opportunities for the fabrication of microwires,[14] nanostructured films,[15] ordered arrays,[16] and dendritic structures.[17] These assemblies are usually established by the means of electrophoretic,[15,16] dielectrophoretic,[14,17] and electrochemical[18,19] forces acting on the particles. An electric-field assisted assembly technique was used by Smith et al. to align gold nanowires in isopropyl alcohol.[64] This electric field effect has been used to induce the growth of carbon nanowalls using the microwave-assisted chemical vapor deposition technique.[65] For example, Nakato and coworkers[66,67] studied the photo induced structure changes of silver nanoparticles under the influence of an electric field.

Although considerable work has been recently reported on electric field effects on colloidal nanoparticles suspended in liquid phase, no work has been reported for the vapor phase. Interestingly, recent work indicated that the deposition efficiency of Si nanoparticles generated by laser ablation was improved by applying an electric field due to the generation of positively charged particles, which were efficiently transferred to the negatively biased electrode.[68] However, no filament assembly was reported. Moreover, the application of a magnetic field has been reported to be effective for the fabrication of arrays of ferromagnetic iron and cobalt nanocluster wires by the thermal deposition of metal carbonyl.[69]

In this chapter a new method to assemble nanoparticles into filaments and tree-like structures in the vapor phase under the influence of an electric field (dc) is described.[70]

3-4-2 Experimental

The LVCC method has been used to prepare and study the influence of an electric field during the vaporization and condensation of several metallic (Ni, Fe), semiconductor (Si), mixed (Si/Pt), and intermetallic (FeAl, Ti_3Al) nanoparticles. The LVCC method is described in section (3-2) with the top and bottom plates of the chamber used as electrodes, and applying an electric field (dc) between them. A bipolar Hewlett Packard 6516A power supply (0-3000 V dc) was used. The bottom plate was always kept grounded while the top plate carried the electrical charge and the two plates were isolated from one another by a quartz ring of 5 cm height.

3-4-3 Results and Discussion

Typically, a 10 ns laser pulse with a power density of (10^6-10^7 W/cm^2) produces about 10^{14} atoms and 10^6 ions from any metal or solid target.[11] Therefore, during the LVCC processes, a significant fraction of charged nanoparticles is produced (by ions and free electrons). As a result, the growth pattern of nanoparticles (neutral and charged) in the vapor phase could be significantly influenced by applying an electric field across the chamber plates. It is known that in the presence of an electric field, the charged particles experience electrophoretic forces and, if this field is nonuniform, the neutral particles as well experience a translational motion known as dielectrophoresis.[71]

Several experiments were conducted to investigate the factors controlling the filament-assemblies of nanoparticles. First, experiments were done that suggested the growth of filament was strongly dependent on the type of nanoparticles assembled. Ni and/or NiO nanoparticle mixtures were prepared (by adjusting the partial pressure of oxygen) in the chamber. These particles were prepared under a constant electric field of 60 V/cm in the LVCC chamber. Over the studied oxygen range of (0.0-15.0 % in He), filament assemblies of nanoparticles were observed. At zero oxygen level, short, thin, and weak Ni filaments, with dendritic structures at the ends, were observed. By increasing the oxide level in the preparation of the nanoparticles, dense, long, and strong filaments (tree-like structures) were obtained. The x-ray diffraction patterns for Ni/NiO filaments prepared with different oxygen percentages (0.0, 0.3, 0.8 and 15.0 % O_2) are shown in Figure 21, along with the database diffraction patterns for bulk Ni and NiO materials [72].

The XRD of pure Ni nanoparticles exhibit diffraction peaks (2θ) of 44.47, 51.79, 76.35 and 92.97 assigned to scattering from the 111, 200, 220 and 311 crystal planes, respectively. Based on the XRD data, the Ni nanoparticles were easily oxidized by reacting with oxygen to form NiO, 0.3% oxygen was sufficient to give a mixture of Ni and NiO nanoparticles. By increasing the oxygen percentage to 0.8 %, more Ni nanoparticles were converted to NiO, and at 15 % oxygen, all the Ni particles were oxidized to NiO; no diffraction peaks for pure Ni were observed. The XRD data confirmed the presence of only one phase (NiO), where its diffraction pattern exhibits peaks (2θ) of 37.29, 43.29, 62.91 and 75.55 assigned to scattering from 101, 012, 110 and 113 crystal planes, respectively. The electric field-assisted Ni/NiO filaments had the same crystal structure as those prepared in the absence of an electric field; good agreement was observed between the database of the diffraction patterns and XRD data.

The average particle size was estimated from the XRD data by using Scherrer's equation:[73]

$$P = \frac{C\lambda}{\beta \cos\theta} \qquad \text{Eq. 3-1}$$

Where P is the particle diameter, C is a constant equal to (0.89), λ is the wavelength of the x-ray used (1.54184 Å), β is the full width at half maxima (FWHM) of the diffraction peak, and θ is the diffraction angle. The estimated average particle size for Ni and NiO nanoparticles using Scherrer's equation are 22.6 and 24.2 nm, respectively.

Under the electric field, nanoparticles were assembled as little chains and stacked end to end once the concentration of particles generated by laser vaporization was

sufficient. Generally, the chains grew perpendicular on top and bottom plates, and parallel to the electric field direction applied between them in the LVCC chamber. Eventually, the chains bridge the top and the bottom metal plates (electrodes), indicating that both negatively and positively charged particles were involved. The fiber and the tree-like morphologies of the filaments were different from the web-like morphology observed with no electric field. The scanning electron micrographs for pure Ni and NiO (Ni with 15.0 % O_2) nanoparticles deposited on a glass substrate and prepared under 60 V/cm are shown in Figure 22 (a-b), and (c-d), respectively. The morphology of the deposited Ni and NiO nanoparticles show the presence of fiber structures. Dendritic structures were observed at the ends of Ni filaments, whereas NiO shows a compact filament structure with fewer dendrites.

Similar results have been observed for iron nanoparticles. Iron particles were prepared using the LVCC method, with and without applying an electric field. Again, only filament and tree-like structures were observed by applying an electric field. The optical photographs of iron tree-like structures prepared in 5.0 and 25.0 % oxygen under 200 V/cm are shown in Figure 23 (a-b), and (c-d), respectively. Assemblies of filaments and tree like structures were observed hanging from the top plate of the chamber as shown with dendritic ends. These filaments (iron oxide) were grown up to 5 cm long (chamber height) by extending the laser vaporization time.

The XRD data for iron nanoparticles prepared under 200 V/cm with different oxygen levels in helium gas (0.0, 0.2, 0.7, 5.0, 10.0, 25.0 and 50.0 % O_2) are shown in Figure 24. It is clear from the XRD patterns that iron diffraction peaks decrease gradually

while iron oxide (Fe_2O_3) diffraction peaks gradually develop with increasing oxygen levels in the gas mixture. At 0.0 % oxygen, the XRD of pure Fe nanoparticles exhibit diffraction peaks (2θ) at 44.66, 65.03 and 82.38 assigned to scattering from 110, 200 and 211 crystal planes, respectively. Some iron oxide peaks were also observed in the diffraction pattern of pure iron nanoparticles. This is due to the handling of the iron nanoparticles in air. These particles have a high surface to volume ratio and therefore, are readily oxidized. Between 0.2 and 0.7 % oxygen in the chamber, iron and iron oxide nanoparticle mixtures were formed. Since there was no significant change in the diffraction patterns between 5-50 % oxygen, all iron nanoparticles were oxidized to iron oxide (Fe_2O_3). The scattering angles at 30.11, 35.53, 43.19, 57.15, 62.77 and 89.85 were assigned to 220, 311, 400, 511, 440 and 731 planes of Fe_2O_3 crystal lattice.

The morphology of the deposited iron particles, in the absence and the presence of an electric field (200V/cm), is shown in the SEM images in Figure 25. Web-like morphologies were observed in the absence of an electric field for iron nanoparticles prepared with 0.0, 5.0 and 25.0 % oxygen, as shown in Figure 25 a, c and e, respectively, while different morphology for the iron/iron oxide nanoparticles prepared under the same experimental conditions but with an electric field (200 V/cm) was observed; these are shown in Figure 25 b, d and f for 0.0, 5.0 and 25.0 % oxygen, respectively. Fiber-like structures with oriented filaments are observable in Figure 25-f, these filaments were connected together through necks as shown.

The influence of an electric field during the preparation of intermetallic nanoparticles, such as FeAl (24% Al by wt.) and Ti_3Al, was also studied.[70] Displayed in

Figure 26 are some optical photographs of the LVCC chamber taken during the preparation of the FeAl nanoparticles under an electric field of 60 V/cm applied between the bottom and the top plate of the chamber. These optical photographs were taken after 30, 60 and 120 min, respectively, irradiation time. After 30 min, the filaments were thin and long enough to join top and bottom plates of the chamber. After 60 min, branched filaments with tree-like structure were observed. Finally, after 120 min, long bundles of filaments were observed that were 5 cm long. It was also interesting to note that these chains stretched at higher field strengths and contracted when the field was turned off. In this experiment, the top plate was carrying a negative voltage of (-300 V). When the voltage was increased to (-400 V), the filaments inclined towards the top plate, while by incrementally decreasing to (-300 V), the filaments relaxed back to the original perpendicular orientation. This elastic behavior of nanoparticles chains was recently reported by Friedlander and coworkers [74,75] for TiO_2, Al_2O_3 and Fe_2O_3 generated by laser ablation.

The transmission electron microscope images for FeAl nanoparticles prepared under the effect of electric field (60 V/cm) are shown in Figure 27. A carbon-coated Cu grid was placed on the top plate of the LVCC chamber for 5 min during the experiment, and then examined under the microscope. The particles were relatively monodispersed, with an average particle size of about (15 ± 2) nm. Particles were assembled in chain-aggregates made of spherical particles, as observed from the TEM results. The electron diffraction (ED) pattern showed a ringed structure pattern, indicating the crystalline nature of the nanoparticles prepared.

The SEM images of the FeAl nanoparticles assembled by the electric field (60V/cm) are shown in Figure 28 at four different magnifications and labeled as (I, II, III, and IV). These images have the following features; a fiber-like structure (I) constructed of chain filaments (II) that are joined together by small connections (III). At high magnification, the SEM image showed that the filaments were highly porous structures (IV).

The XRD patterns for FeAl nanoparticles prepared by the LVCC method under an electric field of 60 V/cm with different oxygen percentages (0.0, 0.1, 0.3, 0.5 and 15.0 %) are shown in Figure 29. At 0.0 % oxygen, the scattering angles (2θ) at 30.81, 44.13, 64.19 and 81.23 were assigned to 100, 110, 200 and 211 planes of FeAl crystal lattice. It is clear that as the oxygen was increased inside the chamber, more FeAl nanoparticles were oxidized. The XRD patterns of the oxide nanoparticles were consistent with the hercinite phase ($FeAl_2O_4$). The scattering angles (2θ) at 30.95, 36.19, 44.51, 58.43 and 64.88 for (FeAl 15 % O_2) were assigned to 220, 311, 400, 511 and 440 planes of $FeAl_2O_4$ crystal lattice.

Filament-like structures were observed for FeAl nanoparticles, prepared under 60 V/cm, with no oxygen and with 0.1 % oxygen. Meanwhile, for the samples prepared in 0.3 % oxygen, only aggregates and islands of particles were observed on the top plate of the chamber. However, when the oxygen percentage was increased to 0.5-15 %, no filaments were observed, only a smooth thin film of nanoparticles with web-like structures was obtained. Shown in Figure 30 are the deposited FeAl nanoparticles on the

top plate, under three different oxygen levels 0.0, 0.3 and 0.5 % oxygen, were filaments, aggregates, and thin film morphologies were obtained, respectively.

Similar results have been observed for titanium aluminide (Ti_3Al) nanoparticles, which were prepared under the same experimental conditions as the FeAl nanoparticles. The same electric field (60 V/cm) was applied during the preparation, with different oxygen levels of (0.0, 0.25, 0.50, 1.0 and 2.0 %). Ti_3Al nanoparticles prepared in 1.0 and 2.0 % oxygen, showed no filament formation, while those prepared in 0.0, 0.25 and 0.5 % oxygen formed filaments. TEM, ED, SEM, and optical photograph of Ti_3Al nanoparticles prepared with 60 V/cm in helium atmosphere are shown in Figure 31. Based on the TEM, the average particle size is about 10 nm, while the SEM revealed that the filaments condensed like a bundle of wires or as in wool yarn. Tree-like structures of several centimeters long of Ti_3Al, in the LVCC chamber, are shown in Figure 31c.

It is not understood why the intermetallic nanoparticles of FeAl, and Ti_3Al oxides show similar electric field effect behavior, since both intermetallic nanoparticles did not form filament-like structures at low oxygen percentages of 0.5 and 1.0 % for FeAl and Ti_3Al, respectively. This may be due to aluminum-rich surfaces of the FeAl and Ti_3Al nanoparticles, since pure Al nanoparticles did not form filament assemblies under 60 V/cm electric field. Aluminum surface enrichment phenomenon have been reported by El-Shall and coworkers[45,46], who prepared FeAl nanoparticles from a bulk FeAl target. The XPS for the FeAl nanoparticles revealed that the surface was enriched with Al, which has a lower surface tension than that of Fe. They have also found that the

crystalline structure of FeAl nanoparticles is (B2-CsCl type structure), same as the bulk structure.

In addition to the effect of the oxide formation on the filament growth, an electric field threshold required for the filament formation was observed. This threshold was found to be material dependent. The values for the electric field required to induce filament assemblies for different materials are shown in Table 5.

For example, when different fields (60, 100 and 200 V/cm), were applied to Si nanoparticles, only at 200 V/cm short Si fractals (~10-15 mm) were observed hanging from the top plate of the chamber, as shown in Figure 32a. When the electric field was reduced to 100 V/cm, isolated particle islands (aggregates) were observed on the top plate of the chamber. Finally, at 60 V/cm, a thin film of Si nanoparticles, deposited on top plate was observed, indicating that the electric field strength used in this experiment was not enough to induce the filament assemblies. Displayed in Figure 33 are the morphology of deposited Si nanoparticles, in the absence and the presence of an electric field (200 V/cm). The SEM images were captured at two different magnifications. The images show a typical web-like morphology for Si deposited in the absence of an electric field. However, in the presence of field highly aligned bundles, consisting of parallel filaments connected together are shown in Figure 33d. These results led to the belief in the presence of an enormous electrostatic aggregation due to dipole forces between the nanoparticles to form chain filaments, and between the chain filaments to form fiber-like structures.

Interestingly, when Si and Pt targets were simultaneously vaporized by laser under the influence of 200 V/cm, unlike pure Si, long tree-like structures were formed inside the chamber, as shown in Figure 32b. The morphology of Si/Pt assemblies showed the formation of dendritic surface aggregates, as shown in Figure 34a. These aggregates were composed of nearly oriented bundles (Figure 34b) with highly porous structures (Figure 34c).

In the above experiment, a mixture of Si and Pt nanoparticles were prepared, as illustrated from the x-ray diffraction data. In Figure 35 the XRD patterns for Si/Pt, Pt and Si nanoparticles are shown. It is obvious that both particles (Si, Pt) were present in the prepared assemblies. The TEM and the EDX results of these nanoparticles, indicated the formation of some core-shell structures, with a Pt core encapsulated in Si shell, as shown in Figure 36. The Pt content in Si/Pt nanoparticles was estimated from the EDX analysis, by integrating the area under Si-Kα and Pt-Lα, as shown in Figure 37 with average Pt content of 13.24 wt.%.

In this experiment, the presence of Pt nanoparticles, in the mixture, is believed to enhance the formation of fiber-like assemblies of Si under the influence of an electric field. The Pt particles (atomic weight 195.078 amu) are more polarizable than the Si particles (atomic weight 28.0855 amu) under the same electric field. The addition of other interaction terms, such as polarizability, to the already existing particle-particle and particle-electric field (electrostatic) interactions, might be the reason for the Pt effect in enhancing the filament's growth.

In conclusion, the effect of the electric field on the formation of the chain aggregates acts through the polarization of the charges on the nanoparticle surface. For larger particles, the effect of the electrostatic charge is overpowered by the effect of gravity, but for nanoparticles the electrostatic forces are predominant. It is believed that there is a mixture of positive and negative charges on the surfaces of the nanoparticles, and that some of the nanoparticles will have net charges. The nanoparticles with net charges will respond to the electric field with the electrophoretic force. However, the neutral particles will experience a dielectrophoretic force caused by polarization effects. The results can be explained within the framework of combined electrophoresis and dielectrophoresis effects. It appears that the initial nucleation and growth starts with the ions (electrophoretic effect) followed by accretion of neutral atoms and clusters (dielectrophoretic effect). Specifically, there are two effects that when combined may lead to the sticking of particles of the same net charge. The dipole force is very strong near the surface of the particle; further away from the surface, the net charge or monopole force becomes more effective. When two individual particles are separated by a certain distance, they will respond to the monopole charge between them, and if the monopoles are the same, the particles will repel. However, by orienting their dipoles so that they are attracting one another, because at this short distance the dipole dominates over the net charge, the two particles will stick together. The observations of enhanced assemblies of intermetallic and transition metal nanoparticles are consistent with the significant dipole forces and electronic polarizability, respectively, in these systems.

In addition, the convective currents in the LVCC method play an important role in nanoparticles assemblies. Convection current carries particles away from the nucleation zone before they grow further. Sites with nonuniform electric field (high energy), and high electric field density (filament terminals) would be favorable sites for newly prepared particles (carried by convection) to stick on and build up filament-like structure. It is also believed that the dendritic structures at the ends of nanoparticles filaments were due to dielectrophoretic forces, since the filaments were connected to the top plate that carry high voltage. The tip of the filament was carrying high electric field density that results in non-homogeneous electric field. The polarity of particles aligned parallel or perpendicular to the applied electric field plays a significant role in the formation of linear or dendritic chain structures. The dielectrophoretic force is given by:[17]

$$F = \pi a^3 \varepsilon_m \varepsilon_o K \nabla E^2 \qquad \text{Eq. 3-2}$$

Where *a* is the particle radius, *K* is the complex Clausius-Mossotti factor, and ε_m and ε_o are the medium and vacuum permittivities, respectively. The dielectrophoretic force in Eq. 3-2 is not, in general, parallel to the electric field, if the electrode has a complex shape. The dielectrophoretic effects, such as F//E and F⊥E in different electrode structures, are supposed to produce chaining structures, where different nanostructures are assembled due to relative alignment (parallel or perpendicular) of the particles with respect to the applied electric field. The energy of interaction between two closely situated polarizable particles can be approximated by:[14]

$$W_{\max} = -C\pi\varepsilon R^6 K^2 E^2 / r^3 \qquad \text{Eq. 3-3}$$

Where R is the particle radius, r the distance between the centers, E the intensity of the field, and ε the dielectric permittivity of the media. The Clausius-Mossotti function, K, for metallic particles ~ 1 and the factor *C*, range from 8 to more than hundreds, depending on the distance between the particles, the higher-order multipolar effects, and the number of particles in a chain. The most important component in the formation of filament assemblies is the attractive electrostatic interaction between the dipoles directed along the electric field.

The tip of growing filaments creates local fields of high intensity and gradient, giving rise to a second component of the dielectrophoretic force, which arises from the interaction of the particle dipoles with the nonuniform electric field and is directed along the field gradient. In order to prove this electrostatic model, FeAl nanoparticles were prepared under the influence of 60 and 500 V/cm, respectively, in the chamber. Figure 38 shows optical pictures, inside the chamber, for both experiments. In the first experiment, under 60 V/cm field, FeAl filaments grew and connected target with the top plate, as shown in Figure 38 a. On the other hand, using a high electric field (500 V/cm) resulted in discharging effect at the filaments' tips growing on the target surface. These filament tips carry a highly-nonuniform electric field density, shown as purple coronas in Figure 38 b. Therefore, these filament tips, which carry a high electric field density, will act as attractive sites for other particles generated by laser vaporization causing the particles to stick to them and form these filament-like assemblies.

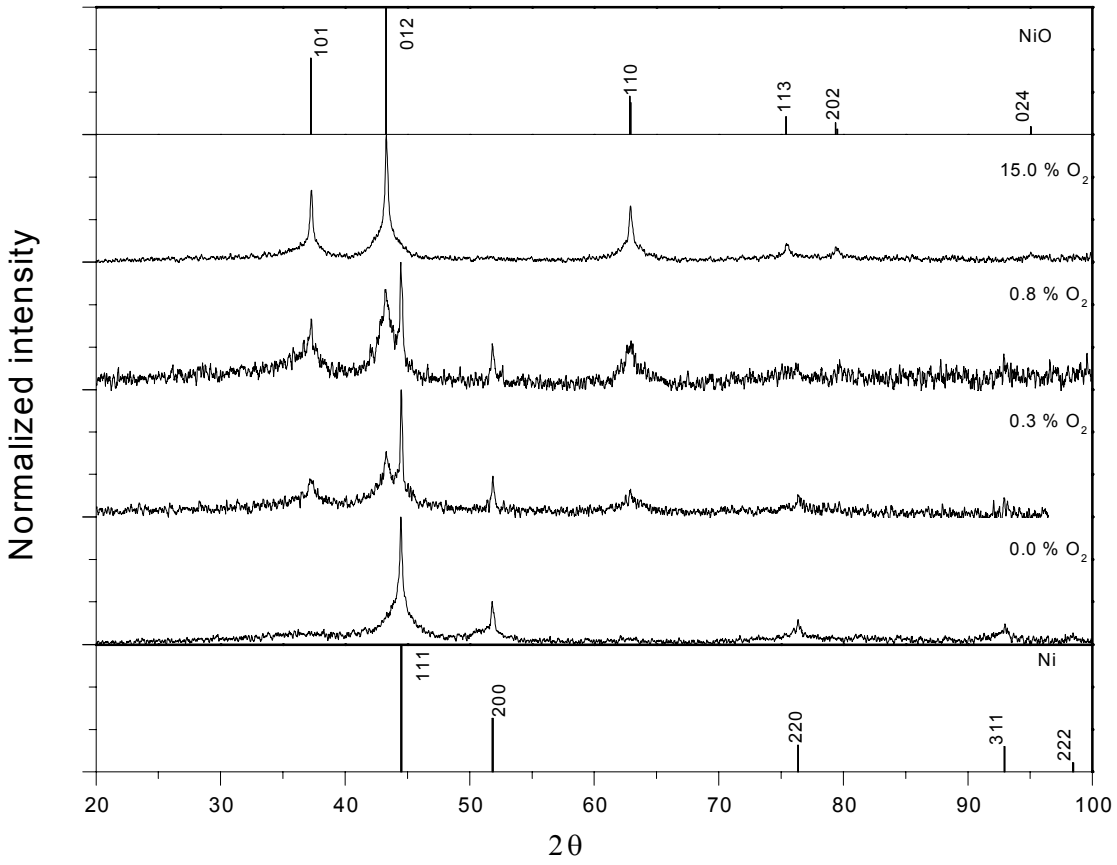

Figure 21. X ray diffraction patterns of Ni nanoparticles prepared under different oxygen levels in the presence of an electric field (60 V/cm) using the LVCC method.

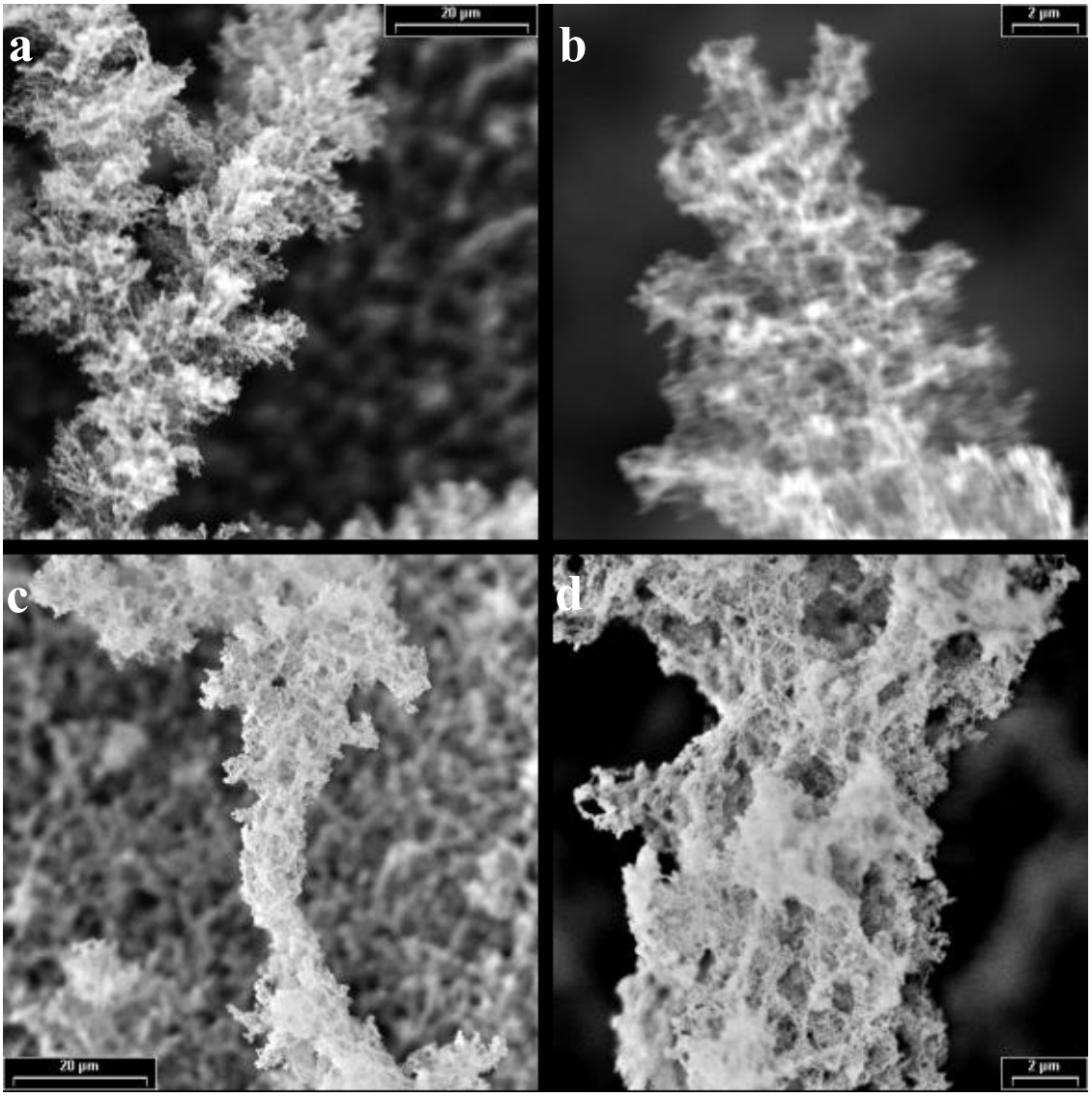

Figure 22. SEM micrographs of Ni (a,b) and NiO (c,d) filament nanoparticles prepared under the influence of an electric field (60 V/cm).

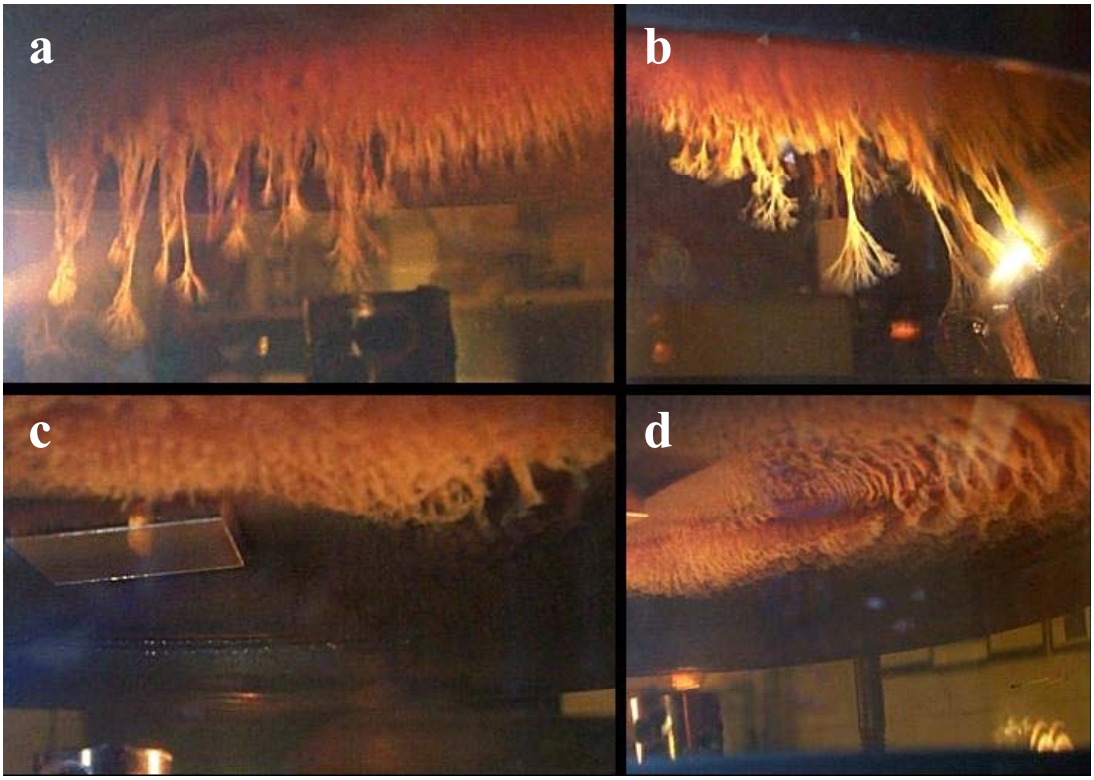

Figure 23. Photographs for iron oxide nanoparticles prepared under high electric field 200 V/cm (a,b) and (c,d) are at 5% and 25% oxygen level, respectively, in the chamber.

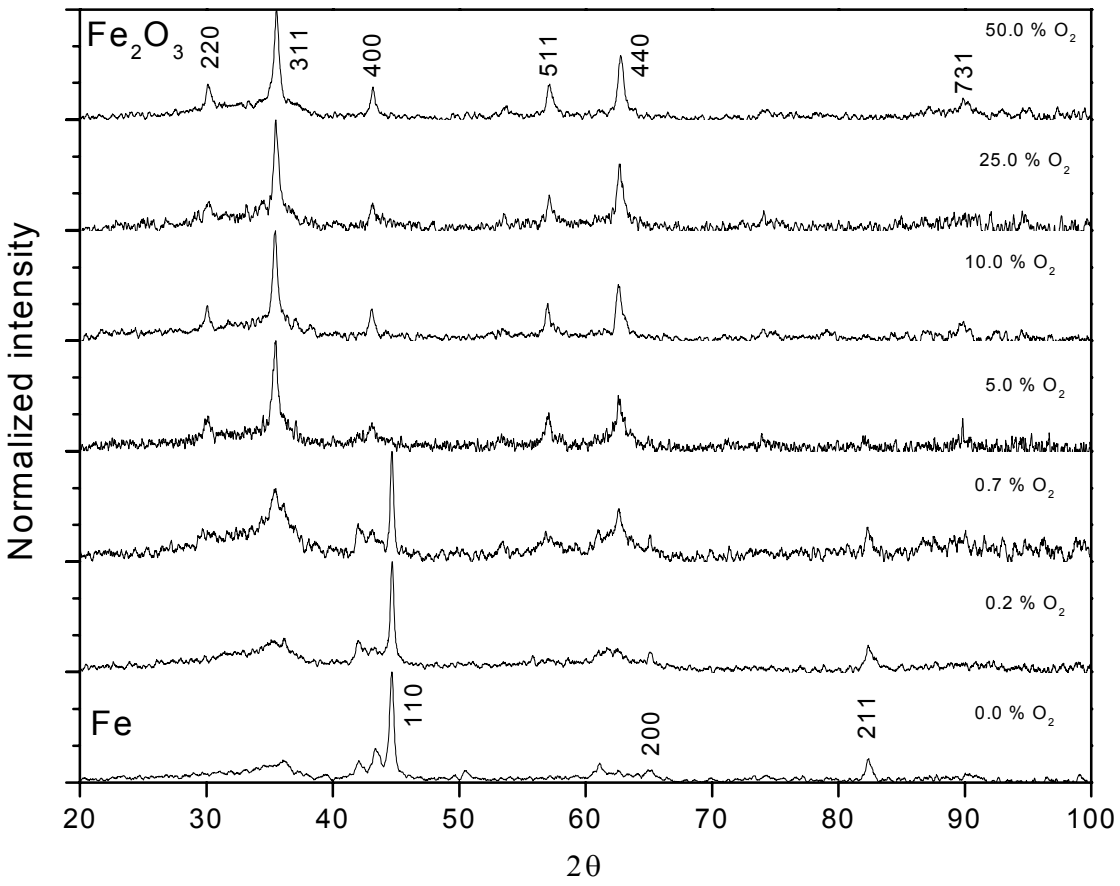

Figure 24. X ray diffraction patterns of Fe nanoparticles prepared under the influence of constant electric field (200 V/cm) and different oxygen levels.

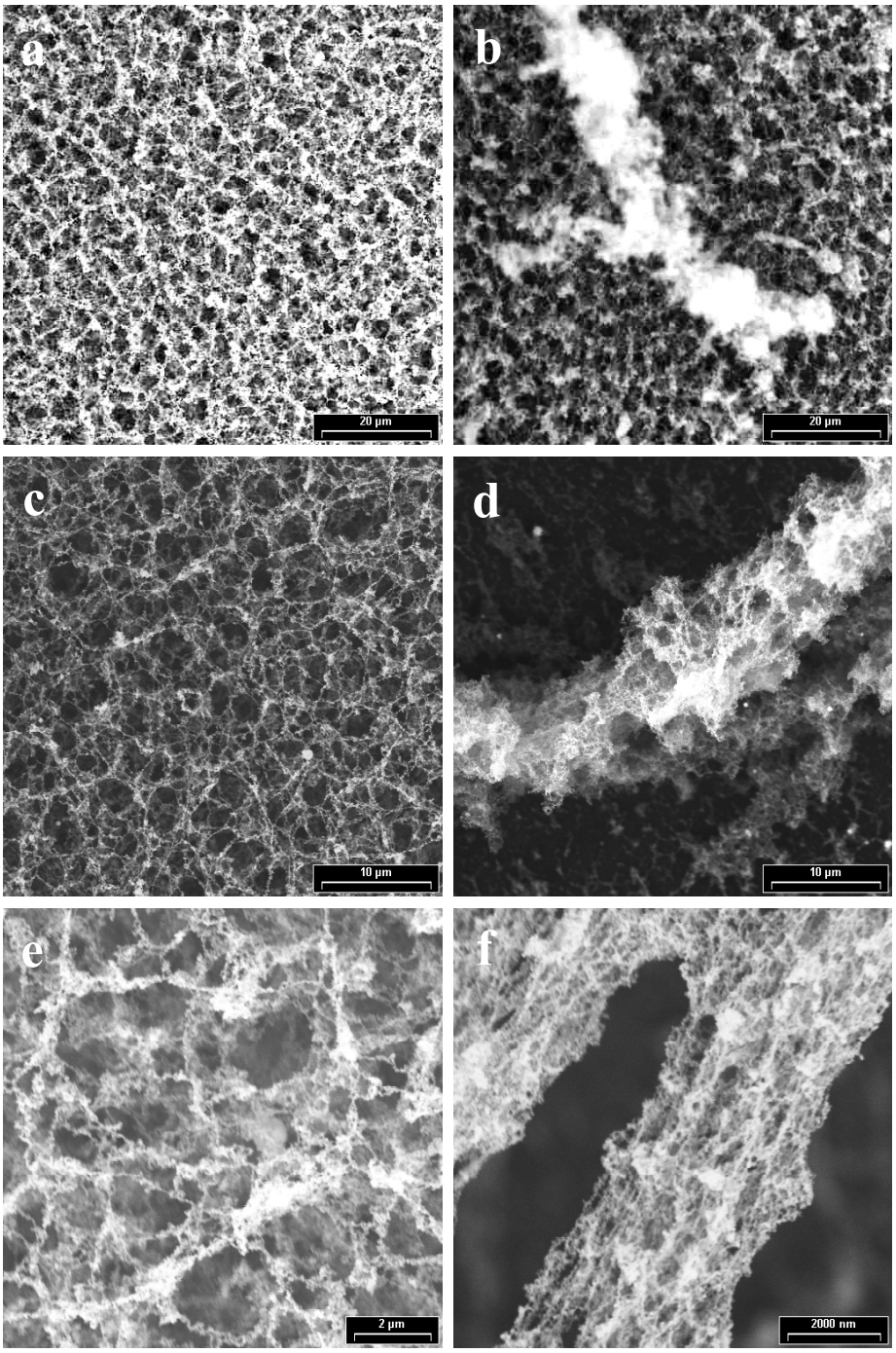

Figure 25. SEM micrographs of Fe nanoparticles deposited in the absence (left images) and presence of electric field (200 V/cm) (right images) prepared under 3 different oxygen levels 0.0, 5.0 and 25.0 %, as displayed in (a-b), (c-d) and (e-f)), respectively.

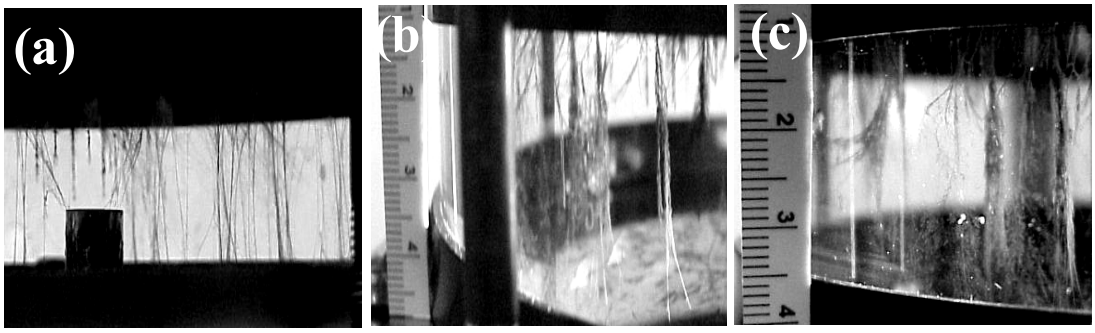

Figure 26. Photographs of FeAl filaments in the chamber (E = 60 V/cm) after 30, 60 and 120 min in a, b and c, respectively.

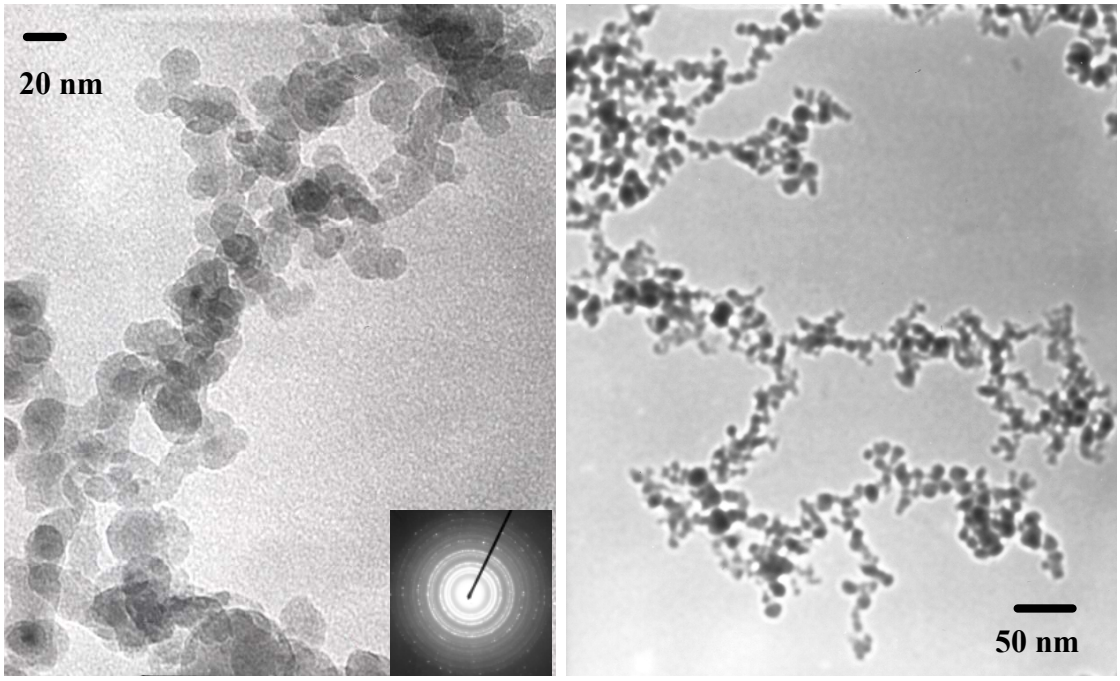

Figure 27. TEM micrographs and ED for FeAl nanoparticles prepared under an electric field (60 V/cm) by the LVCC method.

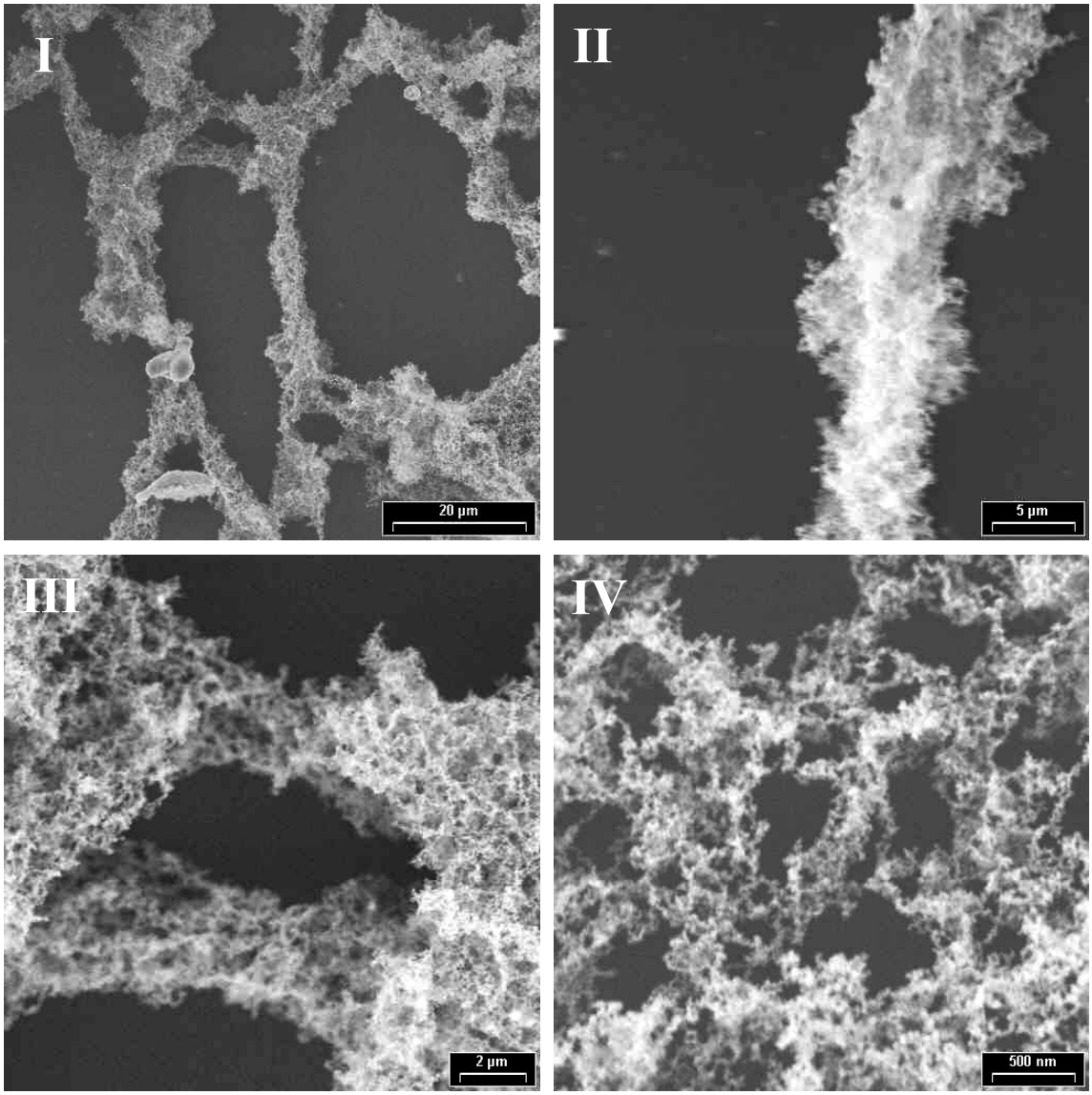

Figure 28. SEM micrographs of FeAl (24% Al) nanoparticles prepared under the influence of electric field (60 V/cm) using LVCC method with different magnifications (I, II, III and IV).

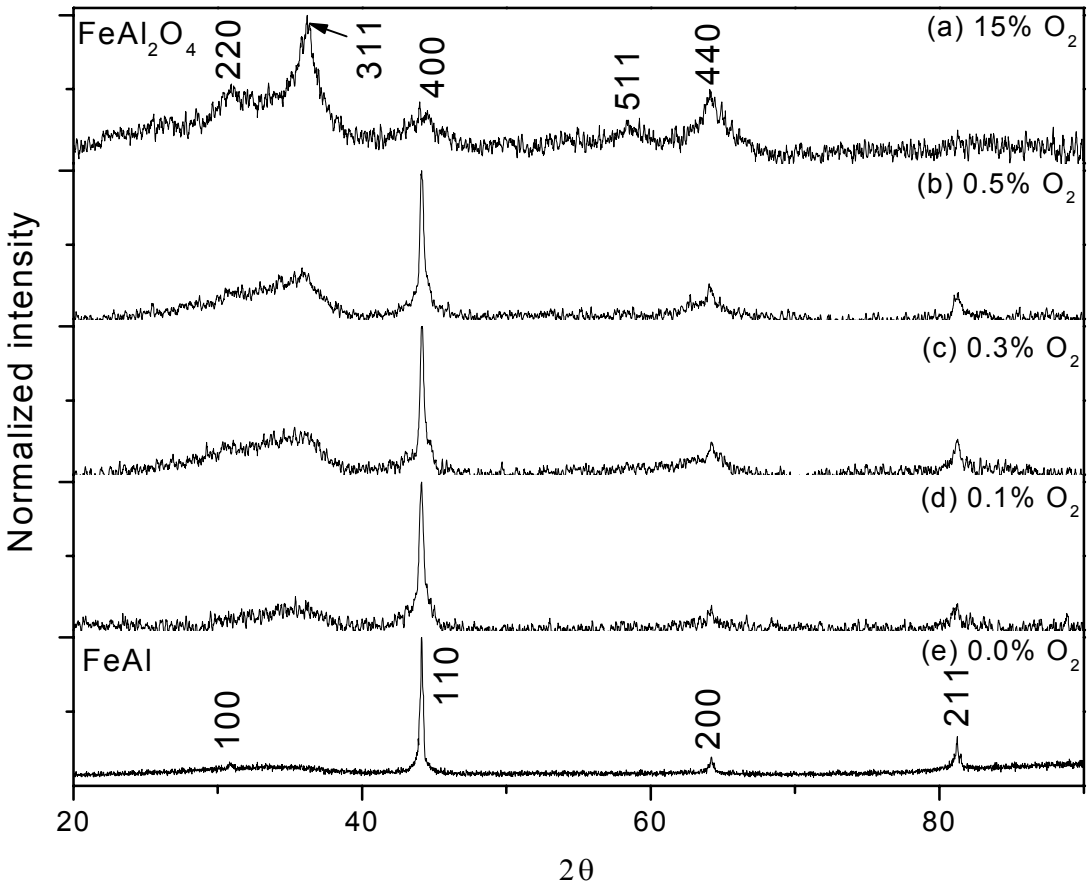

Figure 29. Oxygen addition effect on the fiber formation of FeAl nanoparticles in the presence of an electric field (60 V/cm).

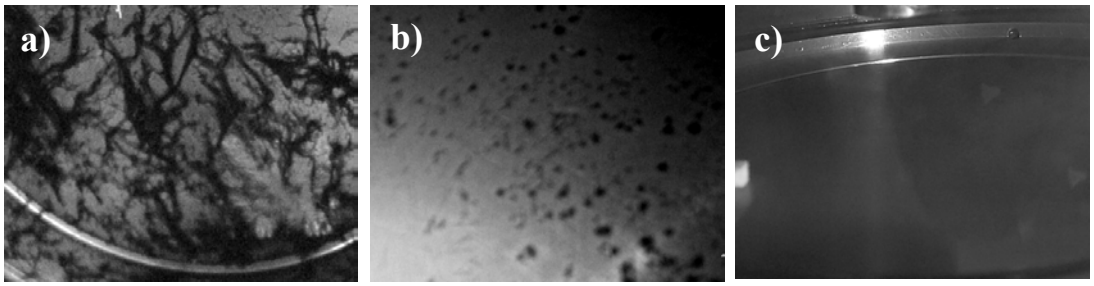

Figure 30. FeAl nanoparticles deposited on top plate under 60 V/cm with three different O_2 levels in the chamber 0.0% (a), 0.3% (b) and 0.5% (c) showing fibers, aggregates and thin film, respectively.

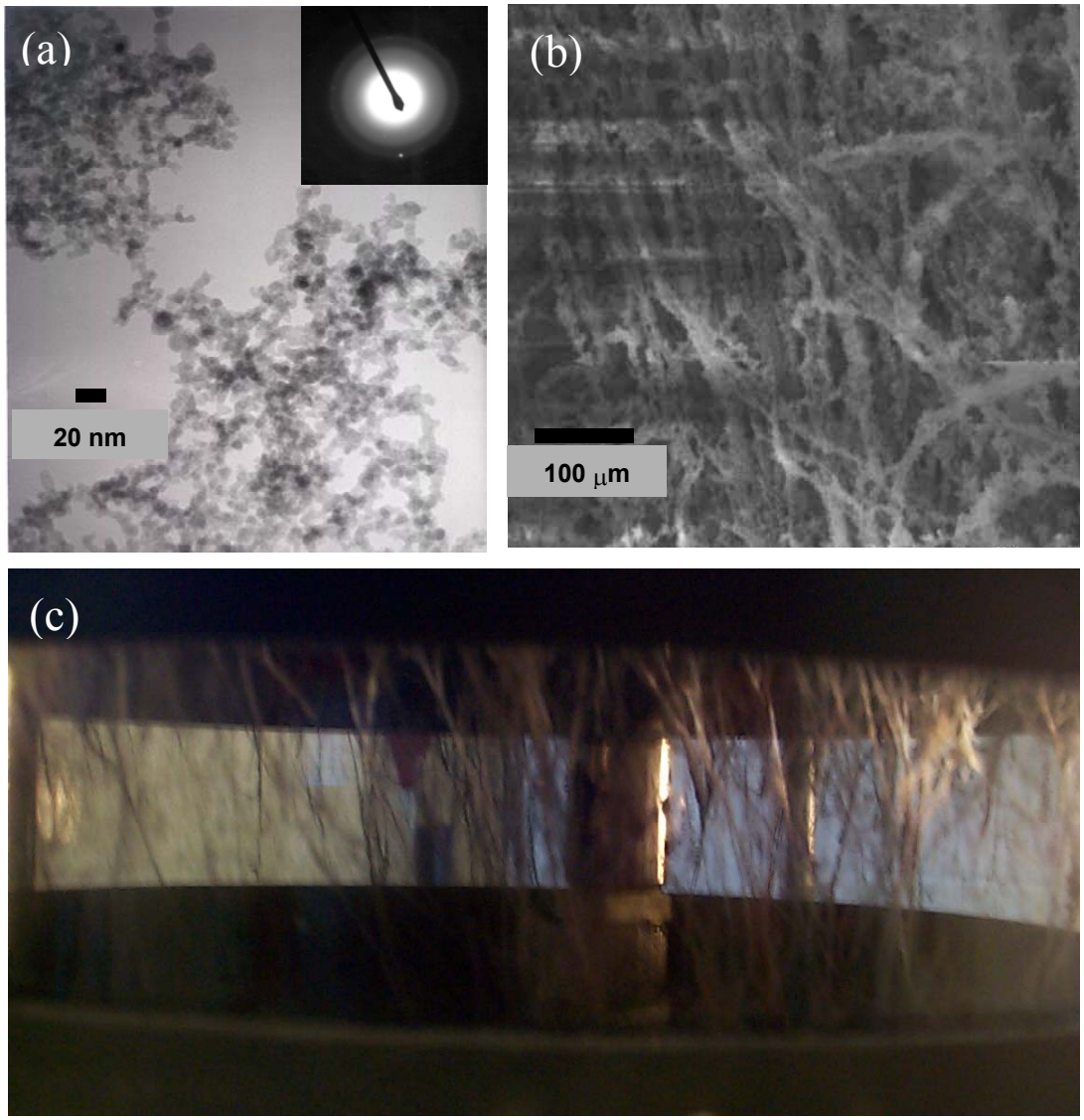

Figure 31. Ti_3Al nanoparticles prepared under the influence of an electric field (60 V/cm), TEM, SEM and photograph of Ti_3Al are shown in a,b and c, respectively.

Table 5. Electric field (dc) effects on the formation of nanoparticle filaments.

Nanoparticles w fibers	Electrical field (V/cm)	Nanoparticles w/o fibers	Electrical field (V/cm)
In	200	Ga	200
Si *	200	Al *	500
Fe	60	B	200
Cu	60	Ge *	200
Zn	60	Sn	200
Ti	60	Gd	60
Ni	60	Er	60
Mg	60		
C	60		
FeAl	6		
TiAl	60		
NiAl	60		

* FTIR shows some oxides.

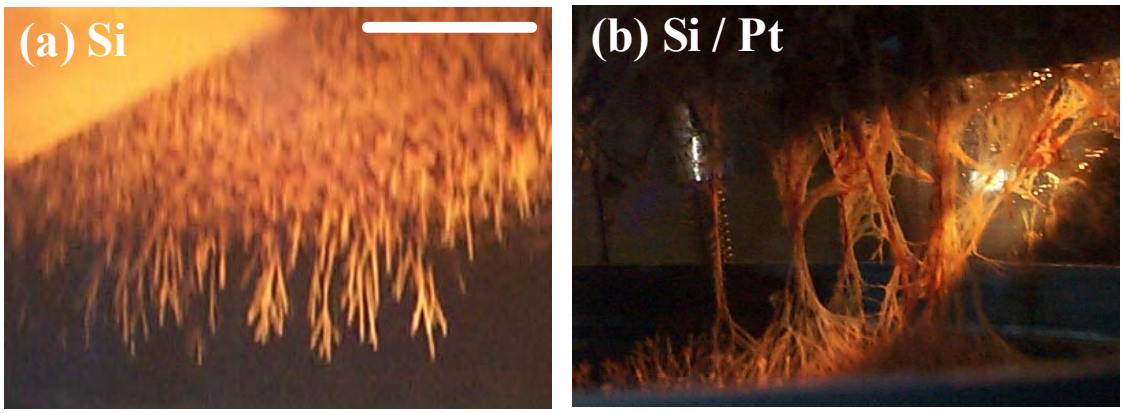

Figure 32. Photographs of (a) Si and (b) Si/Pt nanoparticles assemblied in filament and tree-like structures prepared in the presence of electric field (200 V/cm).

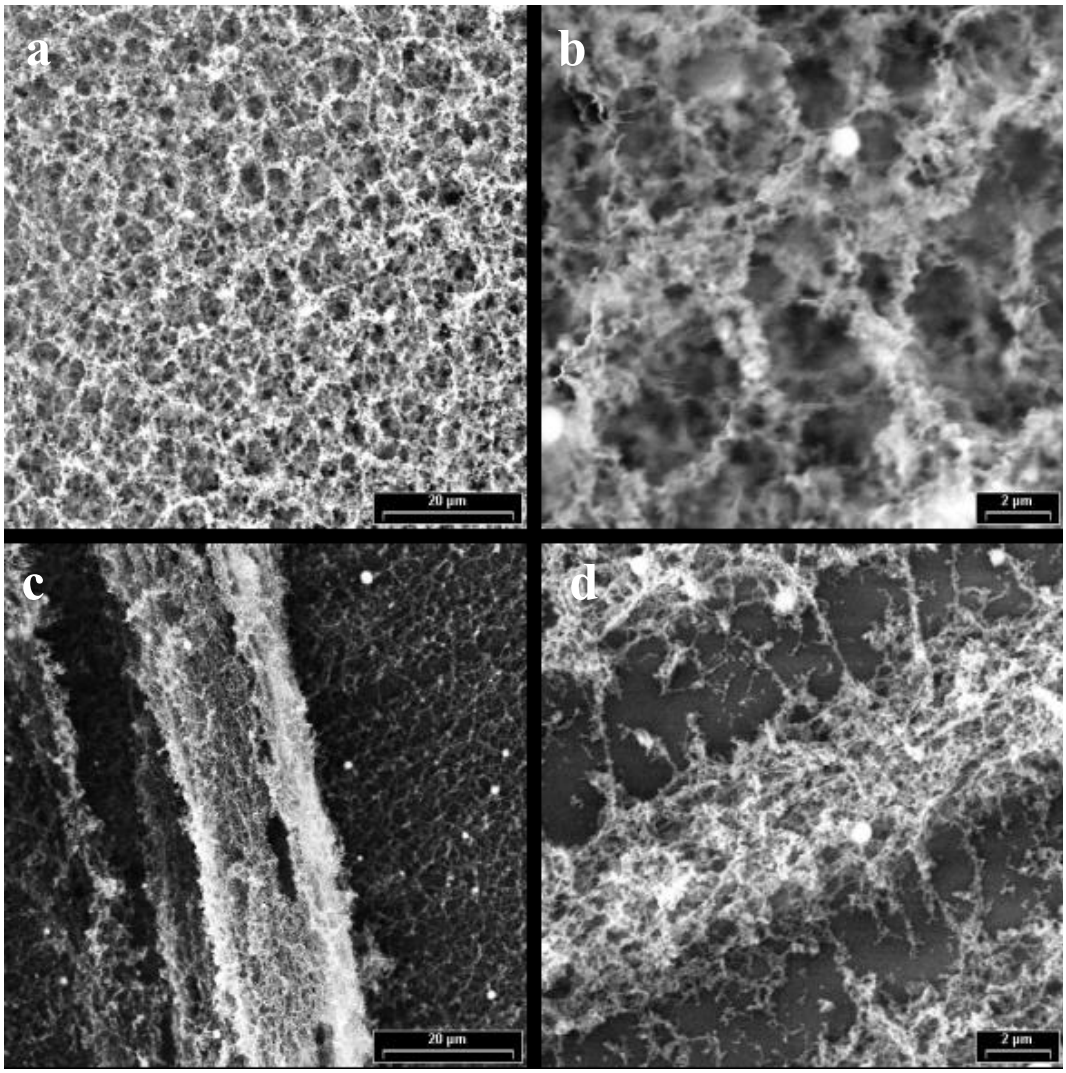

Figure 33 SEM micrographs of Si nanoparticles prepared without (a,b) and with (c,d) electric field (200 V/cm).

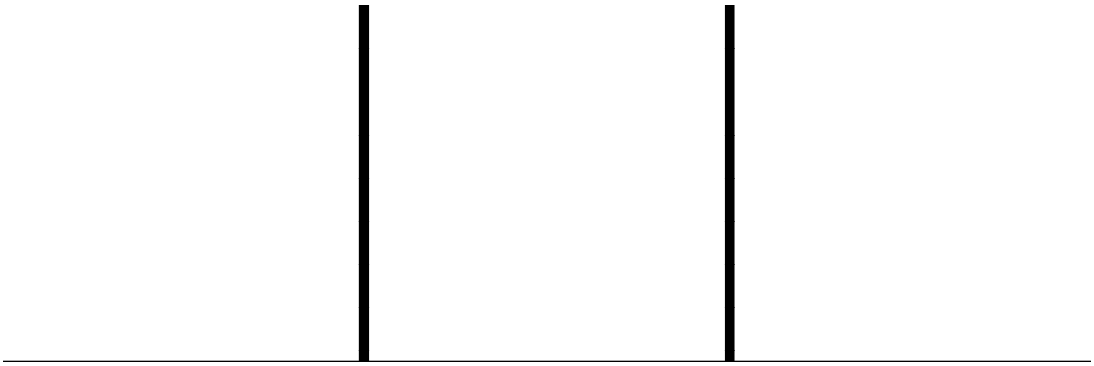

Figure 34. SEM micrographs of Si/Pt nanoparticles prepared in the presence of an electric field (200 V/cm).

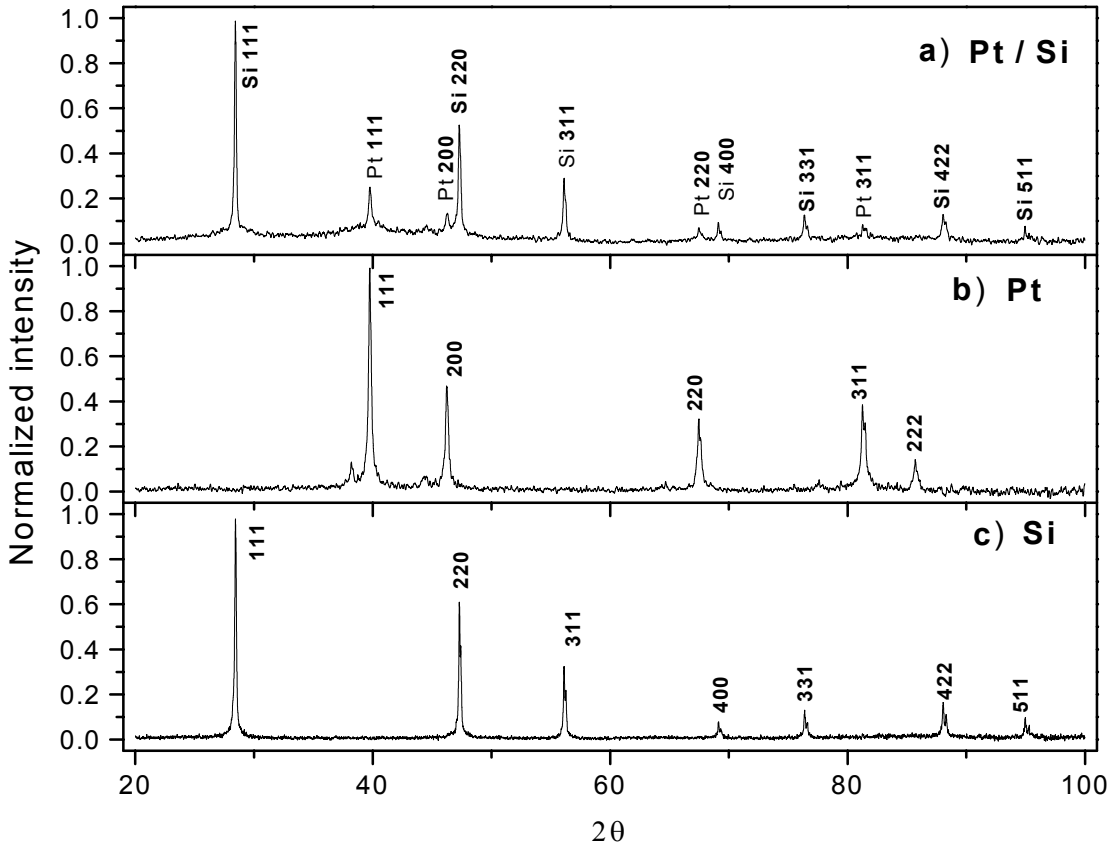

Figure 35. X ray diffraction patterns of a) Pt/Si, b) Pt and c) Si nanoparticles.

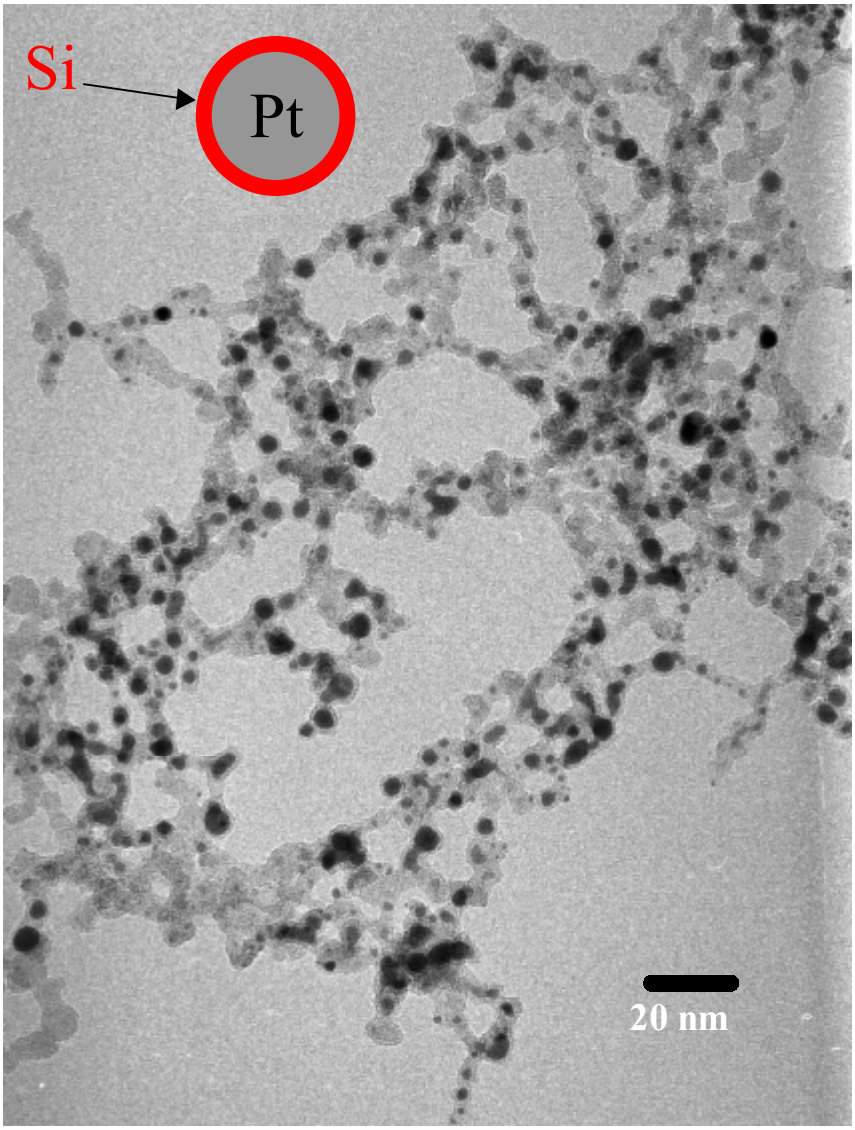

Figure 36. TEM micrograph of Pt/Si nanoparticles prepared in presence of electric field (200 V/cm) with a core/ shell structure.

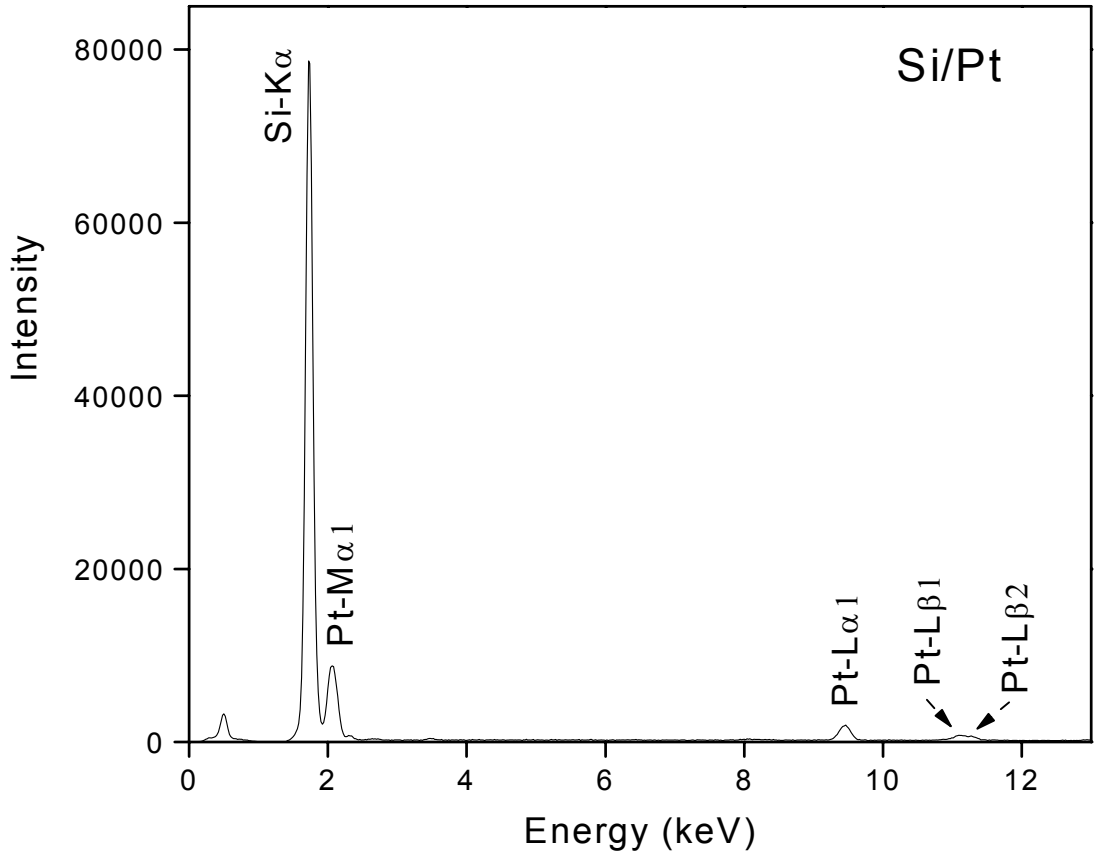

Figure 37. EDX spectra for Si/Pt nanoparticles prepared under 200 V/cm by simultaneous laser vaporization of Si and Pt targets in the LVCC chamber.

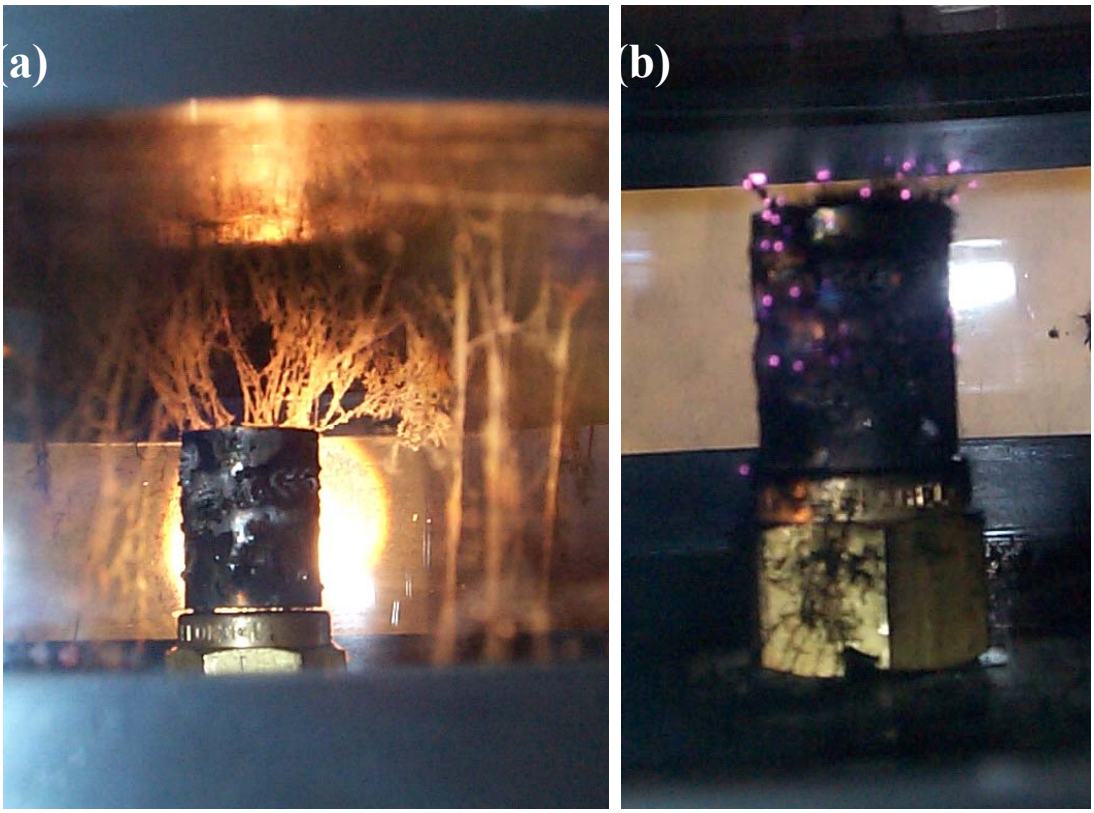

Figure 38. Optical photographs of FeAl nanoparticles growing on target that is connected to the bottom plate of the chamber under (a) 60 and (b) 500 V/cm, respectively.

3-5 Size Selection

3-5-1 Introduction

It is well known that nano-scale materials exhibit unique properties that could be very different from those of bulk materials. Size-dependant properties are observed when nanoparticles are prepared with a narrow size-distribution. For example, size-selected silicon nanoparticles exhibit size-dependent photoluminescence due to quantum size effect,[76-79] monodispersed FePt nanoparticles show high-density magnetization reversal transitions[80,81] and size-controlled gold nanoparticles are used as catalysts of indium phosphide nanowires with tunable diameters.[82] It is well known that such nano-scale properties are largely dependent on the size and the morphology of the nanoparticles. Nevertheless, the control of the size distribution, the crystallinity, and the agglomeration is the most important issue to fabricate the required property of nanoparticles. Monodispersed nanoparticles have been conventionally synthesized via a liquid phase process.[83] However, a significant amount of defects and impurities are associated with the nanoparticles made from solvents with surfactants in a liquid phase process. On the other hand, the gas phase process such as laser synthesis of nanoparticles is one of the processes that reduces

contamination since it can be operated under high purity gas atmospheres.[84] However, it is difficult to control the size and distribution because the nucleation and growth are governed by the random collision of monomers and clusters by Brownian motion. Therefore, the controllability of the size distribution by the laser ablation is limited.

The Laser vaporization and controlled condensation (LVCC) technique was developed to overcome these difficulties by controlling the nucleation, growth and transport of the laser vaporized material.[85] In this technique, various kinds of nanoparticles were synthesized from supersaturated vapor, which was generated by laser vaporization of target materials under well-defined temperature, pressure, and electric field. The LVCC technique has been applied to the synthesis of nanoparticles of semiconductors, metal oxides,[85] and intermetallic alloy.[45] The moderate temperature gradient and electric field suppress the turbulence in the chamber, so that the transport and the deposition of the generated particles can be controlled. Also, they are effective to reduce agglomeration of the primary particles.

Differential mobility analyzers (DMA), which have been widely used in atmospheric aerosol measurement, have begun to be applied to the laser ablation synthesis of nanomaterials.[86] The nanoparticles sorted by the DMA were characterized by an extremely narrow size bands.[87-89] The

ability of the DMA to sort nanoparticles according to their sizes was also enhanced by operating it under reduced pressure conditions.[20] In this work, DMA was basically used as a size classifier, which produces very narrow size ranges of the particles. Additionally, it can be used as a measurement instrument when it is coupled with a detector. However, as it is well known, it is difficult to apply to the industrial scale of the production since the production rate is comparatively low (less than μg<hr).

In this work, the performance of the DMA to obtain the monodispersed nanoparticles is demonstrated. Also, DMA is used as an *in-situ* monitor of the size distribution of the nanoparticles generated by LVCC operated under various conditions. The parameter of the LVCC was such that the temperature gradient, ΔT and the electric field, E were optimized to obtain specific size range of nanoparticles based on the measurement of size distribution using a DMA.

Generation and Transport of Nanoparticles in the LVCC Process

The schematic illustration of particle formation and transport in the LVCC chamber is shown in Figure 39. The nanoparticles were produced by the rapid cooling of supersaturated vapor, which was evaporated from a solid target with pulsed laser irradiation in inert gas. Part of the particles were originally carrying the electrical charge

(most likely in the equilibrium charge state) by the thermal electrons, photoelectrons, and ions generated in the laser-induced plasma plume. The generated particles were then transported by the gas flow, from the bottom to the top of the chamber. By applying an electric field between the two plates, the particles were attracted to one side of the plate by electrostatic force, and they were deposited on the specific side of the plates when the particle electrical velocity was large enough with respect to the gas velocity. Here, the electrostatic velocity of the particles is represented as:

$$v_E = Z_p E \qquad \text{Eq. 3-4}$$

The electrical mobility, Z_p, of particles is expressed as:

$$Z_p = qeC_c/3\pi\mu d_p \qquad \text{Eq. 3-5}$$

Where q is the number of charge, e is the elementally electrical charge, μ is the viscosity of gas, and d_p is the particle diameter. C_c, the Cunninghum's correction factor, is expressed as:

$$C_c = 1 + Kn\{1.257 + 0.40 \exp(-1.10/Kn) \qquad \text{Eq. 3-6}$$

Where Kn is Knudsen number ($= 2\lambda/d_p$; λ is mean free path of gas molecules). The dependence of the mean free path on the pressure of a gas is given by:

$$\lambda = \frac{kT}{\sqrt{2}\pi\sigma^2 p} \qquad \text{Eq. 3-7}$$

Where k, T and σ are the Boltzmann constant, temperature, and collision diameter of a gas molecule, respectively. In the free molecular regime (K_n>>1), the electrical mobility is inversely proportional to the gas pressure, while the relationship between the particle diameter and applied voltage does not change with pressure.

However, when the thermal gradient was applied between two plates of LVCC chamber, the particles were moved by the thermophoretic force. The thermophoretic diffusivity D_T at the temperature T and temperature gradient ΔT was obtained by the following equation:

$$D_T = \alpha_\tau \nu \ (\Delta T/T) \quad \text{Eq. 3-8}$$

Where ν is the kinetic viscosity and α_τ is the thermophoretic constant which is almost constant at 0.54 with particle diameter in the nanometer-size range (Knudsen number; Kn >> 1). The D_T, is almost constant with respect to the particle size, while Z_p has strong dependence on particle size. Therefore, thermophoretic force is available for collecting all sizes of particles on the cold plate, while the electrostatic force is suitable for collecting specific size of nanoparticles.

In order to balance these external forces and to control the transport more effectively, a He gas flow was used as the carrier gas, as shown in Figure 39. Two mesh plates were located at top and bottom of the chamber and a vertical uniform flow in the chamber was produced. The

average gas velocity is simply calculated by ($v_g = Q/A$), where Q is the volumetric flow rate of gas and A is the cross sectional area of the chamber. It should be noted that the negatively charged particles were moving against the gas flow when the positive voltage was applied to the bottom plate. As a result, positively charged particles accelerated toward the outlet (top plate), but negatively charged particles may have balanced with the electrostatic field. By setting specific values for voltage, temperature, and gas flow rate; sizing of the generated particles can be achieved.

3-5-2 Experimental

The synthesis of nanoparticles by LVCC technique was mentioned in section 3-2. In this work, the LVCC was modified to operate in a flow mode rather than in a static mode by using two mesh plates at the top and bottom of the chamber to produce a continuous carrier gas (He) flow in the chamber, as mentioned in the last section. The whole experimental setup is illustrated in Figure 40. The particles were synthesized by a nano-second pulsed Nd:YAG laser vaporization (wavelength, 532nm; power, 70 mJ/pulse) from a bulk target (Si or FeAl). The electric field was generated by applying a positive dc voltage to the bottom plate and by grounding the top plate. Similarly, temperature gradient was produced by feeding hot water (up to 90 ^{o}C) to the bottom and by cooling the top plate by liquid nitrogen. The charged particles, generated by laser vaporization, were condensed and transported by electrostatic force, the thermophoretic force, and the gas stream. The nanoparticles that had a larger velocity than the particle inertia were deposited on the top plate. The size of the deposited nanoparticles was controlled by tuning the strength of the applied field. The morphology and the size of the deposited particles were observed by a scanning and a transmission electron microscope. The crystallinity of the collected particles was also analyzed by x-ray diffraction (XRD). The rest of the

particles, which did not deposit on the plates were transported out of the LVCC chamber with a carrier gas and then introduced into a differential mobility analyzer (DMA). An illustration of DMA principle is shown in Figure 41. In the DMA, the particles were differentially classified utilizing the balance of electrical mobility and gas flow. The mobility of the classified particles was related to the applied voltage to the DMA, *V*, as:

$$Z_p = \frac{Q_s \ln(R_2/R_1)}{2\pi L V} \qquad \text{Eq. 3-9}$$

Where Q_s is sheath gas flow rate, R_1, R_2, and L are radii of DMA inner rod and outer column, and the length of classification zone, respectively. By combining Eq. (3-5) with Eq. (3-9), the mobility equivalent diameter of the nanoparticles can be controlled by the DMA applied voltage. After the classification by the DMA, the particles were collected by impaction onto the solid substrate. By measuring the electric current, *I*, from the singly charged particles, the number density of the particles, N, can be obtained as:

$$N = \frac{I}{eQ_a} \qquad \text{Eq. 3-10}$$

Where Q_a is aerosol flow rate. The mobility size distribution of the gas phase particles can be observed *in-*

situ by scanning the DMA applied voltage and measuring electric current.

3-5-2. Results and Discussion

Size classification by DMA

The performance of the classification process of the newly designed LP-DMA was calibrated by the comparison between the electron micrographs. The calibrations for the DMA were demonstrated at Tsukuba, Japan (*National Institute of Advanced Industrial Science and Technology* (*AIST*)) and the measurements of nanoparticles generated by LVCC were done at Virginia (*Virginia Commonwealth University* (*VCU*)) using the same dimension of the DMA. Size-selected FeAl particles of 30, 14 and 7 nm are shown in Figure 42. The classified particles were directly deposited on TEM microgrids. The size-selected FeAl particles were prepared by varying DMA applied voltage.

Size-Controlled deposition by utilizing the electrostatic force

Shown in Figure 43 are the size distributions of positively charged FeAl nanoparticles with varying electric fields applied between the chamber plates. The peak size is around 12 nm and is slightly larger than Si nanoparticles due to the lower vapor pressure of FeAl. Also, the distribution seems to be composed of two modes of particle peaks at about 12 nm and peak at about 30 nm. The first peak corresponds to small particles generated by the nucleation

of vaporized material, and the second peak might be produced by the field-induced aggregations as discussed in the last section 3-4. It could also be due to droplet-like particles generated by the liquid phase splash induced by ns-laser pulse. When the positive voltage was applied to the bottom of chamber, a significant decrease in the first peak was observed as shown in Figure 43. Since the electric mobility is a function of particle size, then the smaller positive particles, which had a larger velocity would deposit on the top of the chamber. On the other hand, the larger particles, which remained in the gas stream, were slightly accelerated and therefore exited from the chamber and were measured by the DMA. The non-dimensional form of Eq. (3-4) for the electrical velocity, v_E^* is given as:

$$v_E^* = Z_p V / L v_{av}, \quad \text{Eq. 3-11}$$

Where V is the voltage applied to the bottom plate. The value of v_E^* is 2.5 for d_p = 5 nm, 0.43 for 12 nm and 0.04 for 40 nm at E = 1470 V/m. The smaller particles had enough velocity to be deposited by the electric field, but most of the larger particles (> 10nm) accelerated and passed through the mesh at the top plate of chamber. Therefore, the concentration of the first peak decreased, and the secondary mode of the particles (> 20nm) in the outlet of the chamber increased with the electric field.

Similarly, the size distribution of the negative FeAl particles changed drastically with electric field as shown in Figure 44 however, the smaller field (147 V/m) is enough to decrease the number concentration of the particles in the outlet since the direction of the field is opposite to the gas. The generated negative particles were decelerated due to the electric force against the gas flow. Also, there was no increase in the observed number concentration as in the case of the positive particles because most of the particles were trapped in the chamber.

The scanning electron micrographs of the deposited particles with (a) small electric fields (E = 147 V/m) and (b) large electric fields (E = 2940 V/m) were shown in Figure 45. As predicted by the results of the DMA, the particles collected with a weak field showed the fine chain-like structures composed of nanoparticles less than 10nm. On the other hand, the SEM image for the strong fields (Figure 45(b)) shows a more aggregations and rough surface structures. These results were confirmed by transmission electron microscope images of the particles deposited on carbon-coated Cu grid placed on the top plate of the chamber for 60 min at 147 and 2940 V/m, respectively, as shown in Figure 46. The increase in number density of particles at (2940 V/m) compared to at (147 V/cm), is explained by the electrical velocity of small particles, which increased drastically by

increasing the electric field. This results in depositing most of the small particles more efficiently on the top plate. Another TEM images are shown in Figure 47 with more magnification of FeAl nanoparticles depositing for 60 min under 147 and 2940 V/m, respectively.

Shown in Figure 48 are the XRD patterns of generated particles. Obviously, the diffraction patterns show similar peaks with the reference data [68] of one to one alloy of iron and aluminum (FeAl) for both strengths of the electric field. The sample prepared in the weak electric field indicated relatively large and broad peaks of oxides around $2\theta = 33$ degree and also it showed relatively a strong peak for [110] direction, probably caused by the decrease in the particle size.

The effect of temperature gradient on the size distribution

Shown in Figure 49 are the changes in the size distribution of silicon nanoparticles measured by the DMA at the outlet of the LVCC chamber at a constant pressure of 20 Torr, at different temperature gradients, applied to the chamber. In the case where the temperature gradient was zero, the distribution with the peak size of about 10 nm was measured. No significant change in the size distribution was observed up to a temperature gradient of $\Delta T = 50$ °C. By

setting the temperature difference between the two plates to 90 °C, number concentrations of the particles that were exited from the chamber approximately doubled. Increase in the number concentration was observed for all sizes of particles since the thermophoretic velocity is independent of particle size, as mentioned before. The non-dimensional form of Eq. (3-8) is given as:

$$v_T^* = D_T / L v_{av}, \quad \text{Eq. 3-12}$$

Where L (=65 mm) is the distance between two plates. The value of v_T^* is 2.59 at ΔT = 90 °C. The increase in the number concentration occurred because thermophoretic velocity is considered to be in the same order with carrier gas velocity at ΔT = 90 °C. When the top plate was cooled by feeding-in liquid nitrogen, a sudden decrease in number concentration was observed at ΔT = 150 °C, because most of the generated particles were deposited on the cold plate. The value of v_T^* is 4.67 at ΔT = 150 °C, which indicates that the thermophoretic velocity is about 4.7 times larger than the average gas flow velocity. It is clear that ΔT = 90 °C is suitable for obtaining aerosol particles out of the LVCC chamber, and ΔT > 90 °C is required for particle collection in the LVCC chamber. The cut-off normalized velocity, v_T^* for the deposition is considered to be about 3 to 4.

The effect of laser power and pressure on the size distribution

Typical size distributions of positively charged Si nanoparticles prepared under a pressure of 20 Torr He gas inside a newly designed flow-LVCC chamber are shown in Figure 50. The Si nanoparticles were prepared under identical condition, but different laser vaporization powers of 40, 50, 66 and 140 mJ/pulse, respectively. The four size-distribution data show maxima at 9 nm, indicating that most of the Si nanoparticles prepared have a particle diameter of 9 nm regardless of the laser power used. As the laser power increases, the number-concentration of particles increases, including charged particles (detected by DMA). This result can be explained by the fact that when a high-energy laser pulse (high photon density) hits the Si surface, a large amount of energy is dumped into the target surface in a very short period of time, causing its surface temperature elevate very quickly and vaporize from the surface.[90] An estimated of 10^6 ions and 10^{14} atoms within a 10 ns laser pulse have been reported [11].

The pressure effect on the size-distribution of Si nanoparticles is displayed in Figure 51. The size-distribution data were collected at four different pressures (21.4, 26.2, 32.5 and 62.8 Torr). The size-distribution shifts to bigger particle sizes as the pressure increases inside the chamber; at chamber pressure of 21.4, 26.2 and 32.5 Torr, the maxima

of the size-distribution shifts to 6, 7 and 13 nm, respectively. At higher pressure (62.8 Torr), hardly any charged nanoparticles exit from the chamber to the DMA. It was also observed that the number density of particles detected by the DMA decreased with increasing pressure inside the chamber. These results can be explained by the following; when the pressure increases, residence time of particles increases inside the chamber. As a result, the particles will have more of a chance to agglomerate, shifting the size distribution to a larger size regime as well as decreasing the number density since the number of particles generated from laser vaporization is almost constant at the same power. A similar behavior has been reported by Seto and Camata.[20,91]

Summary

The formation and the transport of the nanoparticles were investigated and controlled by coupling a modified LVCC technique with a real-time measurement of particle size distribution by DMA. By analyzing the transport of nanoparticles in the generation chamber, specific size ranges of the particles could be selectively collected. This method was considered to be applicable to the synthesis of nano-materials, which gave novel optical, mechanical, and magnetic properties.

Size distribution of the silicon and iron aluminide (FeAl) nanoparticles generated by the laser vaporization controlled condensation (LVCC) method was analyzed *in-situ* using a low-pressure differential mobility analyzer (LP-DMA). The particles were generated and deposited by the laser ablation of solid targets in the presence of a well-defined thermal and electrical field in a newly designed flow-type LVCC chamber. The deposition rate of nanoparticles was controlled by the balance of the external forces, such as thermophoretic and electrostatic forces, under different synthesis conditions including the pressure of the carrier gas (20 - 200 Torr), the temperature gradient in the LVCC chamber (T = 0 - 190 °C), and the electric field applied between the LVCC chamber plates (E = 0 – 3000 V/m). The results indicated that an electrostatic field of about 147 V/m was effective to selectively deposit small size nanoparticles-films while expelling large droplet-like particles. The performance of the LP-DMA as the size-classifier to fabricate nanoparticles with very narrow band distribution was also demonstrated.

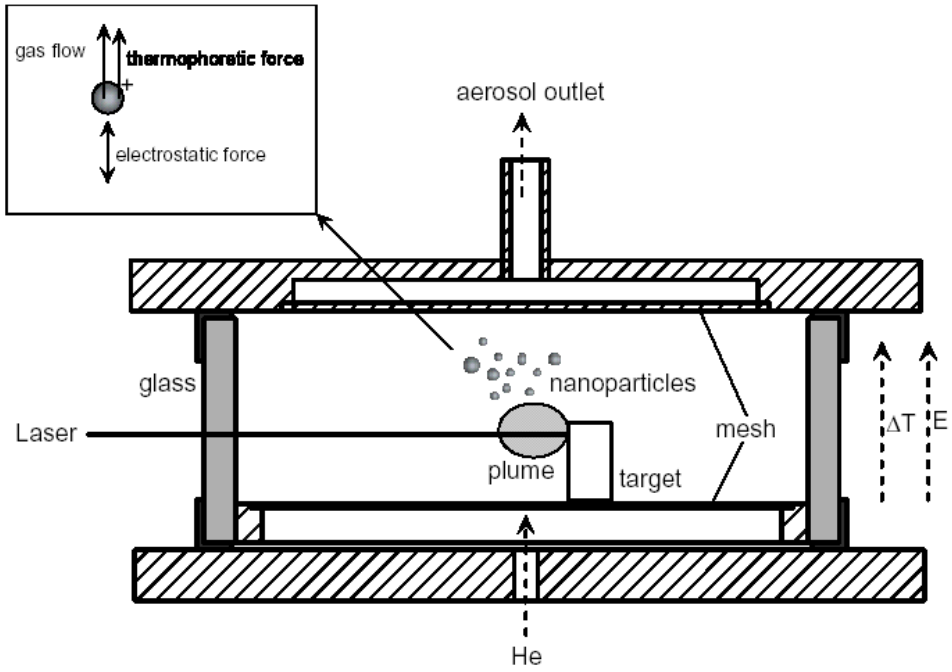

Figure 39. Schematic illustration of particle formation and transportation in the LVCC chamber.

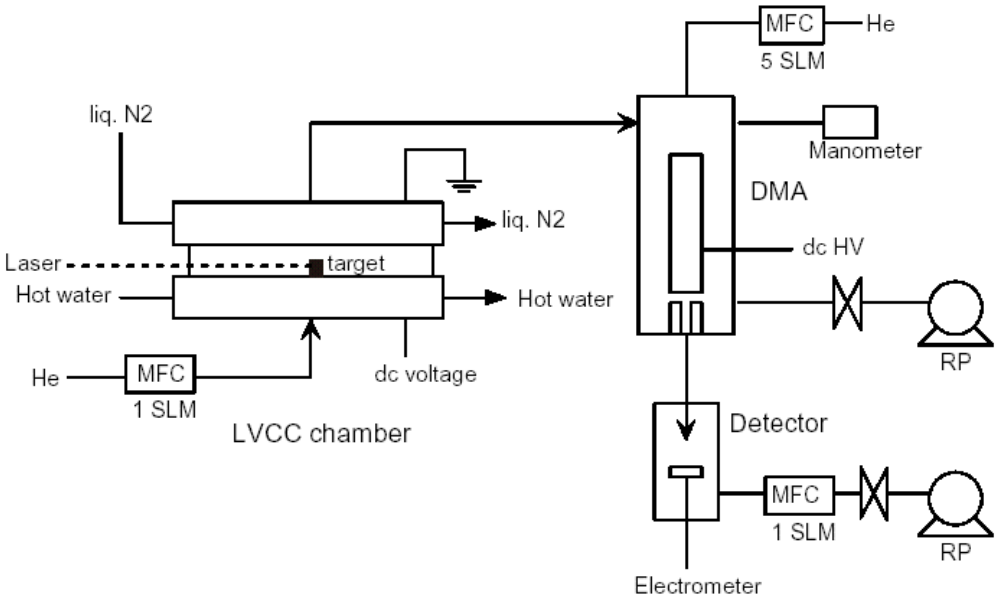

Figure 40. Schematic of the LVCC flow system coupled with DMA for the preparation of size-selected nanoparticles.

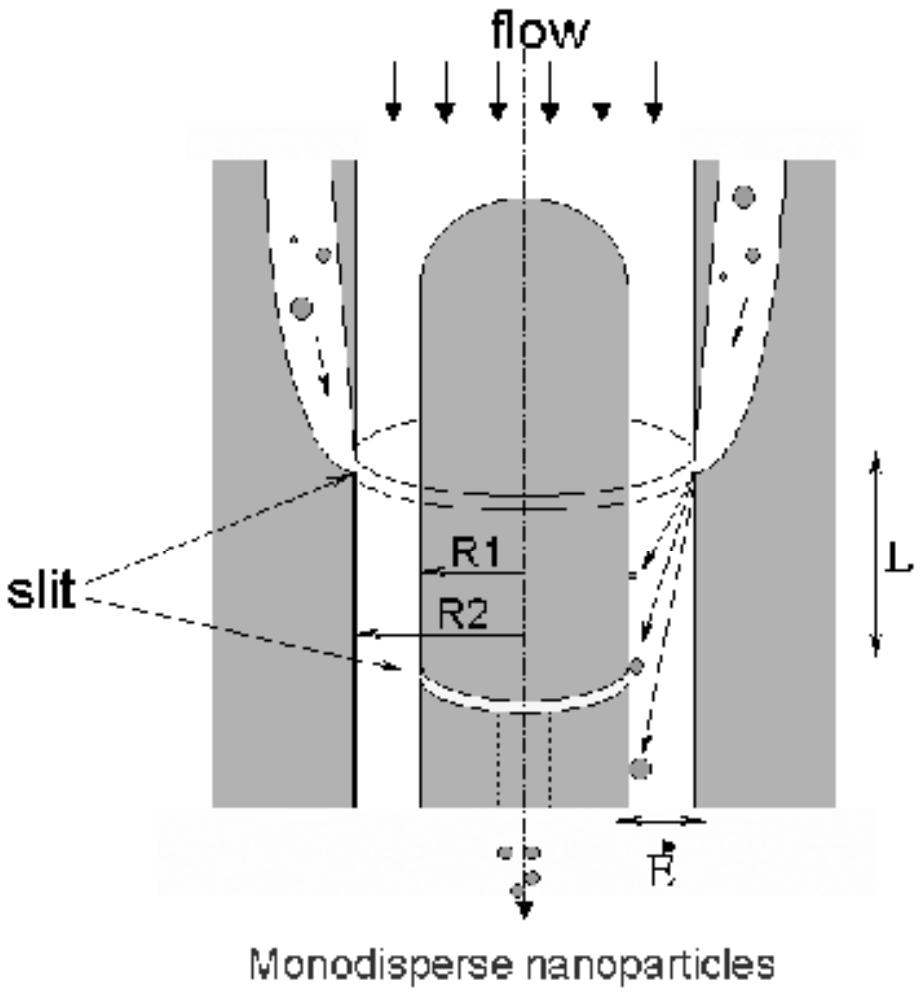

Figure 41. Illustration of the principles of operation of the DMA.

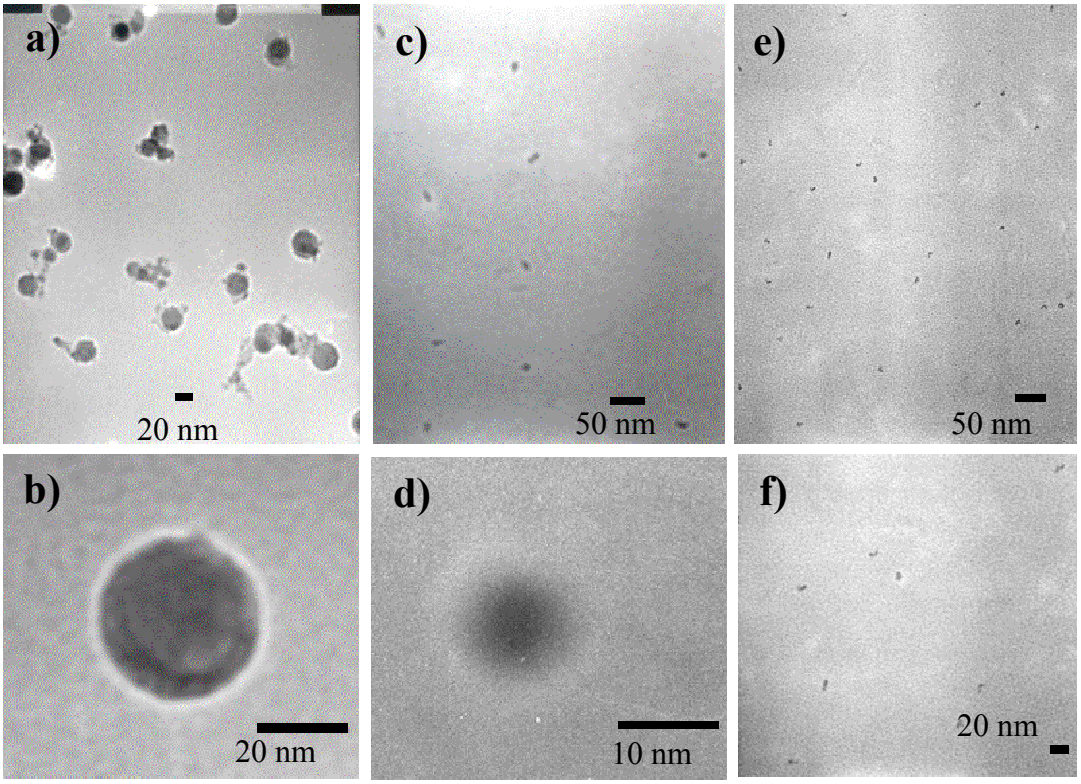

Figure 42. TEM of selected FeAl nanoparticles 30, 14 and 7 nm shown as (a,b), (c,d) and (e,f), respectively.

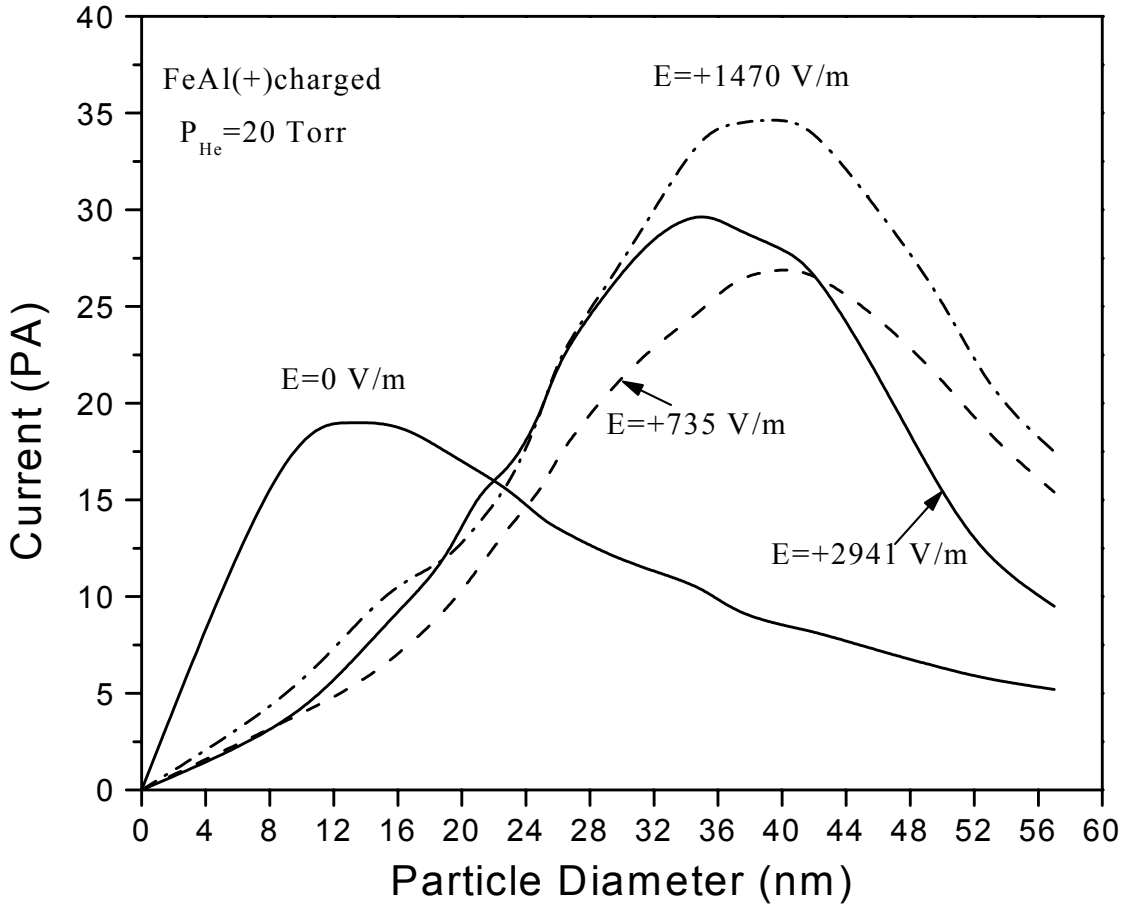

Figure 43. Size distribution of positively charged FeAl nanoparticles with varying electric field.

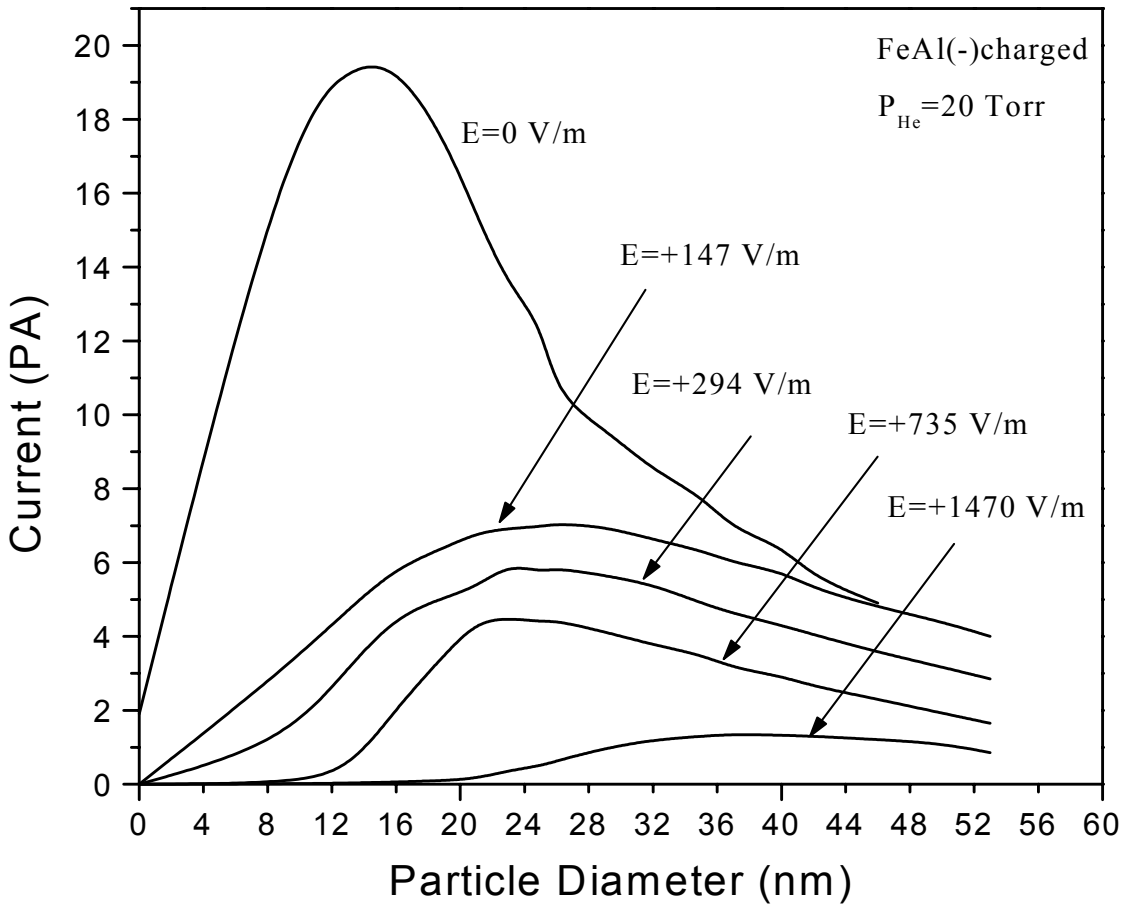

Figure 44. Size distribution of negatively charged FeAl nanoparticles with varying electric field.

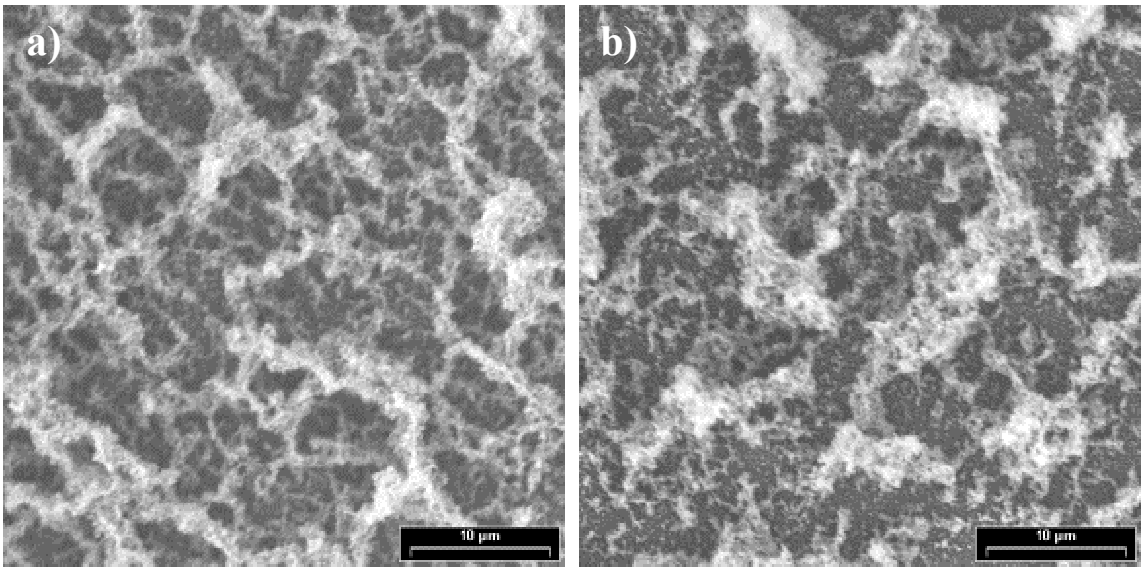

Figure 45. SEM micrographs of FeAl nanoparticles deposited on the top plate of the chamber under electric field of a) 147 V/m and b) 2940 V/m.

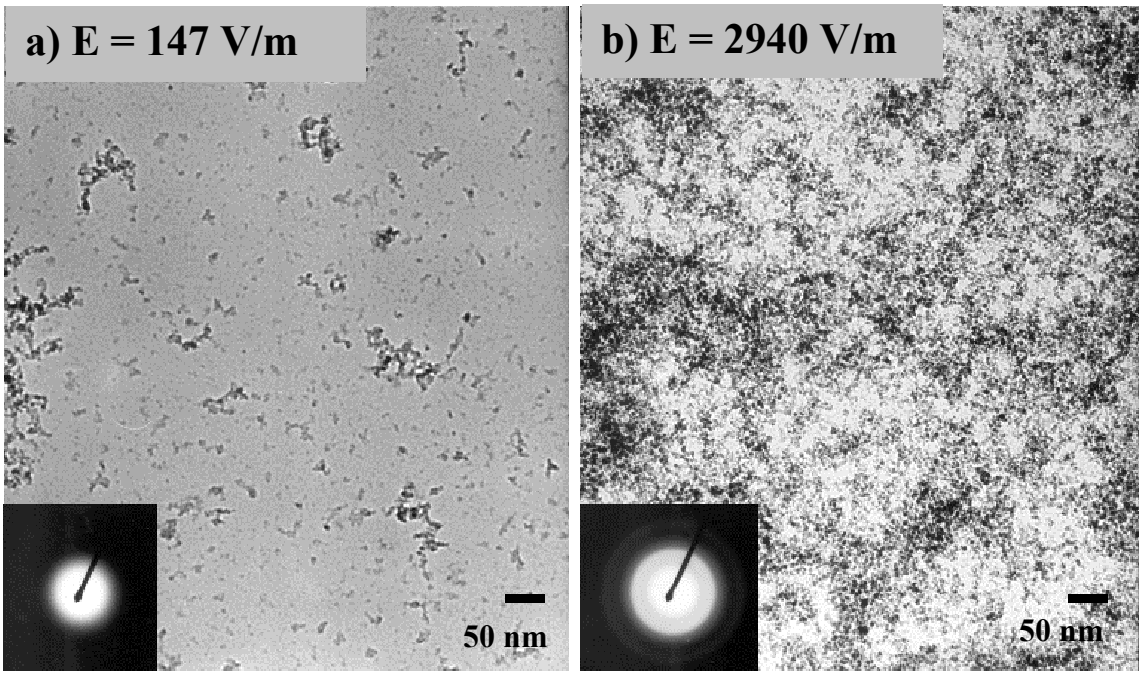

Figure 46. TEM micrograph of as-deposited FeAl nanoparticle for 60 min in the chamber under electric fields of a) 147 and b) 2970 V/m, respectively.

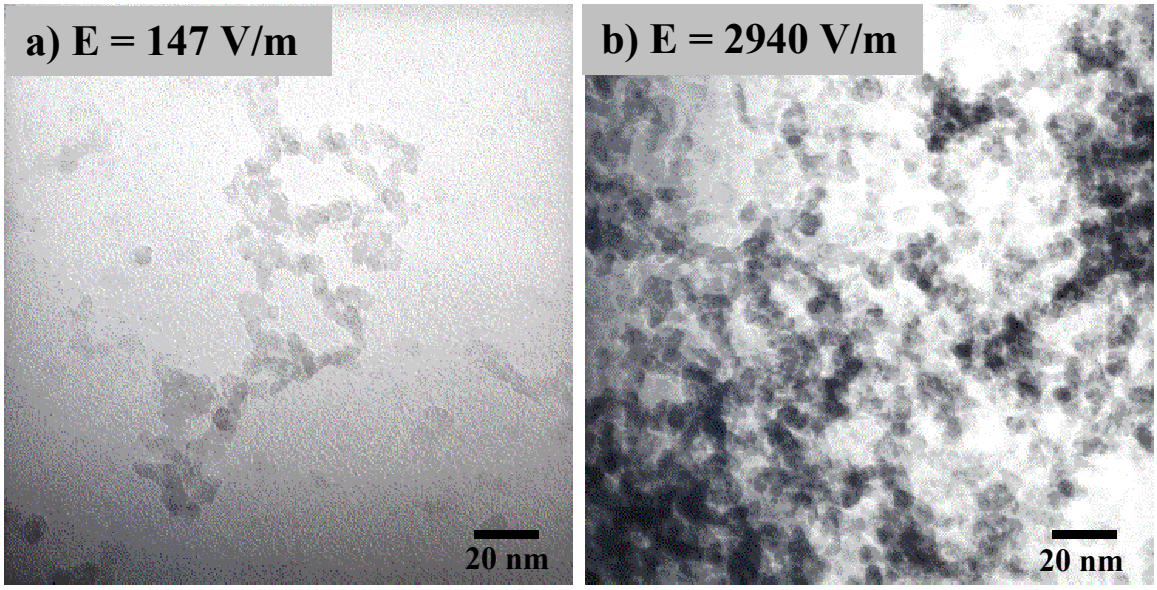

Figure 47. TEM micrograph of as-deposited FeAl nanoparticle for 60 min in the chamber under electric fields of a) 147 and b) 2970 V/m, respectively.

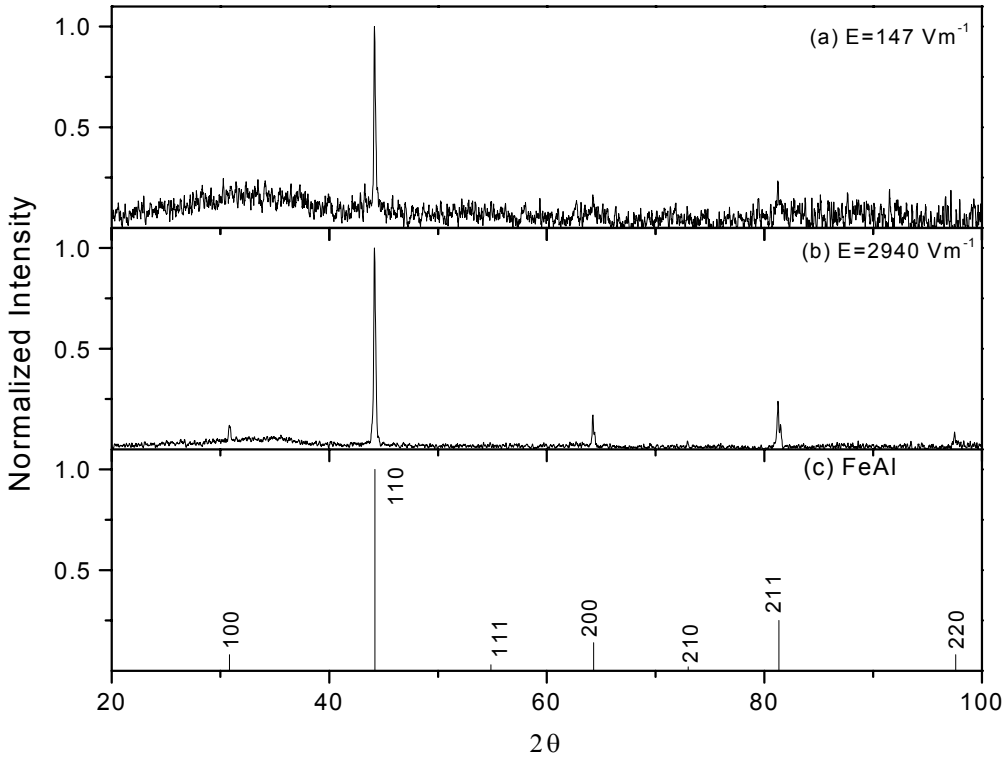

Figure 48. X-ray diffraction patterns of FeAl nanoparticles collected from the chamber with applying two different electric fields a) 147 and b) 2940 V/m, respectively.

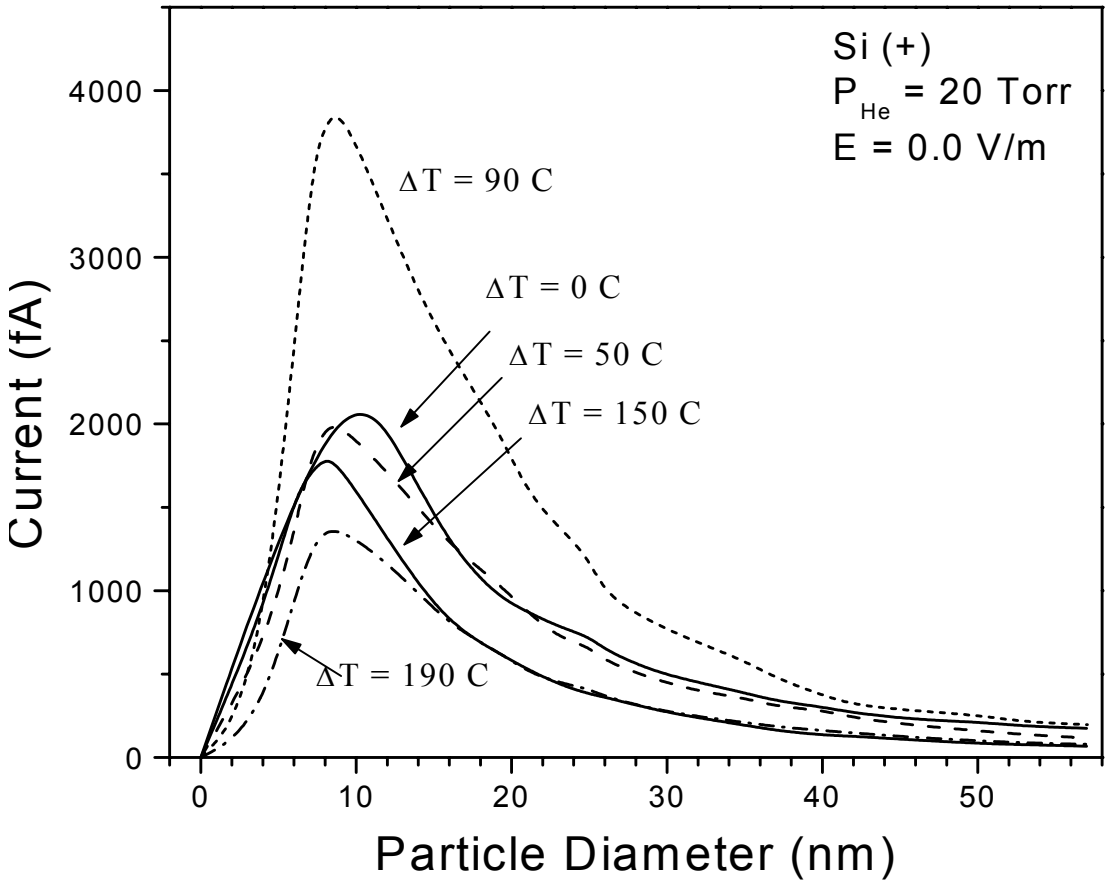

Figure 49. Size distribution of Si (+) nanoparticles at the outlet of LVCC chamber measured by DMA with varying temperature gradient.

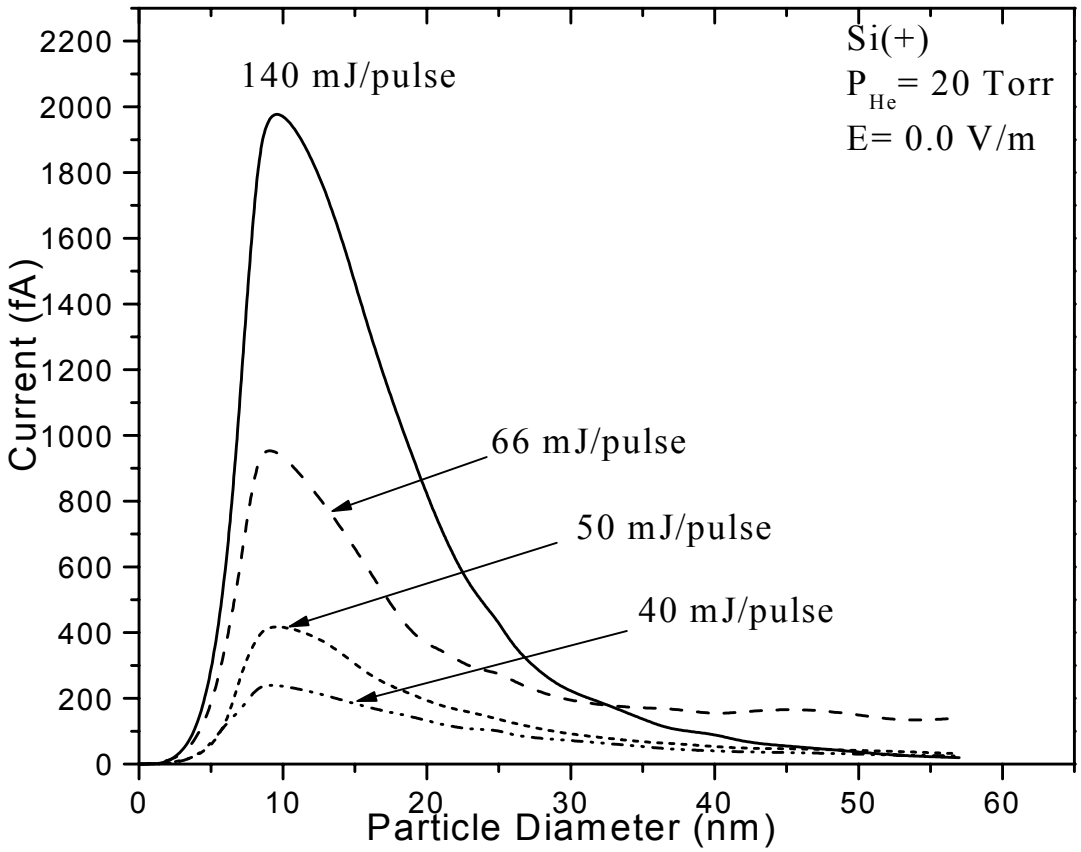

Figure 50. Size distribution of Si (+) nanoparticles at the outlet of LVCC chamber measured by DMA with varying laser power.

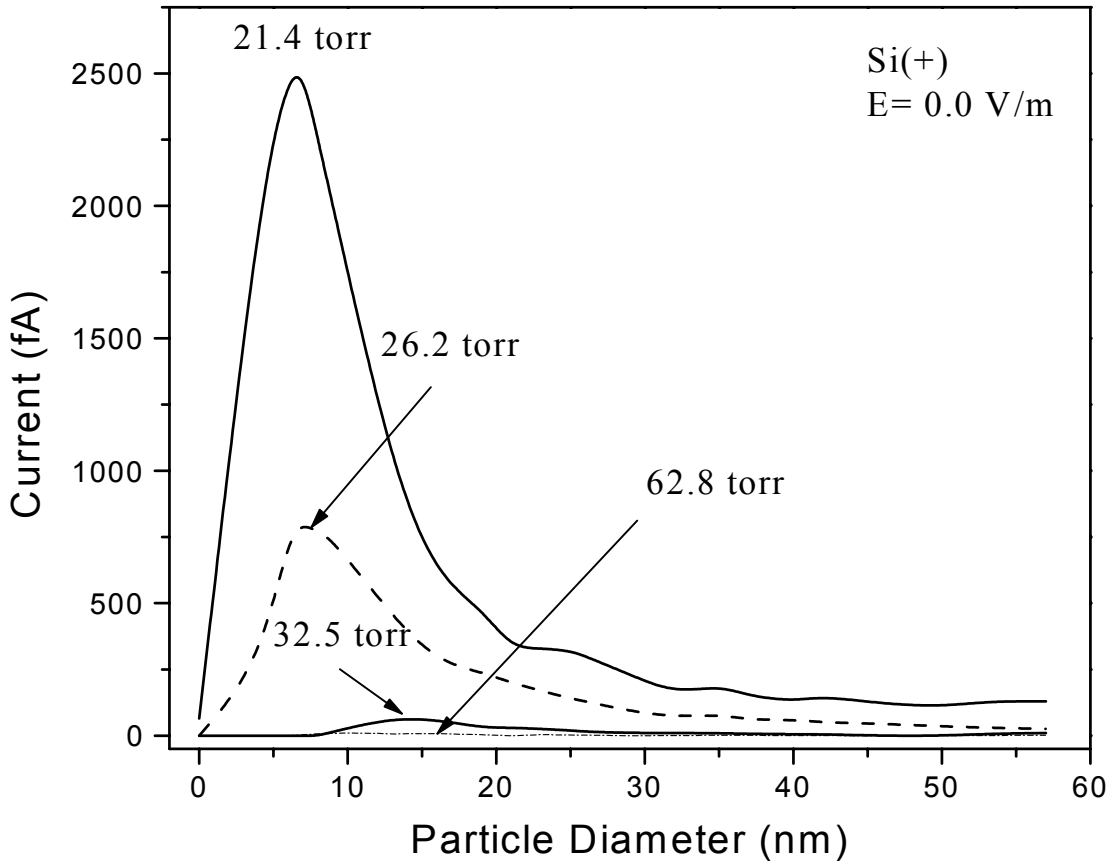

Figure 51. Size distribution of Si (+) nanoparticles at the outlet of LVCC chamber measured by DMA with varying the pressure inside LVCC chamber.

3-6 Optical Properties of Au-Ag Alloy Nanoparticles

3-6-1 Introduction

It is now well established that nano materials (1-100 nm) exhibit unique chemical and physical properties that differ from those of the bulk materials. The applications of these nanomaterials are thus expected to be very important in many fields of advanced technology and science including catalysis, chemical and biological sensors, optoelectronics, drug delivery, media storage, and the photographic industry. For instance, nanoparticles of silver and gold exhibit yellow and red-wine color, respectively, which is different from their bulk color. These nanoparticle colors are attributed to the surface plasmon absorption in the UV-visible region. This phenomenon was first explained by Mie in 1908, who applied a classical electrodynamic model to spherical particles and solved Maxwell's equations with the right boundary conditions. It is known that Ag and Au nanoparticles have plasmon peaks at approximately 400 and 520 nm, respectively. The origin of this surface plasmon band is the collective oscillations of free conduction electrons in metal excited by light at a particular wavelength. The oscillation frequency is determined by four factors;[92] the metal electron density, the effective electron mass, and the shape and size of the charge distribution. As the particle size gets smaller than the mean free path of the free electrons, the plasmon band broadens until it disappears. For example, gold particles less than 1 nm had no plasmon absorption band. To control the surface plasmon band, one needs to control particle size and composition. In recent years, a large number of preparation methods have been proposed for the design

of bimetallic nanocomposites (*i.e.*, alloy and/or core-shell structure) of gold-silver owing to their different catalytic properties, surface plasma band energy and surface-enhanced Raman activity compared to that of monometallic silver or gold nanoparticles.

Gold-silver alloy nanoparticles had been prepared chemically by co-reduction of silver and gold salts via a one-phase method. For example, El-Sayed and co-workers have prepared Ag-Au nanoparticles in water by using sodium citrate as a reducing agent.[93] Lee and co-workers prepared it in chloroform by sodium borohydride ($NaBH_4$).[94] Mono dispersed alloy nanoparticles have been also prepared by a two-phase method. For example, He and co-workers[95] prepared alloy nanoparticles passivated with octanthiol in chloroform/water biphasic solution with particle size of 5nm. Similar work by Kim and co-workers[96] has been reported. They were able to prepare Ag-Au alloy clusters (4nm) in a water/toluene two-phase system by $NaBH_4$, using dodecanethiol as a stabilizer. Water-in-oil microemulsion method had been reported by Chen et al., where hydrazine was used to co-reduce Au and Ag salts.[97] Aside from chemical reduction methods, Papavassliou[98] prepared colloidal Au-Ag alloy nanoparticles. He applied a high ac voltage between bulk Ag-Au alloy and Pt electrodes immersed in 2-butanol. Evaporation and condensation of alloy nanoparticles happened when an electric discharge between the two electrodes took place. More recently, laser ablation methods have been developed to prepare bimetallic and monometallic nanoparticles in solution. In the case of pure gold, Kimura et al. had prepared Au colloid in 2-propanol by the gas-flow solution-trap method.[99] He studied the coagulation of Au nanoparticles induced by applying a continuous (CW) Ar ion laser irradiation. Kondow et al. prepared Au nanoparticles by using the pulsed laser ablation

(λ = 1064 nm) of a gold plate in aqueous solution of surfactant sodium dodecylsulfate (SDS).[100] He studied the laser-induced melting of Au colloidal solution of surfactant by 532 nm, where they were able to reduce the particle size to ~2nm. Others, like Koda and co-workers, prepared Au nanoparticles by chemical reduction in water and then irradiating the solution by the second harmonic of a pulsed Nd:YAG laser (532 nm).[101] They studied the shape changes followed by the size reduction for Au nanoparticles, which depended on the laser power used. They explained these conformational changes to the laser induced melting process by adopting the fact that, gold has a plasmon absorption band around (520 nm) in vicinity to the wavelength of the irradiating light (532 nm).

For Ag nanoparticles, Kondow et al. prepared Ag nanoparticles by laser ablation (λ = 532 nm) of a silver plate in aqueous solution of sodium dodecylsulfate (SDS).[102] They found that by increasing the concentration of SDS in water, under constant laser power, they were able to reduce the particle size. They attributed this to the fact that, at a sufficiently high concentration of SDS molecules, small Ag fragments are stabilized, and hence, coagulation is decelerated. Koda et al. have investigated the effect of the third harmonic light of a pulsed Nd:YAG laser (355 nm) on the irradiation of chemically-reduced Ag nanoparticles in aqueous solution.[103] The reduction of Ag particle size, after laser irradiation, was explained by desorption of Ag atoms from the surface due to light absorption followed by plasmon excitation of Ag particles.

In the case of alloy nanoparticles prepared using light, Hartland and co-workers[104] studied the laser-induced interdiffusion of core-shell structure to alloy nanoparticles in

aqueous solution. Simard et al.[105] prepared Ag-Au alloy nanoparticles by irradiating a metal powder mixture in an aqueous medium with the second harmonic of a pulsed Nd:YAG laser (532 nm). Yeh et al.[106] have also prepared alloy nanoparticles by irradiating a colloidal mixture of pure Au and Ag by laser irradiation (λ = 532 nm).

Most of the previous methods used to prepare bimetallic alloy between gold and silver were carried out in a liquid media. In this work, gold-silver alloy nanoparticles, for the first time, in the vapor phase under Ar atmosphere using Laser-Vaporization Controlled-Condensation method (LVCC) were prepared. One of the advantages in vapor-phase preparation is the contamination-free product compared to chemical reduction in a solution. The interaction between as-prepared alloy nanoparticles with a coherent laser beam of different wavelengths, namely, the fundamental (λ = 1064 nm) and the second harmonic (λ = 532 nm) of a pulsed nanosecond laser will be addressed here.

3-6-2 Experimental

Gold-silver alloy nanoparticles were produced from micron-size powder mixtures of gold and silver by laser vaporization in the vapor phase. Three different compositions, made of gold powder (Aldrich, 99.99+%, < 841 μm) mixed with silver powder (Aldrich, 99.999%, < 590 μm) then pressed (hydraulic IR Die at 500 MPa) into a pellet to form a bimetal target. The first target is 2:1 by wt% silver ($Ag_{0.79}Au_{0.21}$), the second target is 1:1 by wt% silver ($Ag_{0.64}Au_{0.36}$), and the third target is 1:2 by wt% silver ($Ag_{0.48}Au_{0.52}$). The stoichiometric coefficients shown for each composition represent the atomic ratio between gold and silver in the target. The Laser Vaporization Controlled Condensation (LVCC) method was used to prepare gold-silver alloy nanoparticles in the gas phase using Ar as a carrier gas (99.99% pure). In this method laser vaporization of metals was coupled with controlled condensation from the vapor phase. The target was placed in a modified diffusion cloud chamber (DCC). The chamber was made from two circular stainless steel plates separated by a glass ring. The setup of LVCC method is shown in Figure 11. The pressure in the chamber was adjusted to 1000 Torr of Ar gas. The temperature difference between the chamber plates (60-70 °C), along with the high pressure inside the chamber, creates a steady state convection inside the chamber. The target of a certain composition, which was placed on the bottom plate, is vaporized by a second harmonic beam (532 nm, 250 mJ/pulse) of a pulsed Nd:YAG laser (Quanta-Ray, Spectra-Physics) operated at 30 Hz and 2 ns pulse width. The laser beam was focused on the target by a lens of focal length 50 cm. The beam cross-section area was measured on the target to be (0.031 cm^2), with a power density of 8.5 x 10^9 W/cm^2. When the laser

pulse vaporized the target, a shock wave was initiated due to the collisions between the gas and the target atoms and a plume was emitted.[48] Evaporated atoms colloid with the gas atoms at the front of the expanding plume. As a result, the plume atoms were rapidly thermalized within 10-100 microseconds after the laser pulse.[49] The speed of thermalization is related to the efficiency of the energy transferred during gas-target atom collision, which depends on their atomic masses. The cooling plume, confined behind the shock wave, became supersaturated, leading to nanoparticle formation via homogeneous nucleation. The degree of thermalization required for condensation is also related to the vapor pressure of the target material. The temperature of the top plate was maintained at room temperature (25 ^{o}C) while the bottom plate was maintained at (90 ^{o}C). The steady state convection inside the chamber carried the particles from the plume (highly supersaturated with target vapor) before they grow more. The particles were deposited on the top plate of the chamber. After every run the chamber was brought to room temperature and the sample was collected from the top plate.

Scanning electron microscopy (SEM), Energy dispersive X-ray spectroscopy (EDX) and Scanning transmission electron microscopy (STEM) was done on a Quantum DS-130S Dual Stage Electron Microscope. A carbon substrate was placed inside the chamber (on the top plate) to observe the morphology and size of as-deposited nanoparticles under SEM. Electron diffraction (ED) and Transmission electron microscope (TEM) images were obtained using the JOEL JEM-FXII TEM operated at 200kV. High-resolution TEM (HRTEM) images were obtained using JOEL 4000EX operated at 400 kV. Namely, a drop of aqueous dispersed nanoparticles was placed on a

copper grid, which is coated by a carbon film, and then dried in a desiccator. The chemical composition and the phase measurements of the nanoparticles prepared was analyzed using X-ray powder diffraction (XRD) on an X'Pert Philips Materials Research Diffractometer, which uses Cu $K_{\alpha 1}$ radiation. The elemental analyses were done on Inductively Coupled Plasma-Optical Emission Spectrometer (ICP-OES) to measure the amount of gold in the nanoparticles. The ICP measurements were done on Varian VISTA-MPX instruments. The UV-Vis absorption was done on a Hewlett-Packard HP 8453 diode array spectrometer with a quartz cell of 1 x 1 x 4 cm^3. The laser power was measured using (OPHIR optronics LTD., NOVA laser power monitor).

To measure the optical properties of the prepared nanoparticles as well as to reirradiate them, colloidal solutions were prepared by dispersing the Ag-Au nanoparticles in a triply deionized water (18 MΩ) using air ultra sound waves. Typically, 3-6 hours were needed to disperse 5 mg in 20 ml deionized water in a sonicator. Three different concentrations were prepared 26, 52 and 133 mg/L. In a typical laser-irradiation experiment, a 10 ml colloidal solution was held in a 20 ml Pyrex beaker and irradiated under agitation using a magnetic stirrer. The particles were irradiated by either the fundamental of a Nd:YAG pulsed laser (1064 nm, (6.0-7.56) x 10^7 W/cm^2, 10Hz) or the second harmonic of a Nd:YAG pulsed laser (532 nm, (4.25-5.36) x 10^7 W/cm^2, 10Hz). For TEM and STEM, one drop of the colloidal solution was placed on a 200 mesh Cu grid coated with carbon. The grid was left in a desiccator until it dried out.

In order to determine how the composition of the prepared nanoparticles varies compared to the starting composition of the target, the ICP was used to measure the

content of gold in the nanoparticles. Shown in Figure 52 is the relationship between the composition of the Ag-Au nanoparticles prepared by LVCC method and that of the bulk target. It is clear that the molar ratio of gold in the nanoparticle compositions is different from those in the metal powder mixtures. For the metal powder mixtures containing 51.8, 35.6 and 21.2 mol % Au, there are 47.3, 28.7 and 16.6 mol % Au, respectively, in the nanoparticles as shown in Table 6. This can be explained by considering that the generation speed for pure Ag is higher than that of pure Au since the boiling temperature of Au is higher than that of Ag. In fact, the Ag content in Ag-Au nanoparticles is about 1.06-1.20 times those in bulk metal powder mixtures. These results are similar to what Liu and co-workers[57,62] have observed while preparing Fe-Al nanoparticles by hydrogen plasma-metal reaction from a bulk alloy. They found that the content of Al in nanoparticles is higher than that in the bulk alloy. They explained this result in terms of a difference in evaporation speeds of pure metals. For convenience, here after the alloy nanoparticles are referred as $Ag_{0.83}Au_{0.17}$, $Au_{0.71}Ag_{0.29}$ and $Au_{0.53}Ag_{0.47}$ and for pure metal nanoparticles as Ag and Au. The stoichiometric coefficient represents here the actual content of Ag and Au in the nanoparticles as determined from the ICP technique.

3-6-3 Results and Discussion

Alloying in the gas phase.

Pure gold and silver nanoparticles were prepared, under Ar gas, using the LVCC method. Typical SEM micrographs of the as-deposited gold and silver nanoparticles are shown in Figure 53-a and Figure 54-a, respectively. The particles in both cases are aggregated, with more aggregation in the case of gold particles, where the average particle size is smaller compared to the silver particles. The optical properties of pure gold and silver nanoparticles were measured after they were dispersed in 10 ml of ultra pure water (18 MΩ). Shown in Figure 55 are the typical STEM micrographs for gold and silver nanoparticles after they were dispersed in water. The STEM shows that even after particles were dispersed in water, a broad particle size distribution and aggregation were observed for both metal nanoparticles, which is similar to as-deposited particles from the gas phase. The UV-visible absorption spectra of dispersed gold and silver particles in water are shown in Figure 53-b and Figure 54-b, respectively. A single plasmon absorption band at 540 and 406 nm was observed for gold and silver nanoparticles, respectively. As discussed earlier, the position and the shape of the plasmon peaks are strongly dependent on particle size and aggregation, dielectric medium, surface adsorbed species, and chemical composition. The positions of these plasmon peaks are in relatively good agreement with what Kondow et al. had observed.[100,102,107-110] The plasmon band of silver lied on a tail of a broad band extending to the UV region, which originated from the interband transition in the silver particles (250 nm). The broadening in the absorption plasmon bands originated mainly from two

factors. The broad particle size distribution in all the nanoparticles prepared by the LVCC method, in addition to the aggregation effects. Since small particles have a high tendency to aggregate faster than big particles due to their high surface energy. As seen from the SEM and the STEM micrographs, the average particle sizes for gold is smaller than that of silver particles. These results can be attributed to the wavelength used (532 nm) in the vaporization of the metal targets. At this wavelength the absorpitivity of gold is much higher than that of silver owing to its plasmon absorption at (520 nm). When the surface plasmon band of gold was exited by laser-light photons at 532 nm, the photon energy was readily converted into heat because of efficient transmission of the absorbed energy to the internal energy of the gold target, due to the strong electron-phonon interaction. For example, during a single laser pulse, one gold particle in nanoscale dimension was considered to absorb consecutively more than 1000 photons and was heated to its boiling point.[101]

In Figure 56a the absorption spectra of $Ag_{0.83}Au_{0.17}$, $Au_{0.71}Ag_{0.29}$ and $Au_{0.53}Ag_{0.47}$ nanoparticles, prepared under identical conditions, are shown, labeled as (b), (c) and (d), respectively. Distinct peaks are observed, clearly at 431, 465 and 487 nm, respectively. These plasmon peaks are located at an intermediate position between the gold and the silver surface plasmon bands. The single plasmon band implies that the particles are spherical rather than rods[111] or triangles[112,113], which would have two or three plasmon peaks, respectively. It also implies the formation of an alloy between silver and gold particles rather than of a mixture, which would simply have a combination of their spectra (two distinct plasmon bands corresponding to each metal). In order to prove

the alloy formation in the gas phase, the optical absorption of the physical mixture of gold and silver nanoparticles was compared to that of the corresponding alloy. In Figure 57, the UV-visible spectra of the alloy and the mixture having the same molar ratio of Au (71) / Ag (29) is shown. The mixture had two distinct peaks at 421 and 524 nm corresponding to the absorption plasmon of the silver and the gold nanoparticles, respectively, while the alloy nanocomposite shows only a single plasmon peak at 465 nm. The plasmon peak depends on the composition of the alloy prepared. It shifts linearly to higher energy with increased silver content in the nanocomposite alloy, as shown in Figure 56b.

The linear relationship between silver content in gold-silver alloy and its surface plasmon energy has been extensively observed for many alloys prepared by different chemical reduction routes in liquids; for example, in monophasic systems,[93,114] in biphasic systems,[95,96] and in microemulsion systems,[97] also by radiation chemistry[115] and by laser ablation in solution.[105,116] The morphology of deposited Ag-Au nanocomposite alloy, observed by SEM, is shown in Figure 58a. These particles were deposited on carbon substrates placed inside the preparation chamber. The average particle size decreased with increasing gold content in alloy nanoparticles. Similar results have been observed by Koda et al. on pure gold particles.[101] They showed that gold particles under laser irradiation (532 nm) exhibited changes in their shape followed by size reduction. The EDX analysis spectrum of the alloy nanoparticles corresponding to SEM micrographs are shown in Figure 58b, where the relative intensity of Au (Mα) to

Ag (Lα) lines changes as the molar ratio changes, in good agreement with the ICP results.

Gold and silver metals have a face-centered cubic (FCC) crystal structure with a similar lattice constant of 0.408 and 0.409 nm, respectively.[117,118] Due to this fact, they are thermodynamically favorable to mix and form a miscible homogenous solid solution with a FCC crystal structure.[119] The X-ray diffraction patterns of Ag, Au and Au-Ag nanoparticles are shown in Figure 59. It is clear that the characteristic planes (111), (200), (220), (311) and (222) of FCC crystal lattice is retained in all nanoparticles, similarly to bulk crystal structure. However, the relative diffraction intensity was different. For example, the (200) plane intensity at scattering angle ($2\theta = 44.1$ deg.) increased relative to (111) plane, with increasing gold molar fraction in the alloy nanocomposites. This ratio ranges from 0.377 for pure silver nanoparticles to 0.543 for pure gold nanoparticles. Moreover, broader diffraction peaks were observed compared to bulk, owing to their small particle size.

High resolution transmission electron microscopy (HRTEM) micrographs are shown in Figure 60 for dispersed $Ag_{0.71}Au_{0.29}$ in water as prepared by the LVCC method. Seen in the micrographs in Figure 60 are examples of different structures' defects; the particles appeared to be faceted rather than being spheres. This can be explained by different growth rates of silver on various planes of gold particles and vice versa. Stacking faults, as well as single and multiple twins, were also observed. These kinds of defects are very common in metallic alloys. In addition to the above defects, the particles were observed to be "wired" together.

Effect of laser irradiation on alloy nanocomposites in water medium under different wavelengths.

The water-dispersed gold and silver nanoparticles were irradiated with the fundamental (1064 nm) as well as the second harmonic generation (532 nm) of a pulsed Nd:YAG laser at (4.25-7.56) x 10^7 W/cm^2 for 20 min each. In Figure 61 the UV-visible absorption spectra, as well as the corresponding STEM micrograph, are shown for gold nanoparticles as prepared after 532 nm irradiation and after 1064 nm irradiation, respectively. Based on these figures, using the 532 nm light-source, particle sizes decreased, forming almost mono dispersed particles, compared to the non-irradiated particles, where a broad size distribution and nonspherical particles were observed. The corresponding absorption spectra shown in Figure 61 confirms that the plasmon peak was shifted from 540 to 520 nm. According to the Mie theory, this result indicates that the Au particle size was reduced. Also the absorption at wavelengths higher than 600 nm gets smaller after irradiation, which may indicate a decrease in the agglomeration of particles after being irradiated. Similar results have been observed by Koda et al.[101,120], where a chemically-prepared gold colloid was irradiated by the second harmonic generation (532 nm) of a pulsed Nd:YAG laser, which resulted in a size reduction. On the other hand, when 1064 nm laser beam was used, the average particle size decreased, but not as much as with the 532 nm as seen from the STEM. The optical absorption also has been changed, where the plasmon band is slightly blue shifted from 540 to 528 nm. These results indicate, as mentioned above, that using 532 nm radiation results in particle size

reduction due to light absorption by gold followed by melting and vaporization, whereas in case of 1064 nm radiation only vaporization takes place. The previous results were confirmed when silver nanoparticles were irradiated with both wavelengths having the same output laser power. The STEM of silver nanoparticles before and after irradiation with 532 nm and 1064 nm are shown in Figure 62. By comparing the three micrographs, it is clear that the size was reduced upon either irradiation with (532 nm or 1064 nm). The size reduction after 532 nm irradiation is similar to that after 1064 nm irradiation, indicating that the interaction between Ag and light (532 nm and 1064 nm) may be similar. These results were also confirmed from the absorption spectra, where the silver plasmon peak shifted from 408 to 395 and 396 nm after 532 and 1064 nm irradiation, respectively. Also the particle agglomeration decreased after irradiation as indicated by the decrease in absorption at longer wavelengths (> 500 nm). However, in the case of a 1064 nm irradiation there was more agglomeration compared to irradiation at 532 nm. This was observed as a broad peak absorption. The effect of irradiation wavelengths on water-dispersed nanoalloy particles was also examined under TEM. In Figure 63, the TEM micrographs for $Ag_{0.71}Au_{0.29}$ nanoparticles are shown with and without irradiation in water medium. The particles, as prepared from the LVCC in the vapor phase (Ar), were nonspherical with facets and broad size distribution. After being irradiated with 532 nm for 20 min (12,000 laser pulses) in water, size reduction was observed from the TEM results, where melting, reshaping, and vaporization took place to yield almost monodispersed spherical particles. However, at the 1064 nm radiation only small size reduction happened in addition to reshaping to spherical particles. It was also observed

that a broad size distribution still remained, even after 1064 nm irradiation. In Figure 64 the HRTEM for $Ag_{0.71}Au_{0.29}$ nanoparticles are shown with and without irradiation, which confirms the optical absorption data.

A comparison between the absorption spectra for $Ag_{0.83}Au_{0.17}$, $Au_{0.71}Ag_{0.29}$ and $Au_{0.53}Ag_{0.47}$ nanoparticles irradiated with 532 nm and 1064 nm is given in Figure 65. The surface plasmon bands for $Ag_{0.83}Au_{0.17}$, $Au_{0.71}Ag_{0.29}$ and $Au_{0.53}Ag_{0.47}$ nanoparticles were blue shifted from 431, 465 and 487 nm to 410, 440 and 460 nm, respectively after 20 min irradiation with 532 nm. On the other hand, the plasmon bands were shifted to 419, 427 and 441 nm, respectively after 20 min irradiation with 1064 nm. The positions of the plasmon peaks under different compositions and different irradiation conditions are given in Table 7. The broadening in the UV-visible absorption spectra for Ag-Au particles decreased after irradiation, indicating again the decrease in agglomeration and the colloidal formation. The blue shift was also observed after irradiation with either 532 or 1064 nm indicating particle size reduction for all the compositions studied.

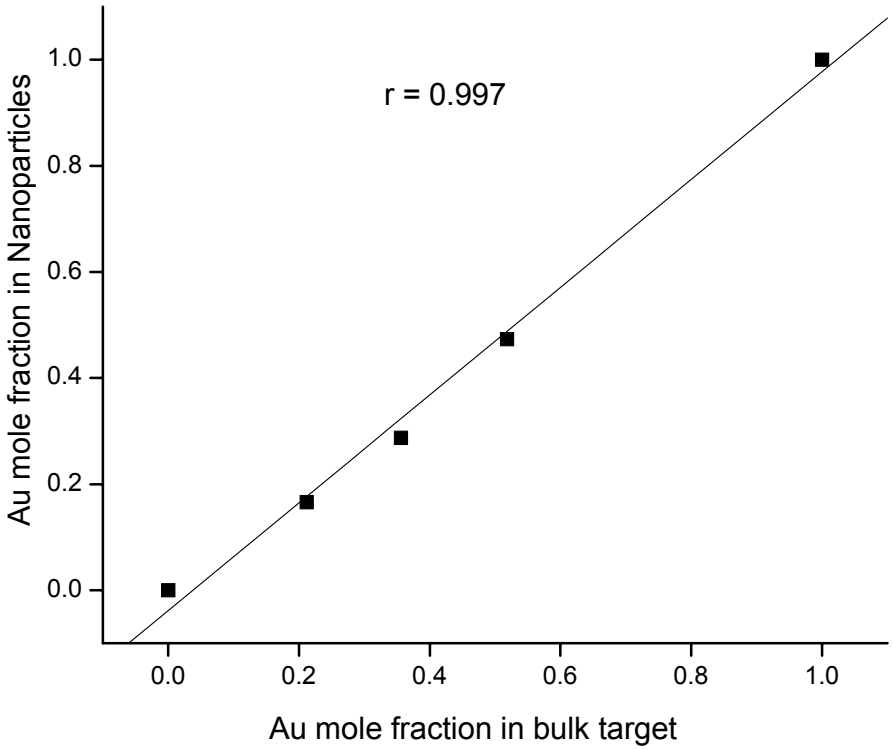

Figure 52. Comparison between Au mole fraction in the bulk target and in the prepared nanoparticles using the LVCC method.

Table 6. Comparison between Au content in the bulk powder mixtures and in the nanoparticles using the Inductive Coupled Plasma Spectroscopy (ICPS).

Composition	Bulk Au mole fraction	Nanoparticles Au mole fraction	Difference between bulk and Nano
$Ag_{0.83}Au_{0.17}$	21.2	16.6	3.61 %
$Ag_{0.71}Au_{0.29}$	35.6	28.7	4.15 %
$Ag_{0.53}Au_{0.47}$	51.8	47.3	10.51 %

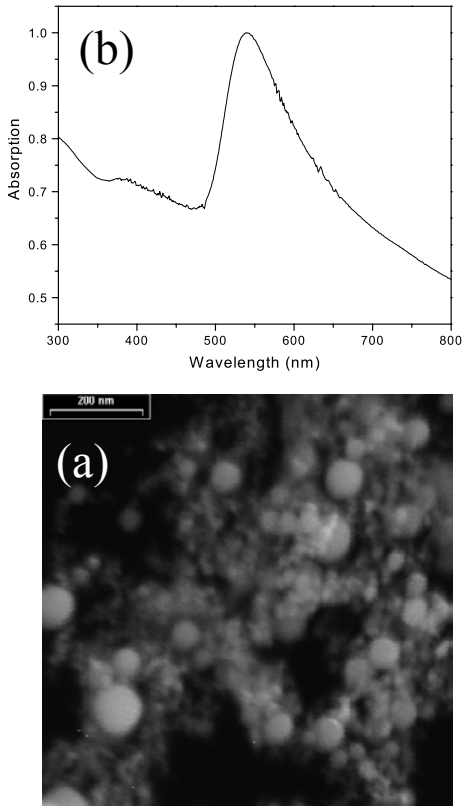

Figure 53. SEM of as-deposited Au nanoparticles prepared by the LVCC method in Ar atmosphere, the scale bar is 200 nm (a), and the UV-visible absorption spectrum of Au nanoparticles dispersed in water (b).

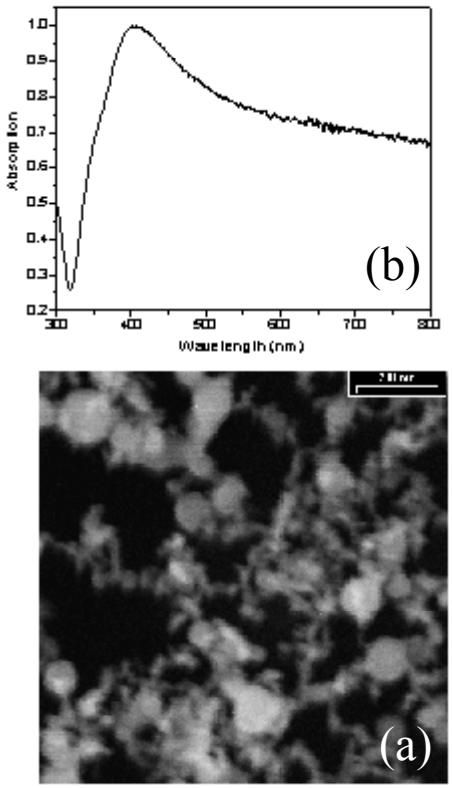

Figure 54. SEM of as-deposited Ag nanoparticles prepared by the LVCC method in Ar atmosphere, the scale bar is 200 nm (a), and the UV-visible absorption spectrum of Au nanoparticles dispersed in water (b).

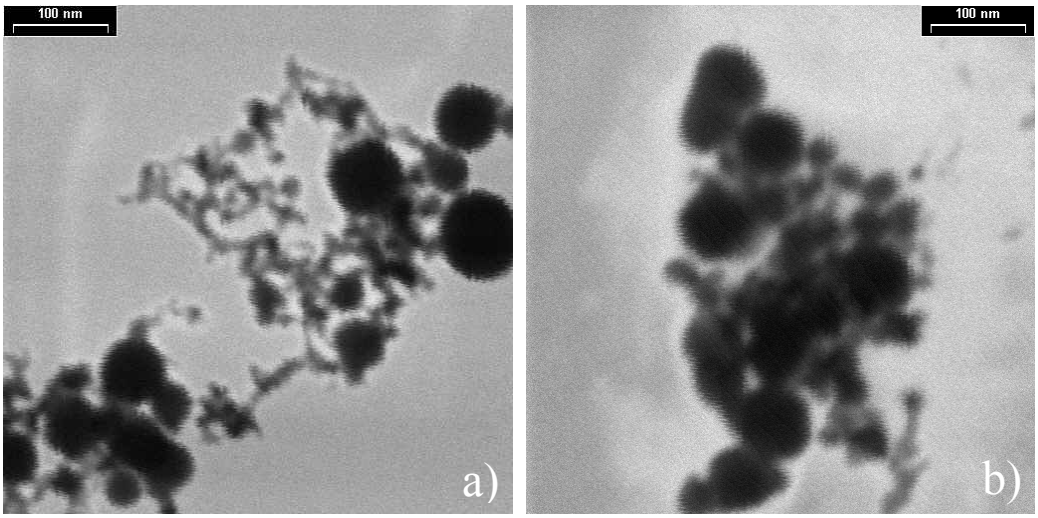

Figure 55. STEM for a) gold nanoparticles and b) silver nanoparticles dispersed in water after they were prepared in the gas phase by the LVCC method. The scale bar is 100 nm.

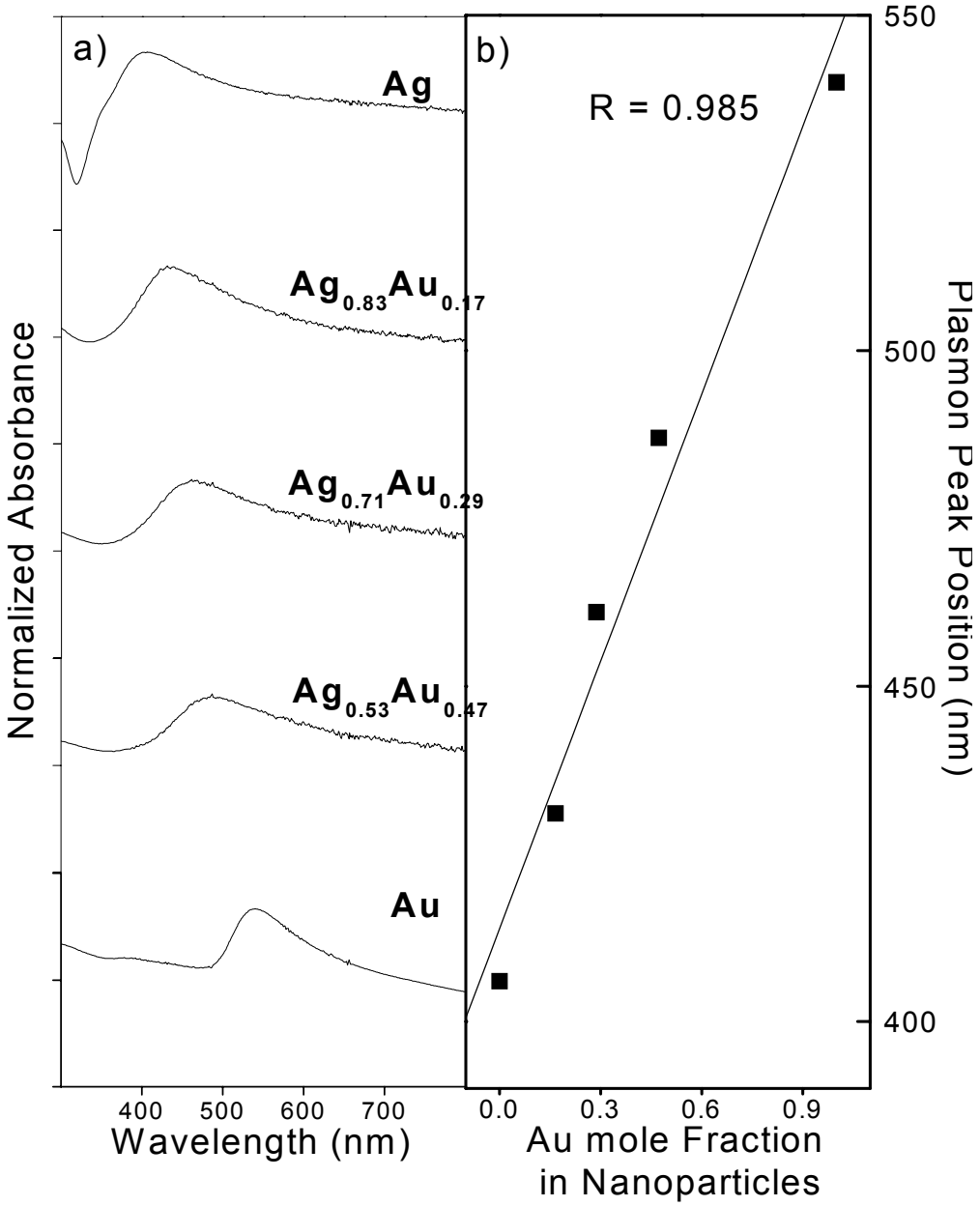

Figure 56. a) UV-visible absorption spectra of Ag-Au nanoparticles prepared by the LVCC method and b) Position of surface plasmon peaks plotted as a function of Au content in the alloy nanoparticles.

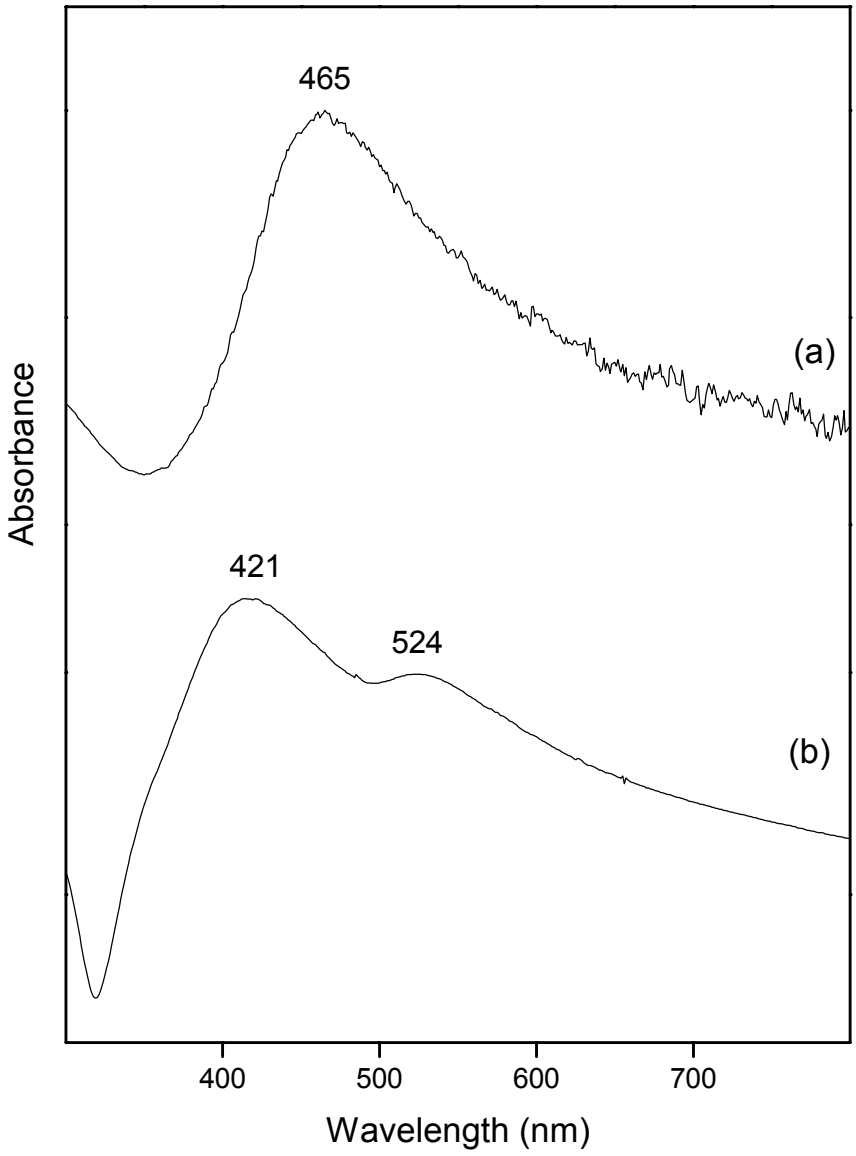

Figure 57. UV-visible absorption spectra of a) $Au_{0.29}Ag_{0.71}$ alloy nanoparticles, b) physical mixture of Au and Ag nanoparticles with the same molar ratio found in the alloy.

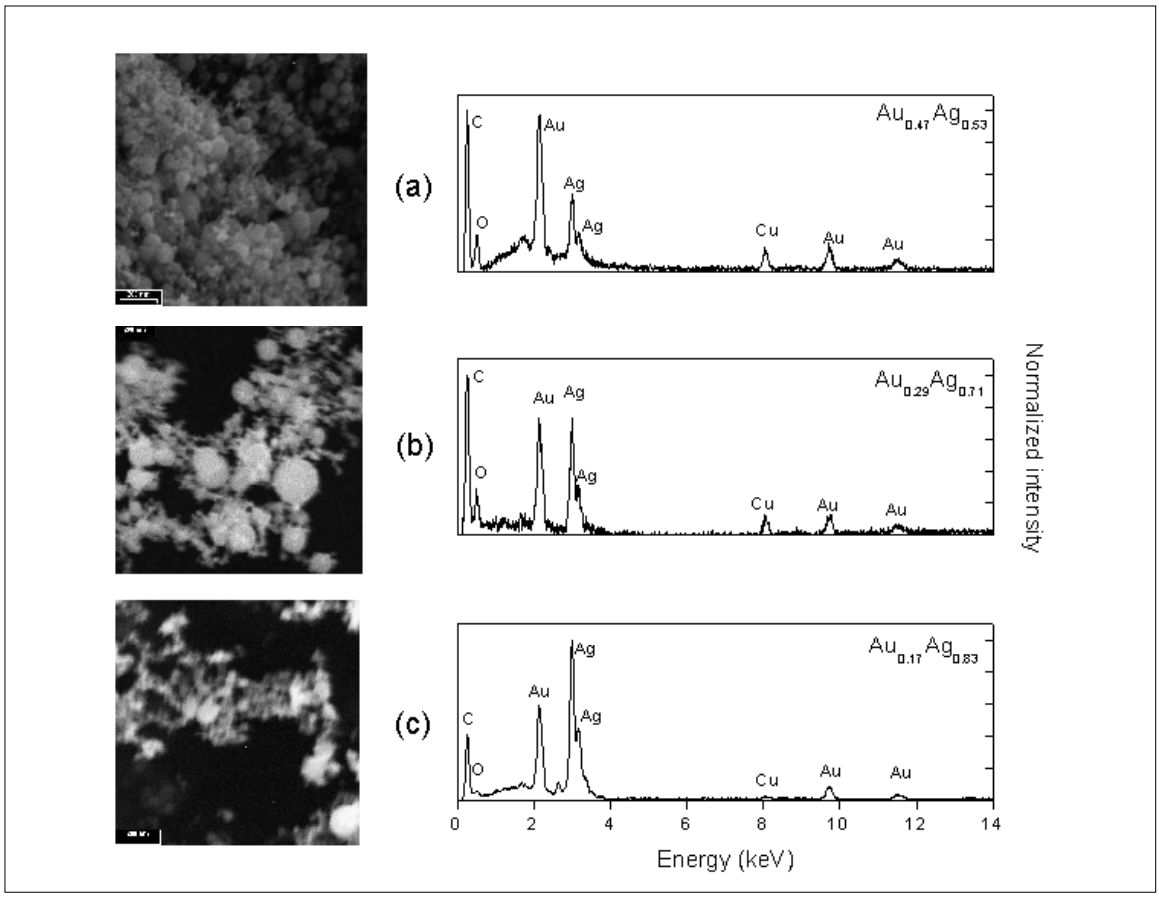

Figure 58. SEM images and EDX spectra for a) $Au_{0.47}Ag_{0.53}$, b) $Au_{0.29}Ag_{0.71}$ and c) $Au_{0.17}Ag_{0.83}$ nanoparticles. The scale bar is 200 nm.

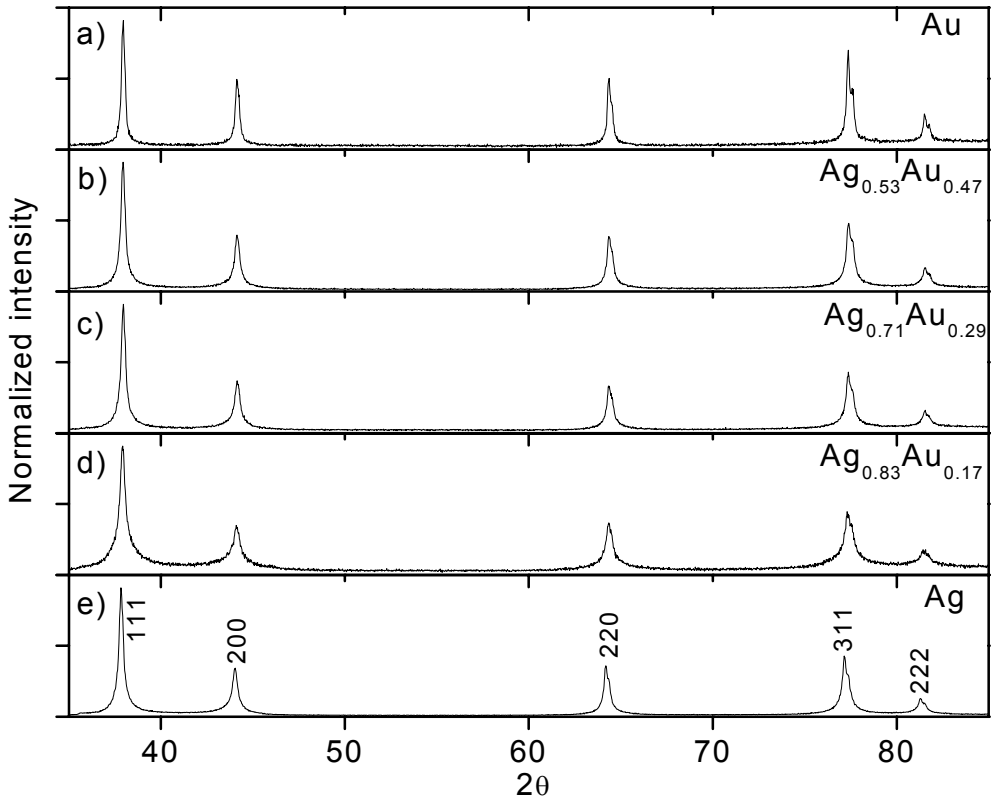

Figure 59. X-ray diffraction of Ag-Au nanoparticles prepared by the LVCC method in Ar atmosphere.

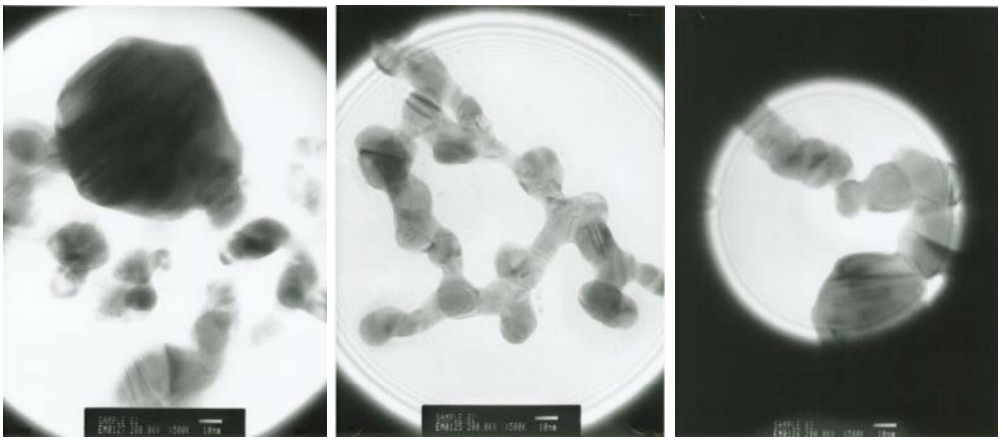

Figure 60. HRTEM for dispersed $Ag_{0.71}Au_{0.29}$ in water as prepared by the LVCC method, the scale bar is 10 nm.

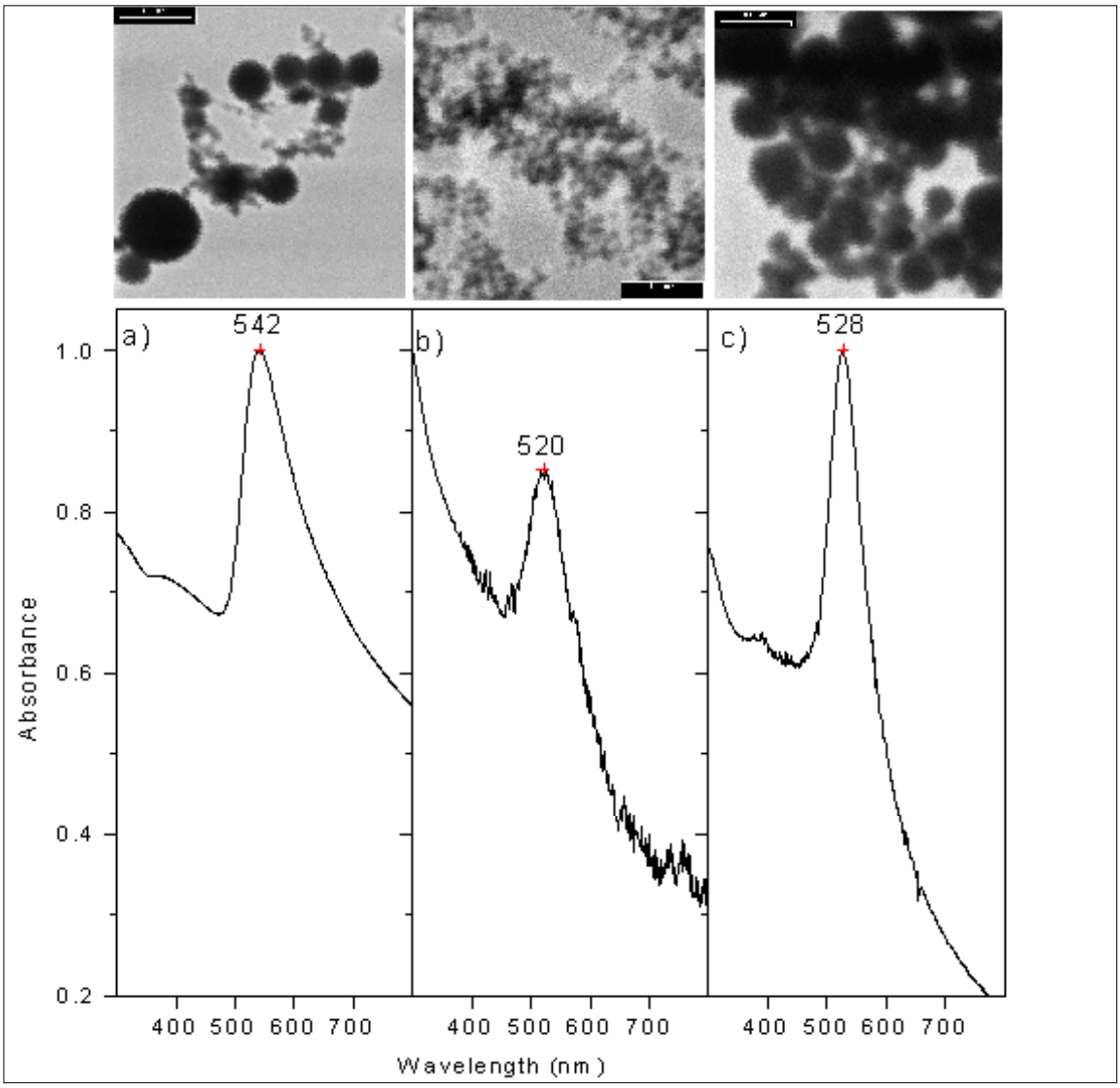

Figure 61. STEM and the corresponding UV-visible spectra for Au nanoparticles a) as prepared, b) after 20 min irradiation with 532 nm and c) after 20 min irradiation with 1064 nm, respectively. The scale bar is 100 nm.

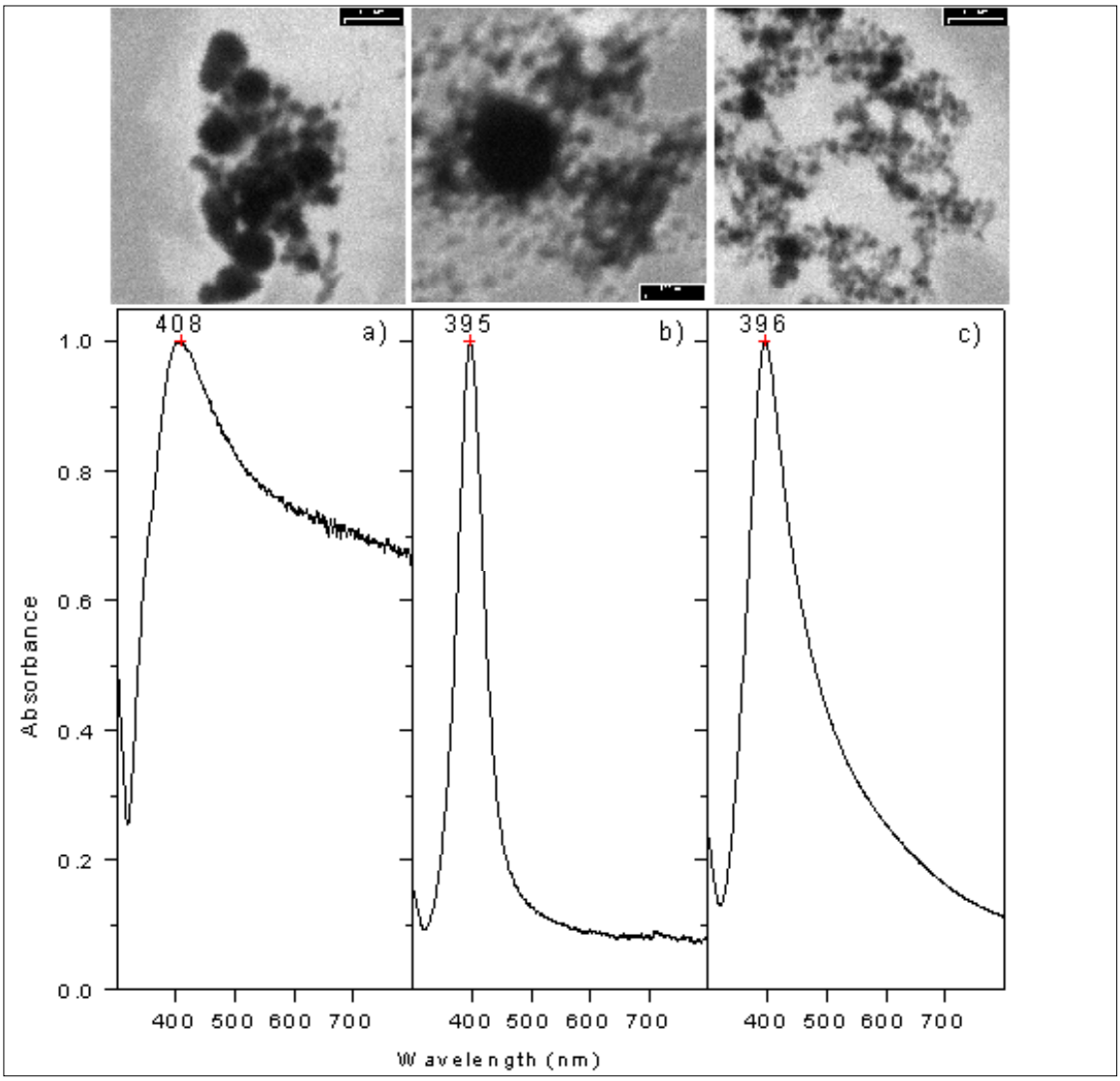

Figure 62. STEM and the corresponding UV-visible spectra for Ag nanoparticles a) as prepared, b) after 20 min irradiation with 532 nm and c) after 20 min irradiation with 1064 nm, respectively. The scale bar is 100 nm.

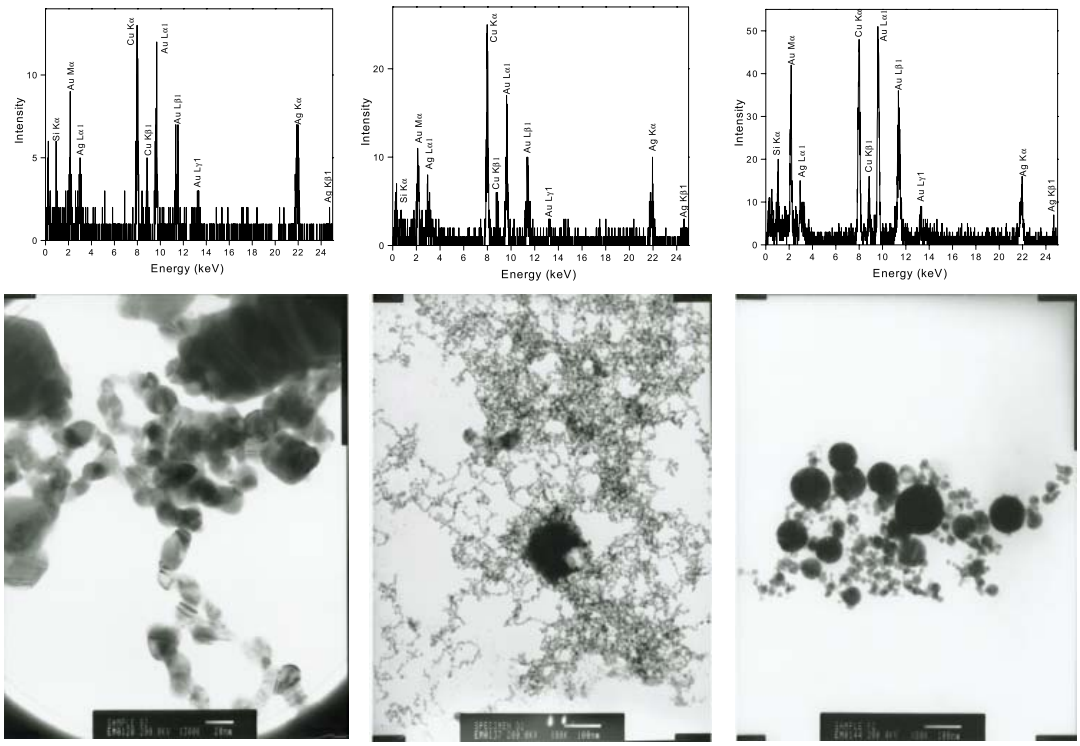

Figure 63. EDX spectra and TEM images for $Ag_{0.71}Au_{0.29}$ dispersed in water a) as prepared, b) after 20 min irradiation with 532 nm and c) after 20 min irradiation with 1064 nm, the scale bar 100 nm.

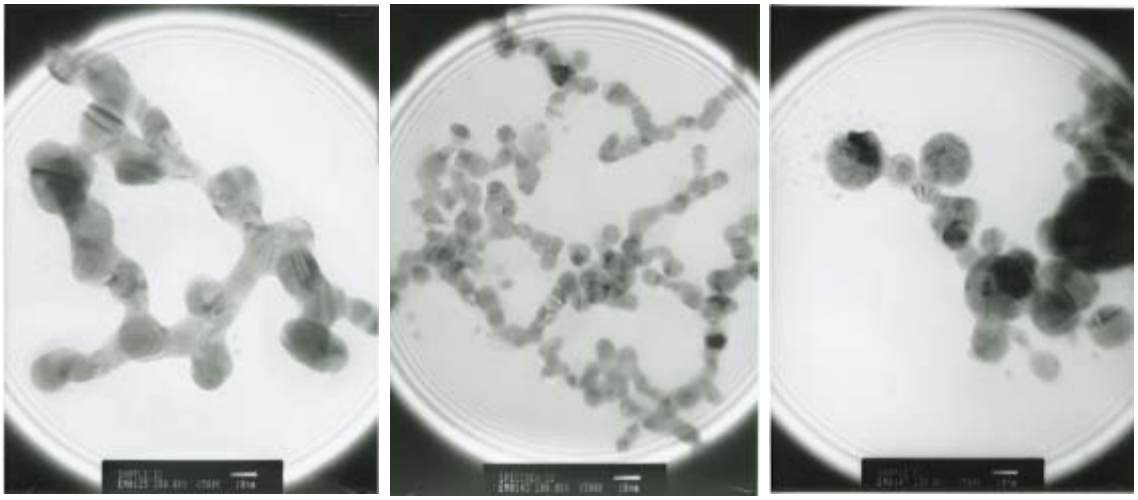

Figure 64. HRTEM images for $Ag_{0.71}Au_{0.29}$ dispersed in water a) as prepared, b) after 20 min irradiation with 532 nm and c) after 20 min irradiation with 1064 nm, the scale bar 10 nm.

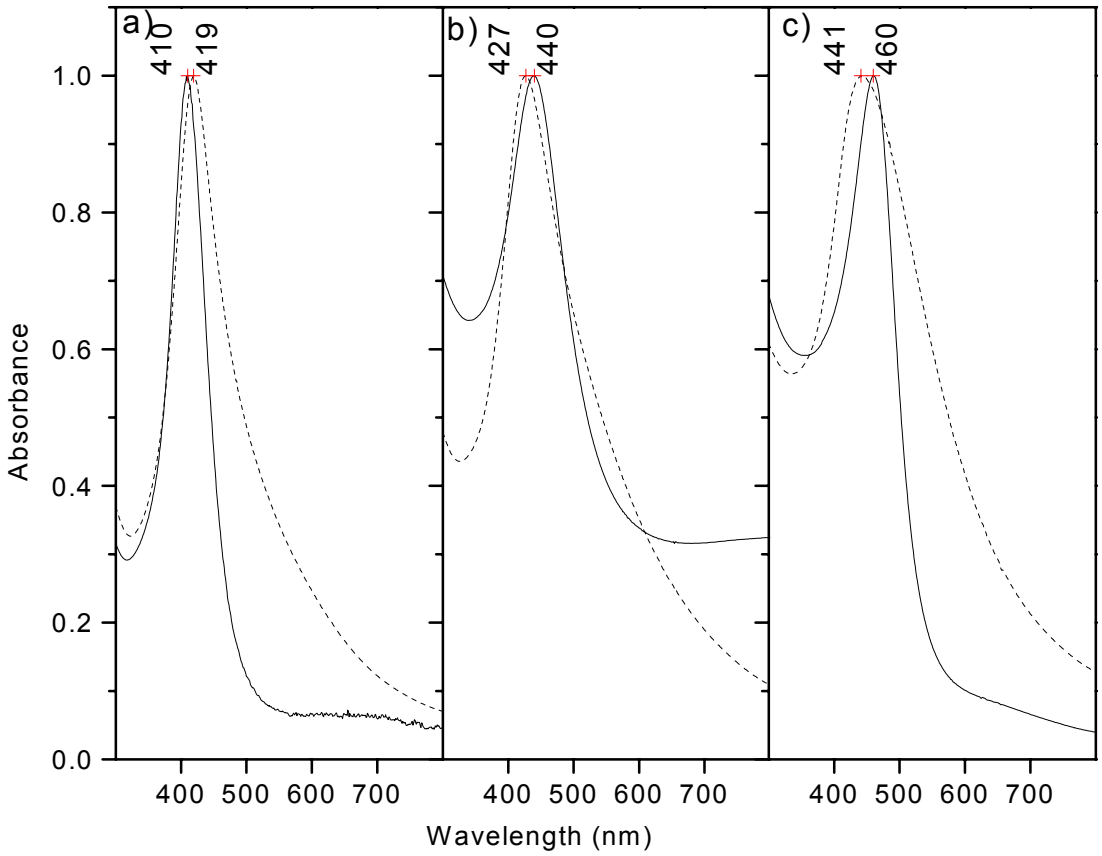

Figure 65. UV-visible spectra of a) $Au_{0.17}Ag_{0.83}$, b) $Au_{0.29}Ag_{0.71}$ and c) $Au_{0.47}Ag_{0.53}$ after irradiated with 532 nm (solid line) and 1064 nm (dotted line) for 20min, respectively.

Table 7. Surface plasmon absorption peaks for Ag-Au system under different irradiation conditions.

	As prepared	After 532 nm irradiation	After 1064 nm irradiation
Ag	406	395	396
$Ag_{0.83}Au_{0.17}$	431	410	419
$Au_{0.71}Ag_{0.29}$	465	440	427
$Au_{0.53}Ag_{0.47}$	487	460	441
Au	540	519	528

Chapter 4 Condensation of Supersaturated Vapors on Mg Nanoparticles

4-1 Introduction

Since the early work of Kohler[121] in 1936, who put forth the first theory of condensation on completely soluble particles, different models of condensation nucleation on aerosols (heterogeneous nucleation) have been proposed. Fletcher,[122] in 1958, investigated the heterogeneous nucleation on insoluble aerosol particles. The properties of both the working vapor as well as the preexisting nucleus play an important role in heterogeneous nucleation. For example, the condensation of supersaturated vapor on neutral particles was influenced by the surface properties, the size of the particles, and the contact angle between the newly formed cluster and the aerosol particle. The condensation onto charged particles is further influenced by the sign and the amount of the charge, as well as by the dipole moment of the condensed vapor molecules.

Here, in the heterogeneous nucleation, the critical clusters always have a lower surface free energy barrier compared to that of the homogeneous nucleation due to the presence of a preexisting surface (nucleus particle). Therefore, at and above a given supersaturation *S*, the preexisting nucleus particle, having a radius of *a*, could have enough condensable monomers adsorbed on the surface to form a stable critical cluster. However, below a given S, fewer monomers could also be deposited to form a cluster, but these monomers would evaporate eventually because of the decrease in the free

energy on association of these monomers was not sufficient to overcome the surface energy barrier to form a critical cluster.

For a given *S*, particles having size of *a* or larger are activated via heterogeneous nucleation and can then undergo growth by condensation of more monomers onto critical clusters. For particles having a radius smaller than *a* in size, these particles are not activated and monomers deposited on the surfaces eventually evaporate back to the vapor phase. Smorodin et al.[123] have found that the energy and rate of heterogeneous nucleation of polar liquids on heterophilic aerosol particles at a constant supersaturation, depend on the particle size. For larger particles, the rate is higher due to the role of increased numbers of the active sites on the surfaces.

It is well known that ultrafine particles (with diameter < 100 nm) play an important role in atmospheric processes such as cloud formation. Therefore, it is important to study the nucleation process on these particles. Unfortunately, only scant data are available for the condensation of supersaturated vapor onto neutral or charged particles with diameters in the range of tens of nanometers. Recently, new tools have been developed for the study of heterogeneous nucleation. For example, the condensation nuclei counter (CNC) has been developed to measure the number concentration of ultrafine particles, onto which a working fluid was allowed to condense. The particles were then grown to a size, where they could effectively scatter light and be detected. Recently, Mavliev et al.[124,125] have used the CNC to study the heterogeneous nucleation of different compounds on various nuclei's compositions (NaCl, KCl, AgCl and Ag particles). Additionally, they also reported the transition from heterogeneous to

homogeneous nucleation for dibutylphthalate on NaCl and WO_x particles. Lee et al.[126] have also studied the condensation of the same working fluids on carbon particles. Chen et al.[127,128] have used the flow cloud chamber (FCC) to study the condensation of supersaturated vapors of *n*-butanol and water on charged and neutral monodispersed nanoparticles.

Despite the advantages of using the condensation nuclei counter (CNC), the calculation of the heat and mass transfer equations was very difficult due to its design [125]. Thus, the supersaturation could not be estimated accurately. Meanwhile, using the upward thermal diffusion cloud chamber (DCC), the supersaturation, the temperature and the pressure inside the chamber could be obtained accurately by solving the heat and mass flux equations.

The DCC has been extensively used to study different types of nucleation like single and binary homogeneous nucleation,[29,30,129] ion-induced nucleation[130,131] and photo-induced nucleation.[132] To the best of our knowledge, very little data has been reported on the condensation of supersaturated vapors on nanoscale particles in the DCC. Caldwell et al.[133] have reported preliminary results for the nucleation of ethanol vapor on Al nanoparticles in the DCC.

In this chapter, a new method was developed that coupled the nucleation process in the DCC chamber (as discussed in chapter two) with the laser vaporization controlled condensation technique (LVCC-discussed in chapter three). This was done by simply vaporizing a target, which could be a metal or a semiconductor, in a condensable vapor of known supersaturation, temperature, and pressure.

It is worth mentioning here that in the process of pulsed-laser ablation of solid targets, highly energetic species are ejected from the target surface forming a plasma plume. Its energy often reached up to several hundreds of eV. Rapid homogeneous phase transition occurs directly from solid to gaseous phase containing a mixture of individual atoms and multi-atom clusters with and without charge. This is attributed to the significant overheating of the material exposed to a short laser pulse.[134]

The research presented in this chapter involved the condensation of supersaturated trifluoroethanol (TFE) vapor on magnesium (Mg) nanoparticles generated by the second harmonic light of a pulsed Nd:YAG laser inside a diffusion cloud chamber. The influence of different factors were studied such as the vapor supersaturation, the total pressure, and the electric field inside the chamber as well as the laser fluence on the nucleation behavior of TFE vapor on Mg particles.

4-2 Experimental

A modified diffusion cloud chamber (DCC) was used in these experiments. A detailed description of DCC can be found in chapter two. The experimental setup is given in Figure 66. A brief description is given here. The chamber consists of two aluminum plates separated by a circular glass ring. A magnesium rod (Aldrich, 99.9+ %) of diameter (6.0 mm) and height of (11.5 mm) was machined and cut with an angle of 45 degree, then placed on the center of the bottom plate. A shallow pool of trifluoroethanol (TFE) (75 mL, Aldrich NMR grade, 99.5+ %) was introduced to the bottom plate. The Mg rod was chemically isolated from the TFE liquid by a Teflon block. The total pressure inside the chamber was adjusted to about 700 Torr, at room temperature, by introducing an inert, noncondensable gas (He, 99.999%) inside the chamber. A temperature difference was set between the top and the bottom plates, to control the supersaturation (*S*) of the vapor, by circulating the proper fluids. In these experiments, the vapor supersaturation of TFE was adjusted below that required for homogeneous nucleation. A single pulse (1.6×10^8 W/cm^2) was fired from a Quanta ray Nd:YAG laser (532 nm, 2 ns pulse width) focused on the Mg target. The nucleating droplets were counted by observing the forward scattering of light from the droplets falling through a horizontal He-Ne laser beam traversing the chamber. The He-Ne laser beam was set above that of the Nd:YAG laser to detect droplets of TFE-coated Mg nanoparticles. A power supply (Bertan 205-05R) was used to apply an electric field (10-1000 V) between the chamber plates to control the nucleation behavior of charged nanoparticles.

4-3 Results and Discussion

Heterogeneous nucleation of supersaturated trifluoroethanol vapor on Mg nanoparticles, prepared by laser vaporization, has been studied under different experimental conditions, such as pressure, supersaturation, laser power, and electric field. The DCC chamber was used here as an amplifier to detect nanoparticle/TFE droplets that grow rapidly to micron sizes, where they can effectively scatter light and be detected through the condensation of the working fluid vapor (TFE).

When a laser pulse hit the Mg metal target, the temperature on the metal surface was elevated very quickly within a few nanoseconds, resulting in metal vaporization into atoms and clusters in the ground and excited states, with some of the generated particles carrying a net charge. At this high metal vapor density, nanoparticles started to form via the nucleation process followed by particle thermalization via collisions with He as well as TFE vapor. In the presence of supersaturated vapor of TFE, some energetic Mg particles would be favored sites for condensation and growth.

In a typical experiment, the supersaturation of the TFE vapor, inside the chamber, was always kept below that required for homogeneous nucleation (S = 2.5 at T = 269.4 K). As a result, no droplets were observed when the experiment ran without generating Mg nanoparticles. However, it was also important to exclude the possibility of photoinduced nucleation; in this experiment, a laser pulse of 532 nm was fired inside the chamber without hitting the Mg target. No nucleation events were observed, implying the absence of any photoinduced nucleation contribution. Additionally, when the laser pulse

was fired on the Mg target, no droplets were observed when there was no temperature gradient between the top and bottom plates of the chamber. This indicates that there was insufficient TFE vapor to condense on the Mg nanoparticles.

In these types of experiments, a wave of nucleating droplets was observed following the laser pulse. The data were recorded as a distribution of the number of droplets over time as detected by the photomultiplier in the chamber. The duration of this nucleation wave varied depending on the experimental conditions. This distribution was expected since the Mg nanoparticles, which were generated by laser vaporization, would take some time to grow and diffuse until they reached the nucleation zone (0.7 H) in the chamber. During this time the small particles (Mg/TFE) would reach the detection area first followed by the big ones. At some point, a maximum was reached, after this point the number of nuclei capable of inducing the heterogeneous nucleation started to drop, so the nucleation rate decreased until it reached zero.

Time profile scans of activated Mg nanoparticles at various supersaturations (1.385-1.826) of TFE are shown in Figure 67. The maximum supersaturation and temperature at the nucleation zone were calculated by solving the mass and heat flux equations. The total number of droplets (proportional to rate of nucleation) decreased by decreasing the supersaturation of the TFE vapor in the chamber as shown from the insert figure. In these experiments, an electric field of 5.54 X 10^3 V/m was applied between the chamber plates and a total pressure of 675 Torr was used. The nucleation peak was shifted to longer times as the supersaturation ratio of the TFE vapor inside the chamber was decreased. At TFE vapor supersaturation of 1.829, 1.580 and 1.387, the maximum

nucleation rate occurred after about 45, 52 and 72 sec. from the laser pulse, respectively. The number of particles that vaporized from the Mg rod after each laser pulse was relatively constant since the same laser power was used. Therefore, from the above results, it is evident that at a high supersaturation (S = 1.829) most of the Mg nanoparticles are activated and the nucleation rate reaches its maximum quickly. On the other hand, at a low supersaturation (S = 1.387) only big particles are activated, since small ones are difficult to activate at low supersaturations. In this case the nucleation rate reaches its maximum at a longer time.

The induction time, which is the time required from the laser pulse until the onset of the nucleation process, increased with decreasing vapor supersaturation inside the chamber. At a low supersaturation ratio, not all particles were activated. Small particles were difficult to get activated at a low supersaturation, and so they diffused faster through the nucleation zone without reaching the critical sizes. However, in the case of big particles, supersaturated vapor condensed easily on them and they reached the critical size and grew faster. As a result, it took those particles more time to grow and diffuse to the nucleation zone.

In the case of high supersaturation, most of the particles generated by the laser pulse did reach the critical size and grew to macroscopic sizes through condensation, even the smaller ones. This proposed mechanism could explain the lower induction time needed to observe nucleation in the case of a low supersaturation. The above results are in good agreement with what Chen et al.[127,128] have reported. They showed that the critical supersaturation decreased with increasing the particle size.

The relationship between the vapor pressure and the particle diameter, when the process of condensation starts to prevail over the evaporation process, is given by Kelvin's equation:[124]

$$\ln S = \frac{4M}{\rho RT}\frac{\sigma}{d_{Kelvin}} \qquad \text{Eq. 4-1}$$

Where d_{Kelvin} is the Kelvin diameter, σ is surface tension, M is the molecular weight, ρ is the density of liquid, R is the universal gas constant, T is the temperature, and S is the supersaturation. At given S values, particles greater than the Kelvin diameter are activated and followed by condensational growth. Particles smaller than the Kelvin diameter are not activated and eventually evaporate.[124] The Kelvin diameters were calculated using (Eq. 4-1) as 4.5, 5.9 and 8.3 nm for *S* values of 1.829, 1.580 and 1.387, respectively. Therefore, it is clear that by increasing the supersaturation, the Kelvin diameter decreases, and more particles should be activated and grow. Similar results have been observed by Mavliev et al., who coupled a modified CNC with the DMA to study the heterogeneous nucleation.[125] When they increased the pressure of octadenoic acid in the CNC, which is equivalent to supersaturation, the size distribution of NaCl particles increased smoothly to larger sizes. They also observed that the dispersion of the distribution increased with increasing the vapor condensation, implying the formation of big condensable droplets.

The electric field effect on the droplet formation at a given supersaturation and pressure has also been investigated. As mentioned before, during laser vaporization of a metal target an estimate of 10^6 ions and 10^{14} atoms within a 10 ns laser pulse were

generated.[11] Therefore, it is expected to see a significant effect by applying an electric field between the chamber plates. Displayed in Figure 68 are different time profiles measured at different electric fields (0.0-15.38 V/m) at a constant TFE supersaturation ratio of 2.39 and a total pressure of 644 Torr. It is observed that the time-width of the nucleation cloud decreased as the electric field inside the chamber was increased. This behavior can be attributed to the total number of the charged particles reaching the nucleation zone by drift velocities, which depends on their mobilities and the magnitude of the applied electric field. In the absence of an electric field, the motion of the neutral and charged particles were described in terms of diffusion. The observed nucleation events reflect the number of particles reaching the nucleation zone by diffusion. By increasing the potential difference between the top and bottom plates, the electric mobility of the charged clusters increased. The electrical mobility (μ_i) of a charged cluster of size *i* is given as:

$$\mu_i = \frac{\nu_i}{E} \qquad \text{Eq. 4-2}$$

Where ν_i is the velocity by which these clusters drift through the nucleation zone and E is the electric field. By assuming that each laser pulse will generate a relatively constant number of neutral and charged nanoparticles, thus, at high electric field, most of the charged Mg particles were swept quickly, due to their high electrical velocity through the nucleation zone before they were activated and grew into macrosize droplets. On the other hand, when the electrical velocity of the laser-generated Mg particles is small, most of the charged particles spent longer time with TFE supersaturated vapor and were

activated. For example, the nucleation cloud formed by Mg nanoparticles under 0 V/m lasts for more than 50 seconds while when an electric field of 15.38 X 10^3 V/m is applied, the nucleation cloud lasts for about 30 seconds.

Shown in Figure 69 is the total number of droplets as a function of the electric field applied in the DCC chamber. The nucleation behavior was studied under an electric field ranging from (-15.38 X 10^3 to +15.38 X 10^3 V/m). It is obvious from the figure that the number of droplets was almost constant, regardless of the polarity of the electric field applied. These results confirmed that both the positive and negative particles had almost the same ability to induce the condensation of TFE vapor. Similar results have been observed by Chen et al.[127,128], who found that the condensation of supersaturated vapor on singly positive/negative charged particles had no obvious charge effect and sign preference. In Figure 69 a sharp decrease in the droplet number is shown as the applied electric field increased (till 0.77 X10^3 V/m), followed by a smooth decrease on both sides (the positive and the negative fields) as the field increased more.

The effect of pressure on the condensation behavior of supersaturated TFE vapor (S = 1.823) on Mg nanoparticles has also been studied at a constant electric field of 0.154 X 10^3 V/m. In Figure 70(a), the time profiles at three different pressures (328, 620 and 934 Torr) are displayed. It is clear that the width of the nucleation cloud increased with increasing the pressure. In the laser vaporization techniques, the laser-induced plasma plume depended mainly on the ambient gas used and on its pressure. Furusawa et al.[135] have studied the laser ablation process of Al target in different ambient gases (He, N2, CF4, and CH4). They have observed that when He gas was used, the size of the plume

was the largest compared to the rest of gasses used due to the confinement effects. The maximum velocities of ablated material was estimated from molecular dynamics simulations as (500-1500 m/s).[134] At higher pressure the laser plume expansion in the chamber is suppressed and confined, compared to that at a lower pressure, due to collision frequency enhancement in the plume as well as the thermalization between Mg particles and He-TFE vapor mixture. When the chamber pressure was reduced to 328 Torr most of the small Mg particles diffuse quickly through the nucleation zone before the TFE vapor condenses on them. However, the rest of the particles are activated and detected by the light scattering method. On the other hand, at relatively a high pressure 934 Torr, most of the generated particles ejected from Mg metal surface, are confined in space and hence the collision frequency between them and the surrounding molecules is enhanced. The residence time of the particles to grow, in the case of a high pressure, is relatively longer than that in the case of a low pressure. This can explain the higher droplets count at 934 Torr compared to the droplet count at 328 Torr pressure in the chamber.

In Figure 70(b) the relation between the nucleation rate and the chamber pressure is also shown. A nearly linear relationship is observed between number of droplets detected and the total pressure inside the chamber.

All the above-mentioned experiments were carried out at a constant laser power of about 1.6 X 10^8 W/cm^2. Finally, the effect of laser power at constant pressure (P = 665.2 Torr), supersaturation (S = 1.825), and electric field (0.154 X 10^3 V/m) was investigated. It is worth mentioning that in the process of pulsed laser ablation of solid

targets, highly energetic species are ejected from the surface; their energy often reaches up to several hundreds of eV within few picoseconds.[135] Wie et al.[136] have used the classical homogeneous nucleation theory to describe the melting process of a superheated solid material induced by ultrafast laser pulse irradiation. Their results show that Al metal should melt within several tens of picoseconds upon laser irradiation.

Displayed in Figure 71(a) are the nucleation time profiles under different laser power density. It is clear from the figure that by increasing the laser power density, the number of activated particles drops. Two important factors could control this effect; the mass concentration (MC), and the number concentration (NC) of the particles generated during the laser pulse. Using a high power density, more material (MC) is vaporized than in the case of a low power density. As a result, bigger particles are ejected that could reach droplet-like sizes, and a rougher surface is left. However, the particle number concentration (NC) at a low power density was larger than that at a high power density. Recently, similar results have been observed by Zhigilei et al. who have performed molecular dynamics (MD) simulations of laser ablation of organic solids.[134] They have found that, below a certain laser fluence, primarily single molecules are desorbed while above this threshold, a collective ejection or ablation took place in which large molecular clusters form a significant portion of the ejected plume. This means that at low power density a large number of particles are generated with a relatively small size distribution that could activate the condensation of TFE vapor to form detectable droplets. On the other hand, the low number of droplets observed by using a high laser power, could be explained by the formation of a plume. The laser-generated plume confined a high metal

vapor density, which facilitates the formation of large particles as well as aggregation of small particles. At low laser power the induction time was observed to be smaller than that at a high laser power due to the fact that small particles diffuse quickly to the nucleation zone (low power density case), while large particles slowly diffuse to the nucleation zone (high power density case). The relation between the laser power density and number of droplets were demonstrated in Figure 71b.

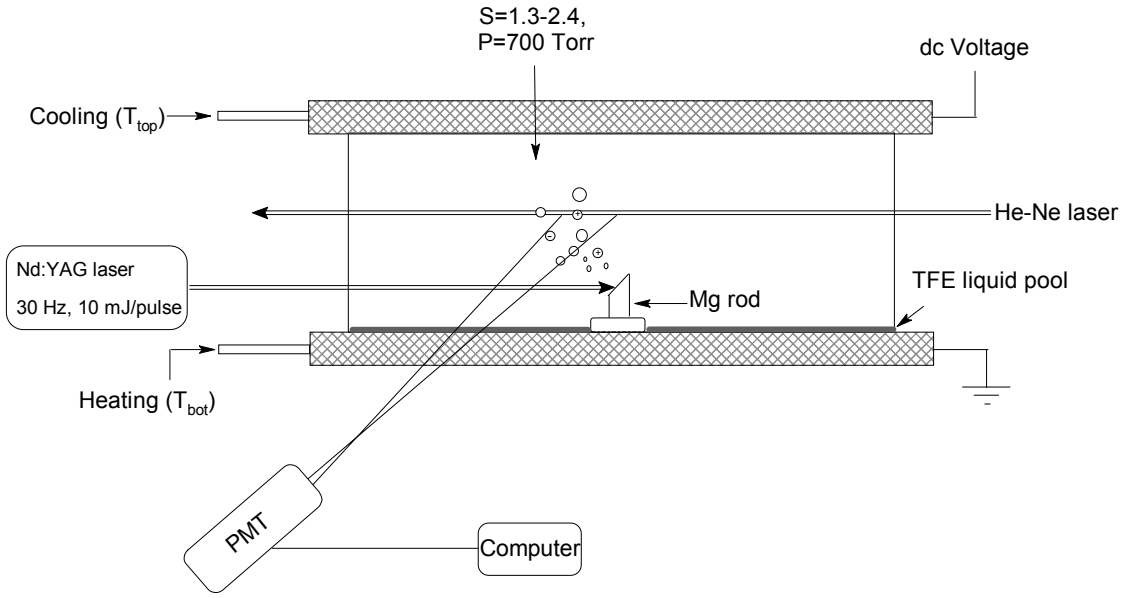

Figure 66. Experimental setup for the Diffusion Cloud Chamber (DCC) used to study heterogeneous nucleation of trifluoroethanol vapors on Mg nanoparticles.

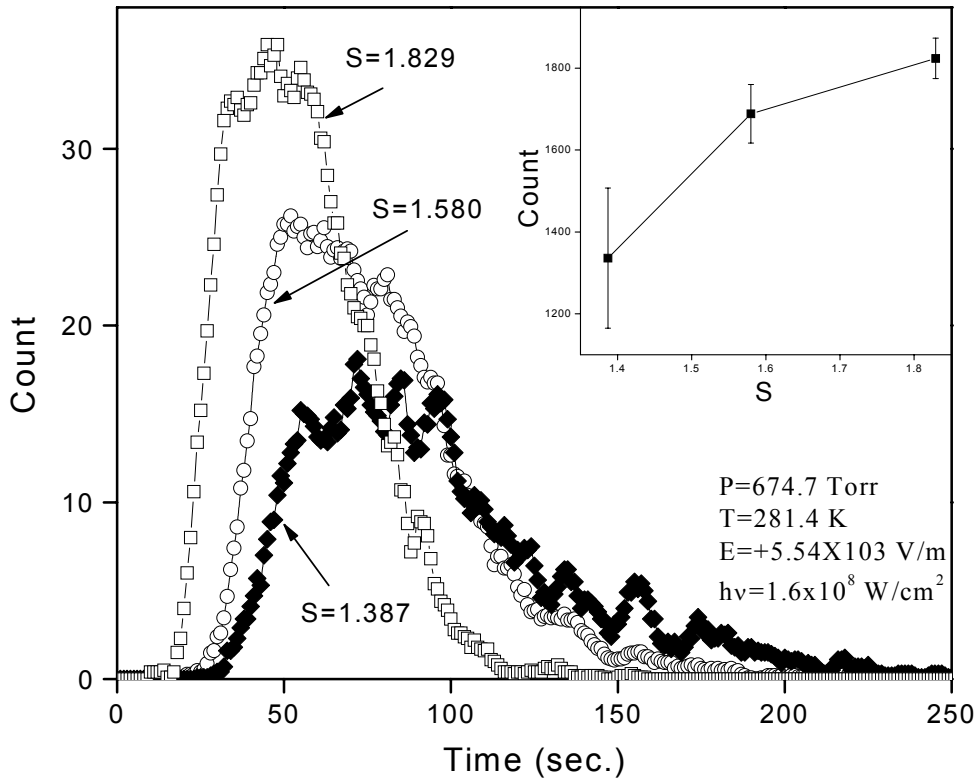

Figure 67. (a) Time profile showing number of droplets of TFE vapor (P = 674.7 Torr, T_{max}= 281.4 K, and E=5.54 X 10^3 V/m) condensed on Mg nanoparticles after a single laser shot (1.6 X 10^8 W/cm^2) at different supersaturations. (b) Relation between total numbers of droplets of TFE condensed on Mg nanoparticles as a function of supersaturation inside the chamber.

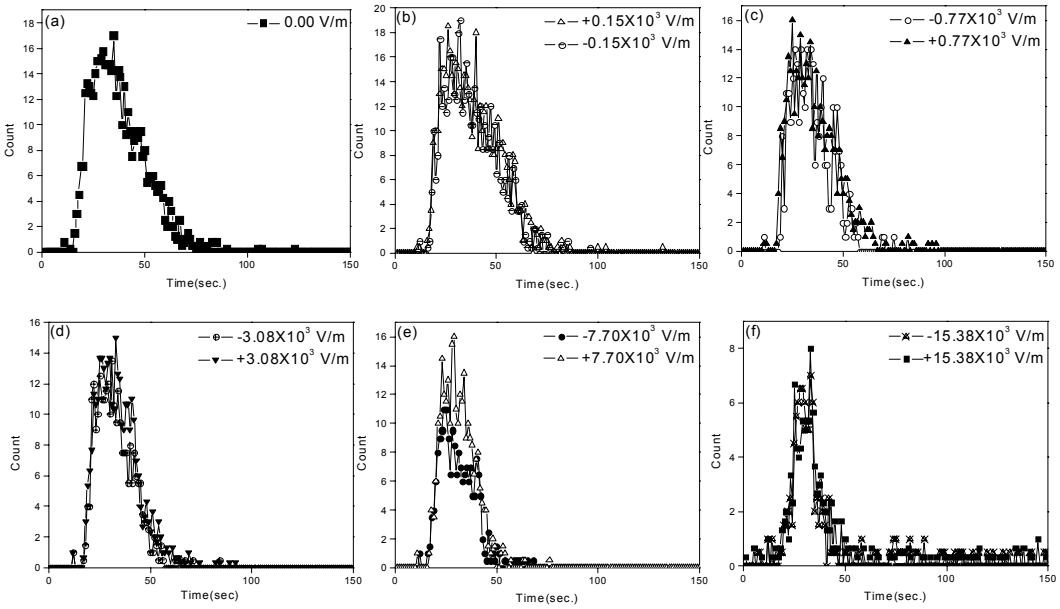

Figure 68. Time profile scan showing number of droplets of TFE vapor (S_{max} = 2.39, T_{max}= 269.0 K, P=644.2 Torr) condensed on Mg nanoparticles after a single laser shot (1.6 x 10^7 W/cm^2) under different electric field applied to the DCC.

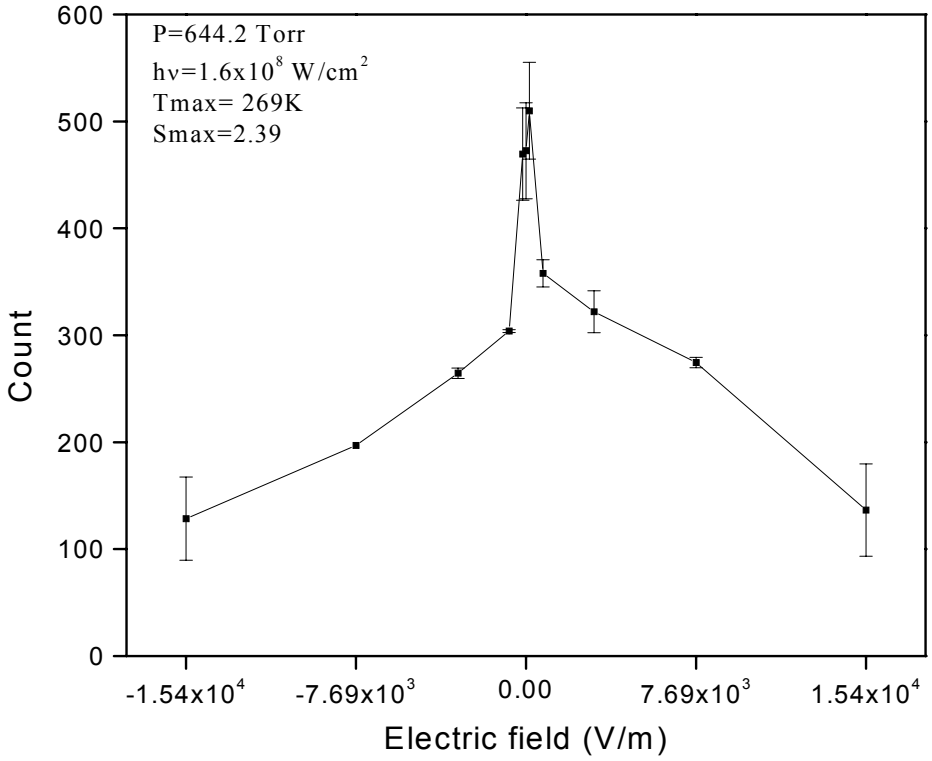

Figure 69. Relation between electric field applied to DCC and total number of droplets of TFE condensed on Mg nanoparticles.

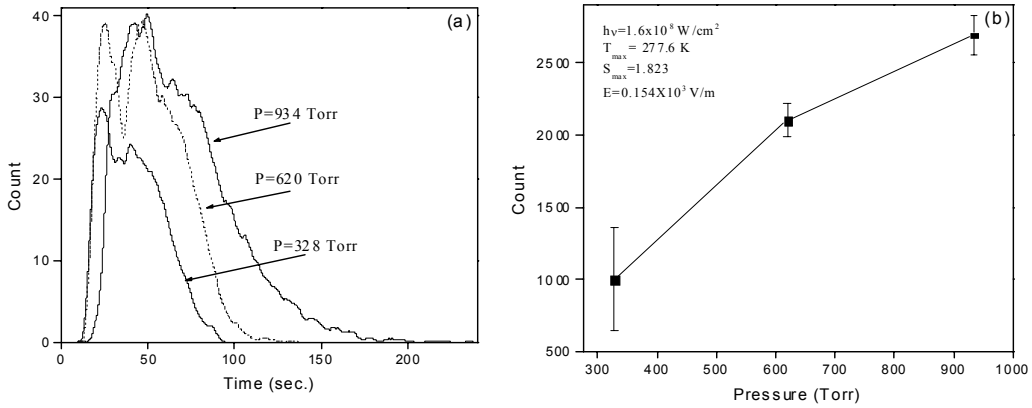

Figure 70. (a) Time profile showing number of droplets of TFE vapor (S_{max} = 1.823, T_{max}= 277.6 K, E=0.154 X 10^3 V/m) condensed on Mg nanoparticles after a single laser shot (10 mJ/pulse) at different pressures. (b) Relation between total numbers of droplets of TFE condensed on Mg nanoparticles as a function of pressure inside the chamber.

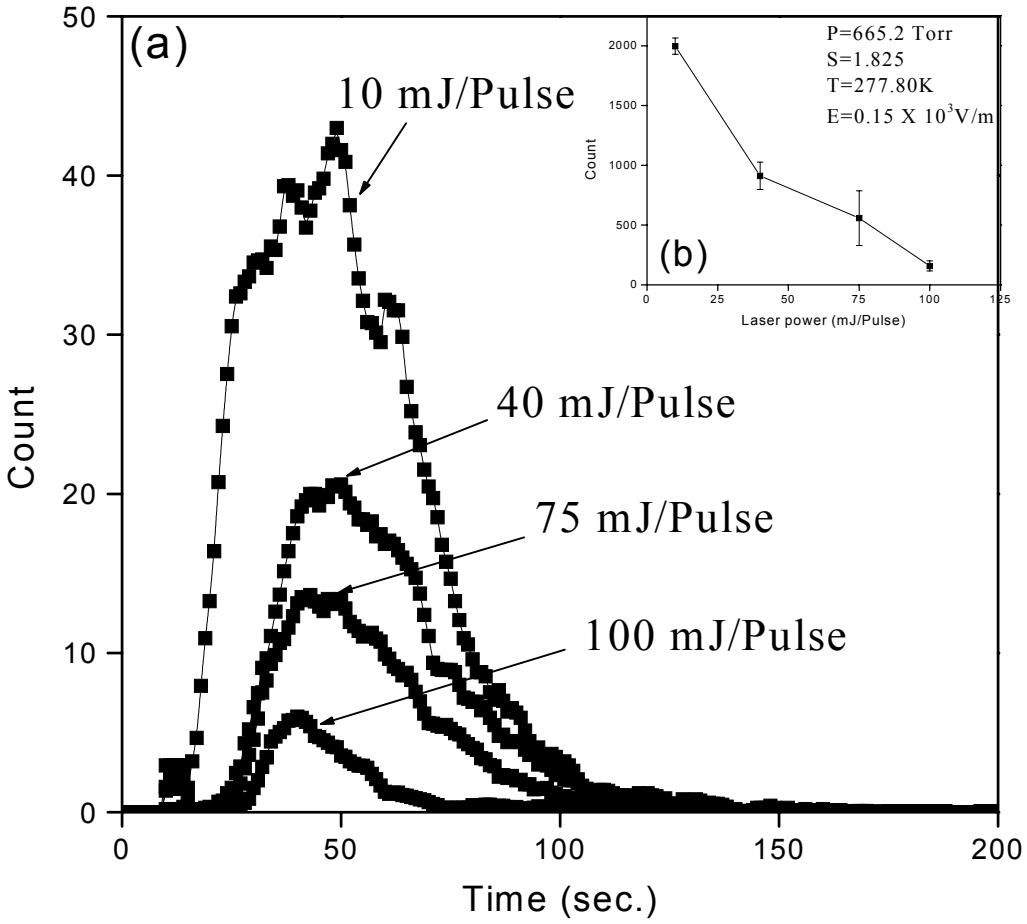

Figure 71. (a)Time profile scan showing number of droplets of TFE vapor (S_{max} = 1.825, T_{max}= 277.8 K, P=665.2 Torr, E=0.15 X 10^3 V/m) condensed on Mg nanoparticles after a single laser shot of different laser power. Insert (b) Relation between total number of droplets of TFE condensed on Mg nanoparticles as a function of laser power used to vaporize it.

Chapter 5 Gas Phase Polymerization on Nanoparticle Surfaces

5-1 Part one: Polymerization Coupled with LVCC

5-1-1 Introduction

The interaction between organic vapors and laser generated plasma formed by the metal ablation process has been previously reported.[36,137-145] Garvey and co-workers[137-139] have studied the laser-assisted interaction between Cu or Ti metal plasma and acetylene/acetone organic vapors. In these reactions a polymeric film was prepared. They demonstrated that the formation of this polymeric film was not only a thermal effect of the laser plasma, but also a catalyzing activity of the metal atoms. El-Shall and co-workers[140,146] have reported the synthesis of polyisobutylene bulk polymer catalyzed by the metal cations that are generated during the laser evaporation of a metallic target (Ti, Zr, or Sn). In these experiments, the metal ions were injected into a cooled liquid of isobutylene monomer, followed by the cationic polymerization reaction. Moreover, cationic polymerization due to charge transfer from Zn^+ ion to isobutylene monomer in the gas phase has also been studied by Daly and El-Shall[140,147] using the high-pressure mass spectroscopy (HPMS). Previously, Castleman[141,142,148] and Duncan[143-145] groups had utilized the laser–ablated plasma of several different metals to generate metallocarbohedrenes (M_8C_{12}) by introducing an appropriate hydrocarbon vapor.

During the laser ablation of a metallic target, ablated in the vapor phase that contains some hydrocarbon fraction, the injection of energetic metal atoms, ions, electrons, and neutral or charged multi atom clusters may initiate or catalyze several reactions, such as dehydrogenation, cyclization, disproportionation, or polymerization of organic monomers. However, the temperature at which these processes takes place (<1000 K) is much lower than that of the laser-evaporated metal plasma (~ 10,000 K).[36,140,146] In fact, the nature of the interaction between the metal plasma and the organic vapor depends on the experimental parameters such as the laser fluence, the nature of the metal, and the hydrocarbon monomer used.[137,139] Under certain conditions, the interaction of the metal plasma with a gaseous hydrocarbon may result in dehydrogenation reactions or polymerization of the hydrocarbon.

Recently, metal nanoparticles embedded in host polymer matrices have become the focus of increasing attention, because of the unique mechanical, optical, electronic, and magnetic properties of these materials.[9] The synthesis of metal-polymer nanocomposites is usually accomplished in solutions through multi-step chemical routes. However, one-step synthesis of metal encapsulated in polymers is scarcely reported in the vapor phase.

Most of the methods used to fabricate metal/polymer nanocomposites are limited by the particles' coagulation in the polymer matrices.[149] Therefore, coupling the LVCC method simultaneously with the polymerization reaction in the vapor phase, could improve the dispersion of nanoparticles in polyhydrocarbon matrices. Additionally, the laser vaporization techniques have potential advantages over the chemical based

techniques, including simple processing, solvent-free products, and full control over metal vapor flux depending on the laser power.

The research presented in this section involved the formation of thin films of various nanoparticles (Pt, Ni and FeAl) encapsulated in poly (hydrocarbon)/carbonaceous films, by taking advantage of the laser-ablated plasma plume of these metallic targets in the polymerization reaction of butadiene-He gas mixtures.

5-1-2 Experimental

The LVCC method, described in chapter three, was used to study the gas-phase polymerization of 1,3-butadiene. In these experiments, the LVCC chamber was filled with a gas mixture of He (inert) and 1,3-butadiene (reactive) at a certain composition. The concentration of the 1,3-butadiene monomer ranges from 1 to 15 % in helium. A high-grade helium gas (He, 99.999%) was used. The hydrocarbon, 1,3-butadiene, was purchased from Aldrich with a purity of 99+%. The total pressure in the chamber was adjusted around 1000 Torr. The temperatures of the top and the bottom plates were kept at 25 and 90 °C, respectively. In some experiments an electric field of (60 V/cm) was applied between the chamber plates. An illustration of the gas phase polymerization of 1,3-butadiene using Ni nanoparticles is shown in Figure 72. In these experiments, the laser-generated plasma on the Ni target is believed to act as a catalyst for gas phase polymerization of 1,3-butadiene. Three different nanoscale materials were examined in these experiments, namely Ni, Pt and FeAl nanoparticles.

The scanning electron microscopy (SEM), the energy dispersive X-ray spectroscopy (EDX) and the scanning transmission electron microscopy (STEM) analysis were done on a Quantum DS-130S Dual Stage Electron Microscope. A glass substrate was placed on the top plate of the chamber, to observe the morphology of the deposited materials under the SEM. The nanocrystalline component in the nanocomposite films was examined by X-ray diffractometer (XRD), using an X'Pert Philips Materials Research

Diffractometer with Cu $K_{\alpha 1}$ radiation. The polymeric resin component was examined by FTIR using the Nicolet 670 FT-IR spectrophotometer.

5-1-3 Results and Discussion

The synthesis of FeAl/Polybutadiene nanocomposites in the vapor phase was done using the laser vaporization of FeAl target in 1,3-butadiene under well defined conditions of temperature and pressure. A rubbery black film was observed depositing on the top plate of the chamber shortly after the experiment started. Figure 73 and Figure 74 display the TEM micrographs for the FeAl-polymer nanocomposites prepared from 1 and 15 % of 1,3-butadiene in He, respectively. Nanoparticles of FeAl, with diameters of less than 20 nm, were observed randomly distributed, but well dispersed, inside an amorphous matrix of polybutadiene resin. It is clear from the TEM results that the amorphous matrix prepared with 15 % butadiene showed thick and dense coating properties for FeAl particles compared to that prepared with 1% butadiene concentration. This can be explained by the degree of polymerization, which depends on the monomer concentration. The more the concentration of the monomer, the thicker and more amorphous the deposit would be. The inserts in both figures display the selected area electron diffraction patterns (SAED) of these films. It is clear that with a low monomer concentration the FeAl nanocomposite has less amorphous structure compared to that with a high monomer concentration. This can be observed from the ringed structure in the electron diffraction pattern of 1% monomer, indicating the presence of some ordered structures (B2 crystal structure of FeAl particles) within the deposited film. At 15 % monomer, the SAED exhibits broad diffused rings, indicating that the resin was more amorphous which is in good agreement with the XRD results. In Figure 75 the x-ray diffraction patterns for the FeAl/polybutadiene film (prepared from 15 % 1,3-butadiene in

He) and the FeAl nanopowder are shown. It is evident that the FeAl/polybutadiene film is amorphous and has no crystal structure since the FeAl particles were embedded deep enough in the amorphous polymer as observed in the TEM results. The XRD data confirms the SAED and the TEM results.

In Figure 76 the morphology of the as-deposited film is displayed. The film was composed of fine long chains, of about (30-50 nm) width, cross-linked together with network structures. In fact, the deposited resin had a different structure compared to the typical web-like structures observed for the metal nanoparticles deposited inside the LVCC chamber. The solubility of the deposited film has been examined in a wide variety of organic solvents (chloroform, benzene, toluene, acetone, carbon tetrachloride, DMSO and n-hexane). The results showed that these films were very difficult to dissolve in most common organic solvents. For example, the FeAl/polybutadiene film showed swelling, especially, in toluene with a high solubility resistance in the rest of the solvents used, due to its cross linked-structure nature as observed from the SEM results. The FTIR spectroscopy results did not show the absorption band at (2850-2950 cm^{-1}), which is characteristic for the stretching vibrations of the (sp^3C-H) group. These results also implied the cross-linked nature of the resin prepared. This resin contains a mixture of cross-linked polybutadiene with carbonaceous species. The polymerization of 1,3-butadiene in the vapor phase could be initiated by more than one factor, such as the laser plasma and the laser-generated nanoparticle material that could act like a catalyst.

It is worth mentioning that when an electric field of (60 V/cm) was applied between the chamber plates, during the preparation of FeAl composite with 1 % 1,3-

butadiene, short filament-like structures were observed on the top plate. On the other hand, when the monomer percentage was increased to 15% in helium, no filament-like structures were observed. These results were expected as discussed before in chapter three, where at 15% 1,3-butadiene the FeAl nanoparticles were completely shielded from the electric field applied between the chamber plates by the cross-linked resin, whereas, at 1% 1,3-butadiene the FeAl nanoparticles were slightly shielded from the influence of the electric field.

Other nanocomposites, like Pt/polybutadiene, were also prepared under identical conditions of monomer concentration (15 % 1,3-butadiene in He), temperature gradient (ΔT=65-70 ºC), and total pressure of about 1000 Torr. Figure 77 displays the scanning transmission electron micrographs (STEM) along with their EDX spectra analysis. It can be observed that the Pt nanoparticles were randomly dispersed, with some particle aggregations, embedded in a matrix of polybutadiene. The average and selected-area EDX analysis for Figure 77b (represented by arrows) are shown in Figure 77 c and d, respectively. It is evident form the EDX spectra that Pt particles were embedded in an amorphous polymer matrix, as presented by the selected-area spectrum, which is composed mainly of Platinum. The crystallinity of Pt particles in nanocomposites was examined by XRD as shown in Figure 78, where the diffraction patterns of the as-prepared Pt nanoparticles and the Pt nanocomposites were given, respectively. Peaks in the diffraction pattern appearing at 2θ values of 39.75, 46.23, 67.47, 81.25 and 85.69 corresponding to (111), (200), (220), (311) and (222) planes of the Pt cubic crystal lattice. The lattice constants were calculated for pure and nanocomposite Pt nanopowders, with

the values of 3.9243 and 3.9477 which were comparable with the bulk lattice constant of Pt (3.9231). The Pt nanocomposite pattern showed a broader diffraction peaks compared to that of a pure Pt nanoparticles. The broadening could be due to the presence of amorphous polymer coating on nanocrystalline particles. Nevertheless, the small Pt particle size could also contribute to the XRD peaks broadening; where laser vaporized Pt particles could be easily thermalized through collisions with 1,3-butadiene molecules, preventing them from further growth. The average particle size of Pt nanoparticles was estimated from Scherrer's equation (Eq. 3-1) as 30 and 18 nm for pure and nanocomposites Pt particles, respectively.

A similar morphology, as of FeAl/polybutadiene, was observed for Pt/polybutadiene nanocomposites, where network of structures composed of tangled branched chains (about 30-50 nm in width) are shown in Figure 79.

Finally, the polymerization of 1,3-butadiene induced by the laser vaporization of a Ni target in a 15% 1,3-butadiene was studied. Figure 80(a-b) display the SEM micrographs of the as-prepared Ni/polybutadiene film with cross-linked chains and web-like structures, as had been previously observed in the other systems studied. In Figure 80c a photograph for a black deposit of Ni/polybutadiene film deposited on the top plate of the LVCC chamber is shown. The film exhibited some elasticity with a rubbery surface, which characterizes the polybutadiene polymer.

The nanoparticles component in the nanocomposite film was confirmed by the XRD analysis. The diffraction patterns of pure Ni nanoparticles and Ni/polybutadiene nanocomposites are presented in Figure 81. The diffraction peak at ($2\theta = 44.47$) assigned

to (111) plane of Ni crystal lattice is still observed in the Ni/polybutadiene nanocomposite, indicating the presence of Ni crystalline nanoparticles coated with an amorphous layer of polymer resin.

In conclusion, similar results for plasma-initiated polymerization of 1,3-butadiene on different nanoparticle surfaces, regardless of their material were observed, indicating that the polymerization process is independent of nanoparticle material used and that the laser plasma induced the process. All nanocomposites prepared using FeAl and Pt or Ni nanoparticles showed the same cross-linked morphologies under the SEM, which made their solubility very minimal. Therefore, their molecular weight could not be determined using gel permeation chromatography (GPC) analysis or their structures using ^{1}H-NMR spectroscopy. The amorphous polymer matrix was commonly observed in these prepared nanocomposites as illustrated from the results of TEM, ED, EDX, and XRD.

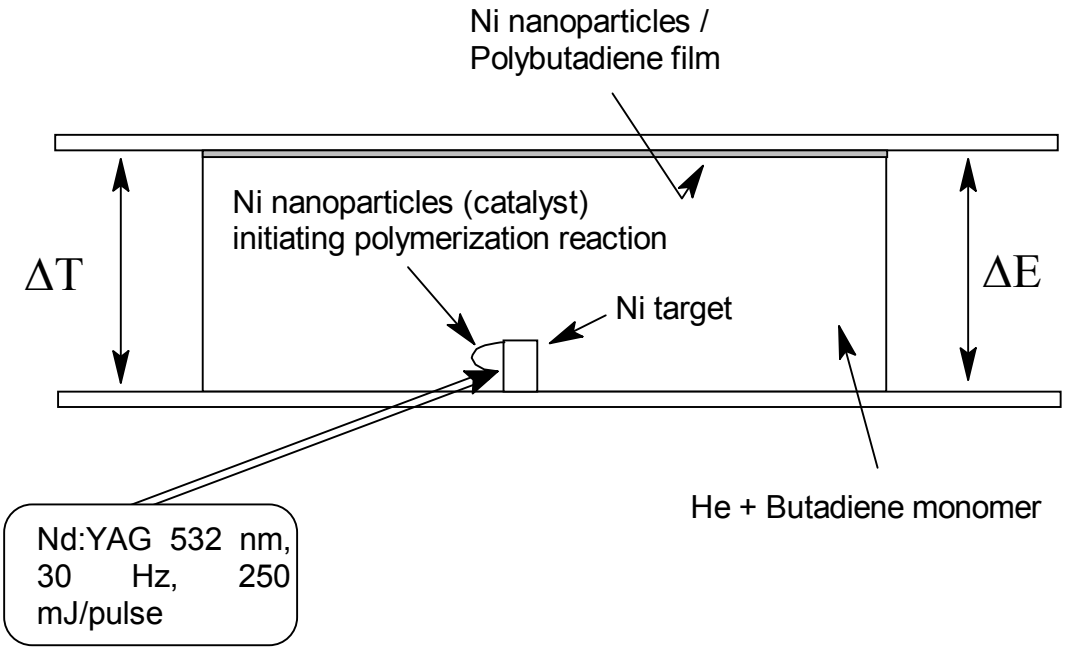

Figure 72. Experimental set-up for the LVCC chamber used in polymerization experiments.

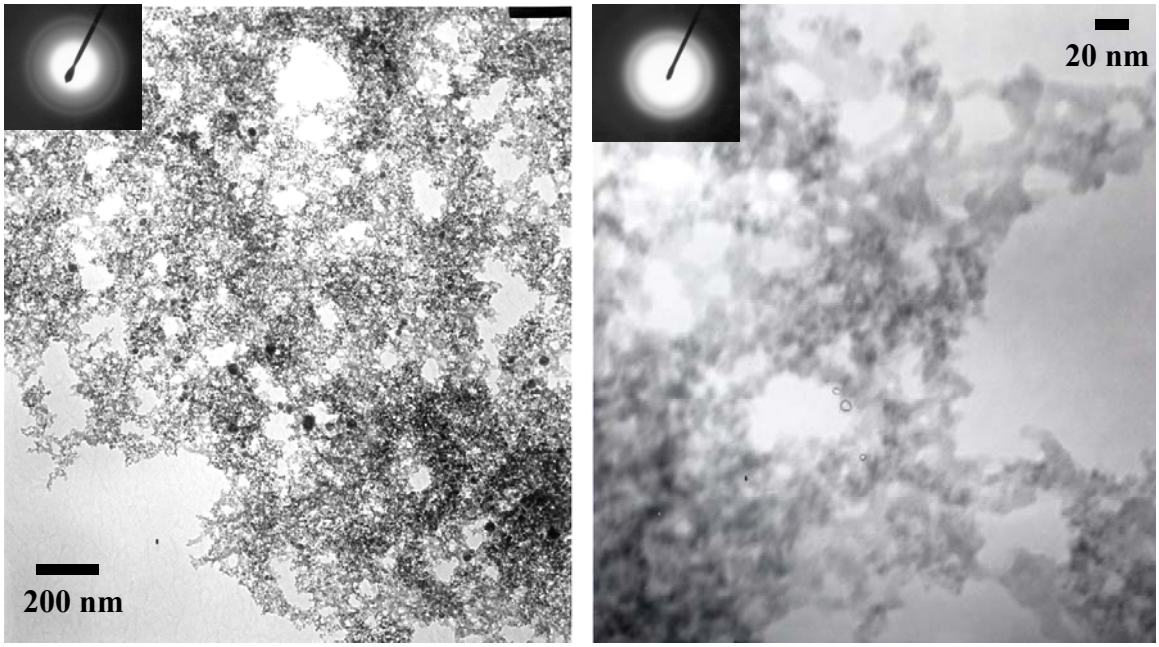

Figure 73. TEM micrographs and electron diffraction patterns (insert) for FeAl nanoparticles embedded in polybutadiene matrix (prepared in 1% 1,3-butadiene in He).

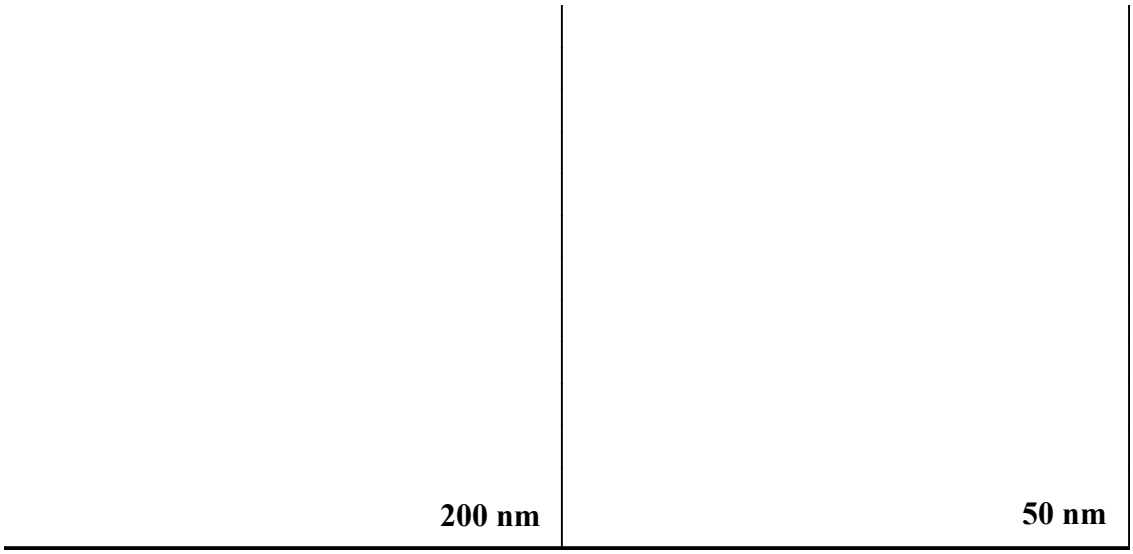

Figure 74. TEM micrographs and electron diffraction pattern (insert) for FeAl nanoparticles embedded in polybutadiene matrix (prepared in 15 % 1,3-butadiene in He).

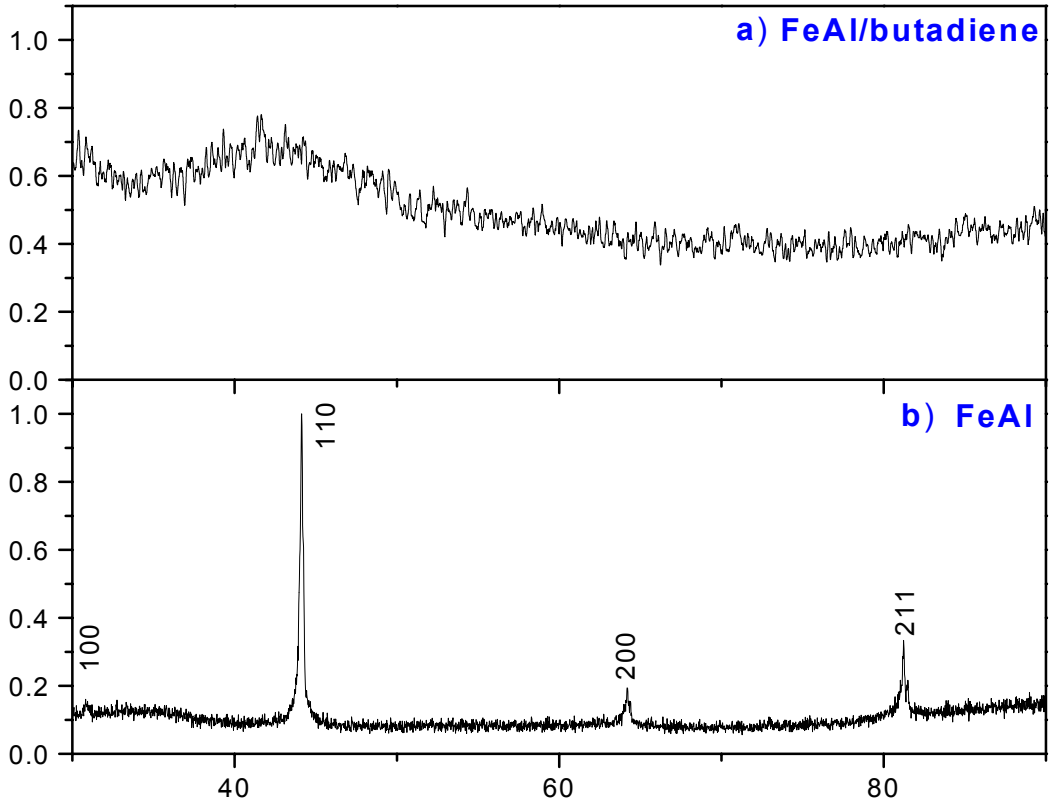

Figure 75. XRD for a) FeAl nanoparticles prepared in a mixture of He and butadiene (15%) and b) FeAl nanoparticles prepared in pure He by the LVCC method.

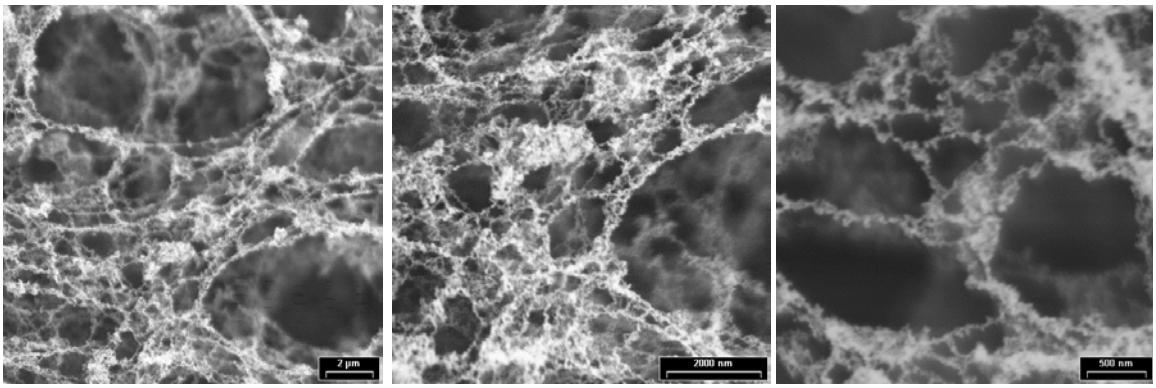

Figure 76. SEM of as-deposited FeAl/polybutadiene nanocomposite prepared by the LVCC method. Scale bar 2µ, 2000 nm and 500 nm.

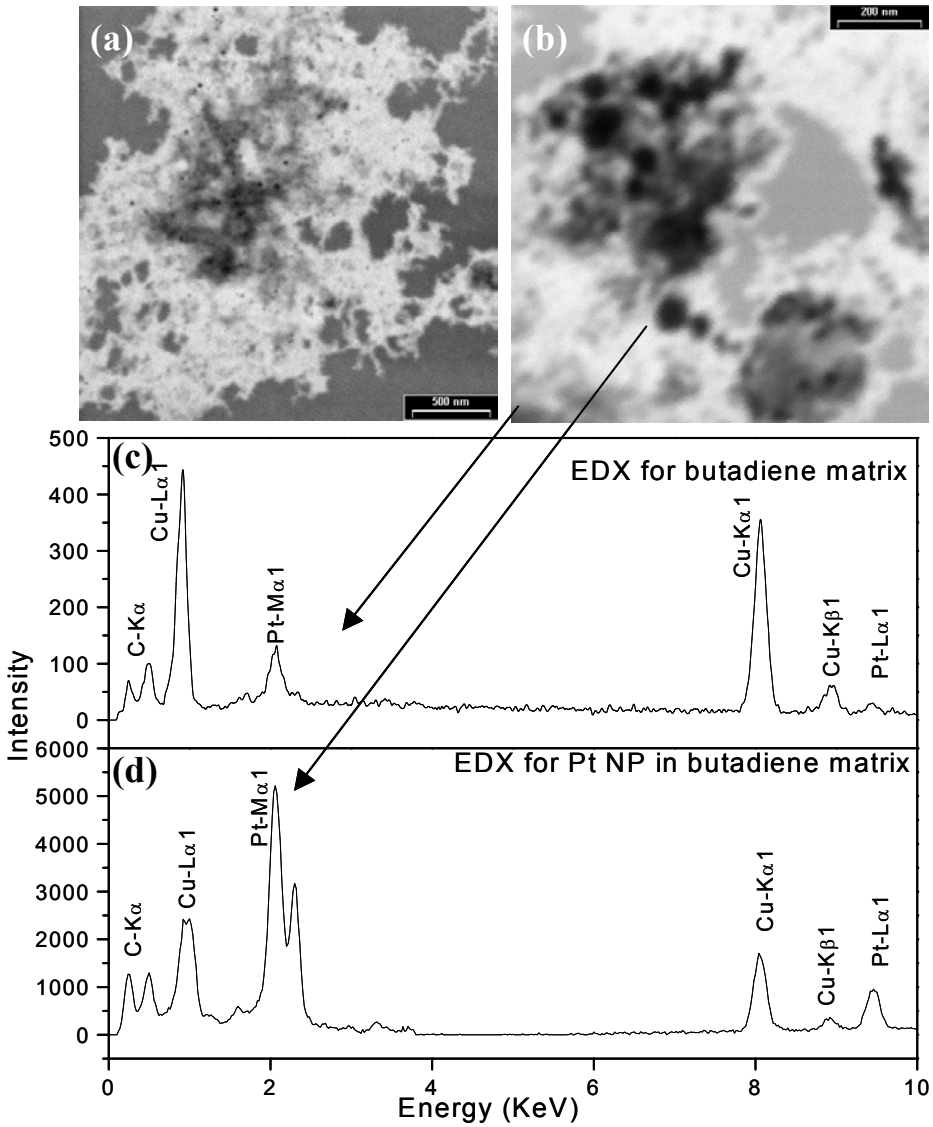

Figure 77. Scanning transmission electron micrograph (a-b) along with their EDX spectra analysis (c) for Pt/polybutadiene matrix, and (d) for Pt nanoparticles in butadiene matrix.

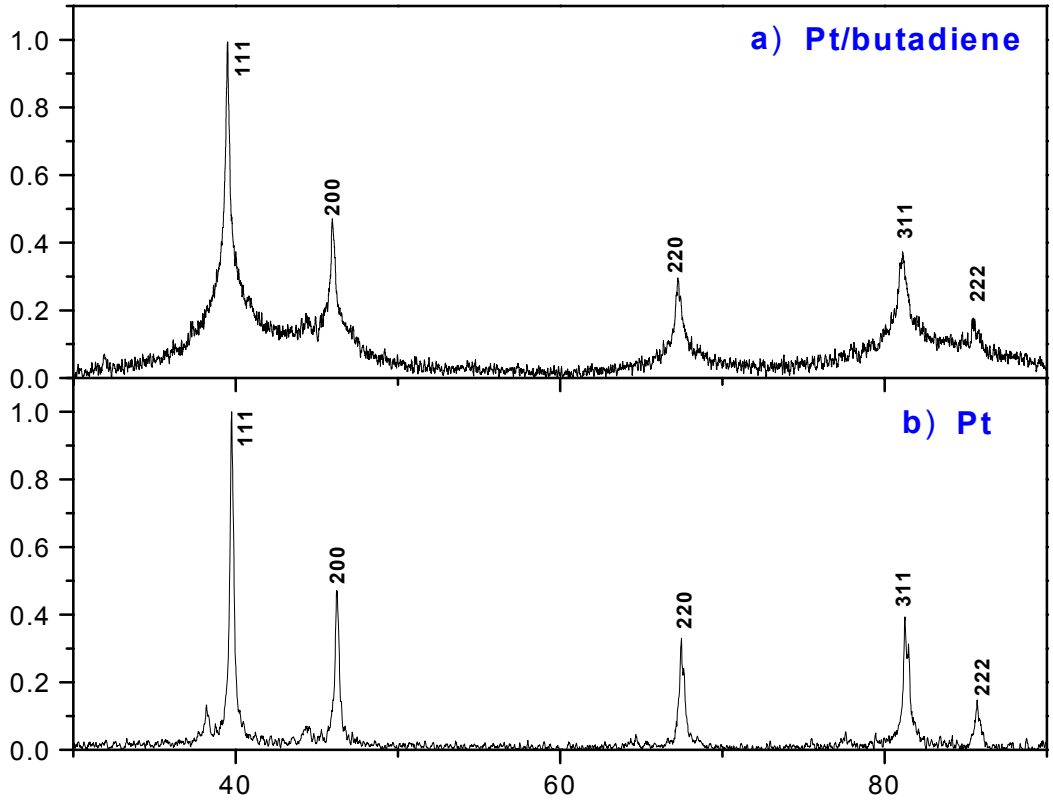

Figure 78. XRD for a) Pt nanoparticles prepared in a mixture of He and butadiene (15%) and b) Pt nanoparticles prepared in pure He by the LVCC method.

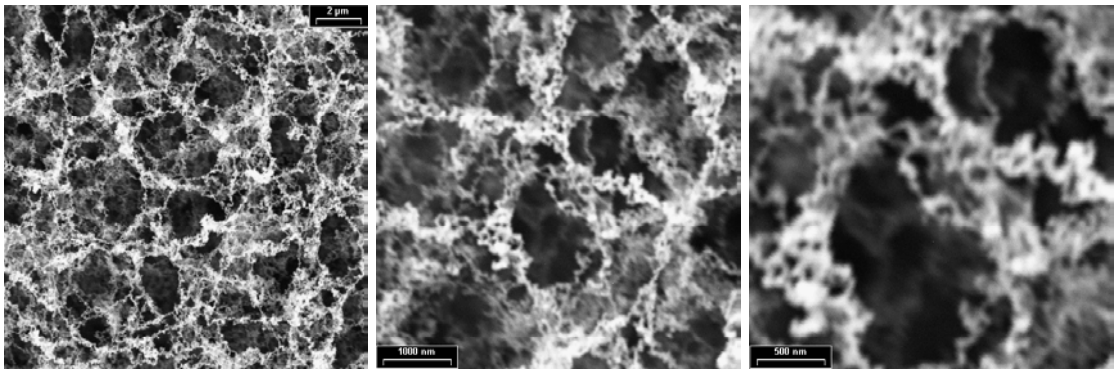

Figure 79. SEM of as-deposited Pt-Butadiene nanocomposite prepared by LVCC method. Scale bar 2µ, 1000 nm and 500 nm.

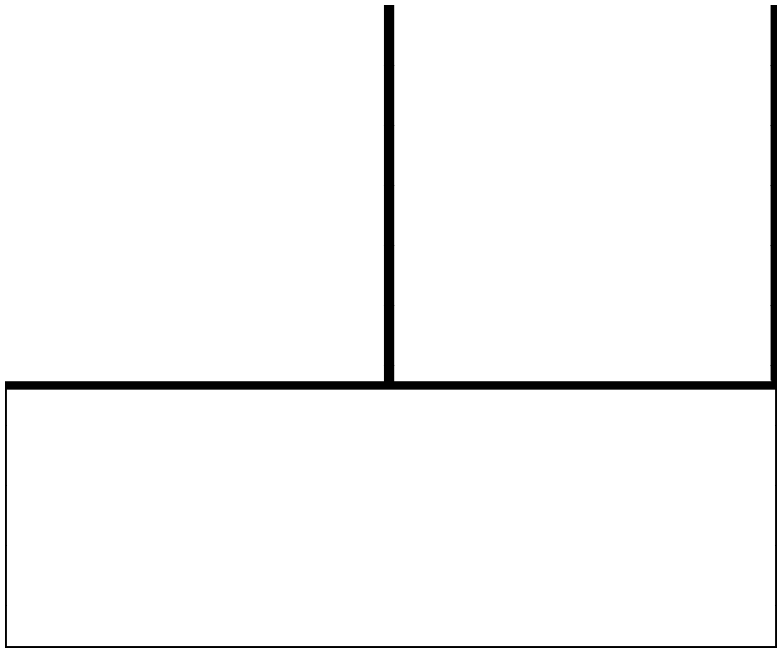

Figure 80. Scanning electron micrographs of deposited Ni-polybutadiene nanocomposite prepared by the LVCC method (a,b) with scale bars of 2000 and 500 nm, respectively, and (c) a photograph of as-deposited thin black rubbery film in the chamber.

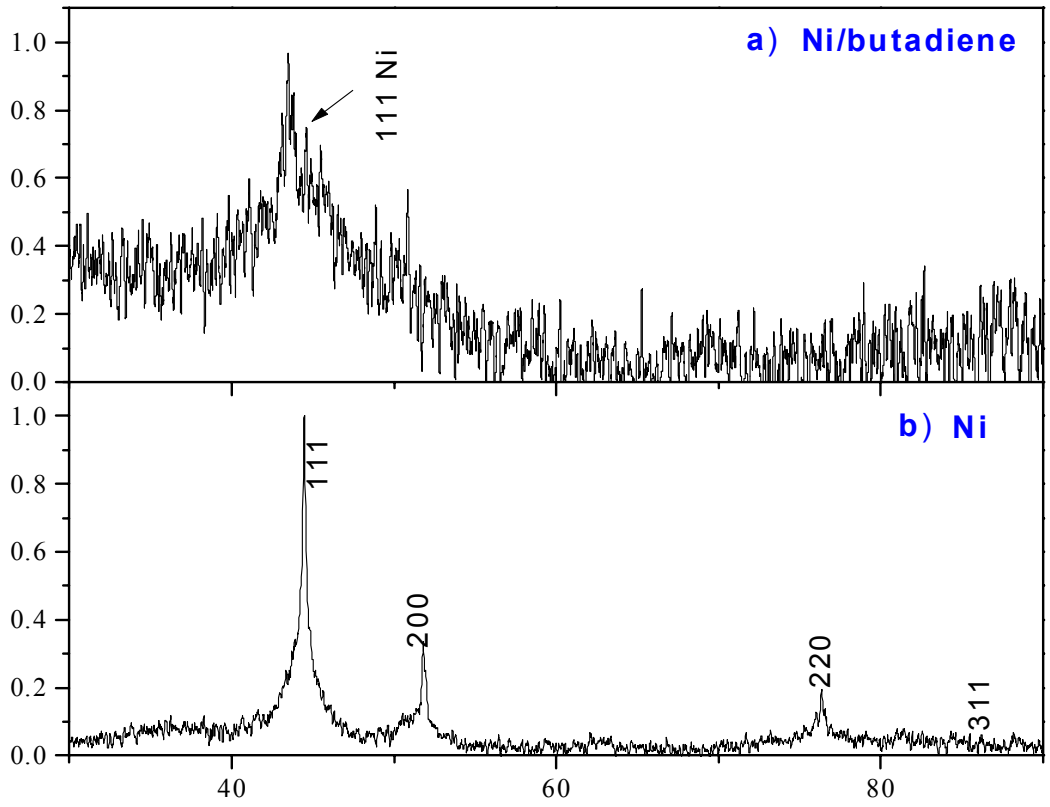

Figure 81. XRD for a) Ni nanoparticles prepared in a mixture of He and butadiene (15%) and b) Ni nanoparticles prepared in pure He by the LVCC method.

5-2 Part two: Free Radical Polymerization on Nanoparticle Surfaces

5-2-1 Introduction

A nanocomposite is a material that is composed of two or more phases, usually a polymer matrix containing particles with grain sizes of less than 100 nm. Nanocomposite materials have the attractive characteristics of polymers, like the noncorrosiveness, the light weight, and the mechanical properties, which when combined with the magnetic,[150,151] optical,[152,153] and electronic[9] properties of the nanoparticles, lead to the fabrication of unique multifunctional materials. There are several methods that have been developed to synthesis these materials, such as those that use microwave plasma processing,[154] sonochemical,[155,156] and γ irradiation[157,158] sources, as well as the sol-gel casting[159,160] and mechanochemical methods.[161]

Nickel nanoparticles have been used extensively in many applications, owing to its mechanical, catalytic, and magnetic properties.[162] It has been also used in the fabrication of media storage and nanocomposite materials and more recently in hydrogen storage materials.

Different techniques have been utilized to prepare polystyrene nanocomposite materials. For example, nickel polystyrene composites have been prepared by *in situ* reduction of Ni formate-polystyrene mixture by ultrasound irradiation.[155] Moreover, microwave plasma polymerization was also used to prepare Fe-polystyrene composite from a mixture of styrene monomer and iron pentacarbonyl.[154] The microwave plasma was used for the thermal decomposition of iron pentacarbonyl into Fe nanoparticles as

well as in the thermal self-initiation polymerization reaction of styrene by free radical mechanism. There have been several reports about the magnetic and thermal properties for iron and iron oxide nanocomposites.[154,159,160,163] In general, most of the prepared nanocomposites have been prepared from the liquid phase, yet no research has been reported from the gas phase. Gas-phase polymerization of styrene has been studied in the upward thermal diffusion cloud chamber.[164,165] The results showed that styrene in the gas phase can be made to polymerize if its vapor is doped with an extremely small charge of peroxide initiator. To the best of our knowledge, the synthesis of Ni-coated polystyrene, by gas phase polymerization of styrene, has never been reported before.

The research presented in this section involved the synthesis of Ni-coated polystyrene nanocomposite using a one-step method, in which gas phase polymerization of styrene vapor took place on the nanoparticle surfaces. 2,2'-Azobisisobutyronitrile (ABIN) was used as a free radical initiator, to initiate the polymerization of styrene vapor on Ni nanoparticle surfaces.

5-2-2 Experimental

Ni nanoparticles were first prepared by the LVCC method, which is previously described in detail in chapter three. A thin film of Ni nanoparticles and free radical initiator (2,2'-Azobisisobutyronitrile ABIN Aldrich 98%) was prepared as follows: A 70.7 mg ABIN was dissolved in 10 ml acetone (Aldrich 99.5+ %). The solution was then sonicated with 8.7 mg of Ni nanoparticles for 30 min, until the Ni nanoparticles became well dispersed in ABIN-acetone solution. The dispersed solution was kept in a Petri dish until it dried in the atmosphere. After the acetone was evaporated, a thin film of Ni nanoparticles coated with ABIN was formed on the walls of the Petri dish. The Petri dish was then placed inside the polymerization chamber.

The experimental setup is shown in Figure 82. It consists of two main parts; the first part is the monomer-feeding source unit, where the styrene vapor is generated. The second part is the polymerization chamber, where the Ni nanoparticles were coated with a thin film of polystyrene. In these experiments, liquid styrene (Aldrich 99+%) was heated in a glass bubbler using a nichrome heating jacket to produce a continuous source of styrene vapor. The heated styrene vapor was then injected into the polymerization chamber through a copper tube. The styrene injection was done by setting temperature and pressure gradients between the polymerization chamber and the glass bubbler. The copper tube was also heated to prevent the condensation of styrene vapor before reaching the chamber. The temperature of the styrene liquid was maintained at about 353.15 °K, while the chamber temperature was maintained at about 373.15 °K. The temperature was

measured from different parts of the system using T-type thermocouple wires connected to a temperature readout. The experiment starts with purging the system with an inert gas, like helium, several times. Finally, the pressure was adjusted at about 40-50 Torr helium. Following this, the styrene was heated to 353.15 °K, where its vapor pressure was about 91 Torr [166] higher than the chamber pressure.

After the experiment, the Ni/polystyrene composites were dissolved in chloroform and reprecipitated in methanol. To ensure the purity of the Ni/polystyrene, the nanocomposites were washed and rinsed several times in order to get rid of any excess styrene monomers.

Infrared spectroscopy analyses were done on Nicolet 670 FT-IR spectrophotometer. The ^{1}H-NMR spectra were done on Varian Gemini 300 MHZ spectrometer. The polymer glass temperature (T_g) was determined using differential scanning calorimetry (DSC, TA instruments Q1000 series). The DSC measurements were done under nitrogen atmosphere at a heating rate of 10 °C/min and flow rate of 100 ml/min. The gel permeation chromatography (GPC) was used to determine the average number molecular weight and polydispersity of the polystyrene film. These measurements were done on Hewlett Packard Series 1100. All the previous techniques were used to characterize and confirm the polymeric component in the prepared Ni nanocomposite film. The morphology of the Ni/Polystyrene composite was determined by the scanning electron microscope. In this experiment, a few drops of Ni nanoparticle dispersed in ABIN-acetone solution were placed on two glass slides and left to dry in the atmosphere; only one slide was exposed to the heated styrene vapor inside the polymerization chamber.

The morphology of the Ni-ABIN film on the glass substrate was examined before and after the polymerization of styrene. The x-ray diffraction (XRD) analyses for the as-prepared nanocomposites were done on an X'Pert Philips diffractometer. Finally, the dispersity of Ni particles in polystyrene was examined by the STEM technique.

5-2-3 Results and Discussion

A new method was developed to prepare polymer-coated nanoparticles in the gas phase. The preparation and characterization of Ni/Polystyrene nanocomposites was studied. The concept of this method is illustrated in Figure 83. First, the Ni nanoparticles were prepared by the LVCC method, which is previously described in detail in chapter three. The particles were then coated with ABIN initiator, which is a well-known free radical initiator for styrene polymerization in the liquid phase.[167] The ABIN-coated Ni nanoparticles were heated enough to decompose the ABIN molecule into free radicals. The particles where then exposed to the heated styrene vapor. The generated free radicals would start to attack styrene molecules and initiated the polymerization reaction in the gas phase. The consumption of styrene monomers in the polymerization reaction ensured its continuous flow from the bubbler to the chamber since the pressure difference between them would remain approximately constant. Therefore, the experiment would stop once all the liquid styrene was thermally vaporized, at this point, there is no pressure difference in the system.

The free radical polymerization mechanism for vinyl monomers, like styrene, can be found elsewhere.[167] It is also important to mention that the probability for the thermal self-initiation styrene polymerization in the gas phase is also present in these experiments. The thermal self-initiation process of styrene is expected to yield a low molecular weight polymer, under the experimental conditions used of temperature and pressure, compared with the styrene polymerization with ABIN free radical initiator. For example, the temperature conditions in these experiments was set higher than the

temperature required to decompose and generate free radicals from ABIN (~ 60 °C)[168] but lower than the temperature required for thermal polymerization of styrene (~ 90 °C)[169] to ensure that mainly a free radical polymerization adduct initiated with ABIN.

Displayed in Figure 84 are the FT-IR absorption spectra for styrene and polystyrene, which were purchased from Aldrich chemicals, along with the Ni/Polystyrene prepared by the gas phase polymerization. By comparing the three spectra, it was obvious that there was a perfect match between the Ni/Polystyrene composite and the pure polystyrene absorption spectra. The Ni/Polystyrene composite spectrum showed absorption features between 2850-2950 cm^{-1} corresponding to the stretching vibration of C-H bond (sp^3 hybridization) absorption, which confirmed the opening of the vinyl group in styrene monomer (ph-CH=CH_2) and the formation of polystyrene. The mismatch between the styrene and the prepared nanocomposite spectra, shown in Figure 84, also confirmed that.

Another piece of evidence confirming the polymerization of styrene in the gas phase came from the proton NMR data. In Figure 85 the ^{1}H-NMR spectra of Ni/Polystyrene nanocomposites along with that of polystyrene beads purchased from Aldrich chemicals are shown. The ^{1}H-NMR spectra shows peak broadening, which is common in polymeric compounds due to the distribution of the chemical shift factor due to different proton couplings. There were no peaks observed between 5-6 ppm in Ni/polystyrene nanocomposite spectrum, which was indicative of styrene absence, since styrene has absorption at chemical shift values of 5.737 and 5.225 ppm.[166] Two sets of absorptions were observed at chemical shifts between 6-7 ppm and between 1-2 ppm.

They were assigned to the aromatic protons of polystyrene rings and the protons of the sp^3 carbons in the aliphatic portion of polystyrene, respectively. The prepared nanocomposites show more peak broadenings compared to reference polystyrene. This might be due to longer polymer chains.

Displayed in Figure 86 is the morphology before and after styrene polymerization. It is clear from the SEM images that the texture of the deposits becomes rougher after the polymerization took place due to the coverage and formation of polystyrene on the Ni-coated substrate.

The average molecular weight of the prepared polymer was determined by GPC analysis. The results showed that the weight average molecular weight was about 76,000 amu and the polymer polydispersity was 3.2. Shown in Figure 87 are the polymer size distribution, obtained from the GPC, for styrene and Ni/Polystyrene composite, respectively. It can be seen that a broad size distribution appeared between 6-9 min., which was assigned to the polystyrene. Meanwhile, for pure styrene a sharper peak appeared at a latter time, after 10 min. The styrene peak had a relatively narrow size distribution, due to its low molecular weight and small polydispersity. The glass transition temperature (T_g) for Ni-polystyrene composite was also measured. In Figure 88 the DSC analysis is shown, where a T_g of 100.57 °C was obtained. The thermal stability of the prepared Ni/polystyrene was similar to that of the pure polystyrene (T_g = 100 °C).[168]

The metal component in the nanocomposites was examined by the x-ray diffraction analysis. The diffraction pattern of Ni nanoparticles before and after the

polymerization of styrene is shown in Figure 89. The diffraction peaks at the scattering angles (2θ) of 44.47, 51.79, 76.35 and 92.97 were assigned to (111), (200), (220) and (311) planes of face centered cubic (FCC) crystal lattice of pure Ni. After Ni particles were coated with polystyrene, the XRD pattern showed an amorphous diffraction pattern with some peaks at (2θ) equals 44.44 and 51.56 assigned to the (111) and (200) planes, respectively. This result confirms that crystalline Ni particles were embedded in amorphous matrix of polystyrene. The STEM micrographs shown in Figure 90, displays the dispersive nature of Ni nanoparticles embedded in the polystyrene matrix. Ni particles, with an average size of less than 100 nm, were randomly distributed in the polymer matrix with some particle agglomeration.

In conclusion, this developed technique for the gas phase polymerization is a promising technique. For example, it could be used as an online polymer coating method, directly from the gas phase.

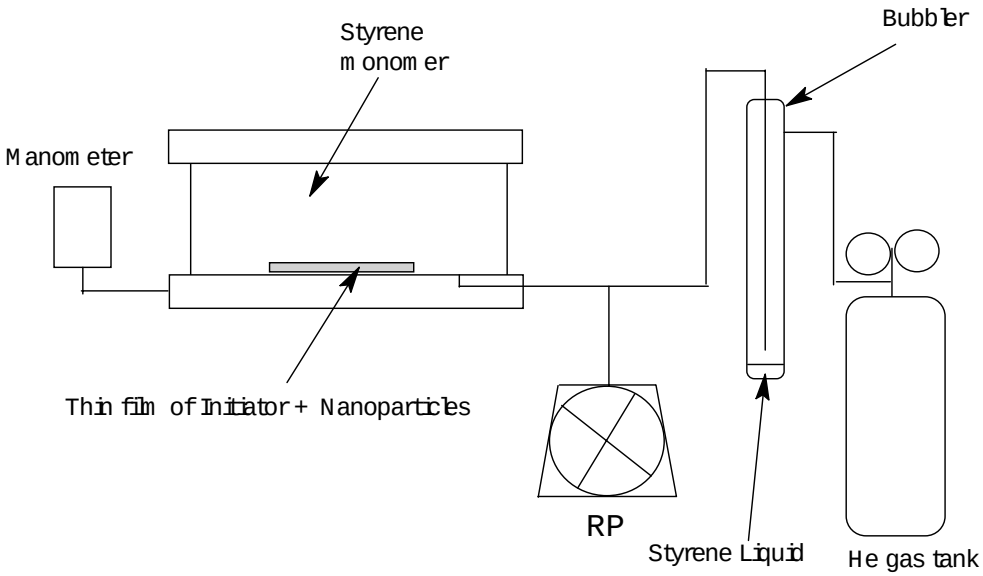

Figure 82. Experimental set-up for the gas phase polymerization of styrene.

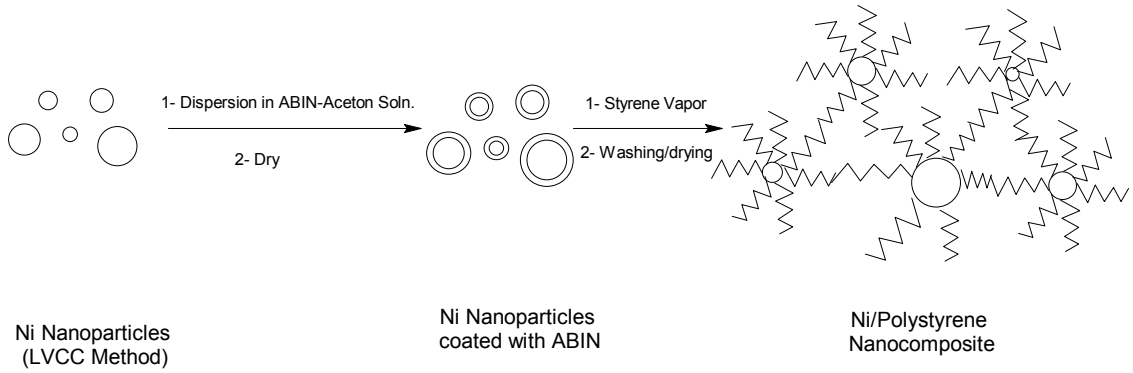

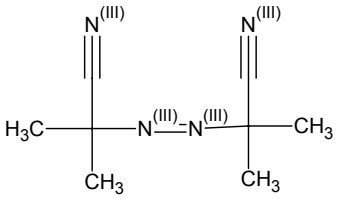

ABIN = 2,2'-Azo-bis-isobutyronitrile

Figure 83. A cartoon illustrating the concept of gas phase polymerization on nanoparticle surfaces.

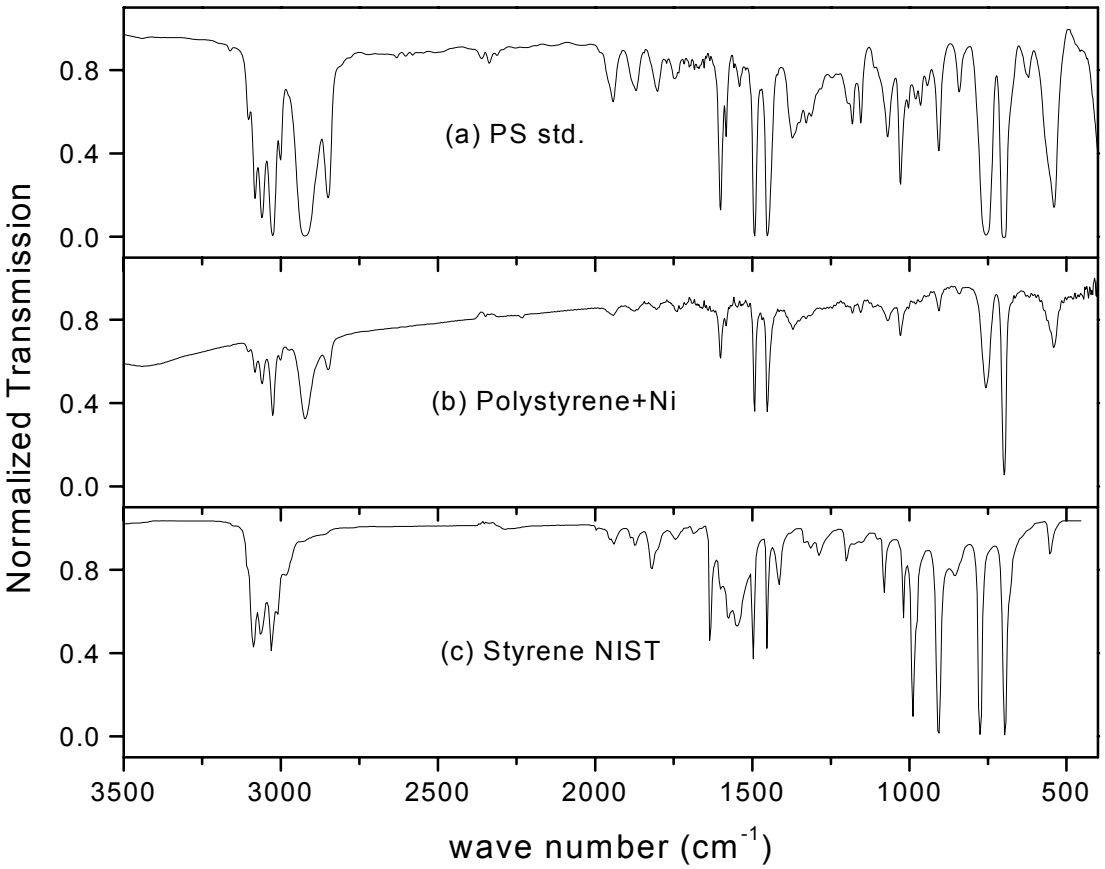

Figure 84. A comparison between FTIR of a) PS standard, b) Ni-polystyrene and c) styrene monomer.

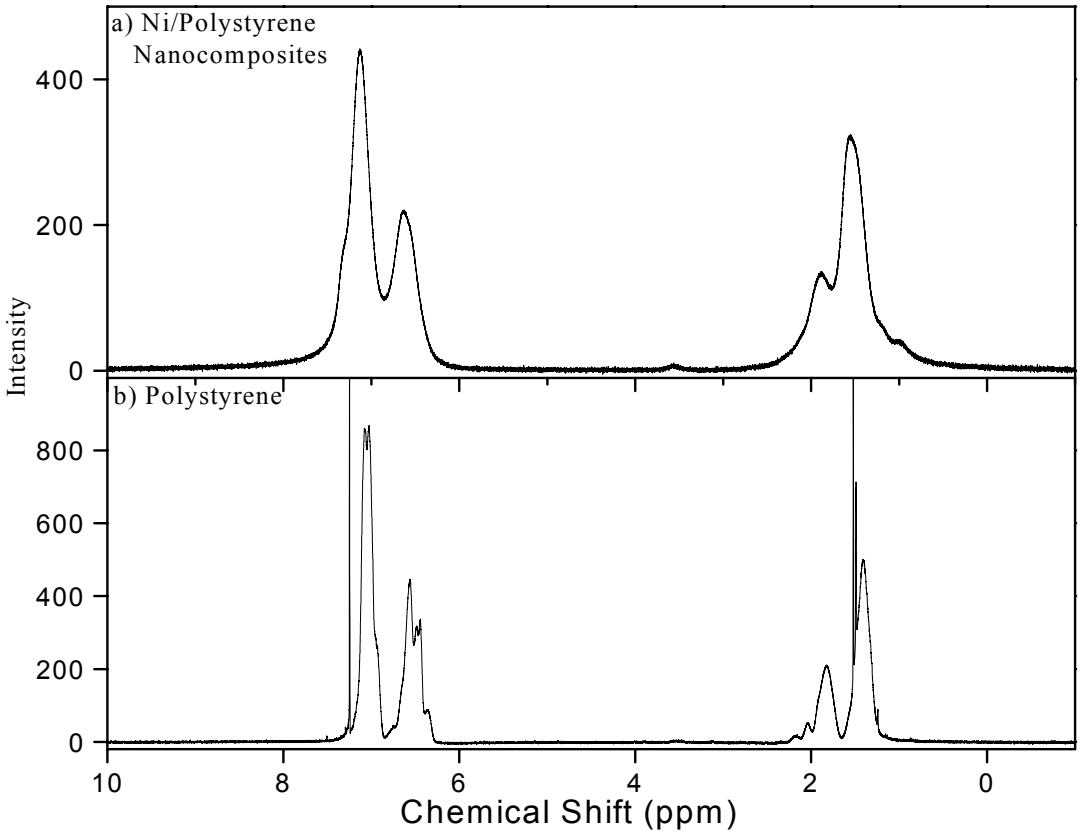

Figure 85. H-NMR spectra for a) Ni-Polystyrene nanocomposites and b) polystyrene from Aldrich.

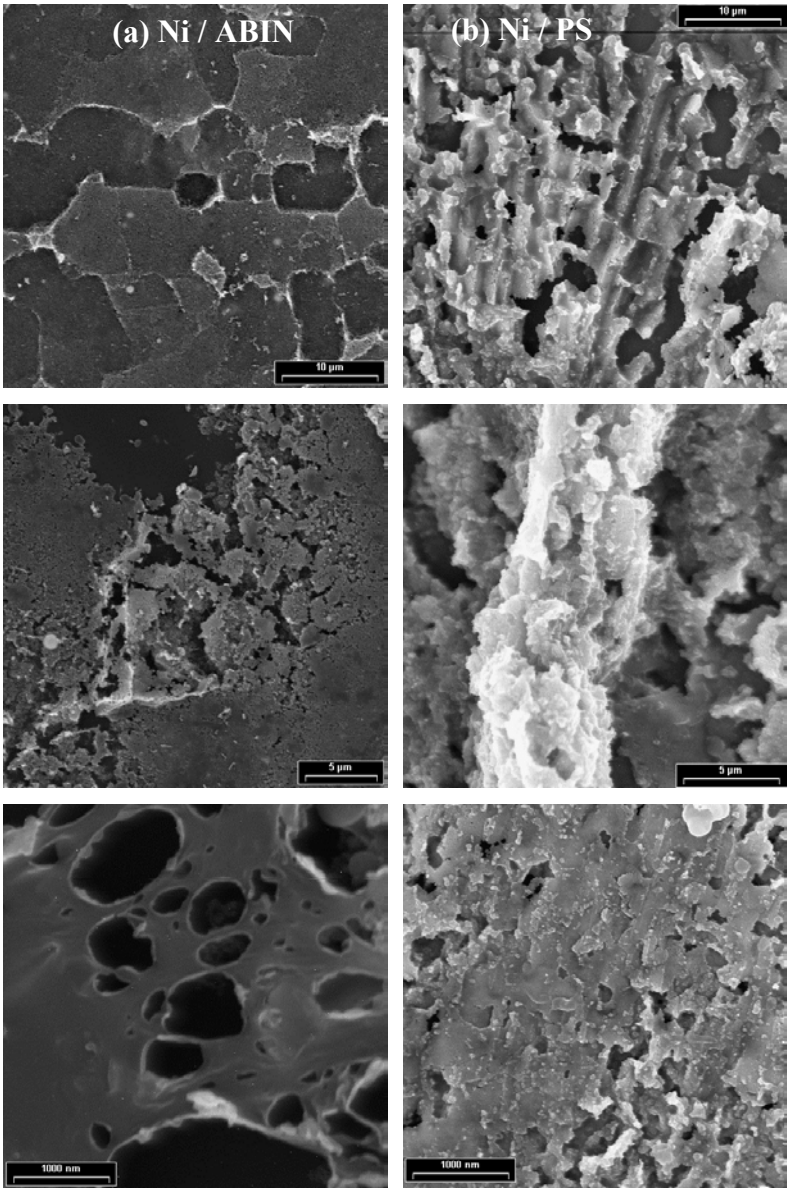

Figure 86. a) Ni nanoparticles with the initiator (ABIN) before polymerization and b) Ni nanoparticles with the initiator after styrene polymerization. The scale bar is 10, 5 and 1 µm from top to bottom.

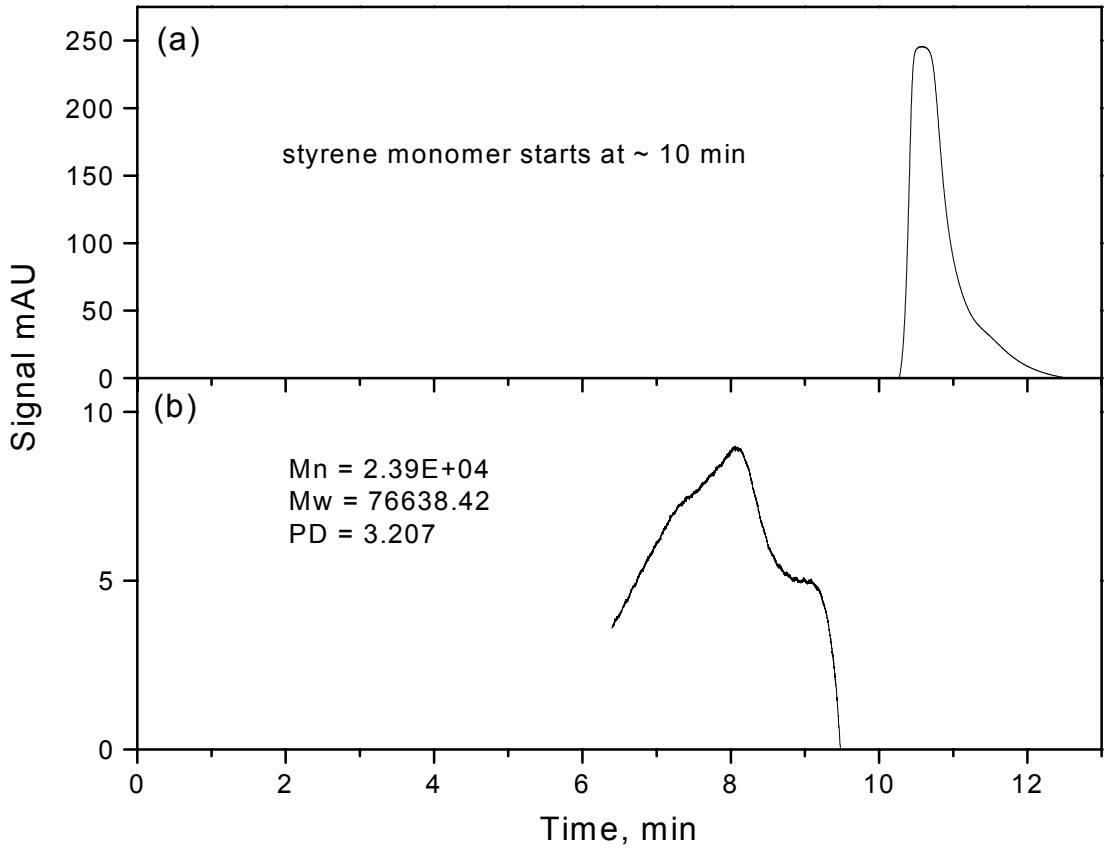

Figure 87. GPC analysis for a) styrene monomer and b) Ni-polystyrene.

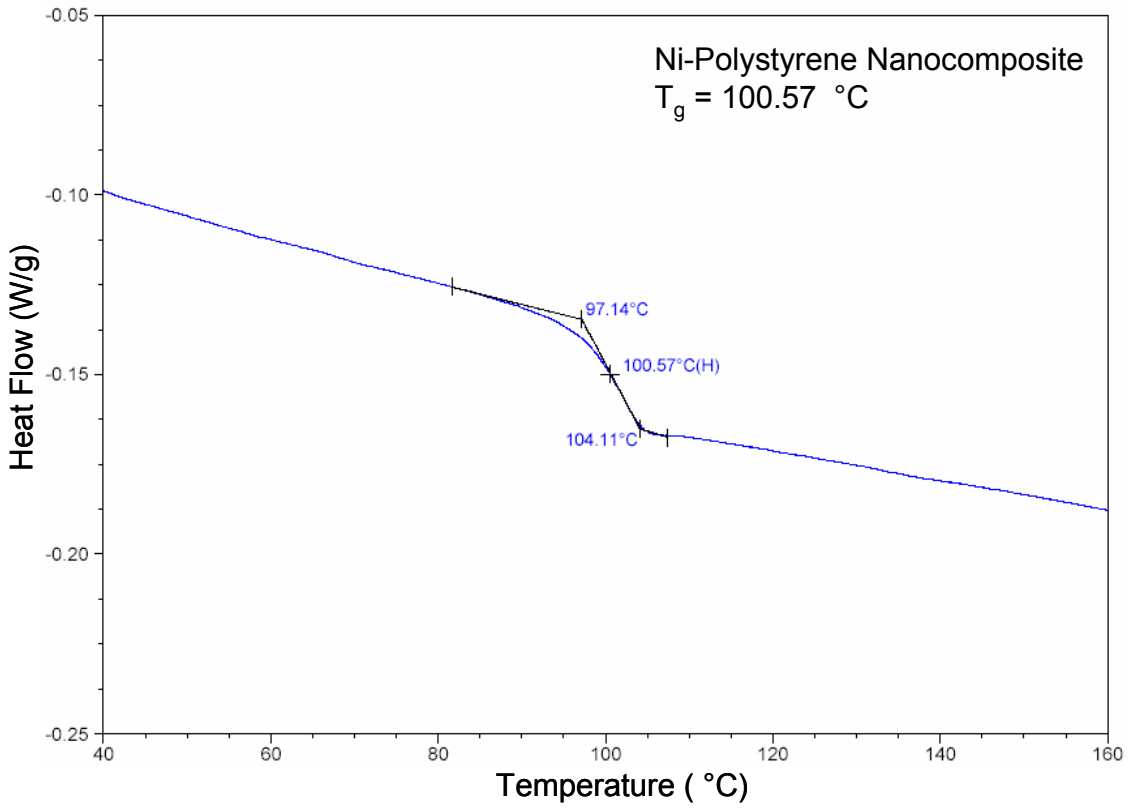

Figure 88. DSC analysis for Ni-polystyrene film with T_g = 100.57 °C.

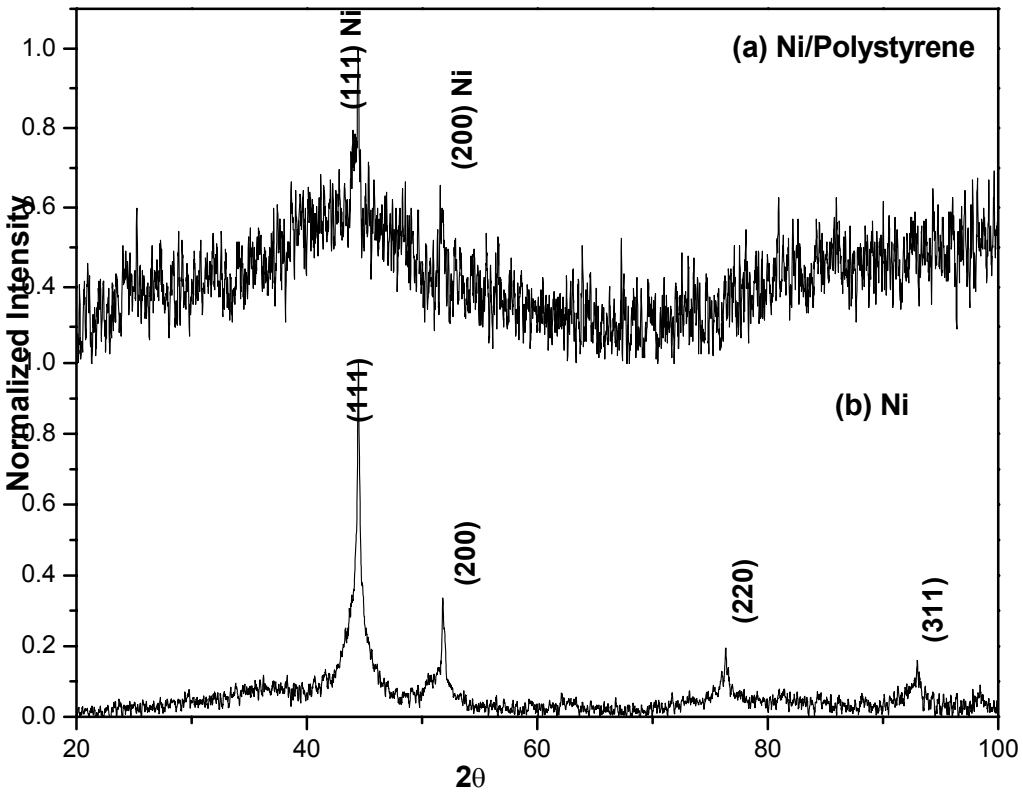

Figure 89. XRD for pure Ni nanoparticles before coating with polystyrene (a) and Ni-polystyrene nanocomposites after coating (b).

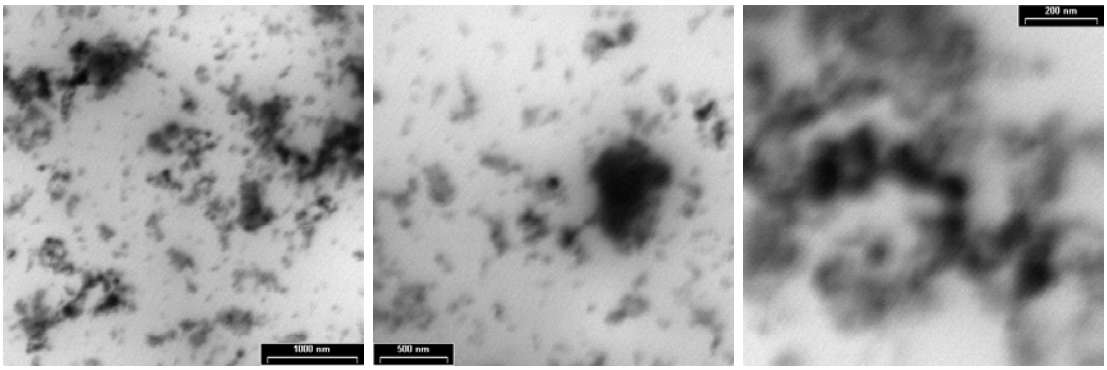

Figure 90. Scanning transmission electron micrograph for Ni nanocomposite prepared by coating Ni nanoparticles with polystyrene, using the gas phase polymerization on nanoparticle surfaces.

Chapter 6 Summary and Conclusions

This research deals with the nucleation and nanoparticle's formation from supersaturated vapors. In Chapter Two, the homogeneous nucleation of 2,2,2-trifluoroethanol using an upward thermal diffusion cloud chamber was presented. Specifically, its critical supersaturations in the temperature range between 266-296 K was studied. The experimental results were compared to the classical nucleation theory and to the scaled and corresponding states models. Interestingly, the comparison reveals that the classical prediction matches the experimental date very nicely. This result is unexpected since trifluoroethanol is a polar molecule (μ = 2.03 D)[170] and, hence, its nucleation barrier is expected to increase due to dipole-dipole interactions within the nucleating clusters. The critical supersaturations for different polar substances[28,171] have been reported before and they showed higher values compared to the classical predictions. One of the parameters, which could play an important role in the predictive power of the classical nucleation theory, is the accuracy of the physical properties used in the theory, such as, the vapor pressure and the surface tension. The surface tension of trifluoroethanol has never been measured experimentally before. Therefore, its surface tension was calculated, which could include some error factor in terms of accuracy. In the classical nucleation theory, the free energy of nucleation is proportional to the cube of the surface

tension. Therefore, any small error could result in a significant change in the classical predictions.

On the other hand, by using the corresponding states model, trifluoroethanol results showed a slight deviation from simple fluids. The scaled law predicts the critical supersaturations of trifluoroethanol correctly. Moreover, it also predicts the critical temperature (T_c) of trifluoroethanol within 1% accuracy.

The condensation of supersaturated vapors of trifluoroethanol on magnesium nanoparticles as discussed in Chapter Four was also studied. In this work, the vapor supersaturation was adjusted below that required for homogeneous nucleation. The effects of different factors, such as the supersaturation, the electric field, the pressure and the laser power, have been studied. The number of droplets detected, following the laser pulse, increases as the supersaturation and pressure inside the chamber was increased. Meanwhile, it decreases as the electric field and the laser power inside the chamber was increased. Increasing the supersaturation results in activating, almost all the magnesium particles generated by laser vaporization. On the other hand, increasing the pressure results in increasing the residence time of nanoparticles inside the chamber, and hence more collision with the trifluoroethanol results. It was observed that increasing the electric field, increases the electrical mobility of charged particles generated by laser. Therefore, a significant fraction is allowed to drift quickly through the nucleation zone before it is activated. The results also showed that there was almost no sign preference on the condensation of trifluoroethanol on charged particles. Finally, by increasing the laser

ablation power, bigger particles are ejected from the magnesium metal surfaces and fewer particles are capable of inducing this heterogeneous nucleation.

The laser vaporization controlled condensation (LVCC) method was used to prepare nanoparticles from the vapor phase, as presented in Chapter Three. A simple method is used to prepare intermetallic nanoparticles of nickel and iron aluminides, where micron-size mixtures of metal powders, of desired composition, are ablated simultaneously by a second harmonic generation of a Nd:YAG laser. For example, results showed that NiAl alloy nanoparticles were prepared when a mixture of nickel (52 atomic%) and aluminum (48 atomic%) metal powders was vaporized. Only one phase is observed (NiAl), even when the composition of the powder mixture varied. For instance, when the aluminum content in the powder mixture was increased, only NiAl alloy nanoparticles and some excess of aluminum nanoparticles were observed that increased as Al content in the powder mixture increased. These results could be explained in terms of the stability of NiAl phase over other possible phases that could also be formed, since NiAl has the highest heat of formation. It is also important to mention, that the alloy formation in the vapor phase depends on many factors, including the vapor pressure of the metallic components and the diffusion coefficient of the metal atoms.

The influence of electric field on the formation of nanoassemblies and fiber-like structures has been also studied. The results showed that there is an electric field threshold required to induce these filaments formation. The strength of the electric field is a material dependent. For example, intermetallic nanoparticles required less electric field compared to metallic and semiconductor nanoparticles to induce filaments formation.

Different experiments have been carried out to understand the filament formation, such as the effect of oxidation and the strength of the electric field used. These results were explained in terms of an electrostatic model, where the electric field played an important role in the polarization of neutral and charged particles generated during the LVCC process.

The LVCC method was also coupled with the differential mobility analyzer in order to prepare monodispersed nanoparticles. The effect of the electric field applied to the LVCC chamber on the size distribution of FeAl nanoparticles was studied. The results showed that the electrostatic force is suitable for collecting a specific size of nanoparticles, since the electrical velocity of particles is proportional to the size. The effect of different temperature gradients that were applied between the chamber plates on the size distribution of Si nanoparticles generated in the LVCC chamber was investigated. The results showed that the thermophoretic force is available for collecting all particle sizes on the cold plate, since it did not depend on the particle size.

The formation of Au-Ag alloy nanoparticles in the vapor phase by the LVCC method using designed targets of compressed Au and Ag micron-sized powder mixtures of selected compositions were also investigated. The five selected targets used in this work represent the compositions of pure Au, $Au_{0.47}Ag_{0.53}$, $Au_{0.29}Ag_{0.71}$, $Au_{0.17}Ag_{0.83}$ and pure Ag. Only one characteristic plasmon peak was observed in the absorption spectra of the alloy nanoparticles (blue-shifted with increasing the silver content) and exhibits a linear dependence on the composition of the nanoparticles. The effects of laser irradiation on the size distribution of the alloy nanoparticles showed two major effects: the first is

the particle size reduction (fragmentation), which is observed when a second harmonic generation of a Nd:YAG laser (532 nm) was used to irradiate water-dispersed Ag-Au nanoparticles, compared to using the fundamental (1064 nm) irradiation. The main reason for this effect is the vicinity of the gold plasmon absorption at (520 nm), which is very close to the laser wavelength used (532 nm). Therefore, the absorpitivity of gold at 532 nm is better than at 1064 nm, which results in melting and fragmentation of the original particles. The second effect is the dispersity of the particles in water (colloidal formation) after laser irradiation.

In the last Chapter, new methods to prepare nanoparticle-polymer composites from the vapor phase were investigated. In the first method, the laser plasma was used to prepare a cross-linked polymer resin made by introducing 1,3-butadiene monomers in the LVCC chamber followed by laser ablation of different metal targets. Similar results have been observed when nickel, platinum and iron aluminide nanoparticle were used, indicating that the laser plasma is the initiator for this reaction.

In the second method, a free radical-thermally initiated polymerization reaction to polymerize the styrene monomer vapor on the surfaces of activated nickel nanoparticles was used. The polymer component in the nanocomposite showed a weight average molecular weight of about 76,000 amu and T_g of 100.57 °C. The characterization of the nanoparticle component showed that, the nickel particles were randomly dispersed in the polymer matrix.

Literature Cited

Literature Cited

(1) Abraham, F. F. "Homogeneous Nucleation Theory" *(Academic, New York, 1974)*.

(2) Kashchiev, D. "Nucleation: Basic Theory with Applications" *(Academic, New York, 1974)*.

(3) Oxtoby, D. W. "Homogeneous nucleation: theory and experiment" *J. Phys.Condens. Matter* **1992**, *4*, 7627.

(4) Laaksonen, A.; Talanquer, V.; Oxtoby, D. W. "Nucleation: Measurements, theory, and atmospheric applications" *Annual Review of Physical Chemistry* **1995**, *46*, 489.

(5) Shiraki, K.; Nishikawa, K.; Goto, Y. "Trifluoroethanol-induced stabilization of the a-helical structure of b-lactoglobulin: implication for non-hierarchical protein folding" *Journal of Molecular Biology* **1995**, *245*, 180.

(6) Jayaraman, G.; Kumar, T. K. S.; Arunkumar, A. I.; Yu, C. "2,2,2-Trifluoroethanol induces helical conformation in an all b-sheet protein" *Biochemical and Biophysical Research Communications* **1996**, *222*, 33.

(7) Stoilov, Y. Y. "Fluorocarbons as volatile surfactants" *Langmuir* **1998**, *14*, 5685.

(8) Abedalsayed, V.; Ibrahim, Y.; Rusyniak, M.; Rabeony, M.; El-Shall, M. S. "Fluoroalcohols as nucleating agents in supersaturated vapors: Efficient clustering with water in the vapor phase" *Journal of Chemical Physics* **2001**, *115*, 2897.

(9) Edelstein, A. S.; Cammarata, R. C.; Editors *Nanomaterials: Synthesis, Properties and Applications*, 1996.

(10) Liz-Marzan, L. M.; Kamat, P. V.; Editors *Nanoscale Materials*, 2003.

(11) El-Shall, M. S.; Li, S. "Synthesis and characterization of metal and semiconductor nanoparticles" *Advances in Metal and Semiconductor Clusters* **1998**, *4*, 115.

(12) Li, S.; Silvers, S. J.; El-Shall, M. S. "Surface Oxidation and Luminescence Properties of Weblike Agglomeration of Silicon Nanocrystals Produced by a Laser Vaporization-Controlled Condensation Technique" *Journal of Physical Chemistry B* **1997**, *101*, 1794.

(13) Li, S.; Germanenko, I. N.; El-Shall, M. S. "Semiconductor Nanoparticles in Contact: Quenching of the Photoluminescence from Silicon Nanocrystals by WO3 Nanoparticles Suspended in Solution" *Journal of Physical Chemistry B* **1998**, *102*, 7319.

(14) Hermanson, K. O.; Lumsdon, S. O.; Williams, J. P.; Kater, E. W.; Velev, O. D. "Dielectrophoretic assembly of electrically functional microwires from nanoparticle suspensions" *Science (Washington, DC, United States)* **2001**, *294*, 1082.

(15) Chandrasekharan, N.; Kamat, P. V. "Assembling gold nanoparticles as nanostructured films using an electrophoretic approach" *Nano Letters* **2001**, *1*, 67.

(16) Hayward, R. C.; Saville, A.; Aksay, A. "Electrophoretic assembly of colloidal crystals with optically tunable micropatterns" *Nature (London)* **2000**, *404*, 56.

(17) Yuan, Y. J.; Andrews, M. K.; Marlow, B. K. "Chaining and dendrite formation of gold particles" *Applied Physics Letters* **2004**, *85*, 130.

(18) Bradley, J.-C.; Chen, H.-M.; Crawford, J.; Eckert, J.; Ernazarova, K.; Kurzeja, T.; Lin, M.; McGee, M.; Nadler, W.; Stephens, S. G. "Creating electrical contacts between metal particles using directed electrochemical growth" *Nature (London)* **1997**, *389*, 268.

(19) Bradley, J.-C.; Crawford, J.; McGee, M.; Stephens, S. G. "A contactless method for the directed formation of submicrometer copper wires" *Journal of the Electrochemical Society* **1998**, *145*, L45.

(20) Seto, T.; Nakamoto, T.; Okuyama, K.; Adachi, M.; Kuga, Y.; Takeuchi, K. "Size distribution measurement of nanometer-sized aerosol particles using DMA under low-pressure conditions" *Journal of Aerosol Science* **1997**, *28*, 193.

(21) Hale, B. N.; Kulmala, M.; Editors *Proceedings of the 15th International Conference on Nucleation and Atmospheric Aerosols 2000, held 6-11 August 2000, in Rolla, Missouri. [In: AIP Conf. Proc., 2000; 534]*, 2000.

(22) Ruzicka, K.; Majer, V. "Simultaneous treatment of vapor pressures and related thermal data between the triple and normal boiling temperatures for n-alkanes C5-C20" *Journal of Physical and Chemical Reference Data* **1994**, *23*, 1.

(23) Hale, B. N. "Application of a scaled homogeneous nucleation-rate formalism to experimental data at T .mchlt. Tc" *Physical Review A: Atomic, Molecular, and Optical Physics* **1986**, *33*, 4156.

(24) Hale, B. N. "The scaling of nucleation rates" *Metallurgical Transactions A: Physical Metallurgy and Materials Science* **1992**, *23A*, 1863.

(25) McGraw, R. "A corresponding states correlation of the homogeneous nucleation thresholds of supercooled vapors" *Journal of Chemical Physics* **1981**, *75*, 5514.

(26) Russell, Y. G.; Heist, R. H. "Homogeneous nucleation in associated vapors. II. Formic and propanoic acids" *Journal of Chemical Physics* **1978**, *69*, 3723.

(27) Heist, R. H.; Colling, K. M.; DuPuis, C. S. "Homogeneous nucleation in associated vapors. I. Acetic acid" *Journal of Chemical Physics* **1976**, *65*, 5147.

(28) Wright, D.; Caldwell, R.; El-Shall, M. S. "Vapor phase homogeneous nucleation of acetonitrile: the effect of dipole-dipole interaction" *Chemical Physics Letters* **1991**, *176*, 46.

(29) Rusyniak, M.; Abdelsayed, V.; Campbell, J.; El-Shall, M. S. "Vapor Phase Homogeneous Nucleation of Higher Alkanes: Dodecane, Hexadecane, and Octadecane. 1. Critical Supersaturation and Nucleation Rate Measurements" *Journal of Physical Chemistry B* **2001**, *105*, 11866.

(30) Katz, J. L. "Condensation of a supersaturated vapor. I. Homogeneous nucleation of the n-alkanes" *Journal of Chemical Physics* **1970**, *52*, 4733.

(31) Fisk, J. A.; Katz, J. L. "Condensation of supersaturated vapors. X. Pressure and nonideal gas effects" *Journal of Chemical Physics* **1996**, *104*, 8649.

(32) Becker, C.; Reiss, H.; Heist, R. H. "Estimation of thermophysical properties of a large polar molecule and application to homogeneous nucleation of l-menthol" *Journal of Chemical Physics* **1978**, *68*, 3585.

(33) Heist, R. H. "Homogeneous Nucleation of Vapors: Critical Supersaturation Measurements for Methanol, Ethanol, 1-Propanol, and 2-Propanol" *Journal of Physical Chemistry* **1995**, *99*, 16792.

(34) Katz, J. L.; Scoppa, C. J., II; Kumar, N. G.; Mirabel, P. "Condensation of a supersaturated vapor. II. Homogeneous nucleation of the normal alkyl benzenes" *Journal of Chemical Physics* **1975**, *62*, 448.

(35) Katz, J. L.; Mirabel, P.; Scoppa, C. J., II; Virkler, T. L. "Condensation of supersaturated vapor. III. The homogeneous nucleation of carbon tetrachloride, chloroform, Freon 11 (CCl3F), and 1,1,2,2-tetrachloroethane" *Journal of Chemical Physics* **1976**, *65*, 382.

(36) Kane, D.; El-Shall, M. S. "Condensation of supersaturated vapors of hydrogen bonding molecules: Ethylene glycol, propylene glycol, trimethylene glycol, and glycerol" *Journal of Chemical Physics* **1996**, *105*, 7617.

(37) Pitzer, K. S.; Lippmann, D. Z.; Curl, R. F., Jr.; Huggins, C. M.; Petersen, D. E. "Volumetric and thermodynamic properties of fluids. II. Compressibility factor, vapor pressure, and entropy of vaporization" *Journal of the American Chemical Society* **1955**, *77*, 3433.

(38) Baehr, H. D.; Klobasa, F.; Scharf, R. "Vapor pressure and liquid and gas densities of 2,2,2,-trifluoroethanol" *International Journal of Thermophysics* **1989**, *10*, 577.

(39) Kabata, Y.; Yamaguchi, S.; Takiguchi, Y.; Uematsu, M. "Measurements of the vapor pressure of 2,2,2-trifluoroethanol in the temperature range from 320 K to 400 K" *Journal of Chemical Thermodynamics* **1991**, *23*, 671.

(40) Fuller, E. N.; Ensley, K.; Giddings, J. C. "Diffusion of halogenated hydrocarbons in helium. The effect of structure on collision cross sections" *Journal of Physical Chemistry* **1969**, *73*, 3679.

(41) Rochester, C. H.; Symonds, J. R. "Thermodynamic studies of fluoro alcohols. 1. Vapor pressures and enthalpies of vaporization" *Journal of the Chemical Society, Faraday Transactions 1: Physical Chemistry in Condensed Phases* **1973**, *69*, 1267.

(42) Malhotra, R.; Woolf, L. A. "Thermodynamic properties of 2,2,2-trifluoroethanol" *International Journal of Thermophysics* **1991**, *12*, 397.

(43) Reid, R. C.; Prausnitz, J. M.; Poling, B. E. *The Properties of Gases and Liquids*, 1987.

(44) Curtiss, L. A.; Frurip, D. J.; Blander, M. "Studies of hydrogen bonding in the vapor phase by measurement of thermal conductivity and molecular orbital calculations. 2,2,2-Trifluoroethanol" *Journal of the American Chemical Society* **1978**, *100*, 79.

(45) Pithawalla, Y. B.; El-Shall, M. S.; Deevi, S. C.; Stroem, V.; Rao, K. V. "Synthesis of Magnetic Intermetallic FeAl Nanoparticles from a Non-Magnetic Bulk Alloy" *Journal of Physical Chemistry B* **2001**, *105*, 2085.

(46) Pithawalla, Y. B.; El Shall, M. S.; Deevi, S. C. "Synthesis and characterization of nanocrystalline iron aluminide particles" *Intermetallics* **2000**, *8*, 1225.

(47) Carlisle, J. A.; Germanenko, I. N.; Pithawalla, Y. B.; El-Shall, M. S. "Morphology, photoluminescence and electronic structure in oxidized silicon nanoclusters" *Journal of Electron Spectroscopy and Related Phenomena* **2001**, *114-116*, 229.

(48) Paszti, Z.; Peto, G.; Horvath, Z. E.; Karacs, A. "Laser ablation induced formation of nanoparticles and nanocrystal networks" *Applied Surface Science* **2000**, *168*, 114.

(49) Angleraud, B.; Girault, C.; Champeaux, C.; Garrelie, F.; Germain, C.; Catherinot, A. "Study of the expansion of the laser ablation plume above a boron nitride target" *Applied Surface Science* **1996**, *96-98*, 117.

(50) Reddy, B. V.; Deevi, S. C. "Thermophysical properties of FeAl (Fe-40 at.%Al)" *Intermetallics* **2000**, *8*, 1369.

(51) Deevi, S. C.; Sikka, V. K. "Nickel and iron aluminides: an overview on properties, processing, and applications" *Intermetallics* **1996**, *4*, 357.

(52) Maziasz, P. J.; Goodwin, G. M.; Alexander, D. J.; Viswanathan, S. "Alloy development and processing effects for FeAl iron aluminides: an overview" *International Symposium on Nickel and Iron Aluminides: Processing, Properties, and Applications, Proceedings from Materials Week'96, Cincinnati, Oct. 7-9, 1996* **1997**, 157.

(53) McFadden, S. X.; Valiev, R. Z.; Mukherjee, A. K. "Superplasticity in nanocrystalline Ni3Al" *Materials Science & Engineering, A: Structural Materials: Properties, Microstructure and Processing* **2001**, *A319-321*, 849.

(54) Pithawalla, Y. B.; Deevi, S. C.; El-Shall, M. S. "Preparation of ultrafine and nanocrystalline FeAl powders" *Materials Science & Engineering, A: Structural Materials: Properties, Microstructure and Processing* **2002**, *A329-A331*, 92.

(55) He, L.; Ma, E. "Nanophase metallic alloys consolidated from powders prepared by mechanical alloying" *Materials Science & Engineering, A: Structural Materials: Properties, Microstructure and Processing* **1995**, *A204*, 240.

(56) Liu, T.; Shao, H.; Li, X. "Oxidation behaviour of Fe3Al nanoparticles prepared by hydrogen plasma-metal reaction" *Nanotechnology* **2003**, *14*, 542.

(57) Liu, T.; Shao, H.; Li, X. "Synthesis of Fe-Al nanoparticles by hydrogen plasma-metal reaction" *Journal of Physics: Condensed Matter* **2003**, *15*, 2507.

(58) Haber, J. A.; Gunda, N. V.; Balbach, J. J.; Conradi, M. S.; Buhro, W. E. "Chemical syntheses of nanocrystalline nickel aluminides" *Chemistry of Materials* **2000**, *12*, 973.

(59) Dong, S.; Hou, P.; Cheng, H.; Yang, H.; Zou, G. "Fabrication of intermetallic NiAl by self-propagating high-temperature synthesis reaction using aluminum nanopowder under high pressure" *Journal of Physics: Condensed Matter* **2002**, *14*, 11023.

(60) Dong, S.; Hou, P.; Yang, H.; Zou, G. "Synthesis of intermetallic NiAl by SHS reaction using coarse-grained nickel and ultrafine-grained aluminum produced by wire electrical explosion" *Intermetallics* **2002**, *10*, 217.

(61) Emsley, J.; Editor *The Elements, 3rd Edition*, 1996.

(62) Liu, T.; Leng, Y.; Li, X. "Preparation and characteristics of Fe3Al nanoparticles by hydrogen plasma-metal reaction" *Solid State Communications* **2003**, *125*, 391.

(63) Chrifi-Alaoui, F. Z.; Nassik, M.; Mahdouk, K.; Gachon, J. C. "Enthalpies of formation of the Al-Ni intermetallic compounds" *Journal of Alloys and Compounds* **2004**, *364*, 121.

(64) Smith, P. A.; Nordquist, C. D.; Jackson, T. N.; Mayer, T. S.; Martin, B. R.; Mbindyo, J.; Mallouk, T. E. "Electric-field assisted assembly and alignment of metallic nanowires" *Applied Physics Letters* **2000**, *77*, 1399.

(65) Wu, Y.; Yang, B. "Effects of Localized Electric Field on the Growth of Carbon Nanowalls" *Nano Letters* **2002**, *2*, 355.

(66) Murakoshi, K.; Tanaka, H.; Sawai, Y.; Nakato, Y. "Effect of photoirradiation and external electric field on structural change of metal nanodots in solution" *Surface Science* **2003**, *532-535*, 1109.

(67) Murakoshi, K.; Tanaka, H.; Sawai, Y.; Nakato, Y. "Photoinduced Structural Changes of Silver Nanoparticles on Glass Substrate in Solution under an Electric Field" *Journal of Physical Chemistry B* **2002**, *106*, 3041.

(68) Muramoto, J.; Sakamoto, I.; Nakata, Y.; Okada, T.; Maeda, M. "Influence of electric field on the behavior of Si nanoparticles generated by laser ablation" *Applied Physics Letters* **1999**, *75*, 751.

(69) Lee, G. H.; Huh, S. H.; Park, J. W.; Ri, H. C.; Jeong, J. W. "Arrays of ferromagnetic iron and cobalt nanocluster wires" *Journal of Physical Chemistry B* **2002**, *106*, 2123.

(70) El-Shall, M. S.; Abdelsayed, V.; Pithawalla, Y. B.; Alsharaeh, E.; Deevi, S. C. "Vapor Phase Growth and Assembly of Metallic, Intermetallic, Carbon, and Silicon Nanoparticle Filaments" *Journal of Physical Chemistry B* **2003**, *107*, 2882.

(71) Pohl, H. A. "Dielectrophoresis" *Cambridge University Press: London* **1978**.

(72) PCPDFWIN X-ray Database, Version 2.00; (JCPDS-ICDD), 1998.

(73) Cullity, B. D. *Elements of X-Ray Diffraction. 2nd Ed*, 1978.

(74) Ogawa, K.; Vogt, T.; Ullmann, M.; Johnson, S.; Friedlander, S. K. "Elastic properties of nanoparticle chain aggregates of TiO2, Al2O3, and Fe2O3 generated by laser ablation" *Journal of Applied Physics* **2000**, *87*, 63.

(75) Suh, Y. J.; Ullmann, M.; Friedlander, S. K.; Park, K. Y. "Elastic behavior of nanoparticle chain aggregates (NCA): Effects of substrate on NCA stretching and first observations by a high-speed camera" *Journal of Physical Chemistry B* **2001**, *105*, 11796.

(76) Orii, T.; Hirasawa, M.; Seto, T. "Tunable, narrow-band light emission from size-selected Si nanoparticles produced by pulsed-laser ablation" *Applied Physics Letters* **2003**, *83*, 3395.

(77) Wu, H. P.; Okano, A.; Takayanagi, K. "Photoluminescence properties of size-selected Si nanocluster films prepared by laser ablation" *Applied Physics A: Materials Science & Processing* **2000**, *71*, 643.

(78) Ledoux, G.; Guillois, O.; Porterat, D.; Reynaud, C.; Huisken, F.; Kohn, B.; Paillard, V. "Photoluminescence properties of silicon nanocrystals as a function of their size" *Physical Review B: Condensed Matter and Materials Physics* **2000**, *62*, 15942.

(79) Ledoux, G.; Gong, J.; Huisken, F.; Guillois, O.; Reynaud, C. "Photoluminescence of size-separated silicon nanocrystals: Confirmation of quantum confinement" *Applied Physics Letters* **2002**, *80*, 4834.

(80) Sun, S.; Murray, C. B.; Weller, D.; Folks, L.; Moser, A. "Monodisperse FePt nanoparticles and ferromagnetic FePt nanocrystal superlattices" *Science (Washington, D. C.)* **2000**, *287*, 1989.

(81) Sun, S.; Zeng, H. "Size-Controlled Synthesis of Magnetite Nanoparticles" *Journal of the American Chemical Society* **2002**, *124*, 8204.

(82) Gudiksen, M. S.; Wang, J.; Lieber, C. M. "Size-Dependent Photoluminescence from Single Indium Phosphide Nanowires" *Journal of Physical Chemistry B* **2002**, *106*, 4036.

(83) Wilson, W. L.; Szajowski, P. F.; Brus, L. E. "Quantum confinement in size-selected, surface-oxidized silicon nanocrystals" *Science (Washington, DC, United States)* **1993**, *262*, 1242.

(84) Chrisey, D. B.; Hubler, G. K.; Editors *Pulsed Laser Deposition of Thin Films*, 1994.

(85) El-Shall, M. S.; Slack, W.; Vann, W.; Kane, D.; Hanley, D. "Synthesis of Nanoscale Metal Oxide Particles Using Laser Vaporization/Condensation in a Diffusion Cloud Chamber" *Journal of Physical Chemistry* **1994**, *98*, 3067.

(86) Seto, T.; Kawakami, Y.; Suzuki, N.; Hirasawa, M.; Aya, N. "Laser Synthesis of Uniform Silicon Single Nanodots" *Nano Letters* **2001**, *1*, 315.

(87) Sakiyama, K.; Koga, K.; Seto, T.; Hirasawa, M.; Orii, T. "Formation of Size-Selected Ni/NiO Core-Shell Particles by Pulsed Laser Ablation" *Journal of Physical Chemistry B* **2004**, *108*, 523.

(88) Ozawa, E.; Kawakami, Y.; Seto, T. "Formation and size control of tungsten nanoparticles produced by Nd:YAG laser irradiation" *Scripta Materialia* **2001**, *44*, 2279.

(89) Elihn, K.; Otten, F.; Boman, M.; Heszler, P.; Kruis, F. E.; Fissan, H.; Carlsson, J. O. "Size distributions and synthesis of nanoparticles by photolytic dissociation of ferrocene" *Applied Physics A: Materials Science & Processing* **2001**, *72*, 29.

(90) Marcus, R. K. "Introduction to glow discharge spectroscopies" *Glow Discharge Spectrosc.* **1993**, 1.

(91) Camata, R. P.; Hirasawa, M.; Okuyama, K.; Takeuchi, K. "Observation of aerosol formation during laser ablation using a low-pressure differential mobility analyzer" *Journal of Aerosol Science* **2000**, *31*, 391.

(92) Kelly, K. L.; Coronado, E.; Zhao, L. L.; Schatz, G. C. "The Optical Properties of Metal Nanoparticles: The Influence of Size, Shape, and Dielectric Environment" *Journal of Physical Chemistry B* **2003**, *107*, 668.

(93) Link, S.; Wang, Z. L.; El-Sayed, M. A. "Alloy Formation of Gold-Silver Nanoparticles and the Dependence of the Plasmon Absorption on Their Composition" *Journal of Physical Chemistry B* **1999**, *103*, 3529.

(94) Kim, M.-J.; Na, H.-J.; Lee, K. C.; Yoo, E. A.; Lee, M. "Preparation and characterization of Au-Ag and Au-Cu alloy nanoparticles in chloroform" *Journal of Materials Chemistry* **2003**, *13*, 1789.

(95) He, S. T.; Xie, S. S.; Yao, J. N.; Gao, H. J.; Pang, S. J. "Self-assembled two-dimensional superlattice of Au-Ag alloy nanocrystals" *Applied Physics Letters* **2002**, *81*, 150.

(96) Han, S. W.; Kim, Y.; Kim, K. "Dodecanethiol-derivatized Au/Ag bimetallic nanoparticles: TEM, UV/VIS, XPS, and FTIR analysis" *Journal of Colloid and Interface Science* **1998**, *208*, 272.

(97) Chen, D.-H.; Chen, C.-J. "Formation and characterization of Au-Ag bimetallic nanoparticles in water-in-oil microemulsions" *Journal of Materials Chemistry* **2002**, *12*, 1557.

(98) Papavassiliou, G. C. "Surface plasmons in small gold-silver alloy particles" *Journal of Physics F: Metal Physics* **1976**, *6*, L103.

(99) Takeuchi, Y.; Ida, T.; Kimura, K. "Colloidal Stability of Gold Nanoparticles in 2-Propanol under Laser Irradiation" *Journal of Physical Chemistry B* **1997**, *101*, 1322.

(100) Mafune, F.; Kohno, J.; Takeda, Y.; Kondow, T. "Full Physical Preparation of Size-Selected Gold Nanoparticles in Solution: Laser Ablation and Laser-Induced Size Control" *Journal of Physical Chemistry B* **2002**, *106*, 7575.

(101) Takami, A.; Kurita, H.; Koda, S. "Laser-Induced Size Reduction of Noble Metal Particles" *Journal of Physical Chemistry B* **1999**, *103*, 1226.

(102) Mafune, F.; Kohno, J.-y.; Takeda, Y.; Kondow, T.; Sawabe, H. "Formation and Size Control of Silver Nanoparticles by Laser Ablation in Aqueous Solution" *Journal of Physical Chemistry B* **2000**, *104*, 9111.

(103) Takami, A.; Yamada, H.; Nakano, K.; Koda, S. "Size reduction of silver particles in aqueous solution by laser irradiation" *Japanese Journal of Applied Physics, Part 2: Letters* **1996**, *35*, L781.

(104) Hodak, J. H.; Henglein, A.; Giersig, M.; Hartland, G. V. "Laser-Induced Inter-Diffusion in AuAg Core-Shell Nanoparticles" *Journal of Physical Chemistry B* **2000**, *104*, 11708.

(105) Zhang, J.; Worley, J.; Denommee, S.; Kingston, C.; Jakubek, Z. J.; Deslandes, Y.; Post, M.; Simard, B.; Braidy, N.; Botton, G. A. "Synthesis of Metal Alloy Nanoparticles in Solution by Laser Irradiation of a Metal Powder Suspension" *Journal of Physical Chemistry B* **2003**, *107*, 6920.

(106) Chen, Y.-H.; Yeh, C.-S. "A new approach for the formation of alloy nanoparticles: laser synthesis of gold-silver alloy from gold-silver colloidal mixtures" *Chemical Communications (Cambridge, United Kingdom)* **2001**, 371.

(107) Mafune, F.; Kohno, J.; Takeda, Y.; Kondow, T.; Sawabe, H. "Formation of gold nanoparticles by laser ablation in aqueous solution of surfactant" *Journal of Physical Chemistry B* **2001**, *105*, 5114.

(108) Mafune, F.; Kohno, J.-Y.; Takeda, Y.; Kondow, T. "Formation of Gold Nanonetworks and Small Gold Nanoparticles by Irradiation of Intense Pulsed Laser onto Gold Nanoparticles" *Journal of Physical Chemistry B* **2003**, *107*, 12589.

(109) Mafune, F.; Kohno, J.-y.; Takeda, Y.; Kondow, T. "Nanoscale soldering of metal nanoparticles for construction of higher-order structures" *Journal of the American Chemical Society* **2003**, *125*, 1686.

(110) Mafune, F.; Kohno, J.; Takeda, Y.; Kondow, T. "Formation of Stable Platinum Nanoparticles by Laser Ablation in Water" *Journal of Physical Chemistry B* **2003**, *107*, 4218.

(111) Link, S.; Burda, C.; Nikoobakht, B.; El-Sayed, M. A. "How long does it take to melt a gold nanorod? A femtosecond pump-probe absorption spectroscopic study" *Chemical Physics Letters* **1999**, *315*, 12.

(112) Sun, Y.; Xia, Y. "Gold and silver nanoparticles: A class of chromophores with colors tunable in the range from 400 to 750 nm" *Analyst (Cambridge, United Kingdom)* **2003**, *128*, 686.

(113) Sun, Y.; Xia, Y. "Shape-Controlled Synthesis of Gold and Silver Nanoparticles" *Science (Washington, DC, United States)* **2002**, *298*, 2176.

(114) Mallin, M. P.; Murphy, C. J. "Solution-phase synthesis of sub-10 nm Au-Ag alloy nanoparticles" *Nano Letters* **2002**, *2*, 1235.

(115) Treguer, M.; de Cointet, C.; Remita, H.; Khatouri, J.; Mostafavi, M.; Amblard, J.; Belloni, J.; de Keyzer, R. "Dose Rate Effects on Radiolytic Synthesis of

Gold-Silver Bimetallic Clusters in Solution" *Journal of Physical Chemistry B* **1998**, *102*, 4310.

(116) Lee, I.; Han, S. W.; Kim, K. "Production of Au-Ag alloy nanoparticles by laser ablation of bulk alloys" *Chemical Communications (Cambridge, United Kingdom)* **2001**, 1782.

(117) Ashcroft, N. W.; Mermin, N. D. *Solid State Physics*, 1976.

(118) Kittel, C. *Introduction to Solid State Physics. Vol. 1. 6th Ed*, 1988.

(119) Okamoto, H.; Massalski, T. B.; Editors *Phase Diagrams of Binary Gold Alloys*, 1987.

(120) Kurita, H.; Takami, A.; Koda, S. "Size reduction of gold particles in aqueous solution by pulsed laser irradiation" *Applied Physics Letters* **1998**, *72*, 789.

(121) Kohler, H. "The nucleus in, and the growth of, hygroscopic droplets" *Transactions of the Faraday Society* **1936**, *32*, 1152.

(122) Fletcher, N. H. "Size effect in heterogeneous nucleation" *Journal of Chemical Physics* **1958**, *29*, 572.

(123) Smorodin, V. Y.; Hopke, P. K. "Condensation Activation and Nucleation on Heterogeneous Aerosol Nanoparticles" *Journal of Physical Chemistry B* **2004**, *108*, 9147.

(124) Mavliev, R.; Hopke, P. K.; Wang, H.-C.; Lee, D.-W. "A transition from heterogeneous to homogeneous nucleation in the turbulent mixing CNC" *Aerosol Science and Technology* **2001**, *35*, 586.

(125) Mavliev, R.; Hopke, P. K.; Wang, H.-C.; Lee, D.-W. "Experimental Studies of Heterogeneous Nucleation in the Turbulent Mixing Condensation Nuclei Counter" *Journal of Physical Chemistry B* **2004**, *108*, 4558.

(126) Lee, D.-W.; Hopke, P. K.; Rasmussen, D. H.; Wang, H.-C.; Mavliev, R. "Comparison of Experimental and Theoretical Heterogeneous Nucleation on Ultrafine Carbon Particles" *Journal of Physical Chemistry B* **2003**, *107*, 13813.

(127) Chen, C.-C.; Tao, C.-J.; Cheng, H.-C. "Condensation of supersaturated water vapor on charged/neutral nanoparticles of glucose and monosodium glutamate" *Journal of Colloid and Interface Science* **2002**, *255*, 158.

(128) Chen, C.-C.; Tsai, W.-T. "Condensation of supersaturated n-butanol vapor on charged/neutral nanoparticles of D-mannose and L-rhamnose" *Journal of Colloid and Interface Science* **2002**, *246*, 270.

(129) Hung, C. H.; Krasnopoler, M. J.; Katz, J. L. "Condensation of a supersaturated vapor. VIII. The homogeneous nucleation of n-nonane" *Journal of Chemical Physics* **1989**, *90*, 1856.

(130) Katz, J. L.; Fisk, J. A.; Chakarov, V. M. "Condensation of a supersaturated vapor. IX. Nucleation on ions" *Journal of Chemical Physics* **1994**, *101*, 2319.

(131) Kane, D.; Daly, G. M.; El-Shall, M. S. "Condensation of Supersaturated Vapors on Benzene Ions Generated by Resonant Two-Photon Ionization: A New Technique for Ion Nucleation" *Journal of Physical Chemistry* **1995**, *99*, 7867.

(132) Wen, F. C.; McLaughlin, T.; Katz, J. L. "Photoinduced nucleation of water vapor" *Science (Washington, DC, United States)* **1978**, *200*, 769.

(133) Caldwell, R.; Wright, D.; El-Shall, M. S. "Nucleation on metal ions in supersaturated vapors" *Zeitschrift fuer Physik D: Atoms, Molecules and Clusters* **1993**, *26*, 189.

(134) Zhigilei, L. V.; Kodali, P. B. S.; Garrison, B. J. "On the threshold behavior in laser ablation of organic solids" *Chemical Physics Letters* **1997**, *276*, 269.

(135) Furusawa, H.; Sakka, T.; Ogata, Y. H. "Characterization of ablated species in laser-induced plasma plume" *Journal of Applied Physics* **2004**, *96*, 975.

(136) Wei, J.; Sun, Z.; Zhang, F.; Xu, W.; Wang, Y.; Zhou, F.; Gan, F. "Thermal melting of solid materials induced by ultrafast laser pulse irradiation as explosively homogeneous nucleation" *Chemical Physics Letters* **2004**, *392*, 415.

(137) Wijekoon, W. M. K. P.; Stry, J. J.; Prasad, P. N.; Garvey, J. F. "On the Nature of Thin Films Generated during the Laser-Assisted Molecular Beam Deposition of Metal Plasma and Organic Vapors" *Langmuir* **1996**, *12*, 4929.

(138) Wijekoon, W. M. K. P.; Lyktey, M. Y. M.; Prasad, P. N.; Garvey, J. F. "Fabrication of a thin film of an inorganic:organic composite via laser assisted molecular beam deposition" *Applied Physics Letters* **1995**, *67*, 1698.

(139) Wijekoon, W. M. K. P.; Stry, J. J.; Prasad, P. N.; Garvey, J. F. "Formation of Polymerized Thin Films during Laser Assisted Molecular Beam Deposition of Cu and Acetylene/Acetone" *Langmuir* **1995**, *11*, 27.

(140) Daly, G. M.; Pithawalla, Y. B.; Yu, Z.; El-Shall, M. S. "Interaction of Zn+ with isobutylene in the gas phase and in clusters. Metal ion induced cationic polymerization" *Chemical Physics Letters* **1995**, *237*, 97.

(141) Guo, B. C.; Wei, S.; Purnell, J.; Buzza, S.; Castleman, A. W., Jr. "Metallo-carbohedrenes [M8C12+ (M = vanadium, zirconium, hafnium, and titanium)]: a class of stable molecular cluster ions" *Science (Washington, DC, United States)* **1992**, *256*, 515.

(142) Guo, B. C.; Kerns, K. P.; Castleman, A. W., Jr. "Ti8C12+-metallo-carbohedrenes: a new class of molecular clusters?" *Science (Washington, DC, United States)* **1992**, *255*, 1411.

(143) Pilgrim, J. S.; Duncan, M. A. "Beyond metallo-carbohedrenes: growth and decomposition of metal-carbon nanocrystals" *Journal of the American Chemical Society* **1993**, *115*, 9724.

(144) Pilgrim, J. S.; Duncan, M. A. "Metallo-carbohedrenes: chromium, iron, and molybdenum analogs" *Journal of the American Chemical Society* **1993**, *115*, 6958.

(145) Pilgrim, J. S.; Duncan, M. A. "Photodissociation of metallo-carbohedrene (\"Met-Cars\") cluster cations" *Journal of the American Chemical Society* **1993**, *115*, 4395.

(146) Vann, W.; El-Shall, M. S. "Novel approach to cationic polymerization using pulsed-laser vaporization/ionization of metals" *Journal of the American Chemical Society* **1993**, *115*, 4385.

(147) Daly, G. M.; El-Shall, M. S. "Polymerization in clusters and in the gas phase using metal ions" *Zeitschrift fuer Physik D: Atoms, Molecules and Clusters* **1993**, *26*, 186.

(148) Wei, S.; Guo, B. C.; Purnell, J.; Buzza, S.; Castleman, A. W., Jr. "Metallo-carbohedrenes: formation of multicage structures" *Science (Washington, DC, United States)* **1992**, *256*, 818.

(149) Collins, D. E.; Slamovich, E. B. "Preparation of a Homogeneously Dispersed BaTiO3/Polymer Nanocomposite Thin Film" *Chemistry of Materials* **1999**, *11*, 2319.

(150) Wilson, J. L.; Poddar, P.; Frey, N. A.; Srikanth, H.; Mohomed, K.; Harmon, J. P.; Kotha, S.; Wachsmuth, J. "Synthesis and magnetic properties of polymer nanocomposites with embedded iron nanoparticles" *Journal of Applied Physics* **2004**, *95*, 1439.

(151) Lopez, D.; Cendoya, I.; Torres, F.; Tejada, J.; Mijangos, C. "Preparation and characterization of polystyrene-based magnetic nanocomposites. Thermal, mechanical and magnetic properties" *Polymer Engineering and Science* **2001**, *41*, 1845.

(152) Du, H.; Xu, G. Q.; Chin, W. S.; Huang, L.; Ji, W. "Synthesis, Characterization, and Nonlinear Optical Properties of Hybridized CdS-Polystyrene Nanocomposites" *Chemistry of Materials* **2002**, *14*, 4473.

(153) Lim, W. P.; Low, H. Y.; Chin, W. S. "IR-Luminescent PbS-Polystyrene Nanocomposites Prepared from Random Ionomers in Solution" *Journal of Physical Chemistry B* **2004**, *108*, 13093.

(154) Srikanth, H.; Hajndl, R.; Chirinos, C.; Sanders, J.; Sampath, A.; Sudarshan, T. S. "Magnetic studies of polymer-coated Fe nanoparticles synthesized by microwave plasma polymerization" *Applied Physics Letters* **2001**, *79*, 3503.

(155) Kumar, R. V.; Koltypin, Y.; Palchik, O.; Gedanken, A. "Preparation and characterization of nickel-polystyrene nanocomposite by ultrasound irradiation" *Journal of Applied Polymer Science* **2002**, *86*, 160.

(156) Breen, M. L.; Dinsmore, A. D.; Pink, R. H.; Qadri, S. B.; Ratna, B. R. "Sonochemically produced ZnS-coated polystyrene core-shell particles for use in photonic crystals" *Langmuir* **2001**, *17*, 903.

(157) Wu, D.; Ge, X.; Zhang, Z.; Wang, M.; Zhang, S. "Novel One-Step Route for Synthesizing CdS/Polystyrene Nanocomposite Hollow Spheres" *Langmuir* **2004**, *20*, 5192.

(158) Liu, H.; Ge, X.; Zhu, Y.; Xu, X.; Zhang, Z.; Zhang, M. "Synthesis and characterization of polyacrylamide-nickel amorphous nanocomposites by g-irradiation" *Materials Letters* **2000**, *46*, 205.

(159) Kuljanin, J.; Marinovic-Cincovic, M.; Zec, S.; Comor, M. I.; Nedeljkovic, J. M. "Influence of Fe2O3-filler on the thermal properties of polystyrene" *Journal of Materials Science Letters* **2003**, *22*, 235.

(160) Govindaraj, B.; Sastry, N. V.; Venkataraman, A. "Thermal and morphological studies on g-Fe2O3 polystyrene composites and the affect of additives" *Journal of Applied Polymer Science* **2004**, *93*, 778.

(161) Rakhimov, R. R.; Jackson, E. M.; Hwang, J. S.; Prokof'ev, A. I.; Alexandrov, I. A.; Karmilov, A. Y.; Aleksandrov, A. I. "Mechanochemical synthesis of Co, Ni, Fe nanoparticles in polymer matrices" *Journal of Applied Physics* **2004**, *95*, 7133.

(162) Fendler, J. H.; Editor *Nanoparticles and Nanostructured Films: Preparation, Characterization and Applications*, 1998.

(163) Burke, N. A. D.; Stoever, H. D. H.; Dawson, F. P. "Magnetic Nanocomposites: Preparation and Characterization of Polymer-Coated Iron Nanoparticles" *Chemistry of Materials* **2002**, *14*, 4752.

(164) El-Shall, M. S.; Reiss, H. "Observation of homogeneous gas-phase catalyzed vinyl polymerization" *Journal of Physical Chemistry* **1988**, *92*, 1021.

(165) El-Shall, M. S.; Bahta, A.; Rabeony, H.; Reiss, H. "Homogeneous gas phase thermal polymerization of styrene" *Journal of Chemical Physics* **1987**, *87*, 1329.

(166) http://webbook.nist.gov/chemistry/.

(167) Odian, G. *Principles of Polymerization. 2nd Ed*, 1981.

(168) Anon. "Handbook of Radical Vinyl Polymerization by Munmaya K. Mishra and Yusuf Yaggi" *Vysokomolekulyarnye Soedineniya, Seriya A i Seriya B* **1999**, *41*, 384.

(169) Pryor, W. A.; Lasswell, L. D. "Mechanism of the initiation step in the self-initiated \"thermal\" polymerization of vinyl monomers" *Polymer Preprints (American Chemical Society, Division of Polymer Chemistry)* **1970**, *11*, 713.

(170) Dean, J. A. *Lange's Handbook of Chemistry, Fourteenth Edition*, 1992.

(171) Wright, D.; Caldwell, R.; Moxely, C.; El-Shall, M. S. "Homogeneous nucleation in supersaturated vapors of polar molecules: acetonitrile, benzonitrile, nitromethane, and nitrobenzene" *Journal of Chemical Physics* **1993**, *98*, 3356.

VITA

Victor Maher Ibrahim Abdelsayed

Personal Information:

Current Address:

Phone No.:

E-mail:

Education:

2000-present	Ph.D. in Physical Chemistry, Virginia Commonwealth University, USA. Title of Dissertation: "Experimental Studies on Nucleation, Nanoparticle's Formation and Polymerization from the Vapor Phase".
1993-1996	B.Sc. in Chemistry at Ain Shams University, Egypt.

Teaching Experience

2000-2003	Teaching assistant at Virginia Commonwealth University, USA. 100 level recitations for general chemistry, 300 level lab. for quantitative analysis chemistry.
1997-1999	Demonstrator at Ain Shams University, Egypt. General Chemistry (Organic, Inorganic and Physical Chemistry) for 1st year students. Physical Chemistry (Kinetics, Surface Chemistry, and Electrochemistry) 3rd and 4th year students

Academic Honors

1994-1996	Best Student Reward from Chemistry department, Ain Shams University, Egypt.
2003-2004	Chemistry Department Fellowship, and School of Graduate Studies Fellowship, Virginia Commonwealth University, USA.

Research Interests

2000-present (Virginia-USA)	1- Synthesis and Characterization of Nanoparticles Prepared from the Vapor Phase by Laser Vaporization Techniques. 2- Optical Properties of Size-Selected Au-Ag alloy nanoparticles prepared from the vapor phase. 3- Homogeneous and Surface Induced Nucleation. 4- Condensation of Supersaturated Vapors on Metal Nanoparticles Using the Upward Thermal Diffusion Cloud Chambers. 5- Developing of New Methods for Gas Phase Polymerization on Nanoparticle Surfaces. Including Plasma-Induced and Free-Radical Polymerization methods. 6- Labview Programming.
1997-1999 (Cairo-Egypt)	Corrosion of Steel in Aqueous Citrate Solutions (Corrosion and Electroplating).

List of Papers Published

1- Vapor Phase Growth and Assembly of Metallic, Intermetallic, Carbon, and Silicon Nanoparticle Filaments
M. Samy El-Shall, Victor Abdelsayed, Yezdi B. Pithawalla, and Edreese Alsharaeh Seetharama C. Deevi
J. Phys. Chem. B, 107 (13), 2882 -2886, **2003**.

2- Vapor Phase Homogeneous Nucleation of Higher Alkanes: Dodecane, Hexadecane, and Octadecane. 1. Critical Supersaturation and Nucleation Rate Measurements
Mark Rusyniak, Victor Abdelsayed, Jason Campbell, and M. Samy El-Shall*
J. Phys. Chem. B, 105 (47), 11866 -11872, **2001.**

3- Fluoroalcohols as nucleating agents in supersaturated vapors: Efficient clustering with water in the vapor phase.
V. Abedalsayed, Y. Ibrahim, M. Rusyniak, M. Rabeony, and M. S. El-Shall
J CHEM PHYS 115 (7): 2897-2900, **2001.**

Oral Presentation and Posters presented at meetings

1- "Vapor Phase Synthesis and Characterization of Au-Ag Alloy Nanoparticles"
V. Abedalsayed, M. S. El-Shall.
Oral presentation at SERMAC **2004.**

2- "Nanoparticles from the vapor phase: Semiconductor, Metallic, Intermetallic, and Nanoparticles in Polymers".
V. Abedalsayed, M. S. El-Shall
Oral presentation at SERMAC **2002.**
3- Synthesis, characterization and novel application of semiconductor and intermetallic nanoparticles: from science to technology.
Pithawalla Y, Abdelsayed V, Germanenko IN, El-Shall MS.[Conference Paper]
Proceedings of the 22nd Riso International Symposium on Materials Science. Riso Nat. Lab. **2001***, pp.365-70*. Roskilde, Denmark.
4- Surfactant induced nucleation in supersaturated vapors
M. Rusyniak, Y. Ibrahim, V. Abedalsayed, M. Rabeony, and M. S. El-Shall.*Proceedings of the 15th International Conference of Nucleation and atmospheric aerosols* **2000***, Rolla, Missouri (USA).*